Studies into tau reconstruction, missing transverse energy and photon induced processes with the ATLAS detector at the LHC

Dissertation

zur

Erlangung des Doktorgrades (Dr. rer. nat.)

der

Mathematisch-Naturwissenschaftlichen Fakultät

der

Rheinischen Friedrich-Wilhelms-Universität Bonn

vorgelegt von

Robindra P. Prabhu

aus

Oslo, Norwegen

Bonn 2010

Angefertigt mit Genehmigung der Mathematisch-Naturwissenschaftlichen Fakultät der Rheinisch Friedrich-Wilhelms-Universität Bonn

Abstract

The ATLAS experiment is currently recording data from proton-proton collisions delivered by CERN's Large Hadron Collider. As more data is amassed, studies of both Standard Model processes and searches for new physics beyond will intensify. This dissertation presents a three-part study providing new methods to help facilitate these efforts.

The first part presents a novel τ-reconstruction algorithm for ATLAS inspired by the ideas of particle flow calorimetry. The algorithm is distinguished from traditional τ-reconstruction approaches in ATLAS, insofar that it seeks to recognize decay topologies consistent with a (hadronically) decaying τ-lepton using resolved energy flow objects in the calorimeters. This procedure allows for an early classification of τ-candidates according to their decay mode and the use of decay mode specific discrimination against fakes. A detailed discussion of the algorithm is provided along with early performance results derived from simulated data.

The second part presents a Monte Carlo simulation tool which by way of a pseudorapidity-dependent parametrization of the jet energy resolution, provides a probabilistic estimate for the magnitude of instrumental contributions to missing transverse energy arising from jet fluctuations. The principles of the method are outlined and it is shown how the method can be used to populate tails of simulated missing transverse energy distributions suffering from low statistics.

The third part explores the prospect of detecting photon-induced leptonic final states in early data. Such processes are distinguished from the more copious hadronic interactions at the LHC by cleaner final states void of hadronic debris, however the soft character of the final state leptons poses challenges to both trigger and offline selections. New trigger items enabling the online selection of such final states are presented, along with a study into the feasibility of detecting the two-photon exchange process $pp(\gamma\gamma \to \tau\tau)p^*p^*$ with early data.

Acknowledgements

Over the last few years, I have had the great fortune to interact with a number of remarkable people without whose guidance, insight, perspectives and sharing of ideas this work would likely never have seen the light of day.

I warmly thank *Prof. Dr. Klaus Desch* for "taking me under his wings", for the opportunity to work on a range of different topics and for providing me with the space to develop and mature and bring the ideas presented herein to fruition. His encouragement, patience and support has been greatly appreciated.

I am equally grateful to *Peter Wienemann*, for the countless discussions we have had on physics and equally often on topics far beyond. His impressive insight and clarity of thought has been an invaluable resource to me throughout and a constant source of wonder and amazement.

I must also thank *Sebastian Fleischmann* and *Mark Hodgkinson* for the fruitful collaboration on the development of PanTau. Their ideas and contributions were instrumental to parts of the work presented in Chapter 2 and I am thankful for all that they have taught me along the way.

I am grateful for the encouragement, constructive critizisms and many helpful comments provided by both *Wolfgang Mader* and *Yann Coadou* in their capacity as conveners for the ATLAS Tau Working Group during my stay at CERN. *Frank Paige*, *Shoji Asai* and *Dan Tovey* also deserve mention for their friendly and helpful input to the studies presented in Chapter 3.

I am hugely indebted to *Andrew Hamilton* for enthusiastically sharing his expertise on two-photon physics at hadron colliders and to *Andrew Pilkington*, *Olya Igonkina*, *Anna Sfyrla* and *Stefania Xella* for all their help and assistance with the ATLAS trigger. A big word of thanks also to *Christian Limbach* for enthusiastically carrying the torch onwards.

I would go amiss if I failed to acknowledge the efforts of all the people who have provided invaluable technical support during the course of this work: *Michael Heldmann* and *Michael Dührssen* for introducing me to the ATLAS software and for patiently answering all my tedious questions during my early months in Freiburg. The "Bonner" administrators have always been equally friendly, accommodating and quick to answer queries. Last but not least, I am indebted to *Wolfgang Ehrenfeld* and the *NAF support team* for accommodating all my computing needs over the last few years.

I wish to thank all members of the HEP groups in Freiburg and Bonn for the good company and friendly atmosphere, especially all the people with whom I have at one point or another shared an office. The "Kochgruppe" at CERN should not be forgotten, thank you all for making my stay at CERN all the more enjoyable. I am indebted to Peter Wienemann and Carolin Zendler for lending their keen eyes to the proof-reading of this manuscript and for the many helpful comments they both provided. *Frau Fürstenberg*

and *Frau Streich* also both deserve a special mention for the countless occasions on which they have extended a helpful hand.

Warm and heartfelt thanks to *Carolin, Duc, Giacinto, Gisela, Henrik, Michael, Natalia, Olav* and *Zong* for all the good times we have shared and for making the past few years all the more enjoyable and worthwhile.

Finally, I wish to thank my dearest parents for their unwavering support and encouragement through thick and thin.

To my parents.

Contents

Contents

Symbols and abbreviations

EFO	**E**nergy **F**low **O**bject
$\mathbf{EFO}_q^{\pm}$	A charged *qualified* EFO
$\mathbf{EFO}^{\pm}$	A charged EFO (qualified or unqualified)
$\mathbf{EFO}^0_{\mathbf{EM}}$	An electromagnetic neutral EFO
$\mathbf{EFO}^0_{\mathbf{HAD}}$	A hadronic neutral EFO
$\mathbf{EFO}^{\mathcal{C}}$	An EFO satisfying a criterion $\mathcal{C}$
τ_{vis}	The visible portion of a τ-lepton decay
τ_{had}	A hadronically decaying τ-lepton
τ_{lep}	A leptonically decaying τ-lepton
τ-induced seed	A seed to PanTau originating from a true τ-lepton decay
jet-induced seed	A seed to PanTau originating from the hadronisation of quarks and gluons
$\not{E}_T$	Reconstructed missing transverse energy
$\not{E}_T^{\mathbf{fake}}$	Reconstructed missing transverse energy from instrumental effects
$\langle \not{E}_T \rangle$	Total estimated missing transverse energy at the generator level
$\langle \not{E}_T^{\mathbf{fake}} \rangle$	Estimated instrumental transverse missing energy at the generator level

Chapter 1

Introduction

1.1 Preface

This document goes into print just as the LHC experiments are presenting some of their first results from recorded collision data to the world scientific community. It is an exciting and fitting occasion to put the ideas and results of the last few years to paper.

The operation of the LHC has long been anticipated, and when eventually ramped up to its design performance is expected to probe a new energy domain often dubbed the *terascale*. At these energies, answers to some of the most perplexing problems in modern fundamental physics are widely expected to be found. To better understand the relevance of the LHC and the proper context of the studies presented herein, it is useful to briefly review some of the key issues it is hoped the LHC will address.

The physical landscape at the onset of the LHC

The Standard Model of particle physics represents the culmination of almost a century of efforts to understand the fundamental constituents of matter and the interactions governing their behaviour.

The model provides an apt description of the inner structure of the cosmos in terms of two classes of fundamental particles known as *fermions* and *bosons*. The fermions include six *quarks* and six *leptons* which together constitute the known matter content of the Universe. Interactions between fermions are mediated through the exchange of bosons. Each particle is uniquely described by way of its mass and quantum numbers, which in turn specify the interaction modes available to the particle.

All fermions may interact by way of the electroweak force (mediated by photons (γ), and the massive gauge bosons $W^{\pm}, Z^0$), the mathematical description of which elegantly synthesizes the electromagnetic and weak interactions into a unified electroweak theory based on a so-called $SU(2)_L \times U(1)_Y$ gauge symmetry group. The quarks are additionally sensitive to the *strong* force (mediated by gluons (g)), the dynamics of which is described by the theory of Quantum Chromodynamics (QCD), based on the symmetry group $SU(3)_C$.

The Standard Model provides a unified description of the electromagnetic, weak and strong interactions between the fundamental particles and has been widely shown to be in good agreement with (nearly) all experimental data collected to date[1]. The electroweak sector of the Standard Model has proven itself remarkably successful, with several predictions tested to per-mille level accuracy with experimental data. Beyond just describing experimental data, the Standard Model has successfully predicted the existence of fundamental particles which were only later discovered by experiments, including the gluon (DESY, 1979), the $W^{\pm}$ and Z^0 bosons (CERN, 1983) and the top-quark (Fermilab, 1995). With the more recent discovery of the tau-neutrino ν_τ (Fermilab, 2000), only *one* particle predicted by the Standard Model remains experimentally unverified: the long elusive *Higgs boson*. Without it (or a similar agent responsible for breaking the electroweak symmetry), all the particles of the Standard Model remain massless in contradiction with observation and the internal consistency of the theory is radically challenged. Profound importance is therefore placed on its discovery at the LHC, where it is widely agreed that the mechanism of electroweak symmetry breaking will be conclusively probed.

Hierarchy problem and new physics beyond the Standard Model

While finding the Higgs and measuring its properties would complete the Standard Model, it is widely believed that the model will "break down" when probing energies at the terascale. While there are several causes for this belief, one profound reason can be found within the structure of the theory itself:

In the Standard Model, the observable mass of a particle is expressed in terms of its bare mass and so-called higher-order loop corrections. When calculating quantum corrections to the Higgs mass (m_H) arising from virtual particle exchanges, mathematical problems arise in the form of infinities. A common approach for circumventing such problems, is to "cut-off" the theory at some high energy scale Λ at which a more complete (yet unknown) theory is believed to manifest itself. Doing so introduces corrective contributions to m_H^2 of $\mathcal{O}(\Lambda^2)$, so that unless there is some uncanny fine-tuned cancellation of the quantum corrections to the Higgs mass, it becomes very difficult to explain why the same mass should be so much smaller than the mass scale at which this new physics appears [1].

This feature of the Standard Model is known as the *hierarchy problem*. Rejecting the notion of a fine-tuned cancellation as "unnatural", it is widely believed that the corrections should cancel in a systematic fashion. Such a solution is offered by the theory of supersymmetry (SUSY) which postulates an underlying symmetry between fermions and bosons, pairing each Standard Model fermionic (bosonic) degree of freedom with a corresponding bosonic (fermionic) *superpartner* with the same quantum numbers. While this pairing procedure doubles the register of fundamental particles, quantum corrections between virtual fermions and bosons cancel to produce a Higgs mass that no longer appears unnaturally fine-tuned. Moreover, SUSY provides an elegant framework to facilitate the unification of strong, weak and electromagnetic forces into a single Grand Unified Theory (GUT).

---

[1]Excepting the measurement of neutrino-oscillations which imply massive neutrinos as well as the existence of right-handed neutrinos.

Despite its many attractions which have beguiled theorists for more than three decades, experimental data has failed to lend conclusive support to SUSY to date. It follows that any *exact* supersymmetry where every superpartner is mass degenerate with its Standard Model partner, has to be broken. While the masses of SUSY particles (should they exist) may be large enough to have evaded the sensitivity reach of previous experiments, there are several good reasons to expect the masses of SUSY particles to lie around the terascale, from which at least two derive from current experimental data [2]:

For one, the low Higgs mass favoured by current electroweak precision measurements agrees well with the predictions of terascale SUSY.

Secondly, many models of SUSY furnish viable candidates for so-called *Dark Matter*. Astrophysical data indicate that visible matter from Standard Model particles only account for $\sim 4\%$ of the energy density in the Universe. The precise nature of Dark Matter, thought to account for as much as $\sim 22\%$ of the Universe, remains an open question in particle physics and cosmology. While the majority of SUSY particles are expected to be heavy and quick to decay, the lightest SUSY particle (LSP) may be stable and only weakly interacting. If SUSY manifests itself at the terascale and the LSP has a mass below a ~ 1 TeV, it would make an ideal candidate for Dark Matter.

A brief outline of the studies presented in this document

At the time of writing, the ATLAS experiment has collected ~ 300 nb^{-1} of collision data at a center of mass energy of $\sqrt{s} = 7$ TeV. As the experiment continues to accumulate more data and the beam energy is further increased, searches for signs of new physics beyond the current frontier is likely to intensify. These efforts require robust tools to both effectively analyse and extract information from recorded raw data and to facilitate the development of new studies using Monte Carlo simulations. They also require a solid understanding of the capabilities, limitations and working performance of the experimental apparatus, as indeed insurance that the potential for extracting measurements of the underlying physics is exploited to the full.

This document presents three separate studies to this end:

The **first study** delves into the topic of reconstruction and identification of hadronically decaying τ-leptons in ATLAS. As is detailed in Chapter 2, it is anticipated that τ-leptons will be important probes for new physics at the LHC, both in the context of Higgs and SUSY. A great deal of emphasis is therefore placed on retaining good τ-identification capabilities in the comparatively harsh experimental climate of the LHC. Rather than optimizing existing reconstruction tools, the studies herein aim to pave the way for a fundamentally different and complementary approach to τ-reconstruction in ATLAS. An attempt is made to factorize the physics of the τ-lepton decay from any related or non-related detector effects. A novel τ-reconstruction algorithm which seeks to identify decay topologies that are physically consistent with a hadronically decaying τ-lepton using resolved "particle"-objects in the detector is presented, and its performance evaluated with simulated data.

The **second study** concerns itself with the challenges associated with the understanding of large missing transverse energy signatures in ATLAS. Often considered a smoking-gun

signature for SUSY scenarios where the LSP escapes undetected, it is vital to attain an early understanding of any instrumental effects that may falsely appear as large missing transverse energy. In the absence of real data, such studies must be performed with simulated data. Herein, a probabilistic method is presented which facilitates the simulation of comparatively rare events from processes with large production cross sections. The method was applied to official production of Monte Carlo data samples in ATLAS, and the resulting samples employed in collaboration wide studies to devise search strategies for SUSY with early data.

The **third study** aims to extend the scope for early physics measurements with ATLAS to include so-called two-photon processes. As is explained in the following, such interactions are unique in an LHC context, yielding clean final states void of the hadronic debris that accompanies most scatters at the LHC. Beyond being interesting Standard Model processes in their own right, they may also find applications in lepton reconstruction studies, luminosity determination, forward detector alignment and as control samples in searches for new physics. The challenge remains to select such events online with a trigger that is not optimized for comparatively rare processes at low transverse momenta. To meet this challenge, new triggers were devised and implemented into the ATLAS trigger menu to facilitate experimental access to generic photon-induced lepton final states. It is hoped that these triggers will facilitate the study of processes that may otherwise have been lost in data filtering. Finally, using these new triggers, a first ATLAS simulation study aiming to explore the feasibility of observing the particularly challenging process $pp \rightarrow (\gamma\gamma \rightarrow \tau\tau)p^*p^*$ with early data is presented.

The presentation of these studies is preceded by an outline of the LHC collider, its associated experiments and the experimental environment in which they operate.

1.2 The Large Hadron Collider and its experimental environment

From its early conception to its final installation and early operation, the LHC project has been a quarter of a century in the making and ranks among the most complex scientific undertakings in history. At the heart of the project is the accelerator facility, installed in the vacated 27 km tunnel of its forerunner LEP[2], at a depth of 75 m below the surface outside the CERN laboratory complex near Geneva, Switzerland. Therein, counter-rotating particle beams are brought to collide at four interaction points around which large detector systems, or *experiments*, are constructed. These include the two multi-purpose experiments, ATLAS and CMS, principally designed to search for new phenomena, as well as two special-purpose experiments, LHCb and ALICE, dedicated to the study of CP-violation and rare decays in the B-meson sector and the study of quark-gluon plasma in heavy ion collisions, respectively. The performance of either

---

[2]The tunnel previously hosted the LEP collider (*L*arge *E*lectron *P*ositron Collider). The most powerful e^+e^- collider to date, LEP was operational from 1989 to 2000 during which time it paved the way for several precision measurements of the Standard Model.
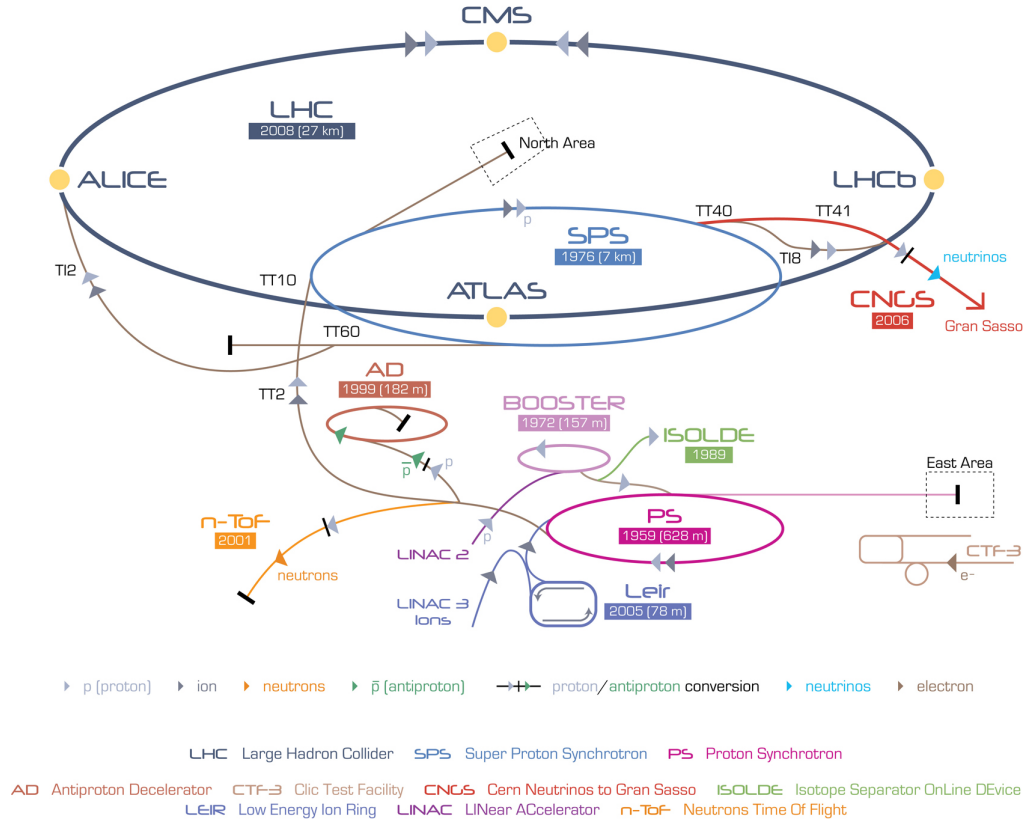
FIGURE 1.1: The CERN accelerator complex. [3]

experiment is contingent on the properties and configuration of the colliding beams delivered by the LHC accelerator.

The following sections aim to highlight some of the key parameters governing the performance of the LHC accelerator and to describe the characteristic features of the experimental environment it generates. A cursory overview of the central components of the ATLAS detector is then given with a description of how they are designed to cope with the challenges provided by the LHC environment.

1.2.1 The LHC machine

Having been constructed in the vacated LEP tunnel, the LHC profits greatly from the existing beam injection infrastructure at CERN. The various components of the accelerator chain are schematically depicted in Figure 1.1, and allow for a sequential acceleration of the protons through a series of smaller machines:

- Initially, the protons are extracted from an ionized gas of hydrogen in a duoplasmatron. After extraction, the protons are accelerated to 750 keV using quadrupole radio frequency (RF) devices and then to a further 50 MeV in the *LINAC2* linear accelerator.

- The *booster* hikes the energy up to 1.4 GeV before injecting the protons into the *Proton Synchrotron* (PS) in which they are grouped into packets of $\sim 10^{11}$ protons
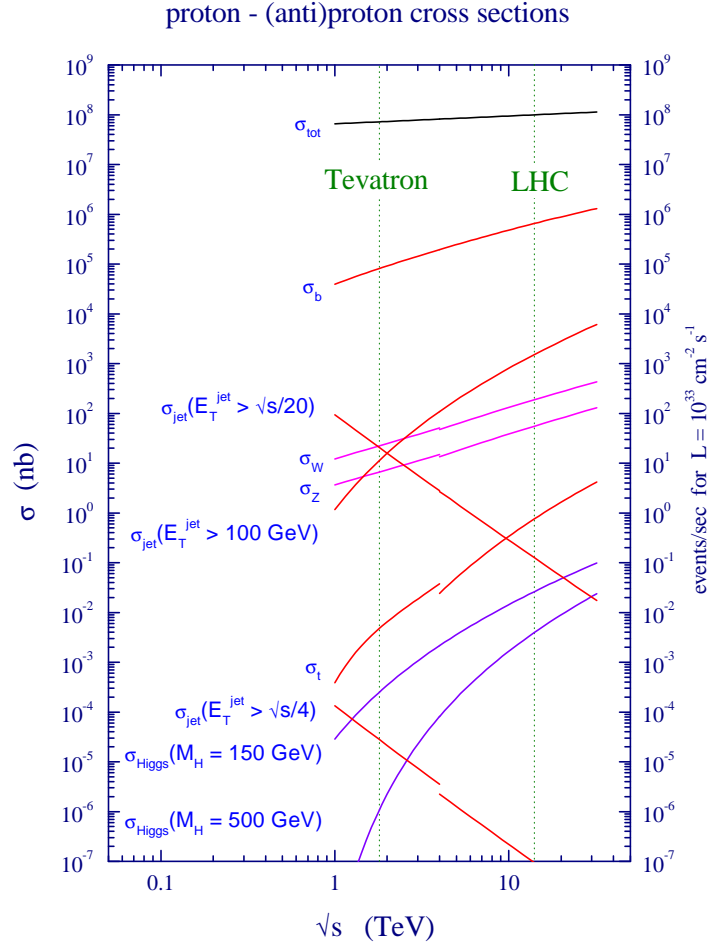
FIGURE 1.2: QCD predictions for expected hard scattering cross sections and production rates at the Tevatron ($\sqrt{s} = 1.96$ TeV) and LHC ($\sqrt{s} = 14$ TeV). [4]

("bunches"). In desired intervals ("bunch spacing"), the protons in a bunch are brought to an energy of 26 GeV.

- In the *Super Proton Synchrotron* (SPS) the proton bunches are accelerated to energies of 450 GeV, before the final injection into the LHC ring.

- Once injected, the proton bunches are accelerated about the LHC ring in two counter-rotating beams through a series of RF cavities accumulating energy at each turn. The beam trajectory is maintained by a series of powerful dipole magnets. Once the desired beam energies are reached, the counter-rotating beams can be crossed at four interaction points at which the experiments are located.

Key parameters governing the performance of the LHC machine in terms of its ability to deliver interesting collision data for the experiments, include the *energy of the colliding beams* and the *instantaneous luminosity* [5].

As is further detailed in Section 1.3, the colliding protons are composite objects. A high beam energy therefore ensures with non-negligible probabilty that collisions between constituents carrying only a fraction of the total proton energy may still ensue at high energy. An upper limit on the deliverable beam energy derives from the ability of the magnet system to keep the beams in orbit along the required trajectory. In order to deliver proton beams at the nominal energy of 7 TeV, the LHC relies on more than 1000 superconducting dipole magnets to produce the necessary 8.33 T magnetic field required to bend the beam trajectory about the ring complex.

In order to ensure experimental sensitivity to rare processes, a high beam energy must be accompanied by a sufficiently high collision rate. The *instantaneous luminosity* is a machine parameter which quantifies the interaction rate per unit cross section:

$$\mathcal{L} = \nu_{coll}\frac{N_A N_B}{A_{eff}} \tag{1.1}$$

where $N_{A,B}$ quantify the number of particles in two incoming bunches A and B, brought to collide in an effective area A_{eff} with frequency ν_{coll}. As indicated by Equation 1.1, the instantaneous luminosity can be amplified by increasing the collision frequency and particle concentration in the colliding bunches, or by reducing the effective collision area.

In order to reduce the effective collision area, powerful quadropole magnets are employed around the interaction points which serve to "squeeze" the bunches from an incoming beam spread of $\sim mm$ to a collisional beam spread of $\sim \mu m$.

Increasing the number of particles in a bunch ("bunch intensity"), will also increase the electromagnetic force field experienced by a particle in an opposing bunch. This field is highly non-linear and may render the colliding beams unstable. Such *beam-beam interactions* place an upper cap on the bunch intensity of $\sim 10^{11}$ protons per bunch [6].

Beam-beam interactions also limit the bunch concentration in the beamline. As the number of bunches per beam increases, so does the probabilty of multiple bunch interactions inside the detector volume[3]. In order to avoid additional unwanted head-on beam collisions, a slight *crossing angle* Φ of $\mathcal{O}(\sim 100\mu\text{rad})$ is introduced along the experimental insertions [5] which serve to reduce the occurrence of multiple short range interactions between bunches inside the detector volume[4].

Operating the LHC with a crossing angle comes at the cost of an increase in the effective collision area and consequently a reduction in instantaneous luminosity. Translated into beam parameters, Equation 1.1 may now be expressed as:

$$\mathcal{L} = f_{rev}\gamma\frac{N_b n_p^2}{\sigma_x \sigma_y}F(\Phi, \sigma_x, \sigma_y) \tag{1.2}$$

---

[3]The interaction regions all have $\sim$120 m straight sections were the counter-rotating beams are contained in the same beam pipe. At the nominal bunch spacing of 7.5 m (25 ns), this corresponds to $\frac{120m}{75m/2} \sim 30$ additional unwanted beam collisions per interaction region (in the absence of a crossing angle).

[4]Long range beam-beam interactions may still occur.

	LHC	Tevatron
Circumference (km)	26.7	6.3
Max. beam energy at collision (TeV)	7	1
Beam energy at injection (TeV)	0.45	0.15
Dipole field at max. beam energy (T)	8.33	4.4
Design luminosity ($cm^{-2}s^{-1}$)	10^{34}	2.1×10^{32}
Bunch spacing (ns)	24.95	396
Proton per bunch (10^{10})	11.5	27(p) / 7.5 ($\bar{p}$)
Number of bunches	2808	36
Total crossing angle (μrad)	285	0

TABLE 1.1: A comparison of main machine parameters at the LHC and Tevatron (Run II) [7, 8]

where f_{rev} is the beam revolution frequency, γ the relativistic Lorentz factor and N_b the number of bunches each containing a total number of n_p protons. The effective collision area is expressed in terms of the transverse RMS beam sizes $\sigma_{x,y}$ at the interaction point and is tempered by a geometric reduction factor $F(\Phi, \sigma_x, \sigma_y)$:

$$F(\Phi, \sigma_x, \sigma_y) = \frac{1}{\sqrt{1 + \left(\frac{\sigma_z}{\sigma^*} \tan \frac{\Phi}{2}\right)^2}} \tag{1.3}$$

which depends on the crossing angle Φ and the ratio of longitudinal to transverse beam profiles σ_z/σ^*.

When operating at design performance, the LHC will collide protons at center of mass energies corresponding to $\sqrt{s} = 14$ TeV with an instantaneous luminosity of $10^{34} cm^{-2}s^{-1}$ at crossing rate of 40 MHz. As such, LHC will significantly extend the sensitivity reach to new physics beyond the current limits provided by the Tevatron collider. Table 1.1 provides a comparison of the main machine parameters of the LHC to those of the Tevatron. Predicted cross sections and event rates for various processes are further shown in Figure 1.2.

The LHC program also includes shorter periods of collision runs with heavy ions. Such collision runs are not considered herein, but are given brief mention in Sections 1.3.4.1 and 4.7.

1.2.2 Early data prospects

The installation of the LHC commenced in 2000, during which time the LEP accelerator was still operational. The assembly was completed in the autumn of 2007 and followed by a period of commissioning during which the various sectors of the ring were gradually cooled to an operating temperature of 1.9 K. On 10 September 2008, first beams where successfully circulated in stages through the ring complex at the injection energy of 450

GeV. Several experiments along the ring collected splash[5] events, thereby demonstrating the operability of the detector apparatus.

On September 29 2008, during a powering test of the magnet circuits in Sector 3-4[6] of the LHC, a resistive zone developed in the (otherwise) superconducting electrical weld between a dipole and a quadropole magnet. Following the local breakdown of superconductivity, an electrical arc formed which punctured a liquid helium cooling enclosure around a magnet, releasing helium into the insulating vacuum of the cryostat. The subsequent pressure wave overwhelmed the escape relief valves, not only causing the release of large amounts of helium from the magnet cooling system into the tunnel, but also damaging and displacing several adjacent magnets [9]. The incident required 53 magnets to be removed from the tunnel and brought to the surface for cleaning and repair, bringing the LHC to a temporary standstill and incurring a delay of one year.

In November 2009, operation briefly resumed at the injection energy ($\sqrt{s} = 0.9$ TeV) in preparation for a longer physics run with 3.5 TeV beams. On 30 March 2010, the first collisions at $\sqrt{s} = 7$ TeV were delivered to both ATLAS and CMS. At the time of writing, it is foreseen that the LHC will continue to deliver $\sqrt{s} = 7$ TeV collisions until $\sim 1\text{fb}^{-1}$ has been collected, before commencing a longer shutdown during which the necessary preparations will be made for operation at the nominal beam energy of 7 TeV [10].

For reasons detailed in Section 1.3.6, the studies presented in Chapter 4 are very sensitive to the evolution of the instantaneous luminosity. Table 1.2 provides some projective estimates for the beam configurations and expected instantaneous luminosities for the 2010 run at $\sqrt{s} = 7$ TeV.

1.3 The phenomenology of proton-proton collisions

The potentially high center of mass energies achievable with a proton collider such as the LHC comes at the price of exceedingly complex collisions. This complexity derives in large part from the composite nature of the colliding protons and their strongly interacting initial state. Because the hard collisions at the LHC take place between the constituents of protons, the energy of the colliding quarks and gluons (partons) is not equal to the center of mass energy $\sqrt{s}$ of the incoming protons. By the same token, the longitudinal component of the four-momenta of the colliding partons is *a priori* unknown. The residual partons, which do not take part in the hard scatter, will typically carry the larger fraction of the available energy. While most of this energy will disappear down the beamline, a non-negligible fraction may still be scattered into the detector volume thereby polluting the signatures of a potentially interesting event created in the hard

---

[5]"Splash events" ensue when a beam is made to collide with an upstream target outside the detector (rather than another colliding beam inside the detector), sending a "splash" of secondary particles into the detector volume.

[6]While the other seven sectors of the LHC had been fully commissioned to hold a beam energy of 5.5 TeV prior to first beam injection on 10 September 2008, Sector 3-4 was the last sector to be commissioned and had not been powered to hold a beam of 5.5 TeV.

Phase	Energy [TeV]	N_p (10^{10})	Fill scheme	β^* [m]	$\mathcal{L}$ [$cm^{-2}s^{-1}$]
Beam commissioning, safe beam limit	3.5	2	2×2	11	2.6×10^{27}
Beam commissioning, safe beam limit, squeeze	3.5	2	$2 \times 2^*$	2	3.6×10^{28}
Bunch trains from SPS	3.5	3	43×43	2	1.7×10^{30}
	3.5	5	43×43	2	4.8×10^{30}
Increase intensity	3.5	5	156×156	2	1.7×10^{31}
	3.5	7	156×156	2	3.4×10^{31}
Introduce crossing angle, truncated 50 ns	3.5	7	50ns - 144**	2.5	2.5×10^{31}
	3.5	5	50ns - 288	2.5	2.6×10^{31}
Increase intensity	3.5	7	50ns - 432	2.5	7.5×10^{31}
	3.5	7	50ns - 796	2.5	1.4×10^{32}

TABLE 1.2: Projective evolution of the beam configuration and instantaneous luminosity during the 2010 physics run at $\sqrt{s} = 7$ TeV at IP1 (ATLAS) [11].
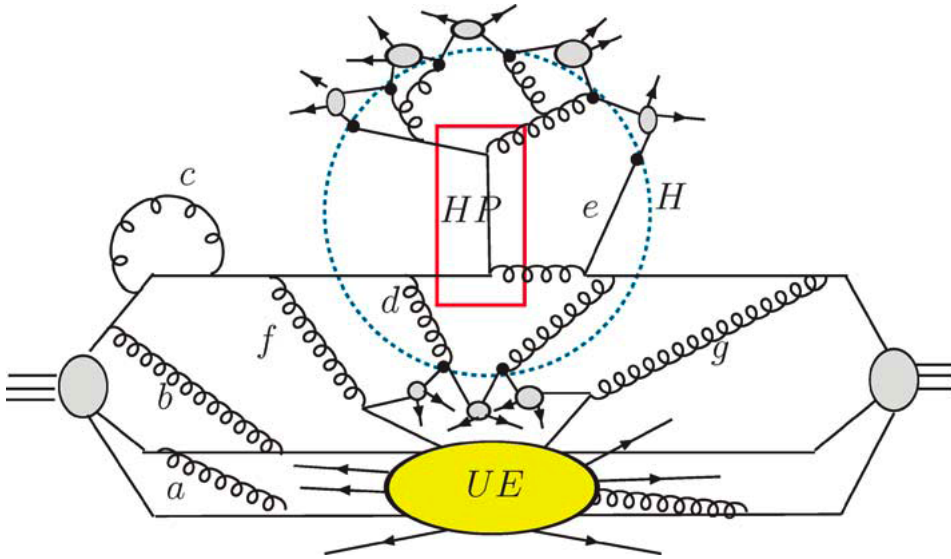
FIGURE 1.3: Schematic highlighting the underlying structure of hard collisions at the LHC, including the *hard process* (HP) and the *underlying event* (UE) [12].

scatter ("underlying event"). This problem is further exacerbated at high luminosity running, where multiple collisions may occur in a single bunch crossing.

1.3.1 Anatomy of hadronic interactions at the LHC

The structure and evolution of proton collisions at the LHC not only gives rise to a complex phenomenology, but in many ways dictates the characteristics of the experimental environment. To better understand the challenges involved, it is instructive to consider the "anatomy" of a generic proton-proton collision.

Figure 1.3 provides a schematic depiction of the evolution of a typical interaction between two incoming protons. Three lines are seen to eminate from either proton, signifying the valence quark constituents. These "quark-lines" are seen to interact by way of gluon exchanges (curly lines).

If the momentum exchange between the constituents of the either proton is sufficiently large, a *hard scattering* event may ensue, whereby the interacting partons are "expelled" from proton confinement and act as quasi-free agents. Such a hard scattering is depicted at the top of Figure 1.3. The final state resulting from the hard interaction will depend on the energy available to the interacting partons and their respective quantum numbers. In rare cases, such interactions may result in the production of heavy particles, such as Z/W bosons or potentially even new physics. The hard process depicted in Figure 1.3 however, counts among the most prolific interactions at the LHC and constitutes a formidable background to all studies presented herein. The two incoming partons, here a quark and a gluon, interact to produce another quark-gluon pair. The outgoing quark and gluon will both continue to radiate until their energies fall below a critical threshold after which they can no longer be considered quasi-free and will be forced to *hadronize* into colour neutral bound states known as mesons and baryons. If these bound states are excited, they will in turn decay into relatively long-lived observable particles such as pions, kaons, protons and neutrons. Such a spray of hadronic debris is known as a *jet*, and the mean direction of the jet constituents is expected to follow along the direction of the instigating quark or gluon. Because the jet constituents are colour neutral objects, whereas the quarks and gluons are not, there is necessarily a *colour connection* between the outgoing partons. Consequently the spatial region between the two jets is likely to be "polluted" by low energy hadronic debris. The implications for the experimental detector systems are profound, in the sense that even a simple di-jet event as depicted in Figure 1.3 may be expected to render final states with a large number of (low energy) particles scattered across the entire central detector volume.

With the hard scattered parton pair ejected from either proton, the proton remnants are left in an unstable colour charged state, still colour connected to the hard subprocess. The proton remains interact primarily via soft scattering processes involving comparatively small momentum transfers. Unlike the products of the hard scattering, the resulting hadronic debris is therefore typically scattered at small angles with respect to the direction of the colliding protons[7]. The *Underlying Event* (UE) comprises everything that accompanies a proton-proton interaction apart from the hard scatter, and serves to further complicate the experimental conditions at the LHC. Not only does the large flux of forward scattered debris put stringent demands on forward detector systems, but the colour connection to the hard subprocess, exemplified in Figure 1.3 through *e.g.* gluon emission *d*, will often result in particle production in the central detector regions overlapping with the signatures of the hard scatter.

The experimental challenges resulting from the complexity of proton-proton interactions, are further exacerbated by the high multiplicity of protons involved in a single bunch crossing interaction. As mentioned in Section 1.2.1, protons are not brought to collide

---

[7]Semi-hard or secondary hard-scatterings may also occur between proton remnant constituents.

individually, but rather in packets ("bunches") of 10^{11} protons. The proton-proton interaction depicted in Figure 1.3 is therefore just one of many interactions taking place between protons in a crossing. While it is unlikely for a single bunch crossing to contain more than one hard scattering event, soft scattering processes between other protons in a bunch are commonplace. Such interactions are dubbed *minimum bias* (or *pile-up* when overlapping with a hard scatter) and are given further mention in Section 1.3.6.

In summary therefore, the key signatures of nearly all interesting scattering events at the LHC are likely to be overlaid with debris from initial and final state radiation, the underlying event created by the beam remnants as well as soft scatters from other proton pairs in the same bunch crossing. The experimental challenge is in part to disentangle the signatures of the hard process under investigation from those of accompanying underlying processes.

In the following, some of the key issues in the phenomenological description of hadronic interactions at the LHC are briefly highlighted.

1.3.2 The hard interaction

At the energies accessible to the LHC, each proton in a bunch crossing may be regarded as a "gas" of quasi-free partons, each carrying a certain momentum fraction x_p of the total proton momentum. As shown in Figure 1.3, the partonic constituents of two colliding protons may interact in different ways and the nature of the interaction will depend on the momentum transfer Q^2 involved. Most processes of interest are relatively rare occurrences and involve mass scales far in excess of the proton mass, such as *e.g.* Z or top production. Such processes only follow from large Q^2 exchanges and are dubbed *hard scattering processes* because the interacting partons both carry a significant proton momentum fraction x_p. Unlike soft scattering processes (low Q^2), hard scattering processes can be described with perturbative QCD within the framework of the parton model.

In general terms, perturbation theory allows one to express the cross section as an expansion in the strong coupling constant α_S[8]:

$$\hat{\sigma} \sim \alpha_S^m \sum_{n=0}^{\infty} c_n \alpha_S^n \tag{1.4}$$

where the exponent m depends on the process under consideration and the coefficients c_n are functions of the momenta of the incoming and outgoing partons. An exact calculation to all orders in the expansion in Equation 1.4 is currently impossible and calls for a focus on the terms that provide the most significant corrections. While *leading order* (n=0) calculations are readily available for most processes expected to occur at the LHC, calculations one and two orders beyond are more scarce. In any

---

[8]Assuming electroweak contributions are small compared to contributions from QCD.
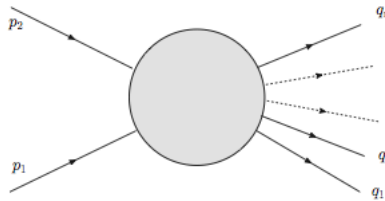
FIGURE 1.4: Generic $2 \to N$ hard scattering process at the LHC.

event, a truncation of the perturbation series is required and in so doing one necessarily introduces a dependence on the *renormalization scale* μ_R^2 [9][13]:

$$\hat{\sigma} \sim \hat{\sigma}_{LO} + \alpha_S(\mu_R^2)\hat{\sigma}_{NLO} + ... + \alpha_S^k(\mu_R^2)\hat{\sigma}_{N^kLO}. \tag{1.5}$$

The cross section $\hat{\sigma}$ quantifies the probability of a transition from an initial incoming state *in* to a final outgoing state *out*. Using the *Lagrangian* of the underlying theory, it is possible to express this probability in terms of the *invariant matrix element* $\mathcal{M}$ for the process under inspection and the momenta of the incoming and outgoing partons involved:

$$P_{in \to out} = |< \text{out}|iT|\text{in} >|^2 = \left|(2\pi)^4\delta^4\left(\sum p_{in} - \sum p_{out}\right)i\mathcal{M}(p_{in} \to p_{out})\right|^2 \tag{1.6}$$

where the transition matrix T is defined in terms of the scattering matrix $S = 1 + iT$ [14]. For the $2 \to n$ process depicted in Figure 1.4, this partonic cross section may take on the general differential form:

$$d\hat{\sigma}_{2 \to n} = \frac{1}{4E_{p_1}E_{p_2}}\frac{1}{\prod_k n_k!}|T|^2\prod_i^n \frac{d^3q_i}{(2\pi)^3 2E_{q_i}}(2\pi)^4\delta^4(p_1 + p_2 - \sum_i^n q_i) \tag{1.7}$$

where $E_p(E_q)$ is the energy of the incoming (outgoing) particles and n_i the number of *identical* particles of type k in the scattered final state [15].

At a hadron collider such as the LHC, the *partonic cross section* as given by Equation 1.7 is not directly measurable, the reason being that the initial state partons are constituents of colliding protons with *a priori* unknown momenta. In order to compute the measurable *hadronic cross section*, it is necessary to fold in the probability of extracting a parton of a particular flavour a carrying a momentum fraction x_a from an incoming hadron A. This information is encoded into so-called *Parton Distribution Functions*

---

[9]If the calculation were to be carried out to all orders, the dependence on μ_R^2 would vanish, but since each term in the expansion separately depends on it any fixed order will necessarily depend on the choice of μ_R^2. In principle, the choice of μ_R^2 is arbitrary, however in order to avoid contributions of the sort $\left(\alpha_S(\mu_R^2 ln\left(\frac{Q}{\mu_R}\right))\right)^n$ from the nth term in the expansion to grow large and compromise the robustness of the fixed order calculation, the renormalization scale is typically placed in the vicinity of the hard scattering scale Q^2.

(PDF) $f_{a/A}(x_a, \mu_F^2)$, which in turn depend on the energy scale μ_F^2 at which the incoming hadrons are probed. The energy scale μ_F^2 is also dubbed the *factorization scale*, as it marks the separation of perturbative short distance physics from non-perturbative long-distance physics. Figure 1.3 shows one of the partons participating in the hard interaction radiating a gluon before interacting with a parton from the opposite hadron. The probability of such a *collinear emission* grows logarithmically with the inverse of the momentum of the emitted gluon and thus potentially blights the convergence of the perturbative expansion in Equation 1.5. However, by way of the so called *DGLAP evolution equations* [16–18], these large logarithms can be absorbed into the PDFs. Aided by *factorization theorems* [19], the observable hadronic cross section can now be expressed as a convolution of the PDFs with the partonic cross section $d\hat{\sigma}$:

$$d\sigma_{p_A p_B} = \sum_{a,b} \int_0^1 dx_a \int_0^1 dx_b f_{a/A}(xa, \mu_F^2) f_{b/B}(x_b, \mu_F^2) d\hat{\sigma}_{a+b \to X}(\mu_R^2) \qquad (1.8)$$

The numerical prediction will depend on the arbitrary choice made for the two unphysical scales μ_R^2 and μ_F^2[10]. This dependence mirrors the uncertainty introduced by neglecting higher order corrections. The total cross section of a process at the LHC is therefore seen to be a combination of both perturbative and non-perturbative contributions, the latter of which are absorbed by the PDFs. These non-perturbative effects imply that PDFs cannot be derived from theory, but must be extracted from experimental measurements. The PDFs on which most predictions for the LHC are based are derived from extrapolations of such measurements performed primarily at the lower-energy colliders HERA and Tevatron, thereby introducing another source of uncertainty into the predictions.

1.3.3   From hard scattering to experimental observables

At the LHC, the outgoing partons will tend to emerge from the hard scattering at comparatively high energies so that initially they may still be regarded as quasi-free agents. As such, they will radiate and lose energy until they are soft enough to hadronize into colour neutral states.

1.3.3.1   Parton showers

The radiation process associated with the final state partons may be described by higher order terms in the expansion of Equation 1.5, or if such corrections are unavailable by way of phenomenological models. Such models are commonly dubbed *parton showering models*. Parton showering algorithms take all outgoing partons of a LO matrix element calculation and allow each parton to branch out into a multi-parton final state through successive splittings of the form $a \to b + c$, as shown in Figure 1.5. Each daughter may branch in turn to form a sequence of consecutive splittings.

---

[10]Conventionally these scales are chosen close to the momentum scale of the hard scatter.
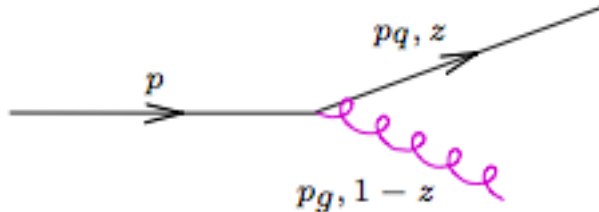
FIGURE 1.5: A schematic representation of shower splitting. A quark line branches out into a gluon and a quark with angular separation ϕ. The daughter quark carries a momentum fraction z of the total parent momentum, and the gluon a momentum fraction $1 - z$.

Successive emissions are ordered in an *evolution variable t*, initialized to some high value t_{max} characteristic of the hard interaction scale. The choice of evolution variable varies between models, but typically involves either (1) the virtuality of the parent parton, (2) the relative transverse momentum of two partons or (3) the angular separation between two partons. Dicing a random number, successive values of the evolution variable $t < t_{max}$ are determined by evaluating the probability that no emission occurs between t_{max} and t. For a parton of flavour a, this probability is given by so called *Sudakov form factors* Δ_a:

$$\Delta_a(t_{max}, t) = \exp\left(-\int_t^{t_{max}} \frac{dt}{t} \int_0^1 dz \mathcal{P}_{ba}(z, t_{max}, t)\right) \tag{1.9}$$

where the function $\mathcal{P}_{ba}$ is associated with the DGLAP splitting function governing the branching $a \to b$ and z is the momentum fraction awarded parton b [20]. This procedure is repeated until $t \sim \Lambda_{QCD}$ where hadronization ensues and perturbation theory is no longer applicable.

Parton showering algorithms are widely employed in the simulated data samples used in all studies presented herein. It is important to note that this is only an approximate procedure that cannot replace an exact calculation to higher order. Its theoretical validity does not extend beyond the soft/collinear limits, where the emission angle is small or the emission energy $E \to 0$. Driven by the need for methods to better describe both existing Tevatron and upcoming LHC data, recent years have seen a surge in new tools that provide matrix element corrections to the parton showering scheme, whereby parton showers in the hard regime are replaced by exact expressions of higher order matrix element calculations [12].

1.3.3.2   Hadronization

As outgoing partons move further apart and lose energy through radiation, the confining properties of QCD provoke the *hadronization* into bound colour-neutral states. At this scale ($\mathcal{O}(\Lambda_{QCD})$), perturbation theory breaks down and phenomenological models tuned to experimental data are called for. In the same way that PDFs described in Section

(a) The string fragmentation model (b) The cluster fragmentation model
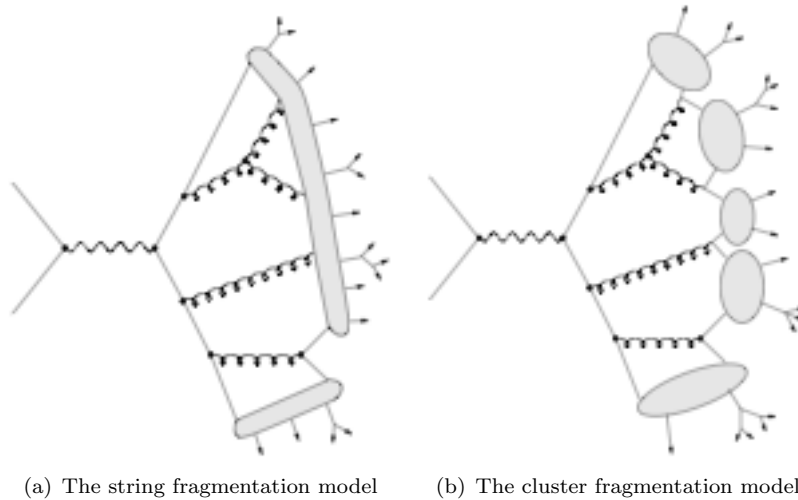
FIGURE 1.6: Schematic representation of hadronization models [21].

1.7 associate the incoming partons of the hard scattering with incoming hadrons, *fragmentation* functions of the form $H_{p\to h}(z, \mu_F^h)$ provide a mapping between "free partons" and bound hadrons. These functions encode the probability that a parton of flavour p hadronizes into a hadron of type h, in the process of which it loses a momentum fraction z. Like the PDFs, such fragmentation functions are sensitive to the factorization scale μ_F^h which separates the perturbative partonic physics from the non-perturbative effects absorbed by the fragmentation functions. Fragmentation functions are employed in various *hadronization models*, whose common underlying assumption is that the parton concentration in a region of the detector before hadronization is reflected in the quark constituents of hadrons in that same region after hadronization [12].

Two widely used models include the *Lund string model* [22] and the *Cluster model* [23], schematically depicted in Figure 1.6.

The former connects quarks and antiquarks via a linearly increasing colour field represented by a string. Gluons appear as kinks along this string. As the $q\bar{q}$-pair moves apart, the potential energy in the string increases until it sufficiently large to produce a $q\bar{q}$-pair, after which the string splits in two as prescribed by the fragmentation functions. This procedure is iterated until all energy is bound up in hadrons.

The cluster model by contrast, initially splits all gluons into $q\bar{q}$-pairs and then attempts to gather all $q\bar{q}$-pairs in the event into colour singlets. These resulting *clusters* are then subsequently decayed into a pair of hadrons.

After hadronization, any unstable hadrons decay into long-lived particles such as $K^{\pm}$, K^0, p, n, $\pi^{\pm}$, π^0, γ, etc. Along with any long lived particles produced in the hard interaction, these particles then make up the experimental observables of the hard scattering.

Properly tuned, both models (and variants thereof) have been found to render final states in good agreement with data [12]. The availability of accurate hadronization models is essential for the development of experimental tools that rely on the "global" and constituent properties of jets, such as the studies presented in Chapter 2.

(a) Photoproduction   (b) Two photon exchange
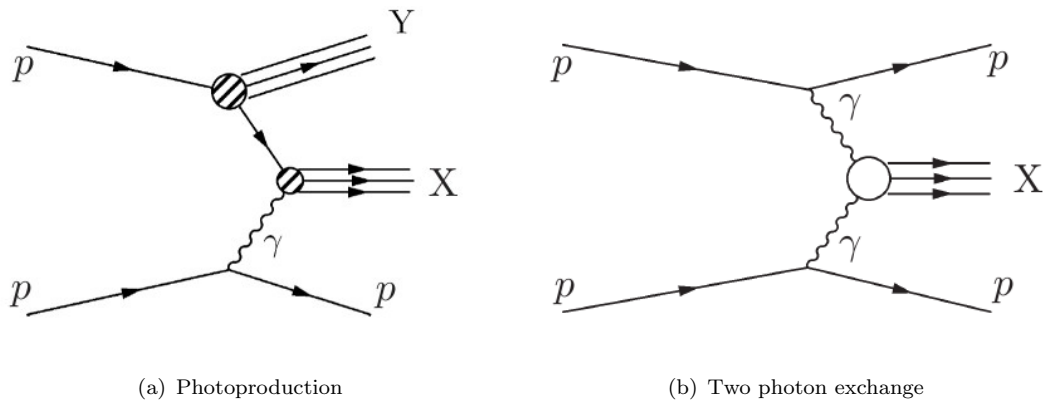
FIGURE 1.7: Proton interactions through photon exchange

1.3.4   Photon interactions in proton-proton collisions

While the large majority of scattering processes at the LHC involve strongly interacting protons, the colliding particles may also interact through the exchange of photons. This will typically be the case when collisions between protons occur at impact parameters too large for any hadronic interactions to take place. As shown in Figures 1.7, the emitted photon may either interact with a proton (*parton*) or with another emitted photon. Figure 1.7(a) typify a class of events labelled *Deep Inelastic Scatters* (DIS), whereby the photon interacts with a quark or a gluon from a proton to produce a system X and the interacting proton dissociates into a system Y. Figure 1.7(b) illustrates a photon-photon fusion process in which a central system X is produced and the emitting protons are both scattered in the forward directions.

The probability that the proton remains intact after a photon emission depends on the *virtuality* of the emitted photon, *i.e.* the degree to which the emission is off-shell. The photon virtuality is defined as the negative of the four-momentum transfer in the emission process:

$$Q^2 = -q^2 = -(p_f - p_i)^2 \tag{1.10}$$

whereby p_i and p_f are the respective four-momenta of the proton before and after photon emisson. Emissions with relatively low photon virtuality will typically leave the emitting proton intact, whereas highly virtual emissions invariably cause the proton to dissociate.

Such interactions stand in stark contrast to the customary hadronic interaction described in Section 1.3.1, as they typically yield remarkably clean event topologies. The absence of colour flow between the photons and protons in the exchange process ensures final states with low particle multiplicities and consequently low occupancies in the detector. The photon emitting proton is typically scattered at such small angles that it escapes the central detector through the beamline. A generic signature for photon interactions is therefore a large *rapidity gap* to at least one side of the central detector. Experimental characteristics and potential tagging techniques of such events are further discussed in Section 1.4.2 and in Chapter 4.

In the following, the theoretical considerations underpinning photon interactions at the LHC are briefly expounded.

1.3.4.1 Theoretical description of photon interactions at hadron colliders

Photon emissions from an incoming beam of hadrons are often described by means of the *Equivalent Photon Approximation* (EPA) [24].

EPA regards the electromagnetic fields of the incoming hadrons as comparable to a flux of photons with spectra $dN(\omega, Q^2)$, whereby $\omega = \frac{E_\gamma}{E}$ is the fraction of the incoming hadron energy associated with this photon flux and Q^2 the virtuality of the photon emission.

By a procedure reminiscent of the factorization employed in the treatment of hadronic interactions in Section 1.3.2, the scattering amplitude for emissions with low photon virtuality may be separated into a (long distance) flux dependent function and the (short distance) cross section of the relevant γp or $\gamma\gamma$ interaction process. The differential cross sections for the scatters depicted in Figures 1.7(a) and 1.7(b) may then be expressed as a convolution of the photon interaction cross section and the photon flux spectra [25]:

$$d\sigma_{\gamma p} = \sigma_{\gamma p \to X} dN(\omega, Q^2) \tag{1.11}$$

$$d\sigma_{\gamma\gamma} = \sigma_{\gamma\gamma \to X} dN(\omega_1, Q_1^2) dN(\omega_2, Q_2^2) \tag{1.12}$$

In this fashion, the dependence on the photon virtuality is moved from the photon interaction cross sections $\sigma_{\gamma p \to X}$ and $\sigma_{\gamma\gamma \to X}$ to the photon flux dN. If the photon cross sections are relatively insensitive to the photon virtuality, the integrated interaction cross sections for the *photoproduction* process depicted in Figure 1.7(a) may be expressed in terms of the *luminosity function* f_γ:

$$\sigma_{pp(\gamma p \to X)pY}(s) = \int_{\omega_{min}}^{1} f_\gamma \sigma_{\gamma p \to X}(\omega, s) d\omega \tag{1.13}$$

whereby f_γ is the Q^2-integrated photon flux, restrained by kinematics or experimental constraints:

$$f_\gamma = \int_{Q_{min}^2}^{Q_{max}^2} dN(\omega, Q^2) dQ^2 \tag{1.14}$$

and s the square *center of mass* energy of the colliding hadron beams.

In a similar manner, the integrated interaction cross section for the *two photon* process depicted in Figure 1.7(b) may be expressed as:

$$\sigma_{pp(\gamma\gamma \to X)pp}(s) = \int_{W_{min}}^{\sqrt{s}} dW_{\gamma\gamma} \frac{dL_{\gamma\gamma}}{dW_{\gamma\gamma}}(W, s) \sigma_{\gamma\gamma \to X}(W) \tag{1.15}$$

where the *relative luminosity* function is defined in terms of the invariant mass $W_{\gamma\gamma}$ of the outgoing system X and comprises the integrated flux of both photons:

$$\frac{dL_{\gamma\gamma}}{dW_{\gamma\gamma}} = \int_{W_{\gamma\gamma}^2/s}^{1} 2W_{\gamma\gamma} f_\gamma(\omega) f_\gamma \left(\frac{W_{\gamma\gamma}^2}{\omega s}\right) \frac{d\omega}{\omega s} \qquad (1.16)$$

The EPA factorization scheme treats the exchanged photons as quasi-real (unpolarized) particles, and its validity is restricted to exchanges where the interaction cross section of the $\sigma_{\gamma p(\gamma)}$ may be considered insensitive to the photon virtuality Q^2, that is to say $Q^2 < \Lambda_\gamma$, where Λ_γ represents some dynamical cut-off scale [24]. For colliding protons at the LHC, this cut-off is provided for by the proton electromagnetic form factors. These form factors reflect the internal electromagnetic structure of composite colliding hadrons and ensure that $\sigma_{\gamma p(\gamma)}$ rapidly falls when $Q^2 > \Lambda_\gamma$ [25, 26]. It is notable that photon-induced interactions typically take place at impact parameters $b \sim 1/\sqrt{Q^2}$ much larger than the strong interaction range [25] and may therefore be considered largely insensitive to the internal structure of the colliding species. As such, one can also expect photon interactions to characterize so called *ultraperipheral* collisions between heavy ions, whereby nuclei of charge Z interact electromagnetically at impact parameters greater than the nuclear radii[11] [27]. The field intensity associated with the colliding species is then enhanced by a factor Z^2, so that the two-photon interaction rate is expected to intensify considerably:

$$\frac{\sigma_{HI}(\gamma\gamma \to X)}{\sigma_{pp}(\gamma\gamma \to X)} \sim Z^4. \qquad (1.17)$$

Figure 1.8 compares the effective two-photon luminosities as a function of the invariant mass of the central system $W_{\gamma\gamma}$ for various colliding species at the LHC and LEPII. The LHC is seen to have both energy and luminosity reach well beyond LEPII, a feature which in recent years has sparked new interest in regarding the LHC as a partial *photon* collider. While photon-induced processes have been extensively studied at both LEP and HERA, the LHC presents the first opportunity to study photon-induced center of mass energies beyond the electroweak scale [29]. By integrating the luminosity spectrum $\frac{dL_{\gamma\gamma}}{dW_{\gamma\gamma}}$, the fraction of the total LHC proton-proton luminosity available for $W_{\gamma\gamma} > 23$ GeV and $W_{\gamma\gamma} > 225$ GeV scatters has been estimated to be 1% and 0.1%, respectively. In light of the comparatively large luminosity available at the LHC, these numbers indicate that even comparatively scarce two-photon processes may have detectable rates [25].

These features combined invite for a range of different studies, both within and beyond the Standard Model, the latter partially exemplified by the diagrams in Figure 1.9. A more detailed discussion of the potential physics programme with two-photon processes at the LHC can be found in [25, 29].

The observation of the process $\gamma\gamma \to l^\pm l^\mp$ with early LHC data is the focus of Chapter 4, and further discussions of topics relevant to the experimental detection of two-photon processes can be found therein.

---

[11]This condition partially protects against the occurrence of simultaneous hard interactions.
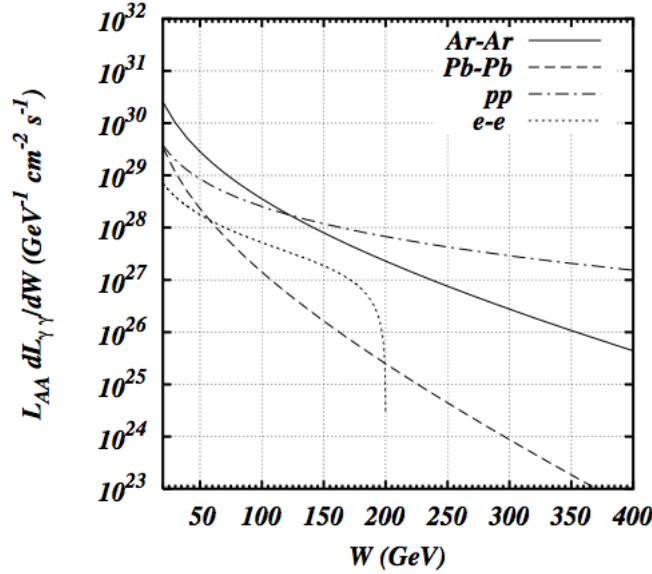
FIGURE 1.8: The effective $\gamma\gamma$ luminosity as a function of $W_{\gamma\gamma}$ for various colliding species at the LHC ($\sqrt{s} = 14$ GeV) compared to LEP ($\sqrt{s} = 200$ GeV). In either case effective luminosity is measured against a total luminosity scenario corresponding to $\sim$ 1 collision per bunch crossing [28].
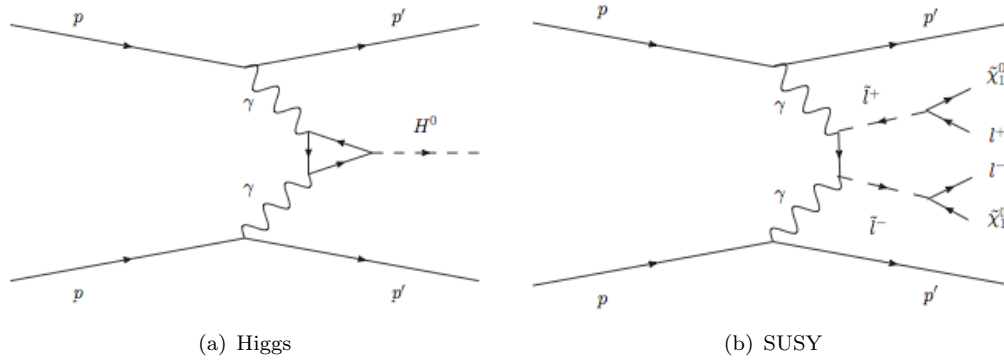
(a) Higgs

(b) SUSY

FIGURE 1.9: New physics beyond the Standard Model in two-photon interactions: (a) Higgs production (b) SUSY slepton production, whereby each slepton decays into a chargino and a lepton.

1.3.5 The underlying event

The previous sections were primarily concerned with the phenomenology connected to the treatment of the *primary interaction*, be it the *hard scattering* between two proton constituents or the exchange of photons between protons.

Only in rare cases, does a primary interaction occur without the participating proton "breaking up", and the remnants following such a dissociation will interact and fragment to produce the *underlying event*.

The physics of the underlying event is non-perturbative and comparatively poorly understood, but the experimental implications will typically depend on how decoupled the primary interaction is from the proton fragmentation.

In the absence of a colour connection to the primary interaction, the fragmentation products are most likely to scatter at small angles with respect to the parent proton directions. With a transverse component $p_T^{remn.} \ll p_z^{remn.}$, it is reasonable to expect the elements of the underlying event to escape undetected down the beamline. This scenario is typically realized in photon interactions as described in Sections 1.3.4 and 4.2.

Primary interactions involving partons extracted from the interacting protons, however, typically leave the proton remnants in a colour charged and unstable state. In such cases, the remnants can only "neutralize" through soft (long-distance) interactions with the partons involved in the primary interaction. As a consequence, the proton fragments may be scattered beyond the very forward directions and into the central rapidity regions. From an experimental standing, the underlying event in such cases pollutes the signatures of the primary interaction and complicates the analysis of the data. The underlying event is in no small part responsible for the high multiplicity final states expected to follow from hadronic interactions at the LHC, and the presence of a large number of additional particles without relation to the primary interaction, can be expected to confuse and degrade the performance of offline reconstruction algorithms such as those described in Chapter 2.

While the structure of the underlying event counts among the least understood aspects of the hadronic environment at the LHC, there are strong indications that so-called *multiple parton interactions* of semi-hard nature play a key rôle. Such scatters were first established in $\gamma + 3$ jet events at CDF, identified as the overlap of a separate γ+jet process and a jet+jet process within the same $p\bar{p}$ interaction [30]. The result implicates a considerable probability for partons in the proton remnants to independently undergo secondary (semi-hard) interactions alongside the primary interaction. Hard scattering interactions typically occur in collisions involving a small impact parameter, hence the harder the primary interaction, the more likely it is that it will be accompanied by secondary partonic interactions. By the same token, multiple interactions are unlikely to occur in photon-exchange processes.

There are, however, also indications that multiple scattering cannot describe the full structure of the underlying event and that an additional highly non-perturbative soft component must be accounted for [12]. In summary therefore, a single strongly interacting proton-proton collision should be regarded as an overlap between the primary hard interaction, any secondary semi-hard interactions and residual soft-interactions of the colour-charged remnants.

Several phenomenological models exist which in various ways attempt to predict the structure of the underlying event. These models are all tuned to experimental measurements performed at previous collider experiments with various degrees of success. There is therefore still considerable uncertainty connected to the validity of these tunings when extrapolated to LHC energies [12].

1.3.6 Pile-up and Minimum Bias

As already alluded to in Section 1.3.1, the protons are not brought to collide individually, but in bunches of high proton density. A high proton density not only increases the chances of a hard interaction to take place, but equally the probability of simultaneous soft interactions between other protons in the same bunch crossing. Interactions in a bunch crossing between proton pairs with no relation to the hard scatter are often referred to as *pile-up* [12]. Pile-up interactions further complicate the interpretation of data, and are particularly detrimental to the selection of photon-induced final states, as is further discussed in Section 4.2.

In general, the number of independent interactions N taking place in a single bunch crossing will follow a Poisson distribution

$$P(N; \nu_N) = \nu_N^N \frac{e^{-\nu_N}}{N!} \tag{1.18}$$

whose mean value $\nu_N = \sigma_{pp}\mathcal{L}\langle\Delta t_{bunch}\rangle$ will depend on the instantaneous luminosity $\mathcal{L}$ and the bunch spacing

$$\langle\Delta t_{bunch}\rangle = \frac{1}{40\text{MHz} \times \frac{N_B}{N_B^{max}}} \tag{1.19}$$

given by the ratio of bunches per beam N_B to the maximal number of bunch slots available[13] [31].

$\mathcal{L}[cm^2s^{-1}]$	N_p / bunch	Fill scheme $(N_B \times N_B)$	$\nu_N(\sigma_{ND+DD})$
7.0×10^{27}	2×10^{10}	2×2	0.02
1.7×10^{30}	3×10^{10}	43×43	0.22
4.8×10^{30}	5×10^{10}	43×43	0.62
1.7×10^{31}	5×10^{10}	156×156	0.60
3.4×10^{31}	7×10^{10}	156×156	1.20
9.4×10^{31}	7×10^{10}	432×432	1.20
1.8×10^{32}	7×10^{10}	796×796	1.25
1.0×10^{33}	—	2808×2808	2.20
1.0×10^{34}	1.15×10^{11}	2808×2808	21.89

TABLE 1.3: The estimated mean pile-up ν_N for various early luminosity scenarios sketched in Table 1.2 assuming $\sqrt{s}$ =7 TeV and σ_{ND+DD} ~62 mb. The two bottom rows assumes $\sqrt{s}$ =14 TeV and σ_{ND+DD} ~69 mb.

Table 1.3 lists the average expected pile-up at various luminosities and beam configurations at the LHC. It is notable that a rise in luminosity following an increase in the number of protons per bunch crossing results in more pile-up than does a luminosity rise

---

[12]The term *pile-up* is often also used to denote the overlap between signals from two consecutive bunch crossings in the detector. Such overlaps may follow whenever the response time of a detector subsystem exceeds the bunch spacing of the colliding beam.

[13]At the LHC, $N_B^{max} = 3564$.

	Cross section (mb)	
Process	PYTHIA	PHOJET
σ_{tot}	**102** (91)	**120** (106)
σ_{el}	23 (19)	35 (29)
σ_{inel}	79 (72)	85 (76)
σ_{ND}	55 (49)	68 (62)
σ_{SD}	14 (14)	11 (11)
σ_{DD}	10 (9)	4 (4)
σ_{CD}	N/A	1 (N/A)

TABLE 1.4: Relative composition of the total proton-proton cross section at the LHC as predicted by the Monte Carlo generators PYTHIA and PHOJET for $\sqrt{s}$ =14 TeV (7 TeV). The discrepancies reflect the uncertainties when extrapolating existing model tunings to LHC energies. The lower section breaks down the contributions to the inelastic cross section σ_{inel} [32, 33].
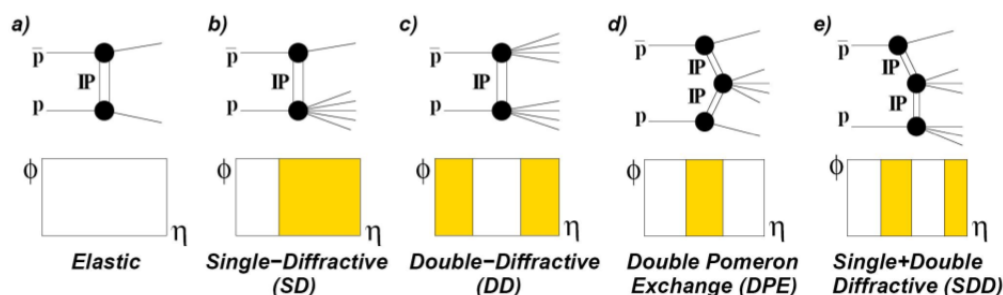
FIGURE 1.10: Various soft elastic and inelastic scattering processes, with corresponding event topologies in $\eta - \phi$ space, whereby coloured regions indicate particle activity and empty regions rapidity gaps [34].

following an increase in the number of bunches. Table 1.3 also indicates that whereas additional pile-up events are comparatively scarce at low luminosity, an average of 22 pile-up events are expected to accompany every hard scatter at design luminosity.

To understand the nature of these additional pile-up interactions, it is instructive to consider the dominant components of the total proton-proton scattering cross section at the LHC. This cross section may be expressed as a sum of its *elastic* (σ_{el}) and *inelastic* (σ_{inel}) contributions, where $\sigma_{el} < \sigma_{inel}$. The large majority of interactions in a bunch crossing, and consequently most additional pile-up interactions, are therefore likely to be soft, inelastic (non-perturbative) scatters. Such scatters are often dubbed *minimum bias interactions* in reflection of their experimental collection under minimal trigger conditions [32], however a distinction is often drawn between *diffractive* and *non-diffractive* contributions. The diffractive contribution may in turn be subdivided into *single-diffractive* (SD), *double-diffractive* (DD) and *central-diffractive* (CD) components, as shown in Figure 1.10. Table 1.4 compares the relative contributions of such inelastic subprocesses and indicates that the total proton-proton cross section:

$$\sigma_{tot}^{pp} = \sigma_{elastic} + (\sigma_{ND} + \sigma_{SC} + \sigma_{DD} + \sigma_{CD}) \qquad (1.20)$$
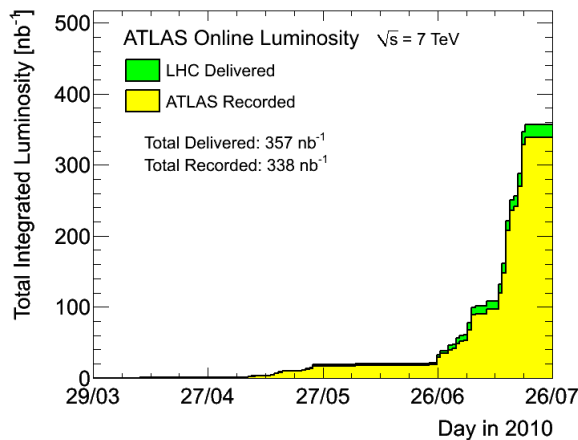
FIGURE 1.11: Cumulative luminosity versus day delivered by the LHC (green) and recorded by ATLAS (yellow) during stable beams at $\sqrt{s}$ = 7 TeV. (The systematic uncertainty associated with the luminosity measurement is estimated at 11%).

is dominated by non-diffractive (ND) inelastic scatters. Non-diffractive inelastic interactions are characterized by proton fragmentation through gluon emission into colour neutral bound states, whereby the hadronic debris is scattered into both forward and central rapidity regions [35]. While the scattered objects are typically very soft, collisions involving an overlap between a photon-induced process and a non-diffractive scatter is likely to render the former non-exclusive.

Diffractive scatters by contrast involve colour-neutral ("pomeron") exchanges between the interacting protons, as depicted in Figure 1.10. Common to all diffractive scatters is the presence of *large rapidity gaps*, which follow from the absence of a colour connection between the scattered protons or between the scattered protons and the central system. Diffractive processes therefore share many experimental similarities with two-photon processes and may be falsely identified as such. Diffraction as a potential background to two-photon processes is further discussed in Chapter 4.

1.4   The ATLAS experiment

The ATLAS[14] experiment counts among the largest scientific collaborations to date, involving almost 3000 scientists and engineers from across 37 different countries[15]. Formally proposed in 1994 [36], the construction and assembly of the experimental apparatus was largely completed in 2008. At the time of writing, the detector is (almost) fully operational and has recorded a total of $\sim 300\text{nb}^{-1}$ of data, as shown in Figure 1.11.

The physics programme of the ATLAS experiment is akin to that of CMS, including both improvements to current Standard Model measurements and extensive searches for new physics beyond. This ambitious programme coupled with the harsh experimental environment of the LHC, have driven the design and technology choices of the ATLAS

---

[14]A Toroidal LHC *Apparatu*S
[15]As of December 2009.

24
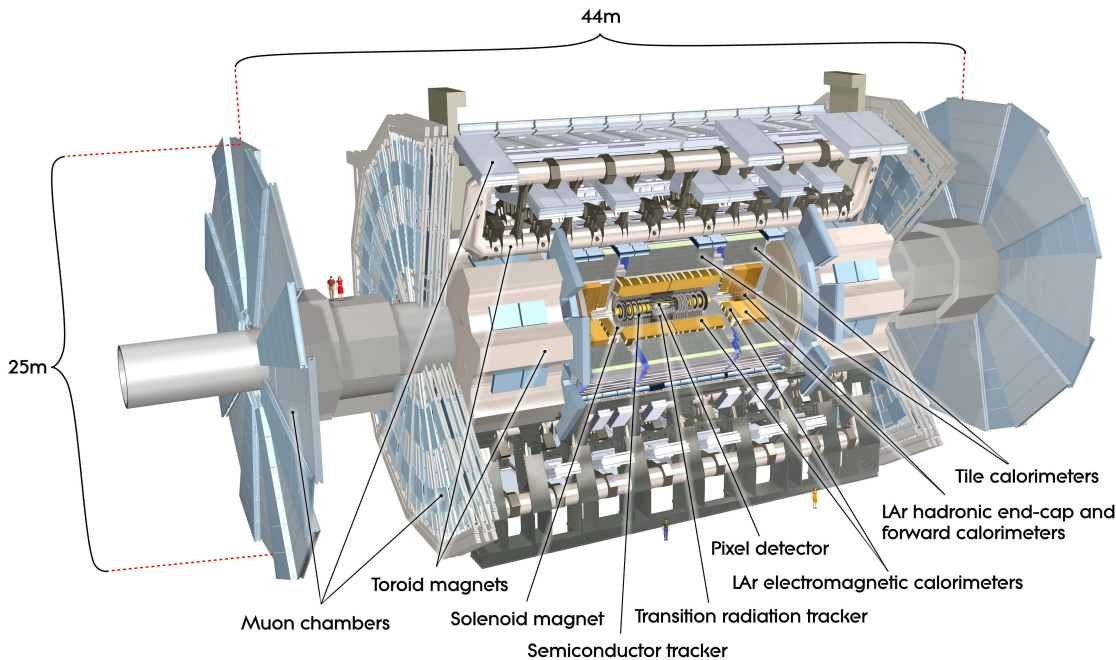
FIGURE 1.12: Cut-away view of the ATLAS central detector with its component sub-detectors [37].

detector. A detailed description of the experimental programme and the various detector components can be found in [32] and [37]. In the following a cursory overview of the various detector systems of the ATLAS experiment is given, with a light emphasis on components of particular relevance to the studies presented herein. The ATLAS coordinate system and relevant associated quantities are summarized in Appendix A.

1.4.1 The central detector systems

Following the general design principles of a typical multi-purpose detector, the central detector system is centered around the interaction region and consists of several specialized subdetectors arranged in layers about the beamline in an approximately ϕ-symmetric fashion. The cylindral volume of any component subdetector is characterized by a coaxial *barrel* flanked by perpendicularly arranged *end-caps* to either side.

Stable and quasi-stable particles emerging from the interaction region will extend into the detector volume and interact with the material therein, whereby the mode of interaction will depend on the properties of the traversing particle and the material through which it is passing. The detection technologies employed in each detector layer are therefore designed to exploit particular forms of particle interactions with matter to render partial information towards the energy and direction of outgoing particles. As discussed in Chapter 2, a full-fledged measurement of the properties of a given particle along with an identification of its type is an involved procedure that typically relies on the combined information provided by several subdetectors.

The composition of the ATLAS central detector is depicted in Figure 1.12. The *inner detector* forms the innermost detector subsystem, whose primary task is to measure the flight paths ("tracks") of charged particles. Surrounding the inner detector is the *calorimetry*, designed to measure particle energies. The outermost detector system comprises the various chambers of the *muon spectrometer*, designed to measure the momenta of charged minimum ionizing particles[16] whose energies are not fully absorbed in the calorimeters. With total dimensions of $44m \times 25m$ and a weight of 7000 tonnes, the ATLAS detector is the largest particle physics detector to date.

1.4.1.1 The innermost tracking detectors

The *inner detector* (ID) comprises the three innermost detector subsystems and is designed to provide accurate measurements of the direction, momentum and impact parameters[17] of charged particles. Using pattern recognition techniques, this information can be exploited to reconstruct the tracks of charged particles as well as any vertices from which several tracks emerge [32]. Their close proximity to the interaction region render the inner tracking detectors particularly exposed to high particle densities and associated radiation levels. At design luminosity, it is expected that roughly 10^3 ionizing particles will be scattered into the ID volume with every bunch crossing. In order to retain the best possible momentum and vertex resolutions in this environment, technologies offering differing levels of granularity are employed at increasing radii from the beamline. The various subsystems of the ID volume are shown in Figure 1.13.

The two innermost subdetectors employ silicon based technologies to provide high resolution measurements where the particle densities are at their highest. When ionizing particles pass through the sensitive semi-conductor material, *electron-hole* pairs are released along their flight path and collected by an electric field created by an externally applied bias voltage [39].

The Pixel Detector

The high particle flux environment in the immediate vicinity of the beampipe mandates the use of pixel technology to obtain the required granularity to secure high resolution measurements. The three innermost layers therefore constitute the *Pixel Detector*, which with its roughly 80 million pixels of size $(R - \phi) \times z = 50 \times 400 \mu m^2$ is capable of delivering spatial resolutions of 10 μm in $(R - \phi)$ and 115 μm in z (barrel) [18]. The first layer, often called the *vertexing layer* or *b-layer*, is located at a radial distance of only 51mm from the beamline. The close proximity to the interaction region allows for an accurate determination of the primary vertex and the identification of any displaced vertices, but at the same time exposes the detector hardware to very large radiation

---

[16]A *minimum ionizing particle* (MIP) is a particle whose mean energy loss through matter is close to the minimum [38].

[17]The impact parameter measures the distance of closest approach in space between a track and the primary vertex.

[18]The resolution is not only limited by the pixel size, but also by any material in front of the sensor material, the angle of incidence, the readout technology, etc.

6.2m

2.1m

Barrel semiconductor tracker

Pixel detectors

Barrel transition radiation tracker

End-cap transition radiation tracker

End-cap semiconductor tracker
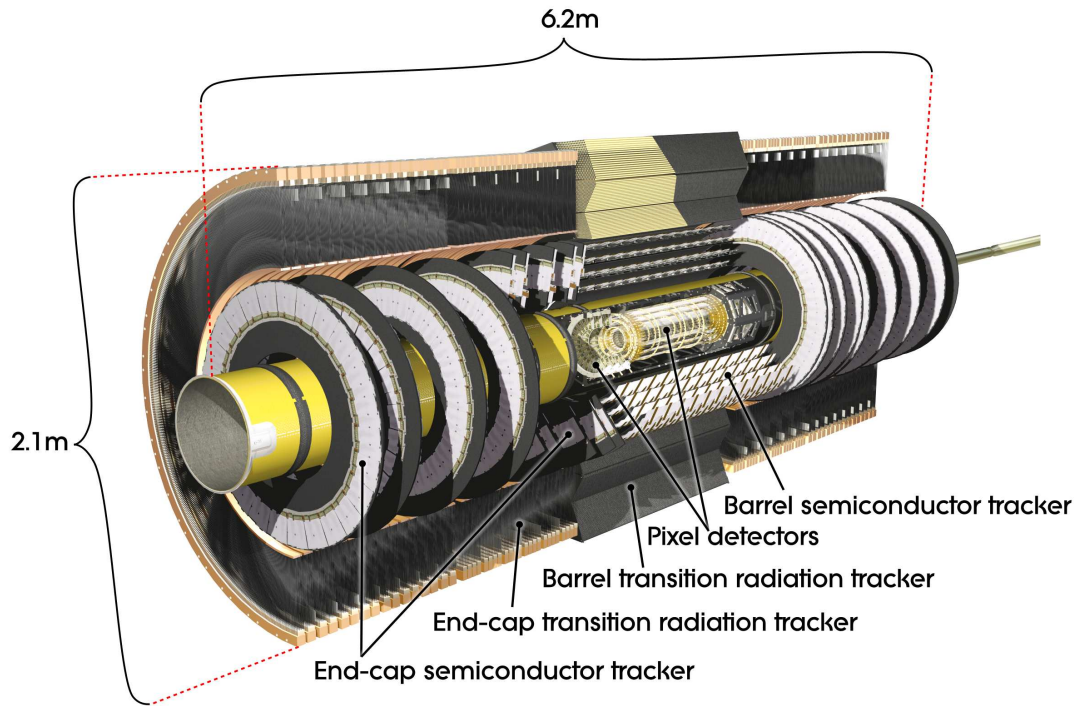
(a) Cut-away view of the ATLAS inner detector volume

R = 1082 mm

TRT

TRT

R = 554 mm
R = 514 mm

R = 443 mm

SCT

R = 371 mm

R = 299 mm

SCT

R = 122.5 mm
Pixels R = 88.5 mm
R = 50.5 mm

R = 0 mm

Pixels
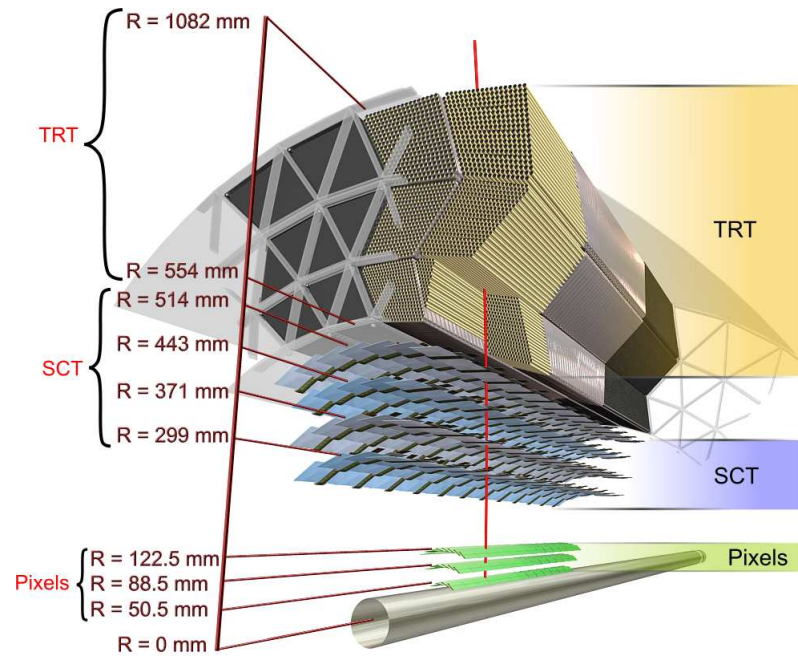
(b) Schematic illustrating the passage of a $p_T \sim$10 GeV charged particle (red line) through the various layers of the inner detector volume.

FIGURE 1.13: The ATLAS inner detector [37].

doses. Consequently it is forseen that the vertexing layer will require replacement after three years of nominal operation.

The Semiconductor Tracker

The high granularity provided by the Pixel Detector comes at the cost of a large number of read-out channels and consequently a high probability of generating a large number of active channels per bunch crossing. It therefore becomes unpractical to use pixel detectors are larger distances from the beamline. Instead, silicon strip detectors are deployed to retain a cost competitive trade-off between read-out complexity and optimal position resolution. The *Semiconductor Tracker* (SCT) envelopes the Pixel Detector and consists of four barrel layers and nine end-cap wheels fitted with single-sided silicon microstrip modules. The modules consist of sensors glued back-to-back with a small stereo angle of 40 mrad and are mounted such that the 80 μm wide strips run parallel to the beamline in the barrel and radially in the end-caps. This arrangement allows for an $(R - \phi)$ measurement to an accuracy of 17 μm, while the slight tilt secures a coupled z-measurement to an accuracy of 580 μm.

The Transition Radiation Tracker

At radii beyond the SCT, silicon based technologies are no longer cost-efficient. And while solid state detectors typically offer the highest resolutions, they also possess higher material densities. Multiple scattering in early silicon layers will degrade the obtainable resolution in later layers and the related energy loss and particle showering will compromise the quality of the energy measurement in the calorimeters.

The outermost layer of the ID therefore utilizes gas-based drift tube technology. Ionizing particles passing through the gaseous volume create electron-ion pairs in their wake. Under the action of an electric field, the charges can be collected at an anode/cathode to produce a signal.

The *Transition Radiation Tracker* (TRT) comprises multiple layers of gas filled straw tubes, arranged parallel to the beamline in the barrel and radially in the end-caps. The straw walls are coated with a conductive material to act as cathodes. The anode is provided by a 30 μm gold-plated tungsten sense wire running through the center of each straw. The particle trajectory through the gaseous volume can then be deduced from the drift times of the charge release. In order to ensure drift times compatible with the high bunch crossing frequency at the LHC, the straw tubes have a diameter of only 4 mm.

The track point measurements of the TRT are limited to $(R - \phi)$ (for which an accuracy of 130 μm per straw is achievable). Nonetheless, its global design is such that traversing particles will typically cross between 35-40 straws. This comparatively large number of track points collected across a longer spatial interval[19], ensures that the TRT still contributes significantly to the overall momentum resolution.

Moreover, the TRT doubles as a particle identification device. The straws are embedded in a transition radiation material, so that any ultra-relativistic particle passing through

---

[19]By contrast, The Pixel Detector and SCT provide 3 and 4 space points, respectively.

the TRT will cross boundaries of differing dielectric constants and emit transition radiation. The detection gas in the straw tubes registers both the ionization energy of the primary particle and any absorbed transition radiation photons. The intensity of the emitted radiation is proportional to $\gamma = E/m$, so that an electron of a given energy E will produce more transition radiation photons than a charged pion of the same energy. As described in Chapter 4, the registration of high threshold hits can therefore be exploited in the separation of electrons from pions.

1.4.1.2 The calorimetry

The ATLAS calorimeters envelop the subsystems of the ID. When particles emerging from the ID volume pass through the comparatively dense material of the calorimeters, their interactions with the material typically generate particle cascades called "showers". While the nature and characteristics of the showering process will vary depending on the properties of the initiating particle, the deposited energy can be translated into a signal whose strength is proportional to the energy of the incoming particle. All the ATLAS calorimeters are *sampling calorimeters*, consisting of alternating layers of an active material and a passive absorber, whereby only a fraction of the total shower energy is measured ("sampled") in the active layers along the longitudinal shower axis and the dense absorbers serve to both provoque the showering process and reduce the physical depth required to fully contain the shower energy.

The resolution of a sampling calorimeter is often parametrized as the quadratic sum of three independent terms:

$$\frac{\sigma(E)}{E} = \frac{a}{\sqrt{E}} \oplus \frac{b}{E} \oplus c \qquad (1.21)$$

The first term ("sampling term" or "stochastic term") reflects statistical fluctuations in the sampled energy. The second term ("noise term") includes uncertainties arising from electronic noise and pile-up in a high rate environment. The last term ("constant term") absorbs any uncertainties arising from detector deficiencies[20] and is independent of the energy of the incoming particle. Equation 1.21 indicates that the sampling term dominates at lower shower energies and that unlike the tracking detectors whose momentum resolution $\frac{\sigma(p)}{p} \propto p$ degrades with increasing particle momentum, the energy resolution of a sampling calorimeter improves with increasing shower energy. This feature is exploited in the concept of *energy flow* discussed in Chapter 2. The resolutions of the various subdetectors of the ATLAS calorimetry as derived from test beam data are summarized in Table 1.5.

A distinction is drawn between *electromagnetic* and *hadronic* showers. While incident electrons and photons will typically shower early upon contact with the calorimeter material to produce comparatively short and laterally contained showers through bremsstrahlung and pair-production, hadrons typically penetrate deeper into the calorimeter

---

[20]These may include imperfections in the active material, shower leakage, non-uniform signal generation, erroneous cell to cell inter-calibration, etc.

Calorimeter subsystem	Test beam configuration	Resolution $\frac{\sigma(E)}{E}$ (GeV)
ECAL	$e^{\pm}$ (1-250 GeV, $|\eta| = 0.687$)	$\frac{10\%}{\sqrt{E}} \oplus 0.17\%$
ECAL + HCAL barrel	$\pi^{\pm}$ (10-300 GeV, $|\eta| = 0.25$)	$\frac{52\%}{\sqrt{E}} \oplus \frac{1.6\%}{E} \oplus 3\%$
HCAL end-caps	$\pi^{\pm}$ (5-200 GeV)	$\frac{70.6\%}{\sqrt{E}} \oplus 5.8\%$
FCAL	$e^{\pm}$ (10-200 GeV)	$\frac{28.5\%}{\sqrt{E}} \oplus 3.5\%$
FCAL	$\pi^{\pm}$ (10-200 GeV)	$\frac{94.2\%}{\sqrt{E}} \oplus 7.5\%$

TABLE 1.5: Fractional (single particle) resolutions of the various calorimeter subsystems as derived from test beam data [37].
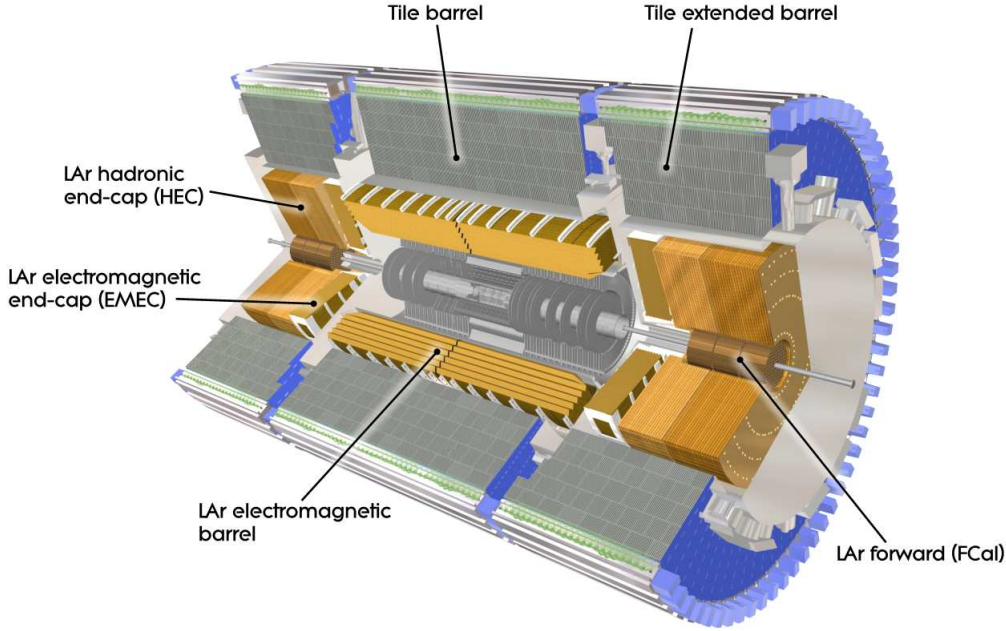
FIGURE 1.14: Cut-away view of the ATLAS calorimeter, with the various components of the electromagnetic, hadronic and forward calorimeters [37].

volume before initiating both broader and longer cascades through strong interactions with the atomic nuclei[21]. A good separation between electromagnetic and hadronic showers is important for particle identification methods, such as those discussed in Chapter 2, and is usually achieved by employing high-Z absorber materials. High-Z absorbers also help contain the shower of very high energy particles inside the calorimeter volume and minimizes leakage into the muon spectrometer. This *hermetic* quality of the calorimeters is vital for an accurate measurement of the missing transverse energy as is further discussed in Chapter 3 and the desire to capture and contain the full energy of the interaction also underpins the wide η-coverage provided by the calorimetry.

The components of the ATLAS calorimetry are schematically depicted in Figure 1.14. The various designs of the electromagnetic, hadronic and forward calorimeters is briefly

---

[21] As is explained in Section 2.3.2.2, charged hadronic showers will also contain an electromagnetic core.

described below.

The electromagnetic calorimeters

The electromagnetic calorimeter (ECAL) is designed to provide precision measurements of light electromagnetically interacting particles.

The ECAL employs liquid argon (LAr) as active medium interspersed with steel plated lead absorbers. The shower particles ionize the LAr and the associated ionization charges are subsequently collected at electrodes under the influence of an externally applied electric field.

The need to embed the ID in a magnetic field comes at the cost of insensitive ("dead") material in front of the ECAL in the form of a solenoid magnet and a cryostat. In order to correct for dead material upstream of the calorimeters, a thin layer of *presamplers* are installed in front of the ECAL to provide a (partial) recovery of any energy lost in dead material.

The central section of the ECAL ($|\eta| < 2.5$) which overlaps with the η-reach of the ID, is longitudinally segmented in three layers of differing granularity, as shown in Figure 1.15(a). This design configuration is an essential prerequisite for the particle flow inspired studies discussed in Chapter 2. The first layer, the so called η-strip layer, is very finely segmented in η to provide a means to disentangle showers from closely spaced photons with origin in $\pi^0 \to \gamma\gamma$ decays from prompt γ showers. While coarser than the $\eta - strip$ layer, the middle layer still provides a comparatively fine granularity across a substantial longitudinal segment of the electromagnetic shower, followed by a thinner back layer with coarser granularity.

Figure 1.15(a) also indicates that instead of employing a conventional parallel geometry, the ECAL absorber and readout plates are embedded in a novel *accordion* geometry, where the plates follow a zigzag pattern along the direction of the incident particle. Rather than crossing a series of separate plates, this configuration ensures that the shower particles cross the same plate repeatedly. With the readout placed on the front and rear faces of the calorimeter, the accordion geometry secures full and crack-free azimuthal coverage.

The hadronic calorimeters

The hadronic calorimeter (HCAL) encapsulates the ECAL and is designed to fully contain and measure hadronic showers. The technologies utilized in the barrel and endcaps differ to better suit the requirements of the local experimental environment.

The two-component *tile calorimeter* (barrel and extended barrel) makes use of plastic scintillator tiles interleaved with steel absorber plates. When particles traverse the active medium, atomic excitations generate scintillation light which is read out by way of wavelength shifting fibers and photomultipliers.
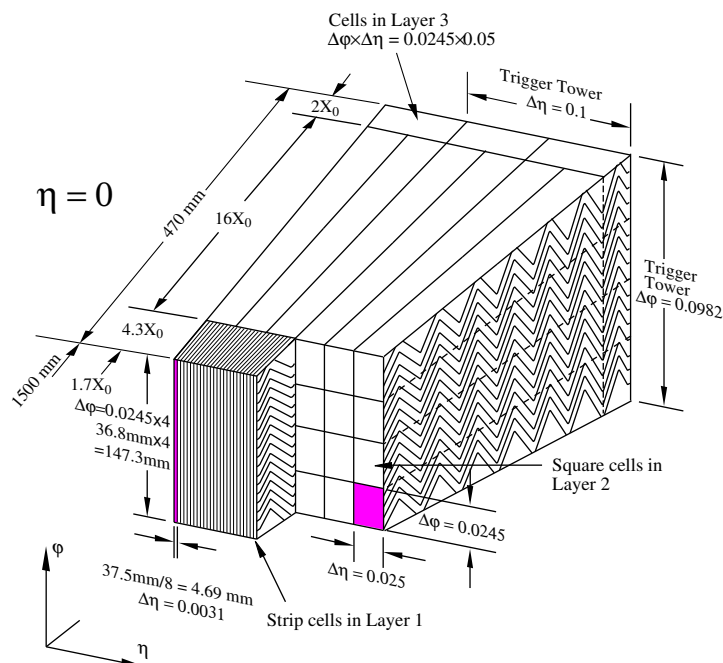
(a) ECAL module
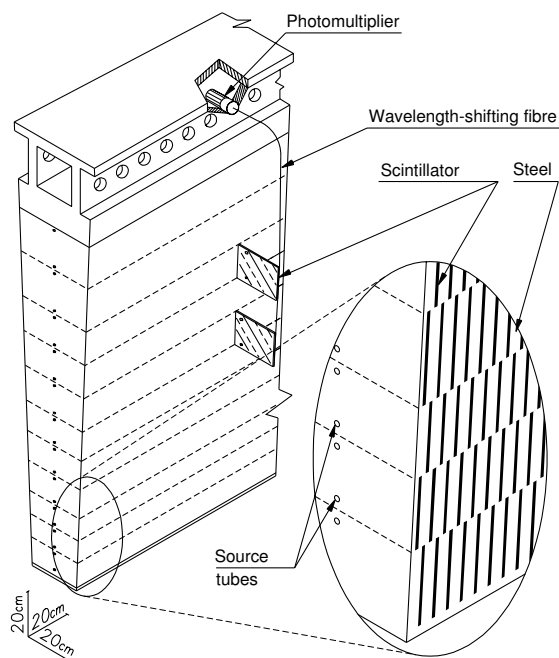
(b) TILE module

FIGURE 1.15: a) Schematic representation of a three-layered barrel module of the central ECAL, with the granularity of each layer clearly visible. b) Module of the barrel HCAL. Scintillating tiles and steel absorbers are interleaved in a parallel arrangement, with fibers and photomultipliers facilitating the readout [37].
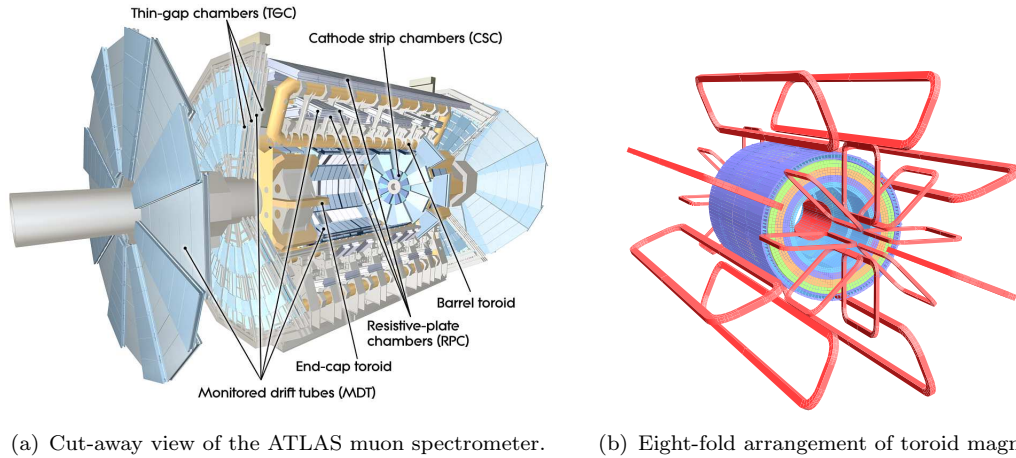
(a) Cut-away view of the ATLAS muon spectrometer.   (b) Eight-fold arrangement of toroid magnets.

FIGURE 1.16: The ATLAS muon spectrometer [37].

The more forward regions are exposed to higher radiation doses, rendering plastic scintillator technology unsuitable. Therefore, the hadronic endcaps employ LAr technology with Cu rod absorbers in a planar geometry configuration.

The forward calorimeters

The forward calorimeters (FCAL) cover the very forward regions $3.1 < |\eta| < 4.9$ and must therefore operate in an environment where the radiation doses are 30 times higher than in the endcap region. Consequently, a very different design is required to ensure containment and fast readout. As indicated in Figure 1.14, the FCAL is segmented in three layers. The layer closest to the interaction point is optimized for the measurement of electromagnetic showers, while the two subsequent layers function as hadronic calorimeters. This comparatively fine segmentation allows for the reconstruction of forward jets. Each layer of the FCAL consists of a dense metal matrix interleaved with active LAr filled tubes running parallel to the beampipe. While Cu is used in the first layer, tungsten is employed in the outer layers to ensure full containment of the forward hadronic showers.

As discussed in Chapter 3, an accurate measurement of the missing transverse energy requires a hermetically sealed detector. The forward calorimeters contribute greatly towards this end.

1.4.1.3   The Muon Spectrometer

While most particles are fully absorbed in the calorimeters, muons will typically traverse the entire detector volume as MIPs. This characteristic property enables a clean detection in the outermost layers of the ATLAS detector, the so called *muon spectrometer*. Its distance from the interaction region, makes the muon spectrometer the largest subsystem in ATLAS. It is embedded in a strong toroidal magnetic field (0.5-1 T) delivered by a triplet of superconducting air-core toroid magnets (one in the barrel and one in each endcap) assembled in an eightfold azimuthal arrangement about the beamline, as

(a) Cut-away view of an MDT barrel station comprising multiple drift tubes

(b) Cross sectional schematic of a muon traversing an MDT drift tube
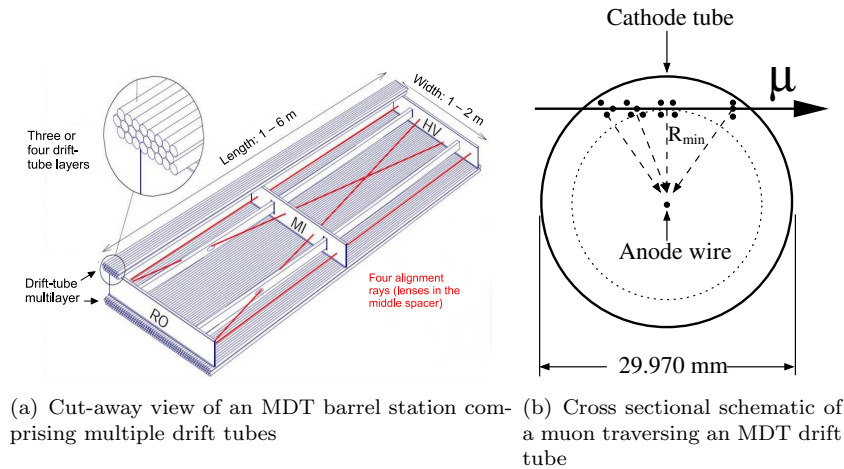
FIGURE 1.17: The barrel MDT of the muon spectrometer [37].

is schematically shown in Figure 1.16(b). Muons passing through this field configuration are bent into the R-z plane and registered in the various chambers of the muon spectrometer. The information from the muon chambers can either be used alone or in combination with information from the inner detector to measure the muon momentum from the curvature of its flight path. The various chambers of the muon spectrometer are shown in Figure 1.16.

High precision momentum measurements are provided by *Monitored Drift Tubes* (MDT) and *Cathode Strip Chambers* (CSC) in the central and forward regions, respectively. As schematically shown in Figure 1.17, the MDTs are gas-filled drift tubes using a detection principle similar to the gas filled straw tubes of the TRT: ionization charges following the passage of a charged particle through the gas are collected on a central anode and the particle trajectory is deduced from the drift time of the charge release.

The inner wheel of the endcaps is exposed to particle rates in excess of the capabilities of the MDTs and is therefore equipped with technology better suited to cope with the local high rate environment. The CSCs are *multiwire proportional chambers* assembled in a configuration where the anode wires are arranged radially and sandwiched between two cathode strip planes segmented parallel and perpendicular to the anode wires. Charges released during the passage of an ionizing particle through the gaseous volume between the cathode plates, are collected on the electrodes, and the flight path deduced from the relative charge induced on neighbouring cathode strips. Unlike the MDTs which only provide precision measurements in the bending plane R-z, the CSCs deliver accurate position measurements in both R and ϕ.

The comparatively clean environment in which muons can be detected, renders the muon spectrometer suitable for online event selection or *triggering* (see Section 1.5). To this end, dedicated trigger chambers with comparatively coarse granularity, but faster readout times have been implemented. These take the form of *Resistive Plate Chambers* (RPC) in the barrel and *Thin Gap Chambers* (TGC) in the forward regions.

The RPC are gaseous parallel plate detectors comprising two opposing electrode plates sandwiching a gaseous volume. The charges created in the gas following the passage of a charged particle, drift to the electrodes with a signal width of 5 ns where they are readout via metallic strips in η and ϕ. With two gas gaps per RPC station, a total of six measurements are provided for a charged particle traversing the barrel. These measurements do not only permit an online selection of muons, but also complements the precision MDT measurement with an estimation of the ϕ-coordinate. In the endcaps, multiwire proportional chamber technology is employed where the bending coordinate is measured by the anode sense wire and the azimuth by the cathode strips.

The trigger capabilities of the muon spectrometer are exploited in the design of new triggers in Chapter 4.

1.4.2 The forward detector systems

The central detector is complemented by a set of detector systems extending the total η-coverage far beyond the reach of the (central) forward calorimeters. These systems all consist of a pair of identical and equidistant detectors, placed on either side of the central interaction point.

Rather than enhancing the particle identification capabilities of ATLAS, these detectors provide a means to identify and trigger on collision events and to monitor and measure luminosity. The ability to detect collision debris scattered into the extreme forward directions, make the forward detectors potentially vital tools in tagging various forward physics processes, such as those discussed in Section 1.3.4.

The location and η-coverage of the various detector systems in ATLAS are depicted in Figure 1.18(a).

A brief description of the forward detector systems follows below in order of their distance from the interaction region.

1.4.2.1 MBTS (z= ±3.6 m, 2.12< $|\eta|$ < 3.85)

Located on the front face of either LAr endcap, the *Minimum Bias Trigger Scintillators* (MBTS) actually form part of the central detector, but is herein classified as a forward detector because of its applicability in forward rapidity gap identification (see Chapter 4). Its primary function is however to act as a trigger for minimum bias processes in the early phase of LHC operation. As shown in Figure 1.19, each wheel of the MBTS consists of 16 wedge-shaped plastic scintillators with an eightfold azimuthal segmentation in two η-rings: an *inner* ring covering $2.83 < |\eta| < 3.85$ and an *outer* ring covering $2.12 < |\eta| < 2.83$.

The scintillator light generated by the passage of particles through the scintillating material is collected by wavelength shifting fibres and amplified by photomultiplier tubes. If the deposited energy exceeds a threshold value, the signal is communicated to the Level
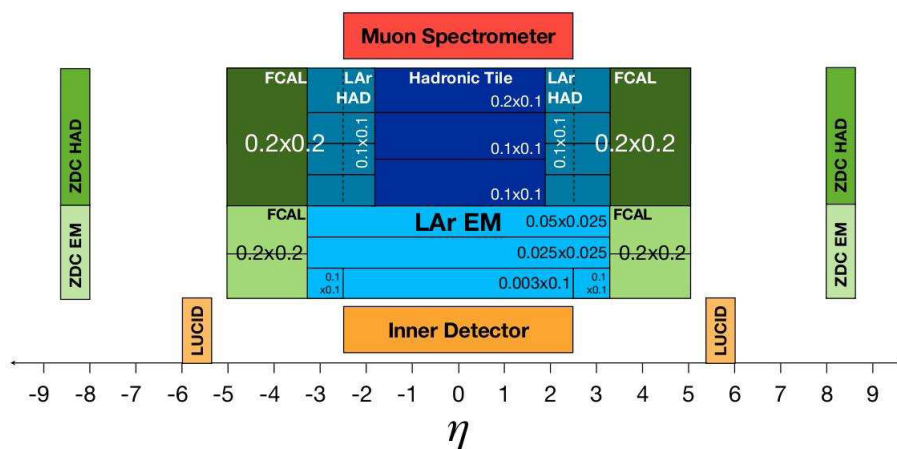
(a) Atlas pseudorapidity coverage
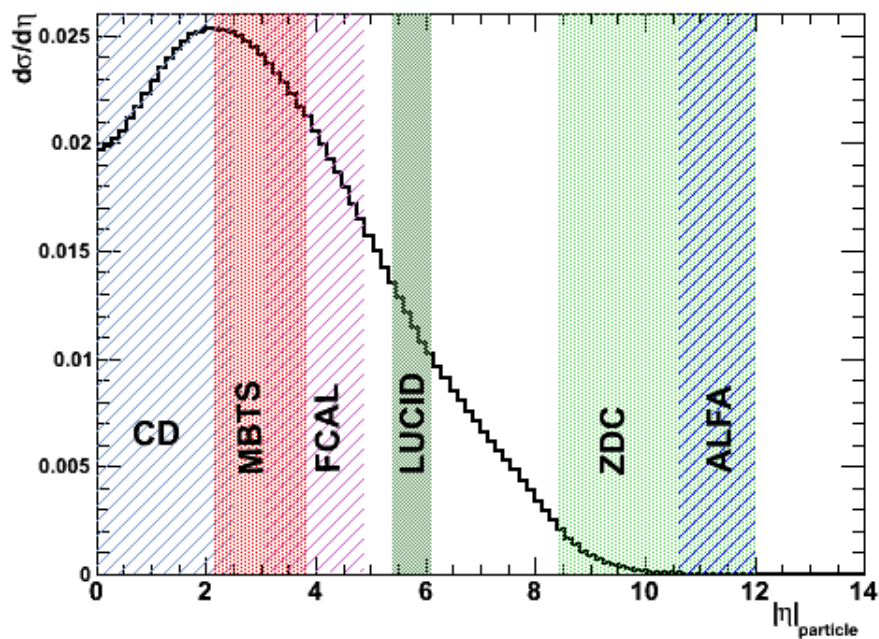
(b) η-spectrum of >100 MeV particles from simulated non-diffractive minimum bias events (PYTHIA) with the fractional coverage provided by the central detector (CD), MBTS, FCAL, LUCID, ZDC and ALFA.

FIGURE 1.18: The location and η-coverage various ATLAS detector subsystems.
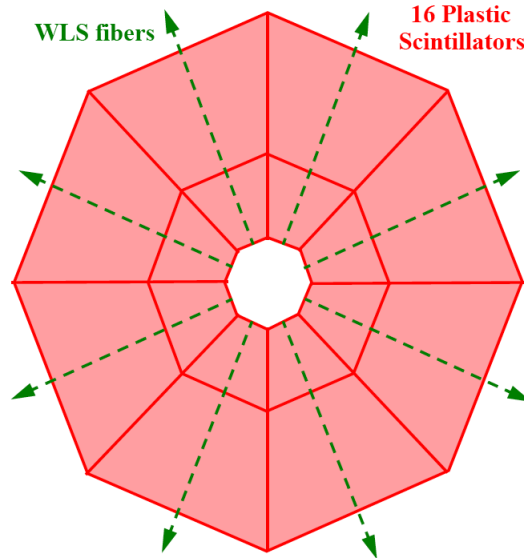
FIGURE 1.19: MBTS disk configuration. One such disk is placed on the inside of each LAr endcap. [40].

1 trigger (see Section 1.5) which is able to execute a logical AND/OR on signals from either side of the interaction point. This feature is exploited in Chapter 4 for triggering on lepton final states from exclusive production processes. The lifetime of the MBTS is limited to the early phase of LHC running at comparatively low luminosity, after which the plastic scintillators will deteriorate from excessive radiation exposure [35].

1.4.2.2   LUCID (z=±17 m, 5.4< $|\eta|$ <6.1)

Located at a distance of 17 m from the interaction point, LUCID (**LU**minosity measurement using Čerenkov **I**ntegrating **D**etector) is principally designed to monitor the instantaneous luminosity and beam conditions through the detection of forward scattered debris from inelastic pp collisions. As the number of charged particles detected is proportional to the number of interactions in a bunch crossing, a rapid luminosity determination is made possible by evaluating the average number of interactions per bunch crossing.

When charged particles traverse one of the several Čerenkov tubes arranged parallel to the beamline, they emit Čerenkov light[22] which can be collected by photomultipliers. The magnitude of the collected signal will be indicative of the number of particles crossing the tube, while ultrafast timing ($\sim$100 ps) allows for a precise separation of subsequent bunch crossings.

As discussed in Chapter 4, LUCID could also be used to identify forward rapidity gaps and tag exclusive processes.

---

[22]Čerenkov light is electromagnetic radiation emitted when a charged particle passes through a medium at a constant speed greater than the speed of light in that medium.

1.4.2.3 ZDC (z=±140 m, $|\eta| >$8.3)

At a distance of 140 m from the interaction point, the ZDC (**Z**ero **D**egree **C**alorimeters) are located where the single "interaction" beampipe bifurcates into two separate beamlines. While charged particles are largely deflected by the beam magnets, the ZDC will readily absorb forward neutral debris from the interaction, such as γ, π^0 and neutrons. The ZDC consists of one electromagnetic and three hadronic sampling calorimeters, each module containing several layers of active quartz rods interleaved with tungsten absorbers.

The ZDC are integral to the detection of forward neutrons from *ultraperipheral heavy ion* collisions (see Section 4.7), but also find applications as additional minimum bias triggers, as a beam gas and beam halo background suppressor[23] and in early beam tuning.

1.4.2.4 ALFA (z=±240 m, 10.6< $|\eta|$ <13.5)

While LUCID provides *relative* luminosity monitoring, ALFA (**A**bsolute **L**uminosity **F**or **A**tlas) aims to provide ATLAS with an accurate measurement of the *absolute* luminosity delivered[24]. This is achieved through the detection of elastic *pp* collisions down to very small scattering angles[25].

To facilitate the measurement of small angle deflections, ALFA is located far from the interaction point and employs *Roman Pot* technology wherein scintillating fiber trackers are moved to a distance of only $\sim$ 1 mm from the beam from above and below. This is only possible in dedicated runs when the beam configuration and optics is especially tuned to ensure the beam divergence does not exceed the small elastic scattering angles.

ALFA may also be used to tag fully elastic exclusive scatters, such as depicted in Figure 1.7(b), by detecting the photon emitting proton whose flight path after emittance is only slightly deflected with respect to the overall beam direction.

1.4.2.5 AFP - ATLAS Forward Proton Project

In addition to the forward detector systems presented above, ATLAS is currently involved in a joint pan-experimental[26] R&D project to evaluate the feasibility of installing *proton tagging* detectors at 420 m from the nominal IP to either side of both ATLAS and CMS [29].

---

[23]A tight coincidence requirement on either ZDC can help reduce backgrounds from beam effects.

[24]The *relative* luminosity is typically derived from fast, reproducible measurements and is proportional to the actual luminosity in an unknown, but constant way. By contrast, an *absolute* luminosity measurement is typically derived from beam parameters or a well known physics process.

[25]The *optical theorem* relates the forward elastic scattering amplitude to the total cross section σ_{tot}, the latter from which the absolute luminosity can be determined.

[26]The FP420 project involves members from the ATLAS, CMS and TOTEM experiments, as well as accelerator scientists and theorists.

The proposed detector systems are designed to operate as a magnetic spectrometer. Protons losing a minute fraction of their longitudinal momenta in a bunch crossing interaction, will typically continue undetected down the beampipe. As the bunch travels along the beamline, the LHC dipole magnets will bend protons carrying a small transverse component into the extremities of the beam envelope. At 420 m from the nominal interaction point, these protons "decouple" from the beam and are detected in several consecutive near-beam silicon tracker planes.

Spatial restriction precludes the use of Roman Pot techniques [41], therefore the proposal foresees the use of a "moving beampipe" in which segments of the LHC beampipe are replaced by custom beampipe modules with a larger diameter and a flattened area along one side where the tracking and timing detectors are located. Bellows connect the modules to the LHC beampipe to allow the sensors to be retracted during beam injection and moved closer to the beam during collisions. In this fashion, FP420 aims to tag and measure protons with fractional momentum losses of order 0.2-2%.

The proton arrival time is measured by the fast Čerenkov timing detectors. This timing information provides a measure for the time of flight from the interaction point and consequently the z-position of the interaction vertex. This in turn, may permit the tagging of *e.g.* elastic two-photon processes in a high luminosity environment with large pile-up contributions.

A major benefit to be derived from the FP420 project is the ability to precisely measure the proton momentum losses ξ. The mass of the centrally produced system can then be measured to high resolution ($\sim$ 2-3 GeV) on an event-by-event basis using the missing mass method [29]:

$$M \sim \sqrt{\xi_1 \xi_2 s} \tag{1.22}$$

where $\sqrt{s}$ is the center of mass energy of the colliding protons. Since this method relies squarely on forward proton tagging, it can be applied to determine the mass of any (resonant) exclusive central system, regardless of how the central system decays.

1.5 Trigger and Data Acquisition

At design luminosity, the LHC will cross bunches 40 million times per second. With an average event size of $\sim$ 1.3 MB, it is technically unfeasible to record collision events at a rate in excess of $\sim$ 200 Hz. The ATLAS trigger and data acquisition (DAQ) decides which 5 per million collision events will be recorded for later offline analysis.

As shown in Figure 1.20, ATLAS employs a three-tiered trigger scheme providing an overall rate reduction from 40 MHz to 200 Hz.

The *Level 1* (L1) trigger is required to make a decision every 25 ns and therefore needs to operate with very short processing times. Custom designed hardware allows time-stamped information from the various detector systems corresponding to roughly 100
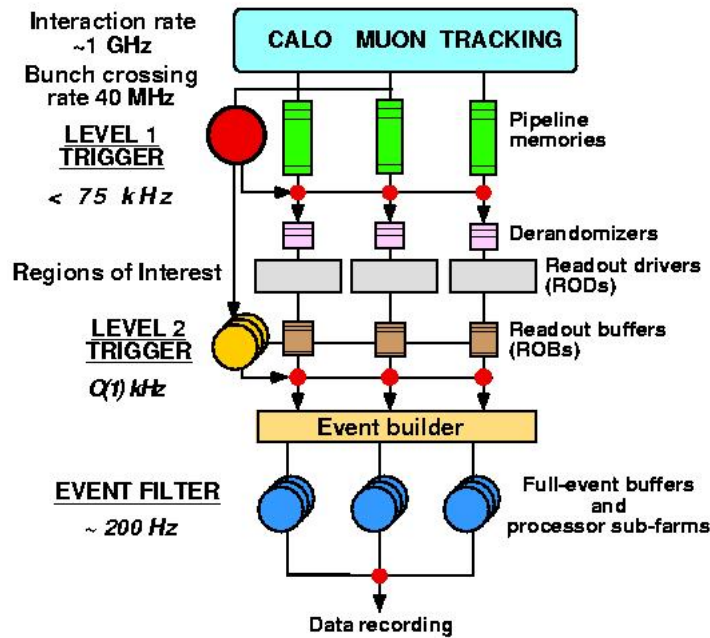
FIGURE 1.20: Schematic representation of the three tiered ATLAS trigger system.

successive bunch crossing to be stored in a memory buffer. With a latency of 2 μs, information from multiple bunch crossings is processed simultaneously by the *Central Trigger Processor*, which decides whether the event should be discarded or passed on to the *Level 2* trigger for further processing. The decision is based on a predefined catalogue of thresholds associated with crude signatures compatible with a $\mu, e/\gamma$, hadronically decaying τ, jet or E_T^{miss}, as well as some combinations thereof. While muon signatures are extracted from the muon trigger chambers, all other signatures derive from course granular ($\eta \times \phi \sim 0.1 \times 0.1$) information drawn from the calorimeters alone. No information from the inner detector is available at L1. If a positive decision is passed, a *Region of Interest* (RoI) in $\eta - \phi$ is built about the triggered objects and the full detector granularity within these RoIs passed to L2. This seeded approach significantly reduces the amount of data transfered and facilitates a speedy trigger decision.

Unlike the L1 trigger, the two subsequent trigger levels[27] are processing farms built from commercially available computer technology. The *Level 2* (L2) algorithms are seeded by the RoIs provided by L1 and have access to the full detector granularity therein, including information from the inner detector. Dedicated software is used to reconstruct and identify signatures within an RoI, enabling a refined decision with respect to L1 and a rate reduction from 75 kHz to 3.5 kHz within a latency of $\sim$40 ms per event.

The *Event Filter* (EF) by contrast, is not limited to the information within the RoI, but has full access to the complete detector granularity. This makes the EF comparatively slow (~ 4 s/event), but enables a much more refined decision based largely on the output of the offline reconstruction algorithms. The raw data of events passing the EF is written out to a central storage at a rate of ~ 200 Hz, with a copy immediately distributed to

---

[27]The two upper levels of the ATLAS trigger are collectively termed the *Higher Level Trigger* (HLT)

one of ten *Tier 1 grid computing nodes* worldwide wherein it is processed and made available for detailed offline analysis to all members of the collaboration.

The ATLAS trigger configuration is steered by a *trigger menu* approved by the collaboration. The trigger menu provides a catalogue of *trigger chains* of which at least one must pass for the event to be recorded to storage. A trigger chain stipulates a sequence of criteria or *signatures* that must be met at each level of the trigger for the chain to pass. To ensure that the total accept rate at the EF does not exceed the upper limit of 200 Hz, some signatures are assigned *prescale factors*. A prescale factor of 1000 implies that only 0.1% of events satisfying the signature requirements are eligible to pass. The combined prescale on a chain is therefore the product of the prescales applied to the signatures at each level. Both chain configurations and the application of prescale factors will evolve with the instantaneous luminosity delivered by the LHC. The choice of trigger menu and the configuration of the chains therein may therefore severely impact the feasibility of offline analyses. These issues are further discussed in Chapter 4.

1.6 A note on Monte Carlo simulations

The complexity associated with an experiment like ATLAS render simulation tools indispensable in nearly all areas of both ATLAS operation and data analysis. Simulated data are not only required to compare recorded data with theoretical predictions, but equally so for testing and evaluating the impact of instrumental effects on recorded data and for the development and validation of both new and existing offline reconstruction algorithms. Simulation tools thus provide robust modeling of the expected instrumental response to a given physical phenomena in a particular experimental environment to high statistical accuracy. In this context, it is appropriate to distinguish between the simulation of a physical interaction process and the simulation of the passage of stable particles emerging from the interaction region through the experimental volume.

The simulation of a physical interaction process encompasses all stages of a scattering interaction, including the hard interaction, hadronization and decay, as well as the underlying event. The modeling of these processes is generic, insofar that it does not depend on the details of the experimental volume in which the processes occur and are typically handled either by one single or a combination of several *Monte Carlo Generators* [20].

The stable particle output of such Monte Carlo Generators is then fed into an experiment-specific *detector simulation* which provides a stepwise propagation of each final state particle through a virtual detector volume, (ideally) taking due account of all interactions with matter along the trajectories. In ATLAS, this virtual detector volume is provided by a *GEANT4* simulation tool [42] configured with an accurate mapping of the material distribution inside of ATLAS.

The simulated interactions with the detector material are then translated ("digitized") into a format identical to that in which real data is recorded.

The subsequent steps involve the translation ("reconstruction") of raw (simulated or recorded) data into lower level objects such as tracks and clusters and subsequently higher level objects such as electrons and taus, whereby information is typically combined from several different detector systems.

Limited only by the accuracy of the detector modeling and the description of particle interactions with the detector material, a *full* GEANT-based simulation will mostly deliver statistically accurate results at the cost of comparatively prolonged computing times. Depending on the particle multiplicity of the physical process under examination, the average CPU-time required for the simulation of a single event will be of $\mathcal{O} \sim 20$ min.

Long simulation times severely limit the viability of producing large samples of full GEANT-based simulated data. As is discussed in Chapter 3, the consequences of insufficient amounts of simulated data can be detrimental for physics analyses. More recent developments therefore attempt to partially alleviate this problem by trading moderate reductions in simulation accuracy for significant reductions in simulation times. This is typically achieved by either simplifying the configured detector geometry or by parametrizing the energy response of particles in the detector (or a combination of both) [43, 44].

Chapter 2

Tau Reconstruction and Identification

2.1 Introduction

The tau lepton (τ) and the tau neutrino (ν_τ) together make up the third generation of leptons in the SM[1]. In the chiefly hadronic environment of the LHC, leptons often count among the most important handles on the hard interaction of interest. As the heaviest lepton in the SM, the τ-lepton plays an integral part in the ATLAS physics programme, not only in the context of the SM, but notably also in many searches for potentially new physics beyond.

The central rôle played by the τ-lepton across such broad range of interesting physics processes, underpins the need for efficient offline reconstruction and identification mechanisms with the ability to furnish offline analyses with the maximal amount of relevant information. This chapter will concern itself with the reconstruction and identification of τ-leptons. After a review of the key properties of tau leptons and the their place within the LHC physics programme, the canonical approaches to τ-reconstruction are briefly summarized before a novel method of reconstructing and identifying tau leptons is introduced.

2.1.1 The decay phenomenology of the τ-lepton

With a mass of 1,776.84 $\pm$ 0.17 MeV [38], the τ-lepton is unique in that it is the only lepton to exhibit decays into hadrons as well as into its lighter counterparts the electron and muon. As shown in Figure 2.1, all τ-lepton decays pass by way of the weak interaction through the exchange of a virtual W boson. Lepton number conservation implies that all τ-lepton decays involve a ν_τ which necessarily renders a portion of the τ four-vector experimentally undetectable. The W couples with universal strength to

---

[1]Incidentally, the tau lepton was the first member of the third generation of fermions to be discovered [45], an achievement for which M. Pearl was awarded the 1995 Nobel Prize in physics.

Decay modes	TAUOLA-CLEO
$\tau \to e\nu_e\,\nu_\tau,$	17.8 %
$\tau \to \mu\nu_\mu\,\nu_\tau$	17.4 %
$\tau \to h^\pm \text{neutr.}\nu_\tau$ (single-prong)	49.5 %
$\tau \to \pi^\pm\nu_\tau$	11.1 %
$\tau \to \pi^0\pi^\pm\nu_\tau$	25.4 %
$\tau \to \pi^0\pi^0\pi^\pm\nu_\tau$	9.2 %
$\tau \to \pi^0\pi^0\pi^0\pi^\pm\nu_\tau$	1.1 %
$\tau \to K^\pm \text{neutr.}\nu_\tau$	1.6 %
$\tau \to h^\pm h^\pm h^\pm \text{neutr.}\nu_\tau$ (three-prong)	14.6 %
$\tau \to \pi^\pm\pi^\pm\pi^\pm\nu_\tau$	9.0 %
$\tau \to \pi^0\pi^\pm\pi^\pm\pi^\pm\nu_\tau$	4.3 %
$\tau \to \pi^0\pi^0\pi^\pm\pi^\pm\pi^\pm\nu_\tau$	0.5 %
$\tau \to \pi^0\pi^0\pi^0\pi^\pm\pi^\pm\pi^\pm\nu_\tau$	0.1 %
$\tau \to K^0_S X^\pm\nu_\tau$	0.9 %
$\tau \to (\pi^0)\pi^\pm\pi^\pm\pi^\pm\pi^\pm\pi^\pm\nu_\tau$ (five-prong)	0.1 %
other modes with K	1.3 %
others	0.03 %

TABLE 2.1: The branching ratios of the dominant τ decay modes, as seen in 10^8 simulated τ decays from $Z \to \tau\tau$ events. The τ-leptons were decayed with TAUOLA, using a form factor tuning provided by the CLEO experiment (adapted from [47]).
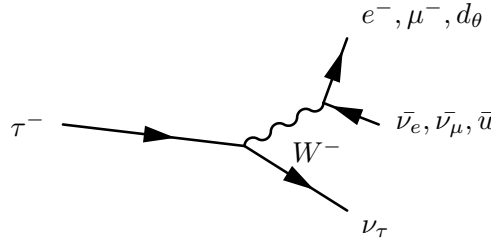
FIGURE 2.1: The decay of a τ-lepton through the exchange of a virtual W-boson.

the charged current to produce five approximately equal contributions to the tau decay spectrum: one from either leptonic decay mode and one from each colour combination of the quark-antiquark pair in the decay $\tau^- \to \nu_\tau \bar{u} d_\theta$ (where $d_\theta \equiv d\cos\theta_C + s\sin\theta_C$ corresponds to the Cabbibo rotated weak eigenstate field) [46].

While the leptonic decays are very well described theoretically, the hadronic decays suffer from the generic uncertainties of non-perturbative QCD. As discussed in Section 1.3.3.2, hadronisation effects will force the quark-antiquark pair into bound states of mesons. This process typically follows via various *mesonic resonances*, such as $\rho^\pm$ or $a_1^\pm$, which in turn decay into an array of light mesons, the most common of which is the pion. As seen in Table 2.1, these unique properties of the τ-lepton furnish a rich decay spectrum, which includes a particularly wide array of hadronic channels.

The experimental detection of leptonically decaying τ-leptons (τ_{lep}) differs fundamentally from that of hadronically decaying τ-leptons (τ_{had}). The relatively short lifetime of the τ-lepton (2.9×10^{-13} s) implicates a mean decay length of only $c \times \tau \sim 87.11 \mu m$.

If the decay proceeds leptonically, there is little to distinguish the visible decay products from primary electrons or muons, save by way the non-zero impact parameter exhibited in their tracks. The challenges associated with this task have traditionally been considered too involved to actively pursue in an LHC environment, though recent work has uncovered considerable scope in the channel $\tau \to \nu_\tau \nu_\mu \mu$ [48]. The presence of an additional neutrino further implies that the visible energy available in a leptonic decay will be less than that available in a hadronic decay for a tau of a given energy, a feature which at low transverse momenta may further challenge the reconstruction and identification of τ_{lep}.

The focus in ATLAS, as indeed herein, is therefore placed on the identification of *hadronically* decaying τ-leptons, which account for roughly 65% of all τ-lepton decay modes. As is seen in Table 2.1, such decays are characterized by an *odd* number of *charged* mesons, of which $\sim 95\%$ involve either one or three pions. In the parlance of τ-physics, a hadronic decay into n charged particles is commonly termed an *n-prong* mode in reflection of the number of charged tracks associated with the decay.

As indicated in Table 2.1, 1-prong modes account for roughly 76% of all τ_{had}, whereas the rest is dominated by various 3-prong modes. The comparatively scarce occurrence of $n > 3$ modes, precludes their consideration in the context of ATLAS and herein.

Table 2.1 further indicates that each n-prong decay may include a neutral component, most commonly in the form of neutral pions. This is particularly true of 1-prong modes, where almost 74% of all decays involve at least one π^0. Among the 3-prong modes, additional π^0 are more rare, occurring in roughly 1/3 of all 3-prong decays.

While the majority of hadronic decays involve $\pi^\pm$ and π^0, a small fraction of decays will involve strange mesons, such as $K^\pm$s and K_s^0s. From the experimental point of view, decays into $\pi^\pm$ and $K^\pm$ are mostly equivalent. The K_s^0 primarily decays into either two charged pions or two neutral pions. Depending on just how they interact within the detector, decays involving K_s^0s may hence be registered as either 1-prong or 3-prong.

In summary, a hadronically decaying tau is therefore principally identifiable by way of its unique decay topology:

- 1 or 3 tracks from the $\pi^\pm$s,

- hadronic energy depositions from the $\pi^\pm$s,

- potential electromagnetic energy depositions from the $\pi^0 \to \gamma\gamma$.

2.1.2   The rôle of tau leptons in the LHC physics programme

The comparatively complex decay phenomenology of the τ-lepton arguably makes it the most challenging charged lepton to reconstruct and identify in the predominantly hadronic environment of the LHC. As was already alluded to in Chapter 1, the abundance of hadronic debris from various QCD processes constitutes a formidable background to
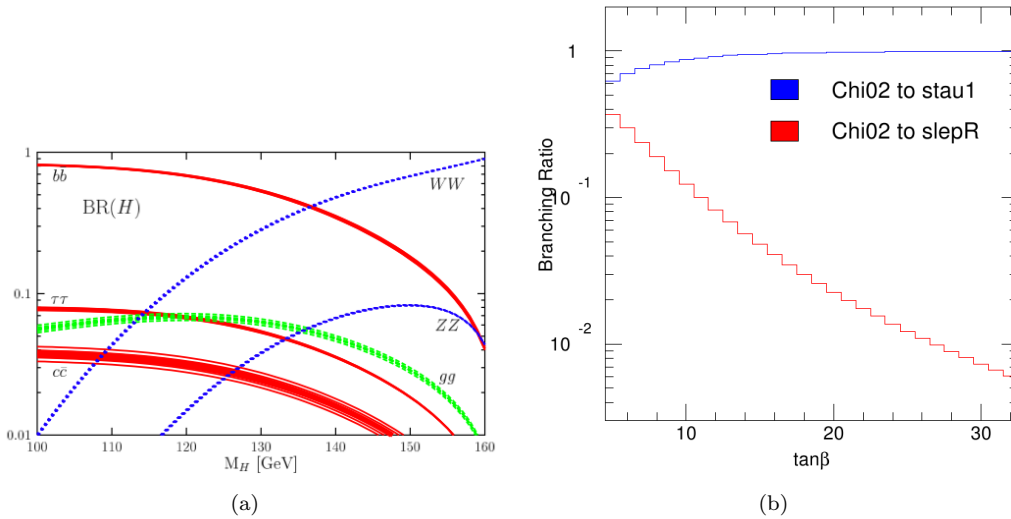
FIGURE 2.2: (a)The branching ratio of various SM Higgs boson decays as a function of the Higgs mass M_H (truncated). A significant decay rate to a pair of τ-leptons is observed in the low mass region. [49]. (b) Branching ratios of the decays $\tilde{\chi}_2^0 \to \tilde{\tau}_1 \tau$ (blue) and $\tilde{\chi}_2^0 \to \tilde{l}_R l$ (red) as a function of $\tan\beta$ in the mSUGRA point SPS1a [50].

the identification of τ_{had}. The call for efficient and accurate τ-reconstruction algorithms despite these inherent challenges is principally motivated by the potentially wide array of scenarios in which τ-leptons may serve as a probe for new physics beyond the Standard Model:

SM Higgs

The combination of comparatively large production cross sections and conspicuous event signatures makes *Vector Boson Fusion* (VBF) an intriguing production mode for the Standard Model Higgs boson at the LHC. As is shown in Figure 2.2(a), the subsequent decay $H \to \tau\tau$ is the second most dominant decay mode at low Higgs masses where it presents itself as a more attractive discovery channel when compared to the more dominant $H \to b\bar{b}$. In fact, VBF $H \to \tau\tau$ is the only channel by which a low mass Higgs ($m_H <$140 GeV) can be observed with only $\sim 30\text{fb}^{-1}$ of integrated luminosity in ATLAS [47].

SUSY

In the context of SUSY, the third generation of sparticles[2] is generally of particular interest as they may provide a handle on the underlying SUSY breaking mechanism [51].

As the heaviest lepton, the τ enjoys the largest leptonic Yukawa coupling and by consequence plays an integral part in phenomenology of many supersymmetric models, often across large regions of the model parameter space. While the mixing between the superpartners of the right and left-handed leptons of the first two generations is expected to be small, it will be more significant in the third generation where the Yukawa coupling is larger. The mixing of $\tilde{\tau}_R$ and $\tilde{\tau}_L$ yields two mass eigenstates $\tilde{\tau}_1$ and $\tilde{\tau}_2$ both of

---

[2]In SUSY jargon, a *sparticle* is a supersymmetric partner of a *particle*.

which frequently appear in SUSY phenomenology to which ATLAS may be sensitive. An illustrative case in point is found in mSUGRA-type models, wherein the $\tilde{\tau}_1$ is the *lightest* slepton and moreover receives a significant $\tilde{\tau}_L$-contribution thereby enhancing its coupling to the wino-dominated light gauginos $\tilde{\chi}_2^0$ and $\tilde{\chi}_1^{\pm}$[3]. An inherent tendency for τ-lepton final states therefore exists, a characteristic often made more pronounced in scenarios with large $\tan\beta$, as shown in Figure 2.2(b).

τ-leptons may then readily appear in the decay of strongly produced squarks and gluinos:

$$\tilde{q} \to q\tilde{\chi}_2^0 \to q\tau^{\pm}\tilde{\tau}^{\mp} \to q\tau^{\pm}\tau^{\mp}\tilde{\chi}_1^0$$

and their successful reconstruction hence provide a handle on the masses and mixings of SUSY particles in the decay chain [52]. Moreover, the *polarization* of the τ-leptons in the above decay chain will depend on the precise bino/wino/higgsino content of the $\tilde{\chi}_1^0$ and $\tilde{\chi}_2^0$ and thus deliver valuable information on their respective couplings, as well as that of $\tilde{\tau}^{\pm}$ [53]. An accurate polarization dependent measurement requires the τ-reconstruction algorithms to not only be able to suppress unwanted background, but also to facilitate the evaluation of the precise decay mode of the τ-lepton [53]. The need for an efficient separation of the various decay modes of the τ-lepton, partially motivates the development of the novel τ-reconstruction algorithm presented herein.

MSSM Higgs

A minimal supersymmetric extension to the Standard Model comes with two Higgs doublets, giving rise to altogether three neutral (h, H, A) and two charged ($H^{\pm}$) physical states.

The decay of the charged Higgs is expected to be dominated by $H^{\pm} \to tb$ and $H^{\pm} \to \tau\nu_{\tau}$, the latter of which provides a more promising avenue for observation in the QCD environment of the LHC. If observed, a rate measurement of $H^{\pm} \to \tau\nu_{\tau}$ may help determine the value of the SUSY parameter $\tan\beta$ [54]. The neutral Higgs states H and A are also predicted to decay into a pair of τ-leptons, with rates significantly larger than the corresponding rate of the Standard Model Higgs across a large portion of the parameter space.

Standard Model

The decay process $W \to \tau\nu_{\tau}$ is the most copious Standard Model source of (isolated) τ-leptons at the LHC and consequently plays an integral rôle in the early commissioning and consolidation of τ-reconstruction and identification tools. However, the most important process for early commissioning is arguably the process $Z \to \tau\tau$. Despite a cross section roughly an order of magnitude below that of $W \to \tau\nu_{\tau}$, the presence of an additional τ-lepton in the event not only serves to suppress backgrounds, but also allows for an *unbiased* collection of τ_{had} through the explicit selection of events in which one τ-lepton decays leptonically and the other hadronically. This invites for

---

[3]The wino only couples to $\tilde{l}_L$. A large wino-admixture therefore suppresses the coupling to other sleptons.
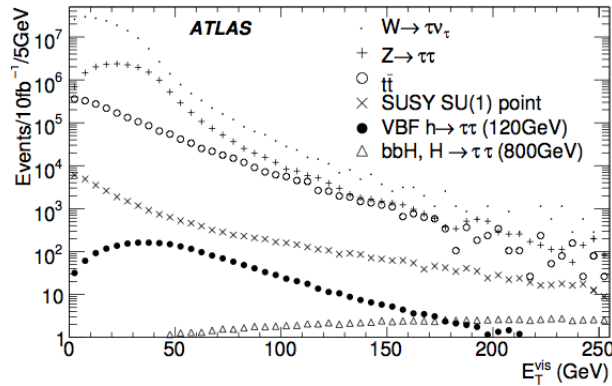
FIGURE 2.3: Visible transverse energy spectrum of τ-leptons in various processes at the LHC, normalized to their respective predicted cross sections ($\sqrt{s} = 14$ TeV) and an integrated luminosity corresponding to 10 fb^{-1} [32].

the use of *tag-and-probe* techniques to measure online and offline reconstruction efficiencies. In addition, a peak is expected to manifest itself in the visible mass spectrum, a feature which in turn can be exploited in the determination of the τ_{had} energy scale. Another prolific source of τ-leptons may be found in *semi-leptonic* $t\bar{t}$ events, where $t\bar{t} \to W(\to q\bar{q})W(\to \tau_{had}\nu_\tau)b\bar{b}$ or $t\bar{t} \to W(\to e\nu_e/\mu\nu_\mu)W(\to \tau_{had}\nu_\tau)b\bar{b}$. While the cross-sections are smaller than for Z/W, so are backgrounds, and the unique event topology of $t\bar{t}$ events allows one to test τ-lepton identification in an environment much resembling that predicted of SUSY. The Standard Model also predicts τ-final states resulting from two-photon processes at the LHC. While the observation of such events remains elusive at hadron colliders, the potential for their detection is discussed at length in Chapter 4.

2.1.3 Kinematics of tau decays at the LHC and challenges to tau reconstruction

The wide array of physics processes in which τ-leptons are anticipated to play a central rôle calls for efficient reconstruction algorithms across a broad kinematic range, as is indicated in Figure 2.3.

While the high end of the kinematic spectrum is relevant for searches involving heavy new particles decaying into a pair of τ-leptons, it is noteworthy that the lower end is relevant to not only Standard Model processes, but also to VBF Higgs and SUSY. The latter is a peculiar case in point, whereby a small mass difference m($\tilde{\tau}_1$)-m($\tilde{\chi}_1^0$)$\lesssim$ 30 GeV will typically imply that τ-leptons emerging from the decay $\tilde{\tau}_1 \to \tau\tilde{\chi}_1^0$ will tend to be comparatively soft.

In the hadronic environment of the LHC, the central challenge to the τ-reconstruction will nearly always be to suppress the overwhelming background from QCD processes whose cross section is typically many orders of magnitude larger than the process of interest. However, subtle, yet important, differences do exist across the various kinematic regions.
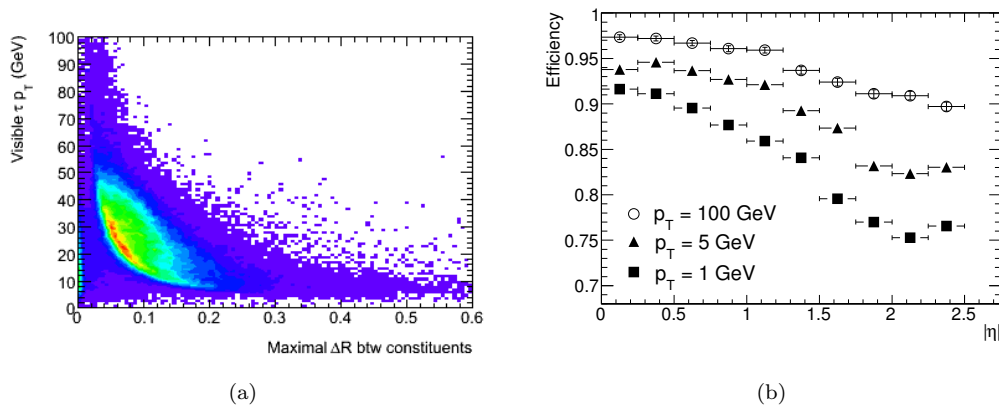
FIGURE 2.4: (a) Maximal distance in ΔR between constituent particles in τ-decays from $Z \to \tau\tau$ vs the true visible transverse momentum of the parent τ-lepton. While the majority of will rarely have a spread greater than $\Delta R \sim 0.2$, low (b) Track reconstruction efficiency for pions at various transverse energies as a function of $|\eta|$. Efficiency degradation is likely to follow from hadronic interactions (and multiple scattering) in the inner detector material [32].

As was alluded to in Section 2.1.1, the conventional strategy for separating τ-leptons from QCD jets relies on the characteristic tendency of the former to produce comparatively narrow and well collimated "τ-jets" formed by a limited number of charged and neutral pions. Quarks and gluons by contrast, will often be colour connected to other particles in the event and are generally expected to produce broader, less collimated jets with higher particle multiplicities.

While this property holds very well at intermediate transverse momenta ($\gtrsim 30$ GeV), it is less robust in the high and low ends of the kinematic spectrum. At high transverse momenta, the Lorentz boost given to the constituents of hadronic jets is likely to make the resulting jet appear more collimated and consequently more τ-like. As the momenta of the charged pion constituents of the τ-decay drop, their bending in the magnetic field of the inner detector becomes more pronounced, effectively widening the τ-jet by increasing the distance between its pion constituents. This tendency is observed in Figure 2.4(a) in which the maximum distance of pion constituents from the visible τ-axis is shown as a function of the visible transverse momentum. The steeply falling QCD jet cross section at the LHC, also implies that the low-p_T region will need to withstand significantly higher background rates.

Even in cases where the "narrow-jet" approximation holds well, it is from the perspective of physics analyses often desirable to not only reconstruct the τ-lepton, but also to extract potentially valuable information from its mode of decay. This requires the reconstruction algorithms to not simply view the τ-decay as a unit entity, but also whenever possible resolve the constituent decay particles. The ability to do so will in large part depend on both the kinematics and topology of the τ-decay and the interaction of the decay particles with the detector material:

The relatively large amount of material in the ATLAS inner detector may occasionally cause charged pions to initiate showering before reaching the calorimeters. As seen in

49

Figure 2.4(b), this effect is slightly more pronounced at low pion energies and such early hadronic interactions will serve to complicate the identification of τ-decay constituents.

In a similar vein, the relatively short lifetime of the π^0 (8.4×10^{-17}s) implies a subsequent instantaneous decay on detector length scales. In $> 98\%$ of cases, the π^0 will decay into two photons ($\pi^0 \to \gamma\gamma$). The photons from the π^0 decay are in turn prone to convert into electron-positron pairs ($\gamma \to e^+e^-$) upon interaction with the material in the inner detector, before reaching the calorimeters. Additional tracks from photon conversions may distort the proper reconstruction of the tau decay, *e.g.* by causing 1-prong decays to be falsely reconstructed as 3-prong or if the parent π^0 is of low momentum result in a scatter of the neutral energy both within and outside the τ-decay cone[4].

In the following, a brief overview of existing approaches to the experimental detection of tau leptons in ATLAS is presented, before a novel method of reconstructing and identifying tau leptons is introduced.

2.2 Conventional approaches to tau reconstruction and identification in ATLAS

The ATLAS experiment currently employs two complementary approaches for the reconstruction and identification of hadronically decaying τ-leptons. By and large, both algorithms treat the τ-decay as a *unit entity* and separation from QCD jets is attempted on the basis of the conspicuous traces left in the tracker and calorimeters:

- a low track multiplicity in a narrow cone

- calorimetric shower shapes and characteristics of the track system

- isolation from other objects in the inner detector and calorimeters

The two algorithms are commonly distinguished in terms of their respective methods for building a τ-candidate: the *calorimeter-based* algorithm (`tauRec`) creates τ-candidates from jets built on calorimeter clusters, whereas the *track-based* algorithm (`tau1p3p`) builds τ-candidates around good quality tracks. Either algorithm combines information from both the calorimeters and tracker to construct a suite of discriminating variables on which either cut-based selections or more complicated multivariate separation methods can be applied. The implementation is such that both algorithms run in a merged configuration, so that if a τ-candidate is seeded by both algorithms, variables from either algorithm are made available for an improved identification.

In the following, only a cursory overview of either method will be given. More detailed descriptions are available in [47, 55, 56].

---

[4]Soft conversion electrons are more sensitive to the magnetic field of the inner detector and may consequently be bent out of the τ-decay cone, potentially rendering a portion of the visible τ-momentum lost to the reconstruction.

Calorimeter based reconstruction

The calorimeter based candidates are seeded by fixed size cone ($\Delta R = 0.4$) jets built on topological calorimeter clusters[5]. The topological clustering algorithm is described Section 2.3.1.1. The seed jets are required to satisfy $p_T^{\text{jet}} > 10$ GeV and $|\eta^{\text{jet}}| < 2.5$. Any qualified tracks found within a cone of $\Delta R < 0.3$ are associated to the τ-candidate.

Track based reconstruction

Rather than using jets built from calorimeter clusters, the track based τ-candidates are seeded by qualified tracks with $p_T^{\text{trk}} > 6$ GeV. The *core* region around the seed track ($\Delta R < 0.2$) is subsequently scanned for additional tracks, and if satisfactory tracks are found ($p_T^{\text{trk}} > 1$ GeV) these are associated to the τ-candidate. If the total number of tracks exceeds eight, the track-based candidate is discarded. Moreover, the total charge on a 3-track candidate must satisfy $|Q| = 1$.

If a calorimeter seeded candidate and a track seeded candidates are found to overlap in a cone of $\Delta R < 0.2$, only one τ-candidate is built. A reconstructed event may therefore contain a mixture of τ-candidates that have either been seeded by *both* the calorimeter and track based approaches, or alternatively by either one of the two.

2.2.1 Tau energy determination

Two distinct methods for determining the τ energy scale are provided. In calorimeter-seeded candidates, all calorimeter cells within a cone $\Delta R < 0.4$ about the barycenter of the seed jet are summed and weighted with an H1-style calibration scheme [58] in which the cell weights are η, ϕ and subdetector dependent functions of the cell. This method was originally intended for jet calibration and consequently (Monte Carlo derived) correction factors are applied to the cell weights to make them more applicable to τ-jets.

The track based tau candidates by contrast employ an energy flow algorithm to determine the energy scale of the tau. To do so, the cells associated with the track seeded candidate are classified in different categories:

- **pure electromagnetic energy** ($E_T^{\textbf{emcl}}$), involving energy collected in a narrow window about an isolated electromagnetic cluster displaying minimal hadronic leakage

- **charged electromagnetic energy** ($E_T^{\textbf{chrgEM}}$, $E_T^{\textbf{chrgHAD}}$), involving energy in a narrow window about the impact point of the tracks in the each layer of the calorimeter

- **neutral electromagnetic energy,** ($E_T^{\textbf{neutEM}}$), involving energy from all unused cells surrounding the cell ($\Delta R = 0.2$) closest to the track impact point in the first three layers of the calorimeter.

---

[5]At the time of writing, the fixed size cone 0.4 jet input is being replaced by Anti-Kt 0.4 jets [57]. The latter are also made to run on topological clusters.

Assuming the absence of hadronic neutrals, the total charged energy deposition E_T^{chrgEM} + E_T^{chrgHAD} are duly replaced by the momenta of the tracks. The potential presence of π^0 mesons is contained in the E_T^{emcl} and E_T^{neutEM}. Two additional empirically derived correction terms arise from the potential overlap between π^+ and π^0 where both deposit energy in the same cells ($\sum \text{res}E_T^{\text{chrgEM}}$) and from charged hadronic leakage outside a narrow cone about the track(s) ($\text{res}E_T^{\text{neutEM}}$). The energy scale of the tau is finally defined as:

$$E_T^{\text{eflow}} = \sum p_T^{\text{track system}} + E_T^{\text{emcl}} + E_T^{\text{neutEM}} + \sum \text{res}E_T^{\text{chrgEM}} + \text{res}E_T^{\text{neutEM}} \qquad (2.1)$$

The motivational backdrop for replacing the energy deposits of cells matched to tracks in this fashion to obtain an improved energy measurement, is discussed in the following section.

2.2.2   Tau identification

Both algorithms provide a handful of discriminating variables to assist the suppression of false candidates from QCD jets. These variables are built from the candidate tracks or associated calorimeter cells, and include among others:

- The profile (radius) of energy deposits in the electromagnetic calorimeters

- Isolation quantities drawn from calorimeter deposits and tracks in an isolation region

- Ratio of calorimetric energy to the sum of track transverse momenta

- Track widths[6], impact parameter significance of leading track and the transverse flight path significance of the τ-candidate vertex

A detailed listing of all available variables can be found in [55]. These variables form the input to various identification methods, ranging from comparatively simple cut-based approaches to more advanced methods making use of different multivariate techniques.

2.3   The case for energy flow in ATLAS

The principles of *energy flow* were first applied to jets at LEP by the ALEPH collaboration [59], and the merits of the this approach were later corroborated at other collider experiments, such as HI, D0 [60] and CDF [61].

Studies of jet fragmentation performed at LEP have revealed the particle composition of a jet to be roughly 62% charged hadrons, 27% photons, 10% long lived neutral hadrons

---

[6]The variance of track $\Delta\eta$ weighted by the track p_T, where $\Delta\eta$ is measured with respect to the τ-candidate axis.
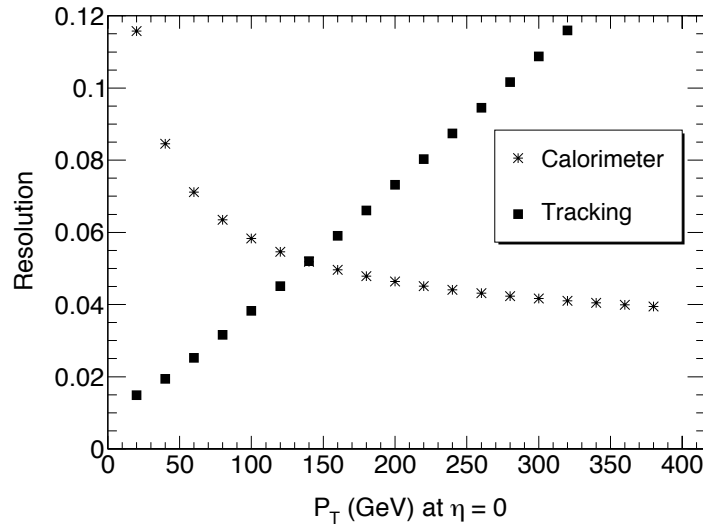
FIGURE 2.5: The relative energy resolution $(\sigma(E)/E)$ and momentum resolution $(\sigma(p_T)/p_T)$ as a function of the $\pi^\pm$ transverse momentum in ATLAS [62].

(*e.g.* n, K_L) and a small fraction ($\sim$ 1%) of neutrinos [60]. It follows that $> 70\%$ of the jet energy will be measured in the hadronic calorimeters and by consequence the jet energy resolution will be limited by the comparatively poor resolution of the hadronic calorimeters. As is shown in Figure 2.5, an improved resolution can be achieved at low and intermediate transverse momenta, if the calorimetric energy deposits from charged particles are removed and replaced by their more accurately measured track momenta. With the momenta of charged particles measured in the tracking detectors, the calorimeters are only used to determine the energies of photons and neutral hadrons and consequently the dependence on the hadronic calorimeters is reduced to a minimum. The challenge will be to properly associate tracks and calorimeter deposits and to avoid any double counting of energy.

With the advent of more granular calorimeters increasingly more capable of separating showers from close lying particles, the concept of energy flow has been extended to include the full reconstruction of the 4-vectors of *individual particles* in the event, drawing on the most favourable combination of information from all subdetectors [60, 63]. In this concept, often known as *particle flow*, composite particle objects such as τ-leptons and jets are not treated as unit entities, but instead as objects derived from the reconstructed particles ($\pi^\pm, \pi^0, \gamma, \mu^\pm$,p, n, etc.) in the event.

In the following, it is shown how the ATLAS calorimeters may lend themselves to energy flow calorimetry, followed by a brief description of the generic energy flow algorithm in ATLAS. Finally, in Section 2.4, a novel approach to τ reconstruction inspired by the ideas of particle flow is presented.

2.3.1 Clustering of calorimeter cells in ATLAS

The ATLAS calorimeters are described in Section 1.4.1.2. As explained therein, most particles traversing the calorimeter material are prone to "shower", depositing their energy in several different calorimeter cells across the various layers of the calorimeter, both along (longitudinally) and perpendicular (laterally) to their direction of flight. In order to reconstruct this shower, the active cells in which the particle energy was deposited need to be grouped into *clusters* of cells representing the calorimetric shower whose total (calibrated) energy reflects the energy deposited by the showering particle. AT-LAS employs two such clustering algorithms to group calorimeter *cells* into calorimeter *clusters*:

> a **sliding window** algorithm in which cells within a fixed size rectangular window in $\eta - \phi$ are collected and summed

> a **topological** algorithm in which cells above a set noise threshold are iteratively collected around an energetic seed cell to form a cluster

Topological clusters form a key ingredient in the generic energy flow algorithm in ATLAS and are in many ways a prerequisite for its operability. Topological clustering will therefore be given a brief description herein. A more detailed description is available in [64].

2.3.1.1 Principle of topological clustering

Topological clustering attempts to create clusters by grouping neighboring cells deemed to contain energy deposits well in excess of the expected background noise level. In sharp contrast to fixed-sized "sliding-window" clusters, topological clusters can therefore be expected to vary both in size and shape, depending on the energy of the incoming particle and the size and complexity of its shower. The algorithm involves a two-step procedure whereby clusters are first built and later split if necessary to separate overlapping showers [64].

Cluster Building

All calorimeter cells with $|E| > t_{seed}$ function as *seeds* for cluster building, where t_{seed} represents a configurable signal to noise ratio. The noise level is determined from the expected RMS of the electronics noise with pile-up contributions added in quadrature. Each seed serves as a protocluster and the list of protoclusters is sorted in descending order in ratio of signal to noise. Each protocluster is then processed in turn, whereby the protocluster is allowed to grow by adding all adjacent cells[7] ("neighbours") whose signal to noise ratio is in excess of a configurable threshold $t_{neighbour}$. If such a neighbouring cell borders more than one protocluster, the protoclusters are merged. Finally all cells along the outer perimeter of the cluster with a signal to noise ratio $< t_{neighbour}$ but $> t_{cell}$

---

[7] Only cells that are not counted as seeds are considered.
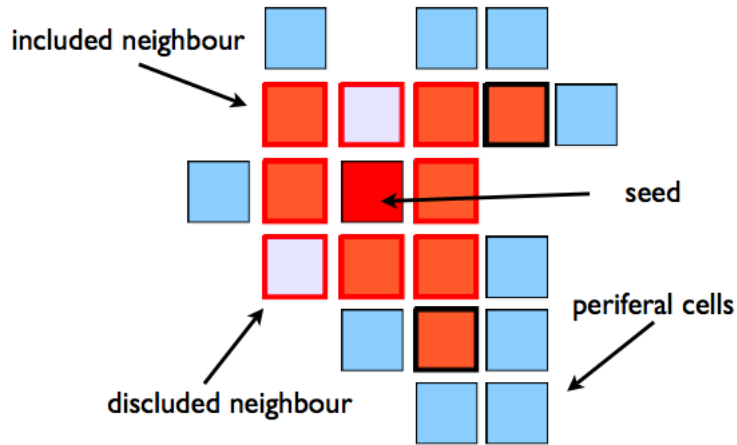
FIGURE 2.6: Principle of topological clustering: a cluster is grown around a seed cell (red) with $|E|/\sigma_{\text{noise}} > t_{\text{seed}}$. The eights cells topologically connected to the seed (red rectangles) count as immediate neighbours. Immediate neighbours with $|E|/\sigma_{\text{noise}} > t_{\text{neighbour}}$ are added to the cluster (orange). Neighbours of neighbours (black rectangle) are added until no further qualified neighbours exist. Finally, any periferal cells satisfying $|E|/\sigma_{\text{noise}} > t_{\text{cell}}$ are included.

are added to the cluster to ensure proper inclusion of shower tails [8]. The protocluster is allowed to grow in this fashion as long as topologically connected cells exist with a signal significance in excess of $t_{neighbour} \times \sigma_{noise}$. This basic procedure is illustrated in Figure 2.6.

Neighbouring cells do not only comprise all 8 immediate adjacent cells within the same layer, but also includes adjacent topologically connected cells overlapping partially in $\eta - \phi$ in adjacent calorimeter *layers* and/or adjacent calorimeter *systems* [9].

The different technologies and configurations employed in the various layers and regions of the calorimeter also give rise to noise levels that vary by several orders of magnitude across the calorimeter. Depending on just how the threshold settings are chosen, topological clusters may therefore form entirely from noisy cells. The number of such "noise clusters" may be estimated using the complementary error function of the seed threshold:

$$N_{clusters}^{noise} = N_{cells}\sqrt{\frac{2}{\pi}} \int_{t_{seed}}^{\infty} e^{\frac{-t^2}{2}} dt \qquad (2.2)$$

which predicts 11.9 noise clusters in each event using the default settings $t_{seed} = 4, t_{neighbour} = 2$ and $t_{cell} = 0$ on the full set of 187652 calorimeter cells [64]. *Confusion* arising from the presence of such pure noise clusters can be expected to degrade the performance of any particle flow inspired reconstruction of τ-leptons.

---

[8]The default setting $t_{cell} = 0$ includes all positive energy cells neighbouring the cluster perimeter regardless of their energy content.

[9]If the granularity of the ATLAS calorimeters was uniform across the different layers, a typical seed cell would be surrounded by 10 neighbouring cells. However, since the granularity of the various calorimeter layers differ widely, the number of neighbouring cells is typically much larger.

Cluster Splitting

Ideally the topological clustering algorithm as described above should render a one-to-one correspondence between cluster and isolated showering particle, however without some measure to resolve overlapping showers, this correspondence is rarely achievable in ATLAS. Overlapping showers result in part from showering particles in too close a separation, but also from the granularity and configuration of the calorimeters. In the more forward regions of the detector, the comparatively coarse granularity of the endcaps and FCAL combined with the typically higher density of particle debris often result in very large topological clusters. In order to remedy unwanted cluster growth from shower overlaps, all *primary* topoclusters resulting from the aforementioned clustering procedure are subjected to a splitting algorithm. The splitting algorithm seeks to separate overlapping showering particles by identifying *local maxima* in the primary topoclusters. A local maximum is defined as an energetic ($E > 500$ MeV) clustered cell with more energy than any of its neighbouring cells, of which there needs to be a minimum of 4. To suppress noise cluster formation, cells from the presampler are excluded from this procedure, while cells from the the strips and the HCAL are only used if they do not $\eta - \phi$ overlap with a primary local maximum. Consequently, hadronic topoclusters with a significant energy deposits in the ECAL are likely to split along their electromagnetic core, while hadronic clusters with small electromagnetic components may be separated, if required, using the coarser maxima located in the HCAL.

It is noteworthy that this splitting procedure may have both desirable and undesirable consequences. In the context of a physical τ-decay, the splitting procedure may in some cases help resolve the shower overlap between a $\pi^{\pm}$ and a π^0, while it in other cases may divide a single cluster resulting from a $\pi^{\pm}$ with an early shower in the ECAL. These issues will be touched upon in Section 2.3.2.3.

Once all local maxima have been located in the primary topoclusters, *secondary* topoclusters are re-grown about the local maxima following the aforementioned prescription with the key difference that only cells forming part of a primary cluster are used (rendering the application of thresholds redundant) and no cluster merging takes place, so that each resulting cluster will contain only one local maximum. If a cell is found to border more than one proto-cluster, its energy is shared in a weighted fashion between the two proto-clusters containing the two most energetic neighbours. Primary topoclusters in which no local maxima were found are kept intact.

The final collection of topological clusters passed as input to the energy flow algorithm, therefore contains a mixture of primary topoclusters and secondary topoclusters re-grown about local maxima, some of which may share cells along the perimeter.

2.3.1.2 The application of topological clustering to τ-decays

Figure 2.7 shows the structure of the topological clusters produced in response to a relatively soft $\tau \rightarrow \nu_\tau \pi^{\pm} \pi^0$ decay in the first three layers of the electromagnetic calorimeter. A comparatively high granularity combined with intelligent clustering is seen to render
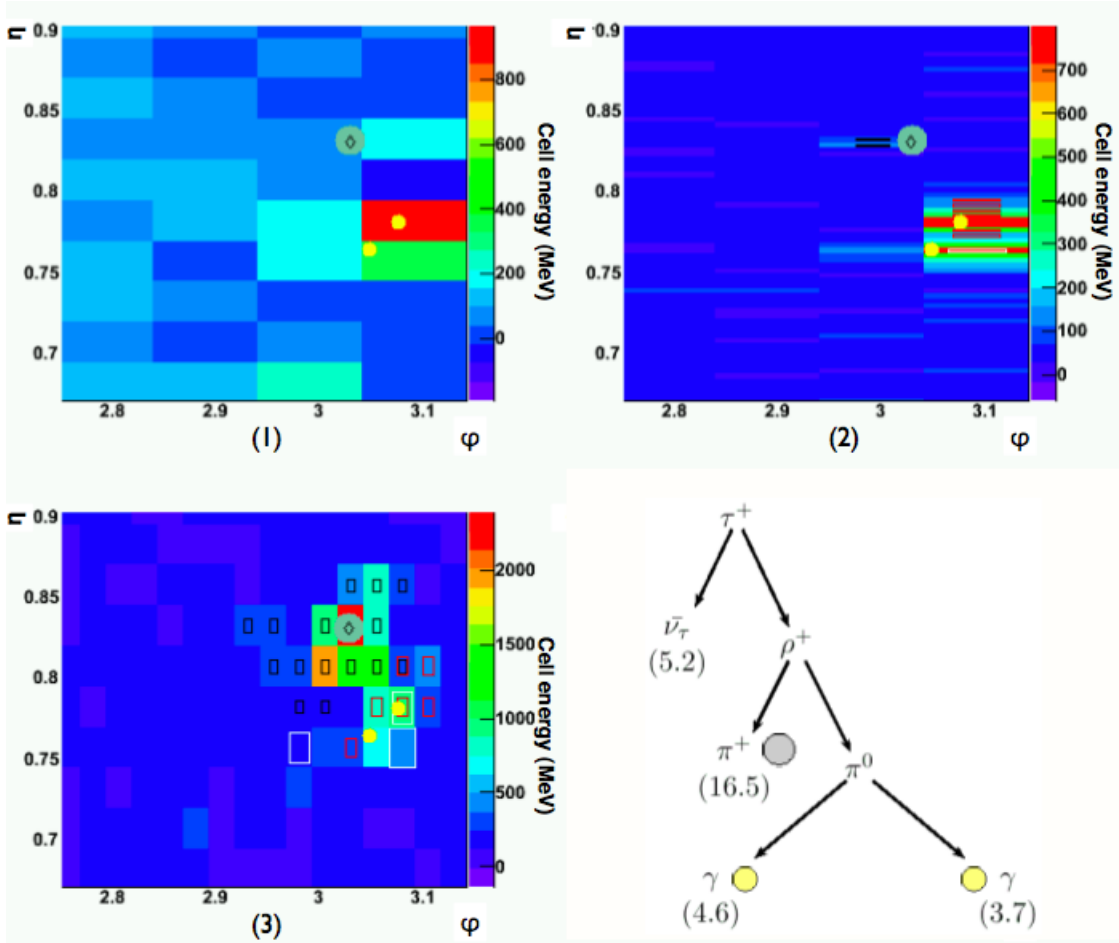
FIGURE 2.7: Topological clustering in the first three layers of the electromagnetic calorimeters: (1) presampler, (2) η-strip layer and (3) middle layer (ref. Figure 1.15(a)). The true $\pi^{\pm}$ is marked as grey dot, the two photons emerging from the decay $\pi^0 \rightarrow \gamma\gamma$ by two yellow dots. The track associated with the $\pi^{\pm}$ is marked by a diamond. The cells forming part of a topocluster are marked by coloured rectangles. A separation of the $\pi^{\pm}$ shower (black cluster) from the the π^0 shower in (red cluster) is achieved, despite a small spatial separation. In the finely segmented η-strip layer, the individual photons are resolved.

resolved charged and neutral pion clusters. In order to resolve close lying showers into separate clusters, it is important that the topoclusters do not grow too large, while still properly accounting for all the deposited energy. In this context, preliminary studies were performed to investigate whether the default topocluster settings governing cluster growth ($t_{seed} = 4, t_{neighbour} = 2, t_{cell} = 0$) provide the most optimal separation of pion clusters in τ-decays. A comparison of matched cluster multiplicity in 1-prong τ-decays using different topocluster settings is provided in Table 2.2, which indicates that configurations with a tightened $t_{\mathrm{neighbour}}$ threshold (notably 4-4-0) typically result in more compact clusters which are easier to resolve. These findings were corroborated in a different, more extensive study in the context of $H \rightarrow \tau\tau$ searches [65]. For technical reasons however, the default topocluster configuration (4-2-0) has been used in all studies presented herein, and results obtained with alternative configurations are mentioned for completion only.

Decay topology	$t_{\text{seed}} - t_{\text{neighbour}} - t_{\text{cell}}$	1 cluster	2 clusters	3 clusters
	4-4-0	11 %	89 %	-
	4-3-0	14 %	86 %	-
	4-2-0	20 %	80 %	-
$\tau^\pm \to \pi^\pm\pi^0$	5-5-0	11 %	89 %	-
	5-4-0	13 %	87 %	-
	6-6-0	12 %	88 %	-
	6-5-0	13 %	87 %	-
	4-4-0	3 %	24 %	73 %
	4-3-0	4 %	29 %	67%
	4-2-0	8 %	38 %	55%
$\tau^\pm \to \pi^\pm\pi^0\pi^0$	5-5-0	3 %	25 %	68%
	5-4-0	4 %	26 %	71%
	6-6-0	3 %	26 %	68%

TABLE 2.2: The fraction of events with reconstructed topoclusters matched to a true pion ($\Delta R < 0.1$) emerging from a decaying τ-lepton with 20 GeV$< p_T^{\text{vis}} <$25 GeV using different topocluster configurations.

2.3.2 Energy flow in ATLAS

As indicated in Section 2.3, the merits of energy flow calorimetry depend in large part on the accuracy with which energy deposits in the calorimeter can be associated with the correct particles in the event. In practical terms, this necessitates the ability to distinguish charged particle deposits in the calorimeter from neutral particle deposits, a feature which may be achieved by matching reconstructed tracks to calorimeter clusters. This is a relatively straightforward task in scenarios with well contained and isolated calorimeter clusters corresponding to a few true particle energy deposits, but becomes increasingly more complex as the separation between particle deposits become smaller. If care is not taken, overlaps between charged and neutral showers may render part or all of the neutral energy deposit lost after track momentum subtraction. Conversely, if a hadronic shower is not fully contained in a single cluster, but split into multiple clusters during reconstruction, the shower fragments without a track match are likely to be falsely identified as additional neutral deposits and consequently the energy of the showering particle is effectively double-counted.

Uncertainty of this sort is minimised by effective pattern recognition, provided in part by granular calorimeters and efficient topological clustering, but equally important by accurate track-cluster association and appropriate replacement of charged cluster deposits in the calorimeter by track measurements.

A general ATLAS algorithm for the latter is provided by the `eflowRec` software package [62, 66].

The input to *eflowRec* is a collection of tracks (`TrackParticles`) and a collection of uncalibrated default (4-2-0) topological clusters (`CaloTopoClusters`). In a sequence of steps, these objects are combined to form *energy flow objects* (EFOs) which may later serve as input to particle reconstruction algorithms:

1. Each track is extrapolated to the first layer of the electromagnetic calorimeter.

2. Using the extrapolated track coordinates, the nearest topological cluster is located.

3. The energy of the nearest cluster should agree with the expected energy deposit $E_{\exp}(\sigma_{\exp})$ of the track match. Therefore, the closest cluster is required to satisfy:

$$E_{\text{cluster}} > E_{\exp} - k_2 \times \sigma_{\exp}$$

   where E_{cluster} represents the cluster energy at the *electromagnetic scale* and $E_{\exp}$ the expected electromagnetic scale energy deposit from a charged pion with the energy and pseudorapidity corresponding to those of the track, as determined from a reference sample. $\sigma_{\exp}$ represents the width of $E_{\exp}$ and k_2 is a free parameter. If the clusters satisfy the above condition, the expected energy deposit is removed from the cluster:

$$E'_{\text{cluster}} = E_{\text{cluster}} - E_{\exp}.$$

   This procedure is repeated for any other tracks matched to the same cluster.

4. After subtracting expected energy deposits from the cluster energy, any remaining energy should ideally not originate from the particle(s) producing the track(s). Therefore a final check is performed on the cluster:

$$E'_{cluster} > k_1 \times \sigma_{\exp}$$

   where k_1 is again a free parameter. If the condition is satisfied, the cluster is kept and appropriate calibrations applied, otherwise the cluster is discarded.

2.3.2.1   Determining expected energy deposits

The expected energy deposits $E_{\exp}(\sigma_{\exp})$ are derived from reference samples of various *fixed energy single $\pi^{\pm}$*. Clusters are collected in a cone ($\Delta R < 0.4$) about the track axis in the calorimeter, whereby the leading cluster is required to contain $> 95\%$ of the energy in the cone and to be matched to the single pion track[10]. The expected energy deposits are binned in track energy and pseudorapidity (and layer of first interaction in the calorimeter).

2.3.2.2   Subtraction of energy deposits

The evolution of a hadronic cascade is chiefly characterized by a series of successive inelastic hadronic interactions. While hadrons of various types are all produced as secondary particles, the particle content of the cascade is dominated by pions. Neutral pions comprise roughly 1/3 of all pions produced in each inelastic interaction and these will initiate electromagnetic *subshowers* inside the hadronic cascade. Because electromagnetic showers are comparatively well collimated, the electromagnetic component will

---

[10]The requirement on the cluster energy acts as a protection against showers split into several clusters.

typically concentrate in a narrow cone about the hadronic shower axis. By contrast, the hadronic component will typically show a much wider lateral spread.

The erratic nature of hadronic showers make shower shape templates susceptible to (potentially large) fluctuations in the evolution of the hadronic cascade. Care must therefore be taken when removing expected energy deposits from clusters matched to tracks. Rather than subtracting the expected energy deposit from the cluster[11], eflowRec espouses a cell-ordered subtraction approach whereby rings of cells around the extrapolated track are removed in order of decreasing energy density until the subtracted energy corresponds to the track momentum.

In order to achieve this, eflowRec needs to determine in which calorimeter layer the incoming pion initiated its showering, the expected evolution of the cascade about the shower axis and finally which cells to remove from the cluster.

Determining the layer of first interaction

While the cluster and shower axes may overlap reasonably well in isolated clusters, they are not necessarily commensurate when the cluster is formed from overlapping showers. As discussed in Section 2.3.1.1, a τ-decay into a charged pion and neutral pion(s) may readily produce a single cluster if the showers are spatially overlapping. In such cases, the charged shower axis is better approximated by the extrapolation of the matched track into the calorimeter. Because the radiation length X_0 is shorter than the hadronic interaction length λ_{had}, the energy density along the extrapolated track (longitudinal profile) is expected to be characterised by a peak about the electromagnetic core followed by a slowly decaying tail, the first of which may be readily identified as the point of shower initiation. Identifying the calorimeter layer in which the hadron began to shower is therefore tantamount to determining the longitudinal energy density profile about the shower axis. However, when calculating the energy density along the extrapolated track, care must be taken to avoid including cells from overlapping showers. Therefore, the contribution from each cell is weighted as a function of its η-ϕ distance from the extrapolated track. The average energy density about the shower axis in calorimeter layer l may then be expressed as[12]:

$$\rho_l = \sum_{cell\,i} w_i^l \left(\frac{E_i^l}{V_i^l} \frac{1}{(X_0^l)^3} \right) \tag{2.3}$$

where X_0^l is the radiation length in layer l accounting for the variable size of electromagnetic showers in different materials and w_i^l is a two-dimensional gaussian weighting function centered along the extrapolated track coordinates:

---

[11]This possibility is optionally available in eflowRec and works well for isolated clusters.

[12]To conserve CPU time, the sum only extends to cells within $3\sigma_i$ of the extrapolated track axis.

$$w_i^l = \int \int_{celli} g_i^l(\eta, \phi) d\eta d\phi \tag{2.4}$$

$$= \frac{1}{2\pi\sigma_l^2} \int \int exp\left(\frac{(\eta_i - \eta_p^{trk})^2 + (\phi_i - \phi_l^{trk})^2}{2\sigma_i^2}\right) d\eta d\phi \tag{2.5}$$

Finally, the longitudinal profile (energy density in each layer) may be expressed as a function of calorimeter depth measured in interaction lengths λ_{had}:

$$P_l = \frac{<\rho>_l - <\rho>_{l-1}}{<\lambda>_l - <\lambda>_{l-1}} \tag{2.6}$$

and the layer of first interaction defined as the calorimeter layer preceding the largest gradient of this profile.

Radial shower shapes and cell ordering

Once the starting point of the shower to which the track is matched is identified, a method is called for by which the relevant cells along the extrapolated track are removed. Since hadronic cascades are prone to fluctuate considerably, mean shower shapes will necessarily be inaccurate. Because the electromagnetic core is more predictable and contains the majority of the shower energy concentrated along the shower axis, the energy density provides a viable order for cell subtraction. The stability of this region with respect to variations in lateral spread allows one to assume a radially symmetric profile about the extrapolated track[13]. Assuming radial symmetry, the radial energy density profile may be computed in each layer. For a reference sample of single charged pions of a given energy E, η and shower initiation in calorimeter layer l, cells about the track are binned in radial distance from the extrapolated track axis to form rings of thickness $\Delta R_l = \frac{1}{2}\sqrt{(\Delta\eta_l)^2 + (\Delta\phi_l)^2}$,where $\Delta\eta_l$ and $\Delta\phi_l$ represent the cell dimensions in calorimeter layer l. The rings in all layers are then ordered in energy density to provide the overall order in which cells can be removed from the matched cluster.

In summary, the entire cell subtraction process therefore amounts to executing the following steps on all matched tracks in order of descending p_T:

1. Determine the layer of first interaction in the matched cluster and retrieve the appropriate ordering as defined by the track energy and η and the layer of first interaction.

2. For each layer in the matched cluster, order cells by radial distance from the extrapolated track coordinates and order the resulting "cell rings" according to the ordering scheme derived in (1).

3. Subtract rings of cells in order of decreasing energy density until p_{track} has been removed.

---

[13]The validity of this assumption may be increasingly challenged as one moves away from the core of the shower.
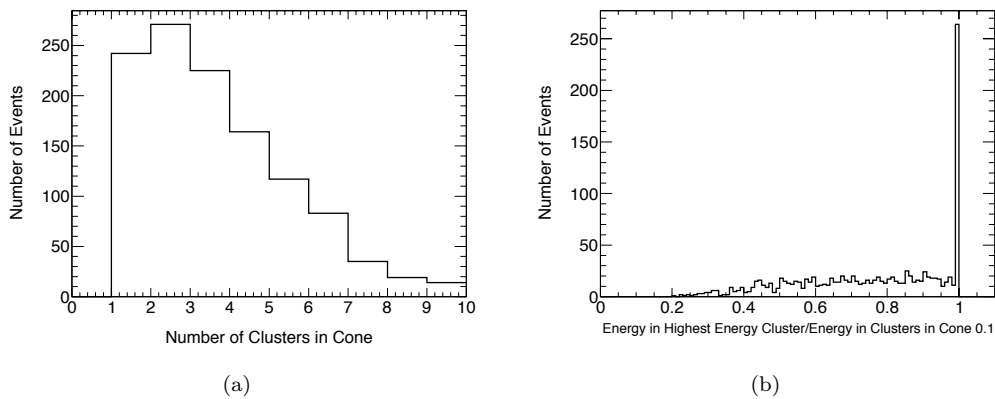
FIGURE 2.8: (a) The number of topological clusters inside a cone of size $\Delta R < 0.1$ about the extrapolated track coordinates of a single 6 GeV $\pi^{\pm}$. (b) The fractional "cone" energy contained in the leading topological cluster. [62].

After subtraction, all remaining clusters are calibrated with the *Local Hadron Calibration Scheme* [67], which employs cluster moments to determine the hadronic or electromagnetic nature of a cluster and to classify it accordingly.

2.3.2.3 Recovering split showers

As is indicated in Figure 2.8, the topological clustering algorithm presented in Section 2.3.1 will not always contain a shower in a single cluster. The erratic nature of hadronic showers may sometimes lead to the formation of several clusters[14]. Even if the entire shower is contained in a single primary topocluster, the presence of local maxima may cause it to split both longitudinally and laterally.

Split showers degrade the performance of the energy flow algorithm, because fragments of a charged particle hadronic shower will be falsely identified as neutral EFOs surrounding a charged EFO. Depending on the degree of fragmentation, the charged EFO cluster will have an energy inconsistent with the matched track momentum.

Since shower fragmentation or "cluster splitting" is an inherent feature of both hadronic showers and the topological clustering algorithm, a certain fraction of hadronic showers will always be falsely reconstructed as several neutral EFOs around a charged EFO, the latter of which is likely to have a cluster energy inconsistent with its matched track momentum. This inherent confusion degenerates the ability of `eflowRec` to precisely account for the energy of charged particles using information from the tracker, and limits the capacity to correctly identify all constituent particles in *e.g.* a decaying τ-lepton. This in turn compromises the basis for an efficient constituent based identification of reconstructed τ-leptons.

---

[14]Hadronic interactions may *e.g.* create particles that are scattered at large angles with respect to the shower axis. Such particles may travel a distance before showering, to the effect that their showers may be reconstructed as separate clusters.

In order to counter any performance degradation resulting from cluster splitting, an attempt is made to *recover* fragmented showers by re-associating additional neutral EFOs with the appropriate parent charged EFO:

(i) Identify all charged EFOs whose associated cluster energy is found to be inconsistent with the expected charged deposit as determined by the matched track (and optionally also any EFOs for which no cluster match was found).

(ii) Build a cone $\Delta R < 0.2$ around the extrapolated track axis.

(iii) Subtract the expected charged energy deposit from any neutral EFO (topoclusters) whose barycenter is located inside this cone.

(iv) Calibrate any remaining neutral EFOs using the Local Hadron Calibration scheme.

Despite the simplicity of the recovery algorithm described above, Figure 2.9 shows that it provides a good working performance, correcting for the large majority of cases where charged pion showers fragment into multiple EFOs. While not run by default in `eflowRec`, the recovery algorithm has therefore been applied to all results presented herein.

2.3.2.4 Applications to tau reconstruction

With the potential to access the substructure of (hadronic) τ-decays using the ATLAS calorimeters, it is germane to consider the potential benefits of applying generic energy flow techniques at an early stage in the τ-reconstruction. Figure 2.10 compares the transverse energy resolutions obtained in $\tau^{\pm} \to \rho^{\pm} \to \pi^{\pm}\pi^0$ and $\tau^{\pm} \to a_1^{\pm} \to \pi^{\pm}\pi^0\pi^0$ decays using only calibrated topological clusters and using EFOs. Improvements of 19% and 5%, respectively are found in case of the latter. These improvements currently come at the cost of an energy scale overestimation of 4%, to be compared with an underestimation of 0.5% using only topological clusters [62]. (It has also been established that the reconstructed ρ-mass distributions have notably fatter right-sided tails. At the time of writing this bias is not understood and under investigation[68]).

2.4 PanTau - particle flow inspired τ-reconstruction

The two canonical approaches to τ-lepton reconstruction and identification in ATLAS were described in Section 2.2. In what follows, an entirely different approach to τ-reconstruction will be discussed in the context of a newly developed τ-reconstruction algorithm for ATLAS, known as **PanTau**[15].

---

[15]PanTau (Particle Analysis of Taus) is named after a character by the same name in a Czech/German children's television series from the late 1960s and 1970s, known for his magic bowler hat.

(a) $\tau^{\pm} \to \pi^{\pm}\nu_{\tau}$, no recovery

(b) $\tau^{\pm} \to \pi^{\pm}\nu_{\tau}$, with recovery

(c) $\tau^{\pm} \to \rho^{\pm}\nu_{\tau} \to \pi^{\pm}\pi^0\nu_{\tau}$, no recovery

(d) $\tau^{\pm} \to \rho^{\pm}\nu_{\tau} \to \pi^{\pm}\pi^0\nu_{\tau}$, with recovery
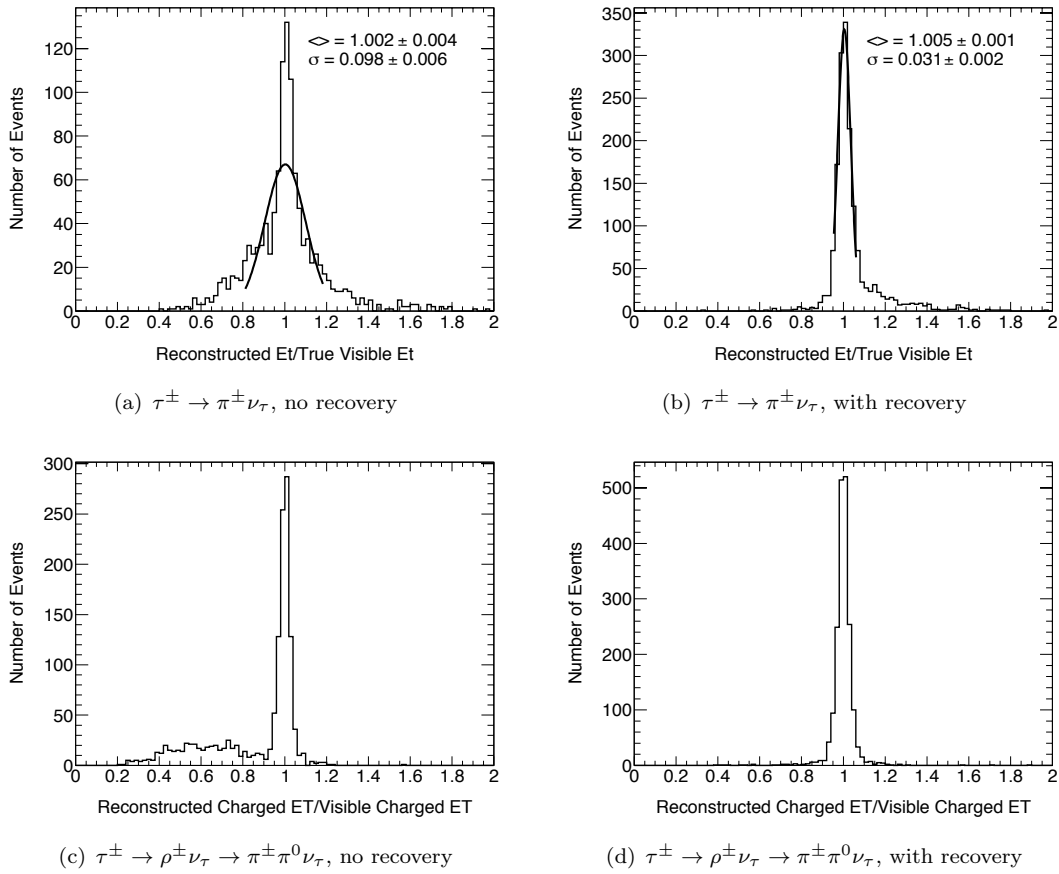
FIGURE 2.9: Transverse energy resolutions with and without the split cluster recovery algorithm. The resolutions are calculated using all EFOs in a cone of size $\Delta R < 0.2$ about the charged EFO [62].

This work is the result of a joint effort with *Sebastian Fleischmann*, with whom all credit is shared[16]. Important contributions have also been made by *Christian Limbach* and *Peter Wienemann*. The invaluable support and close cooperation with `eflowRec`-author *Mark Hodgkinson* is also gratefully acknowledged.

2.4.1 The philosophy of PanTau

Inspired by the ideas of particle flow, PanTau aims to identify τ-leptons by way of their resolved constituent decay particles. Rather than approaching the hadronic decay of a τ-lepton as a narrow jet in the detector, PanTau seeks to recognize decay topologies consistent with a hadronically decaying τ using information from resolved "particles" in its decay wake. Any potential decay information provided by the topological clustering of calorimeter cells is harnessed through the exclusive use of EFOs provided by the `eflowRec` algorithm. These EFOs form the base units of operation in the algorithm, under the assumption that they mirror the particle content of the τ-lepton decay and that most observable properties of the τ-lepton can be derived from these objects alone.

---

[16]The authour retains responsibility for any errors, omissions or misgivings in the text.

(a) $\tau^\pm \to \rho^\pm \nu_\tau \to \pi^\pm \pi^0 \nu_\tau$ (Topological clusters)

(b) $\tau^\pm \to \rho^\pm \nu_\tau \to \pi^\pm \pi^0 \nu_\tau$ (Energy flow objects)

(c) $\tau^\pm \to a_1^\pm \nu_\tau \to \pi^\pm \pi^0 \pi^0 \nu_\tau$ (Topological clusters)

(d) $\tau^\pm \to a_1^\pm \nu_\tau \to \pi^\pm \pi^0 \pi^0 \nu_\tau$, (Energy flow objects)
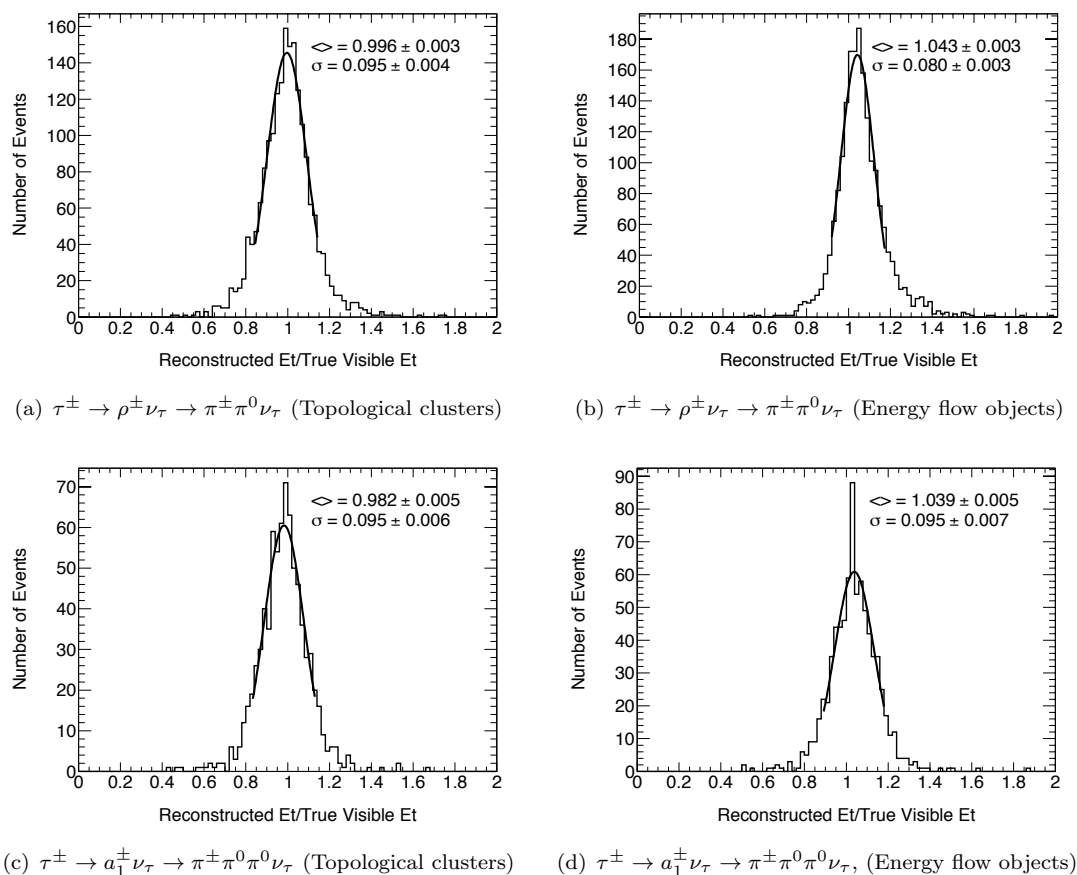
FIGURE 2.10: A comparison of transverse energy resolutions obtained with *calibrated* topoclusters (left) and EFOs (right) in 1-prong τ-decays with additional neutrals [62]

Rather than explicitly drawing on information from the detector (such as *e.g.* the number of hits in the η-strip layers of the calorimeter or the transverse shower profile of the τ-jet), the aim throughout is to rely squarely on the use of constituent EFOs to identify signatures deemed compatible with a physical τ-decay in a manner dissociated from the details of the underlying detector configuration.

As such, PanTau elicits a natural separation between the *physics* of the τ-lepton decay and any *detector effects* that are sensitive the underlying technology. It is hoped that this separation, combined with an increasingly modular approach to the combined reconstruction of τ-leptons, may facilitate an improved interpretation of data and a better understanding of effects that may impact traditional τ-reconstruction tools in ATLAS.

2.4.2 General overview

The overall structure of PanTau is illustrated in the flow chart depicted in Figure 2.11. The details of the implementation of the this software into the ATLAS software framework ATHENA is detailed elsewhere [69]. Here, only a qualitative description of the structure of the algorithm will be given with aim to highlight any departures from default τ-reconstruction in ATLAS. Moreover, this document will only concern itself with

the reconstruction of *hadronically* decaying τ-leptons. The reconstruction of *leptonically* decaying τ-leptons within the framework of PanTau is described in [48].

I Input

The raw input to PanTau are EFOs provided by the `eflowRec` algorithm described in Section 2.3.2.

In order to identify objects corresponding to a τ decay, some measure must be provided by which the relevant EFOs are collected and passed to PanTau for inspection. The simplest (if not necessarily always the best) method of collecting the relevant EFOs is by way of jet algorithms made to run on all EFOs in a given event.

II Seed selection & classification

These jets serve as *seeds* for the PanTau algorithm. Each seed is scanned to determine its composition through a simple count of its constituent charged and neutral EFOs. Seeds whose composition is found to be inconsistent with the expected particle configuration of a τ decay (*e.g.* seeds containing 8 charged EFOs) can therefore be discarded early. Seeds with a composition compatible with a τ decay are categorized according to their "particle content". In this manner, seeds with *e.g. one charged* EFO and *one or more neutral* EFO(s) can be classified as $\tau_{vis} \to \pi^{\pm} + n\pi^0$ candidate decays, whereas seeds with *e.g. three charged* EFOs and *no neutral* EFOs are classified as $\tau_{vis} \to \pi^+\pi^-\pi^+$ candidates. As such, the constituent composition of the input seeds provides both a rough discrimination against false candidates, as well as an estimate of the most probable decay mode of the τ-lepton candidate. It also follows that any remaining seeds that do not originate from a true τ decay but still pass the initial selection are likely to greatly resemble a true τ decay and will be challenging to separate from true τ-leptons.

III Feature determination

Following the comparatively simple classification of seeds, more involved quantities derived from the constituent objects are computed. These quantities, henceforth called *features*, provide the basis for the separation of τ-induced seeds from jet-induced seeds. Unlike the discriminating variables used in the τ-reconstruction algorithms described in Section 2.2, the seed features all derive squarely from the system of constituent EFOs and the EFOs themselves. No information is drawn directly from the calorimeter or tracker.

IV Kinematic fit

Seeds classified as compatible with a $\tau_{vis} \to \pi^{\pm} + n\pi^0$ decay may optionally be subjected to a *kinematic fit*, constrained by the masses and widths of the ρ and a_1 resonances. (At the time of writing, this method is still in a testing phase and will therefore not be discussed further herein. It is mentioned here for completion only).

V Multivariate discrimination

Several seed features may be combined into a *multivariate discriminant* to enhance signal identification efficiency and background suppression. The most appropriate suite
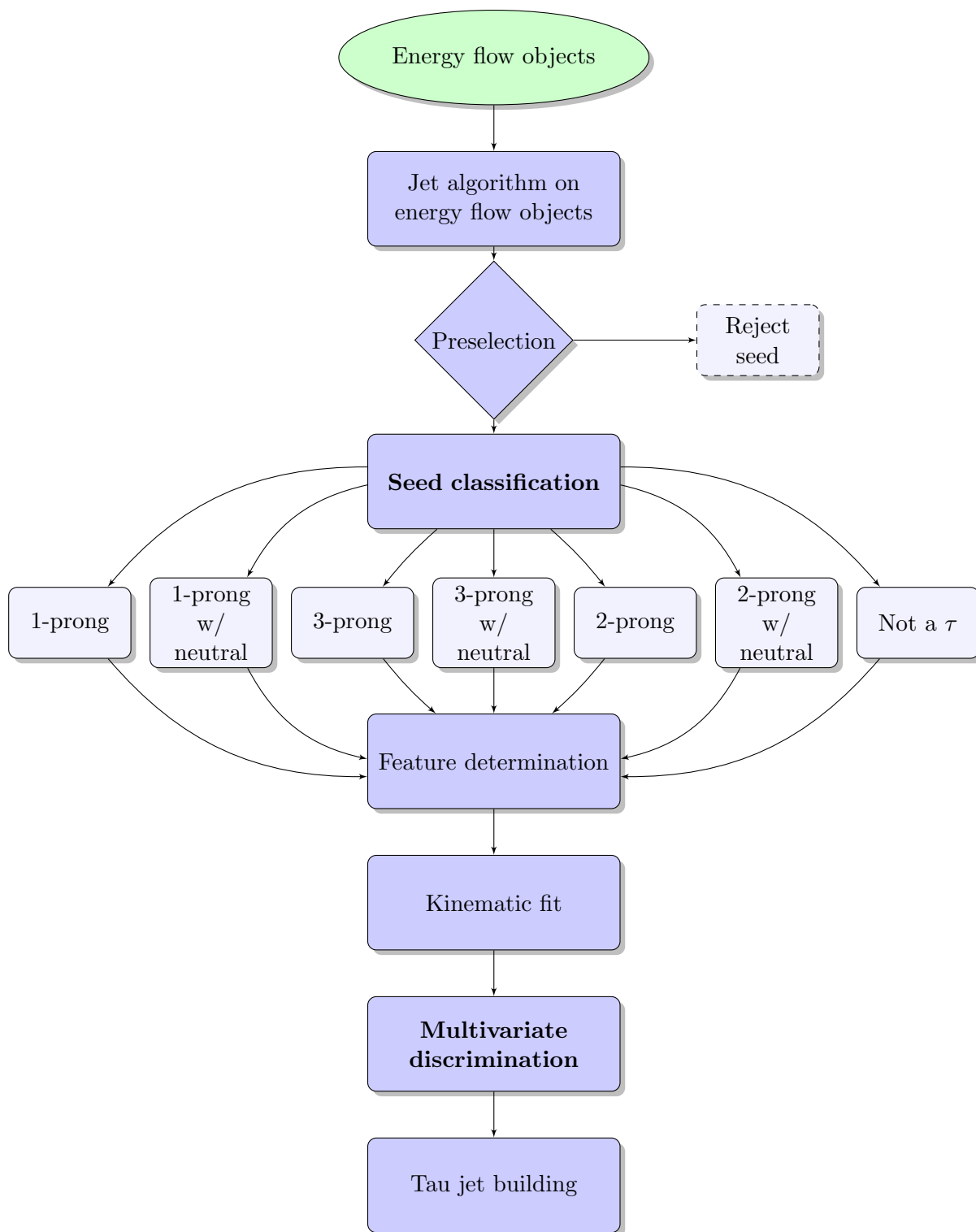
FIGURE 2.11: Data flow in PanTau: EFOs form the raw input to the algorithm. These are collected by a jet algorithm to form τ-seeds. The seeds are subsequently classified according to content, if found to satisfy a basic preselection. (Seeds classified as 2-prong or 2-prong w/neutral have two $EFO_q^{\pm}$.) After classification, properties of the seeds are derived from the constituent objects and fed into a multivariate discriminant to facilitate the separation of QCD-induced fakes.

Category		Classification requirements		
`1-prong`	1	$EFO_q^{\pm}$	and	*absence* of neutral energy
`1-prong+neutral`	1	$EFO_q^{\pm}$	and	*presence* of neutral energy
`3-prong`	3 or 4	$EFO_q^{\pm}$	and	*absence* of neutral energy
`3-prong+neutral`	3 or 4	$EFO_q^{\pm}$	and	*presence* of neutral energy
`2-prong`	2	$EFO_q^{\pm}$	and	*absence* of neutral energy
`2-prong+neutral`	2	$EFO_q^{\pm}$	and	*presence* of neutral energy
`Other`	0 or > 4	$EFO_q^{\pm}$	or	otherwise failing alternative classification

TABLE 2.3: The PanTau seed classification scheme.

of features to combine will vary according to the characteristics of each seed category. The multivariate training is therefore performed separately in each category.

VI Tau-object building

The final step involves the building of a τ-object intended for use in an offline analysis, with all associated properties as estimated by previous steps in the algorithm.

In the following, a more elaborate discussion of the details pertaining to steps **II**, **III** and **V** above is provided.

2.4.3 Seeding

With the input EFOs scattered across the detector, some association measure is required by which relevant systems of EFOs are identified, collected and passed on to PanTau for closer inspection. In this context, jet algorithms provide a simple method of gathering all EFOs that may be relevant to the identification of a τ-decay. The resulting jets may then act as seeds for the τ-reconstruction. Unless stated otherwise, fixed size $\Delta R = 0.4$ *cone* jets (ref. Section 4.4.4) built on default EFOs have acted as seeds for all results presented herein. The drawbacks of this approach are discussed below in Section 2.4.3.2.

After an initial scan of its constituent composition, the seed is retained if accepted by a rough pre-selection designed to enable an early rejection of seeds whose EFO-composition is plainly incompatible with a hadronically decaying τ-lepton:

1. $|\sum^{EFO} \text{Charge}| > 0$ and $|\sum^{EFO} \text{Charge}| \leq 5$

2. $0 < N_{EFO^{\pm}} \leq 4$

3. $|\eta^{\text{seed}}| \leq 2.7$

Seeds passing the minimal preselection are subsequently classified into seven different categories in accordance with their "particle content" as detailed in Table 2.3.

In order to facilitate a more accurate classification, the track selection on charged EFOs is moderately tightened with respect to the default track selection applied in `eflowRec`.

Charged EFOs whose associated tracks satisfy these criteria are henceforth referred to as *charged qualified* and labelled $\text{EFO}_q^{\pm}$. An *EM neutral* EFO is defined as an EFO with $E_T > 1$ GeV whose associated cluster has *not* been tagged as hadronic (HAD) by the Local Hadron Calibration scheme. All considered EFOs are further subjected to a *pion mass hypothesis*, whereby their 4-vectors are corrected for the charged or neutral pion mass.

The presence of neutral energy in the seed is defined by way of the ratio

$$\frac{\sum\limits_{\text{neutral EFO}} E_T^{\text{EFO}}}{\sum\limits_{\text{charged EFO}} E_T^{\text{EFO}}} \tag{2.7}$$

which if found to be smaller than 0.3, qualifies the seed for the appropriate `X-prong` (w/o neutrals) category. Otherwise the seed will qualify for an appropriate `X-prong+neutral` category provided it does not contain an excess of hadronic neutral transverse energy:

$$\frac{\sum\limits_{\text{HAD neutral EFO}} E_T^{\text{EFO}}}{\sum\limits_{\text{all EFO}} E_T^{\text{EFO}}} < 0.4 \tag{2.8}$$

Seeds failing condition 2.8 will be classified as `Other`, indicating an inconsistency with the expected composition of a hadronically decaying τ-lepton, unless the leading hadronic neutral EFO accounts for a sizeable fraction of the total neutral energy in the seed:

$$\frac{E_T^{\text{leading HAD neutral EFO}}}{\sum\limits_{\text{neutral EFO}} E_T^{\text{EFO}}} > 0.4 \tag{2.9}$$

and the total number of charged EFOs (qualified and unqualified) remains low

$$N_{\text{EFO}^{\pm}} < 4 \tag{2.10}$$

The latter requirements protects against cases where EM neutral energy in τ-induced seeds is falsely tagged as hadronic.

2.4.3.1 Seed classification performance

The performance of the classification scheme described above is shown in Figures 2.12 and 2.13, in which the distribution of τ-induced seeds (seeds matched to a true τ) and jet-induced seeds (seeds for which no match to a true τ was found) across the different classification categories is detailed.
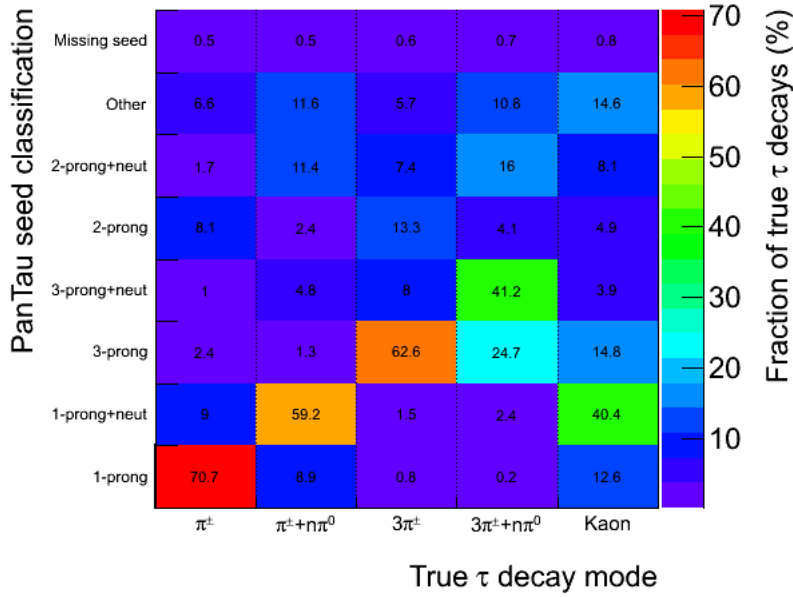
FIGURE 2.12: The PanTau classification performance w.r.t. various true τ-decay modes in $W \to \tau\nu_\tau$ and $Z \to \tau\tau$ normalized to the total number of true τ-decays of a given decay mode satisfying $p_T^{vis} > 10$ GeV and $|\eta^{vis}| < 2.0$. The matrix is normalized by column to indicate the relative fraction of a true decay mode classified in the various reconstructed categories.

Figures 2.12 and 2.13 contain several noteworthy features:

- The largest subset of seeds induced by any given true decay mode is always found in the corresponding reconstructed category. In the most dominant decay modes, this number exceeds 50%, indicating that in most cases more than half of all τ-induced seeds will be correctly classified. "Off-diagonal" migrations are significant, most notably in the 3-prong sector, but also among $\pi^\pm + n\pi^0$ decays. The impact of such false classifications on the identification performance is further discussed in Section 2.4.4.

- The fraction of τ-induced seeds classified as `Other` (not immediately consistent with a τ-decay) is roughly 6% in the `X-prong` categories and roughly 11% in `X-prong+neutral`. Between 75-85% of all 1-prong induced seeds classified as `Other` contain zero qualified charged EFOs and therefore fail alternative classifications[17]. As seen in Figure 2.4(b), this is roughly consistent with the expected tracking inefficiency of charged pions caused by early interactions in the inner detector material. Among 3-prong induced seeds classified as `Other` a more even distribution is found between seeds failing to provide sufficient qualified charged EFOs, seeds providing too many qualified charged EFOs and seeds otherwise rejected by the other categories. The asymmetry observed between $1/3\pi^\pm$ and $1/3\pi^\pm n\pi^0$ induced seeds can be attributed to cases where the seeds are falsely rejected by condition 2.7.

---

[17]Between 60-70% of 1-prong induced seeds with no qualified EFO also contain no unqualified charged EFOs.
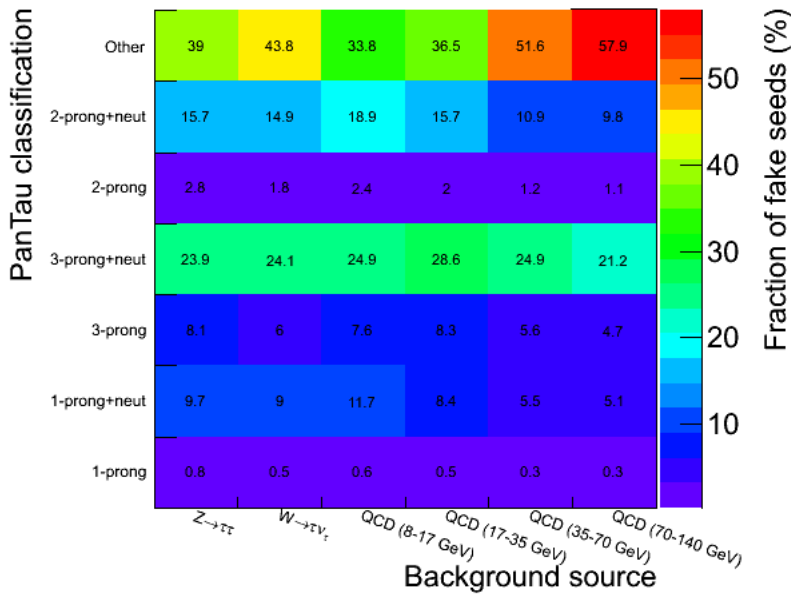
FIGURE 2.13: The distribution of jet-induced seeds (fakes) from various samples across the different PanTau classification categories normalized to the number of jet-induced seeds in each sample satisfying seed $p_T > 10$ GeV and seed $|\eta| < 2.0$.

- In all τ-decay modes, a small fraction ($\sim 0.5\%$) of decays fail to produce an adequately matched seed. Entries in the `Missing Seed` category shown in Figure 2.12 typically correspond to τ-decays of comparatively low visible momenta (< 15 GeV).

- A significant fraction ($\sim 30 - 60\%$) of jet-induced seeds are immediately classified as `Other`. The remainder are largely distributed across the `X-prong+neutral` categories, most notably `3-prong+neutral`. The fraction of jet-induced seeds falsely classified in an `X-prong` category is small by comparison and does not exceed a few percent in either category. It naturally follows that jet-induced seeds falsely associated with any `X-prong(+neutral)` category will significantly resemble τ-induced seeds classified in the same category.

2.4.3.2 A note on the choice of jet algorithm

As described above, the primary purpose of the seed jet is to collect and associate EFOs that may originate from a τ-decay. The substructure of the seed jet is subsequently probed to determine whether the seed composition is compatible with a hadronic τ-decay or not. While the choice of the underlying jet algorithm used to produce the seed jets is arbitrary, the seeding performance will necessarily depend on the details of the algorithm that govern which EFOs to associate with a seed jet and which to exclude.

Ideally the collection process should be such that only EFOs associated with the seed producing particle are contained in the resulting seed jet. The drawbacks of a fixed-sized cone approach are apparent: a large cone size runs the risk of including unassociated

EFOs, whereas a small cone size may exclude relevant EFOs. Either case may result in either an incorrect classification and/or a reduced identification performance.

Moreover, the appropriate cone size will depend on the energy and showering properties of the seed producing particle. The distance between constituent objects of a τ-lepton decay may be comparatively large at low transverse momenta and considerably smaller at higher momenta. While a narrow cone ($\Delta R \sim 0.2$) is arguably more suitable for the collection of τ-decay constituents beyond the very low-p_T regime, it is likely to grossly underestimate the true composition of jet-induced seeds from quarks and gluons, artificially making them appear more τ-like. To avoid unwanted truncations, a comparatively broad cone ($\Delta R = 0.4$) has been used in the studies presented herein.

While a wide cone approach may have its merits in event topologies were the τ-leptons are relatively isolated, it is arguably more problematic in busy environments where close-lying unassociated EFOs may be included in the seed jet. Furthermore, a jet-based approach to seeding is only justified whenever a τ-decay results in several EFOs. In decay modes such as $\tau \rightarrow \pi^{\pm}\nu_{\tau}$, in which only one EFO is expected, a jet-based seeding is no longer warranted. Alternative seeding methods are therefore being explored.

2.4.4 Discrimination against QCD jets

While a decent fraction of jet-induced seeds are seen to be filtered away during seed classification, the various X-prong(+neutral) categories still remain "contaminated" by a significant fraction of falsely classified jet-induced seeds. The base composition of these jet-induced seeds is likely to greatly resemble that of their $\tau-$induced counterparts. In order to separate τ-induced seeds in a given category from falsely classified jet-induced seeds, it is necessary to identify properties of either seed type that enable an efficient differentiation. For an enhanced separation, several such characteristic seed features can be combined in various multivariate discriminants. The most appropriate choice of features to combine will often depend on the comparative characteristics of the *signal* (τ-induced seeds) and *background* (jet-induced seeds) in each classification category[18]. The most appropriate feature suite will also depend on the background composition (*e.g.* gluon jets vs. quark jets) in a given category and their relative contributions in different kinematic regimes.

2.4.4.1 The relative composition of the signal within categories

An accurate prediction of the expected appearance of τ-induced seeds in a given category is a helpful tool to facilitate a separation from jet-induced seeds wrongly classified in the same category. To enable such a prediction, it is desirable to keep the fraction of τ-induced seeds from the target decay as high as possible and to minimize any "contamination" from unwanted off-diagonal migrations. The impact of off-diagonal migrations

---

[18]Some features are only properly defined if the seed constituents satisfy some base criteria, *e.g.* that the seed contains a certain number of EFOs of a given type.
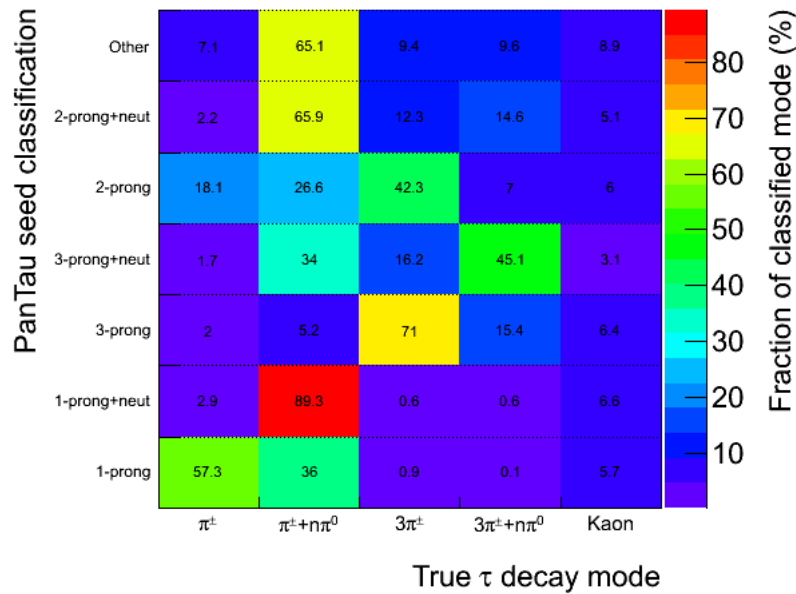
FIGURE 2.14: Fractional composition ("purity") of each PanTau classification category with respect to true τ-decays from $W \to \tau \nu_\tau$ and $Z \to \tau\tau$ satisfying seed $p_T > 10$ GeV and seed $|\eta| < 2.0$. The matrix is normalized by row to indicate the relative contributions from the various true decay modes in each reconstructed category.

are seen in Figure 2.14 in which the fractional population of various true decay modes in each reconstructed classification category is shown.

While the categories `1-prong+neutral` and `3-prong` are notably "clean" with the majority contribution originating from the target decay process, large admixtures are seen in all other reconstructed categories. Significant "contamination" from falsely classified $\pi^\pm + n\pi^0$ decays are seen in both `1-prong` and `3-prong+neutral` categories. The `2-prong` category receives roughly equal contributions from 1-prong and 3-prong decays, whereas the `2-prong+neutral` category is more dominated by $\pi^\pm + n\pi^0$ decays. (Kaon decays are seen to distribute themselves more evenly across the different categories). Large spreads between decay modes, such as those seen in the `3-prong+neutral` and `2-prong` categories makes it more difficult to identify unique features to separate τ-induced seeds from jet-induced seeds.

2.4.4.2 The p_T dependence of the classification of fakes

As discussed in Section 2.1.3, the most prolific source of jet-induced seeds at the LHC is arguably QCD jet production involving a hard scatter between two coloured particles. Such processes will often be accompanied by (comparatively soft) gluon radiation both before and after the hard scattering. Jet-induced seeds may arise from both hard scattered particles and radiated gluons, and the resulting seeds will typically distribute themselves unevenly across the various PanTau classification categories. As seen in Figure 2.15, jet-induced seeds originating from comparatively soft gluon emissions are seen to dominate the background in nearly all classification categories in the lower kinematic
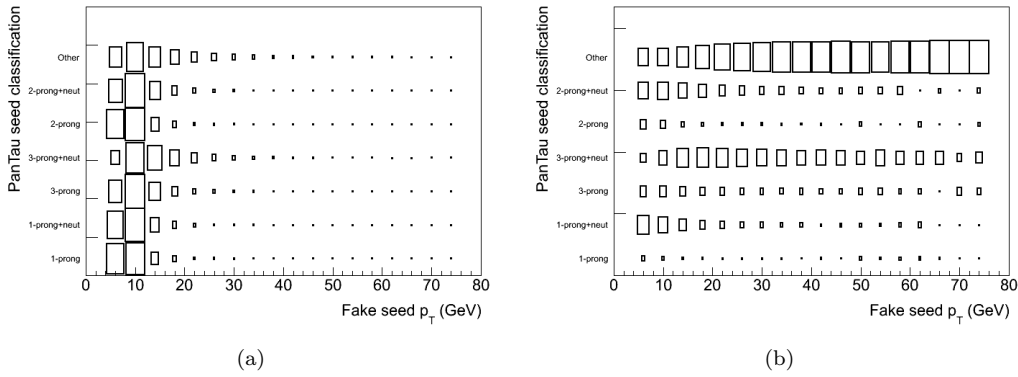
FIGURE 2.15: Transverse momentum distribution of jet-induced seeds from QCD in the various classification categories: (a) normalized to the respective total number of fake seeds in each category, (b) normalized to the total number of fake seeds of a given transverse momentum.

region (< 20 GeV). At higher transverse momenta, jet-induced seeds are seen to be more readily classified as `Other` or `3-prong+neutral` and are consequently less likely to contribute to the fake contamination of any other category. This strong p_T-dependence is particularly visible in the 1-prong categories, and may illicit the use of different sets of discriminating variables at low transverse momenta and at higher transverse momenta.

2.4.4.3 Feature classes and feature definitions

In line with the philosophy of PanTau, all seed features are constructed squarely from the constituent "particles" (EFOs) found in the input seeds. As the EFOs form the base unit of all discriminating features, information from the tracker and calorimeters is only drawn upon in an indirect manner. A large number of features with varying degrees of discriminating power have been implemented in PanTau which may be broadly organized in seven different *feature classes*. Rather than providing a detailed listing of all available features, examples from either feature class are highlighted below. Distributions for these features in the various categories are shown in succeeding section.

Class 1: Seed object composition

Even after seed classification, differences in the relative multiplicities of EFOs of a given type are typically observable between τ-induced and jet-induced seeds. Simple multiplicity variables of the type

$$N_{\text{EFO}}^{\mathcal{C}} \tag{2.11}$$

are constructed, where $\mathcal{C}$ represents some criteria imposed on the counted EFOs, *e.g.* that they be charged with a qualified associated track or that they be tagged as EM neutral.

Another simple, but often useful feature reflecting the seed composition includes the *sum charge* of all charged EFOs:

$$\sum_{\text{EFO}^{\pm}} Q \tag{2.12}$$

Class 2: Seed shapes and moments

The seed topology will typically vary between τ-induced and jet-induced seeds across the various classification categories.

Analogous to event shape variables, *seed shapes* may be deduced from the constituent EFOs. These shapes encode information on the spatial distribution of objects and energy inside a seed in a continuous fashion. An example of such a seed shape is the *sphericity* defined in terms of the eigenvalues of the sphericity tensor:

$$S^{\alpha\beta} = \frac{\sum\limits_{\text{EFO}} p_i^{\alpha} p_i^{\beta}}{\sum\limits_{\text{EFO}} |p_i|^2}$$

where α, β represent the x, y and z components of the EFO momentum vectors. Diagonalizing $\mathcal{S}^{\alpha\beta}$ gives three eigenvalues ($\lambda_1 \geq \lambda_2 \geq \lambda_3$), from which the sphericity

$$\mathcal{S} = \frac{2}{3}(\lambda_2 + \lambda_3) \tag{2.13}$$

is constructed. The sphericity $\mathcal{S} \to 1$ for isotropic distributions, and will therefore typically be larger in jet-induced seeds than in τ-induced seeds. (In a similar fashion, the seed topology may be described through alternative quantities such as the *thrust*, *oblateness*, *Fox-Wolfram moments*, etc. [70]).

The topology may also be described in terms of various *moments*:

$$< k^n > = \frac{1}{\sum\limits_{\text{EFO}} E_T} \times \sum_{i \in \text{EFO}^{\mathcal{C}}} E_T^i k_i^n \tag{2.14}$$

where the sum in the numerator runs over all EFOs satisfying some critieria $\mathcal{C}$. The variable k may be *e.g.* the distance in $\eta - \phi$ space between the EFOs under consideration and the seed axis.

Class 3: Angles

Angular relations ($\angle$) between constituent objects or between constructs derived from constituent objects can be exploited in the separation of τ-induced seeds from jet-induced seeds. Such relations may be defined "globally" using all seed constituents:

$$\angle(\mathcal{P}^{\pm}, \mathcal{P}^0) \tag{2.15}$$

where the $\mathcal{P}^{\pm}$ and $\mathcal{P}^0$ are determined from the sum 3-vectors of constituent charged and neutral EFOs. Angles may also be measured between select objects in a seed, *e.g.* the average angle between the three leading charged qualified EFOs:

$$\angle_{mean}(3 \text{ leading EFO}_q^{\pm}) = \frac{1}{3} \sum_{i,j \in \{1,2,3\}; i \neq j} \angle \left(\text{EFO}_q^{\pm}(i), \text{EFO}_q^{\pm}(j) \right) \qquad (2.16)$$

Angular measures between planes spanned by a system of EFOs are also provided.

Class 4: Invariant masses

Because the constituent EFOs of a seed are ideally tantamount to *decay particles*, it is straightforward to derive the *invariant mass* $\mathcal{M}_{\text{EFO}^{\mathcal{C}}}$ of EFOs satisfying a given criteria $\mathcal{C}$ from their respective four-momenta. As is discussed in Section 2.4.6.2, the invariant mass may not only help separate τ-induced seeds from jet-induced seeds, but also help distinguish between decay modes within a given classification category.

Class 5: Geometric & kinematic spreads

Measures of the spatial distribution of EFOs with respect to an appropriate point of reference in the seed often provide effective discriminants against jet-induced seeds. The point of reference is typically taken as the seed-jet axis, but may also be another EFO, *e.g.* the leading $\text{EFO}_q^{\pm}$. The transverse energy weighted mean geometrical spread about a given point of reference (PoR) is defined as:

$$\overline{\Delta R}(\text{EFO}^{\mathcal{C}}, \text{PoR}) = \frac{1}{\sum\limits_{\text{EFO}} E_T} \frac{\sum\limits_{i}^{N_{\text{EFO}^{\mathcal{C}}}} \Delta R(\text{EFO}_i^{\mathcal{C}}, \text{PoR})}{N_{\text{EFO}^{\mathcal{C}}}} \qquad (2.17)$$

While most of the energy in τ-induced seeds will be concentrated in a few EFOs, jet-induced seeds are typically characterized by higher object multiplicities and a more even distribution of energy among constituents. The transverse energy spread across the various constituents of jet-induced seeds is therefore expected to be smaller than that of τ-induced seeds. Kinematic spreads of this sort are captured in features such as:

$$\frac{\sigma_{E_T}}{\sum E_T} = \frac{1}{\sum\limits_{\text{EFO}} E_T} \left(\left(\frac{\sum\limits_{i}^{N_{\text{EFO}^{\mathcal{C}}}} E_{T,i}^2}{N_{\text{EFO}^{\mathcal{C}}}} \right) - \left(\frac{\sum\limits_{i}^{N_{\text{EFO}^{\mathcal{C}}}} E_{T,i}}{N_{\text{EFO}^{\mathcal{C}}}} \right)^2 \right)^{\frac{1}{2}} \qquad (2.18)$$

where the EFOs may optionally be required to satisfy some criteria $\mathcal{C}$.

Class 6: Isolation

The highly collimated nature of τ-induced seeds merits the use of isolation variables which aim to measure the concentration of energy at various radial distances from the seed axis. Using constituent EFOs, isolation may be expressed in terms of quantities such as:

$$\mathcal{I}_{x/y} = \frac{1}{\sum E_T} \frac{\displaystyle\sum_{\text{EFO}} E_T(\Delta R < x)}{\displaystyle\sum_{\text{EFO}} E_T(\Delta R < y)} \tag{2.19}$$

where $x < y$ represent fixed ΔR-distances from the seed axis, or alternatively in terms of "η-rings" around the seed axis:

$$\mathcal{I}_{(x_a-x_b)/(y_a-y_b)} = \frac{1}{\sum E_T} \frac{\displaystyle\sum_{\text{EFO}} E_T(x_a < \Delta R < x_b)}{\displaystyle\sum_{\text{EFO}} E_T(y_a < \Delta R < y_b)} \tag{2.20}$$

where $x_a(y_a) < x_b(y_b)$ and $x_{a,b} < y_{a,b}$.

Class 7: Impact parameters

In τ-induced seeds, the track associated with the leading $\text{EFO}_q^{\pm}$ is expected to originate from a vertex slightly displaced from the primary vertex. Such a displacement is typically expressed in terms of the *transverse impact parameter d_0*, measuring the shortest distance between the track and the primary vertex in the transverse plane. The corresponding *transverse impact parameter significance* is defined as d_0 divided by its estimated error. From this quantity, a modest discrimination can usually be achieved, especially in 1-prong induced seeds.

2.4.5 Prong-dependent feature selection

The classification scheme described above, naturally invites usage of separate multivariate discriminants in each classification category. Jet-induced seeds wrongly classified in a category different from `Other` are likely to bear significant resemblance to τ-induced seeds in the same category. The success of any separation will in large part depend on how sensitive the discriminating features are to the characteristics of the respective category and on the uniformity of the characteristics within a given category.

In what follows, some distributions $T(x)$ displaying strongly peaked behaviour have been deliberately transformed by an *inverse sigmoid* function:

$$T(x) \to T(x)' = -\ln\left(\frac{1}{x} - c\right) \tag{2.21}$$

where c is a constant. The transformation serves to smear out peaks and to ease any subsequent spline-fitting of distributions.

In a similar vein, *default* values assigned to seed features failing definition (*e.g.* because the required $\text{EFO}^{\mathcal{C}}$ are not present in the seed), have been moved out of the range in which the feature variable is defined and smeared with a gaussian function to facilitate better spline-fitting and the exploitation of any information therein.

2.4.5.1   Category: `1-prong`

The expected content of seeds classified in this category is *one* $\text{EFO}_q^{\pm}$ and little else. While the background contamination is comparatively scant in this channel, the low object multiplicity provides only a limited set of handles with which τ-induced seeds can be separated from jet-induced seeds. Moreover, the background is concentrated at low transverse momenta and the low available statistics of jet-induced seeds in the intermediate kinematic range do not allow for an accurate modeling of distributions. At intermediate transverse momenta, this category is therefore trained together with `1-prong+neutral`. Candidate feature selections chosen for this category are listed in Tables 2.4 and 2.5.

The features were chosen in reflection of the expected characteristics of τ-induced seeds classified in this category:

- Expect only one charged object. Additional unqualified charged objects are likely to originate from jet-induced seeds.

- Expect the charged object to be very well aligned with the jet axis. Contamination from $\pi^{\pm}n\pi^0$ decays may skew the balance slightly.

- Jet-induced fakes may well contain hadronic neutrals. Falsely tagged hadronic neutrals from $\pi^{\pm}n\pi^0$ decays are likely to be closer to the jet axis.

The discriminating power of these features with respect to jet-induced seeds in the kinematic region 10-25 GeV is shown in Figure 2.25. The low degree of separation observed, is testimony to the many similarities between τ-induced seeds and jet-induced seeds in this particular category.

2.4.5.2   Category: `1-prong+neutral`

The `1-prong+neutral` category enjoys the highest purity of all the categories, with roughly 90% of all τ-induced seeds originating from the target process $\tau^{\pm} \to \pi^{\pm}n\pi^0$. Most of these τ-decays will pass by way of either a $\rho^{\pm}$ or $a_1^{\pm}$ resonance to produce a decay topology consisting of *one* charged pion accompanied by *one* or *two* additional π^0. Ideally therefore, most τ-induced seeds classified in this category should contain one charged (qualified) EFO *and* one or two neutral EFOs, the latter ideally tagged

Feature class	Classification category					
	1-prong	1-prong+neutral	3-prong	3-prong+neutral	2-prong	2-prong+neutral
Composition	$\sum Q$	$\sum Q$	$\mathrm{Num}(\mathrm{EFO}_q^\pm)$ $\sum Q$	$\mathrm{Num}(\mathrm{EFO}_q^\pm)$ $\sum Q$		$\mathrm{Num}(\mathrm{EFO}^\pm)$
Shapes & moments	Sphericity $\mathcal{S}$ $\langle\Delta R\rangle(\mathrm{EFO},\text{ jet axis})$	$\langle\Delta R\rangle(\mathrm{EFO},\text{ jet axis})$	Sphericity $\mathcal{S}$ $\langle\Delta R\rangle(\mathrm{EFO}^\pm,\text{ jet axis})$	Sphericity $\mathcal{S}$ $\langle\Delta R\rangle(\mathrm{EFO}^\pm,\text{ jet axis})$	Sphericity $\mathcal{S}$ $\langle\Delta R\rangle(\mathrm{EFO},\text{ jet axis})$	Sphericity $\mathcal{S}$ $\langle\Delta R\rangle(\mathrm{EFO},\text{ jet axis})$
Spreads	$\overline{\Delta R}(\mathrm{EFO}^\pm,\text{ jet axis})$ $\overline{\Delta R}(\mathrm{EFO}_{\mathrm{HAD}}^0,\text{ jet axis})$	$\overline{\Delta R}(\mathrm{EFO}_{\mathrm{EM}}^0,\text{ jet axis})$	$\overline{\Delta R}(\text{leading EFO}^\pm,\mathrm{EFO}^\pm)$ $\overline{\Delta R}(\mathrm{EFO}_{\mathrm{HAD}}^0,\text{ jet axis})$	root square sum of: $\overline{\Delta R}(\mathrm{EFO}_{\mathrm{EM}}^0,\text{ jet axis})$ $\overline{\Delta R}(\mathrm{EFO}_{\mathrm{HAD}}^0,\text{ jet axis})$		$\overline{\Delta R}(\mathrm{EFO}_{\mathrm{EM}}^0,\text{ jet axis})$
Energy spreads				$\sigma_{E_T}/\sum E_T$		$\sigma_{E_T}/\sum E_T$
Angles		$\angle(\text{leading EFO}_q^\pm,\text{ jet axis})$ $\angle(\mathcal{P}^\pm,\mathcal{P}^0)$	$\angle_{\mathrm{mean}}(\text{3 leading EFO}_q^\pm)$			$\angle(\text{leading EFO}_q^\pm,\text{ jet axis})$ $\angle(\mathcal{P}^\pm,\mathcal{P}^0)$
Isolation	$\mathcal{I}_{0.1/0.2}\times\sum E_T$	$\mathcal{I}_{0.2/0.4}$	$\mathcal{I}_{0.1/0.4}\times\sum E_T$	$\mathcal{I}_{0.1/0.4}\times\sum E_T$	$\mathcal{I}_{0.1/0.4}\times\sum E_T$	
Impact parameter		d_0/σ_{d_0}			d_0/σ_{d_0}	d_0/σ_{d_0}

TABLE 2.4: Feature variable suites, 10-25 GeV

Feature class	Classification category			
	1-prong / 1-prong+neutral	3-prong	3-prong+neutral	2-prong / 2-prong+neutral
Composition	$\sum Q$	$\mathrm{Num}(\mathrm{EFO}_q^\pm)$ $\sum Q$	$\mathrm{Num}(\mathrm{EFO}_q^\pm)$ $\sum Q$	$\mathrm{Num}(\mathrm{EFO}^\pm)$
Shapes & moments	Sphericity $\mathcal{S}$ $\langle\Delta R\rangle(\mathrm{EFO},\text{ jet axis})$	Sphericity $\mathcal{S}$ $\langle\Delta R\rangle(\mathrm{EFO}^\pm,\text{ jet axis})$	Sphericity $\mathcal{S}$ $\langle\Delta R\rangle(\mathrm{EFO}^\pm,\text{ jet axis})$	Sphericity $\mathcal{S}$ $\langle\Delta R\rangle(\mathrm{EFO},\text{ jet axis})$
Spreads	$\overline{\Delta R}(\mathrm{EFO}_{\mathrm{EM}}^0,\text{ jet axis})$		root square sum of: $\overline{\Delta R}(\mathrm{EFO}_{\mathrm{EM}}^0,\text{ jet axis})$ $\overline{\Delta R}(\mathrm{EFO}_{\mathrm{HAD}}^0,\text{ jet axis})$	$\overline{\Delta R}(\mathrm{EFO}_{\mathrm{EM}}^0,\text{ jet axis})$
Energy spreads			$\sigma_{E_T}/\sum E_T$	$\sigma_{E_T}/\sum E_T$
Angles Isolation	$\mathcal{I}_{0.2/0.4}$	$\angle_{\mathrm{mean}}(\text{3 leading EFO}_q^\pm)$ $\mathcal{I}_{0.1/0.4}\times\sum E_T$	$\mathcal{I}_{0.1/0.4}\times\sum E_T$	
Impact parameter	d_0/σ_{d_0}			d_0/σ_{d_0}

TABLE 2.5: Feature variables suites, 25-50 GeV

as electromagnetic [19]. Whenever resolved and properly tagged, EM neutral EFOs are expected to be located close to the jet axis in τ-induced seeds, whereas a larger spread can be expected in jet-induced seeds.

Candidate feature selections chosen for this category are again listed in Tables 2.4 and 2.5. The presence of additional neutrals in both signal and background provides more handles for separation, *e.g.* through the use of angular relations.

The discriminating power of these features with respect to jet-induced seeds are depicted in Figures 2.26 and 2.27, indicating a clear improvement when compared to the `1-prong` category.

2.4.5.3   Category: `3-prong`

The `3-prong` category has the second highest "purity" of all the categories, with roughly 70% of all τ-induced seeds decending from the target process $\tau^\pm \to \pi^\pm \pi^\mp \pi^\pm$. The large majority ($\sim 90\%$) of these τ-induced seeds will contain precisely *three* charged qualified EFOs. These $\mathrm{EFO}_q^\pm$ provide a distinct handle on the separation of τ-induced seeds from jet-induced seeds in this category.

The feature suites considered at low and intermediate transverse momenta are listed in Tables 2.4 and 2.5, and a comparison of these features in signal and background is provided in Figures 2.28 and 2.29.

2.4.5.4   Category: `3-prong+neutral`

Unlike the `3-prong` category, the `3-prong+neutral` category contains a significant admixture of different true τ-decays. While 60% of τ-induced seeds in this category descend from 3-prong decays, almost 35% stem from falsely classified $\pi^\pm + n\pi^0$ decays. This "contamination" from 1-prong decays dilutes some of the discriminating power seen in the variables involving the leading charged EFOs seen in the `3-prong` category. The challenge is exacerbated by the large background in this channel, the largest of all the `X-prong(+neutral)` categories.

The feature suites considered at low and intermediate transverse momenta are listed in Tables 2.4 and 2.5, and a comparison of these features in signal and background is provided in Figures 2.30 and 2.31.

2.4.5.5   Category: `2-prong`

The `2-prong` category contains the largest admixture of different τ-induced seeds, and consequently presents itself as the most challenging category. With roughly one half

---

[19] It should be noted, that while it is possible that the decay $\pi^0 \to \gamma\gamma$ may yield two resolved γ-clusters, studies have shown this to be a comparatively rare occurance ($\sim 5\%$) in ATLAS [71].

stemming from 1-prong decay modes and the other from 3-prong decay modes, it becomes increasingly more difficult to identify features that capture the unique properties of each decay topology. This problem is exacerbated by the $\sim 2 : 3$ ratio of 1-prong induced seeds from $\pi^\pm$ to 1-prong induced seeds from $\pi^\pm + n\pi^0$. Hence a small variable suite is chosen at low transverse momenta, focusing largely on the global properties of classified seeds. These are listed in Table 2.4 and a comparison of the corresponding distributions in signal and background are shown in Figure 2.32. At intermediate transverse momenta, this category is trained together with the `2-prong+neutral` category.

2.4.5.6   Category: `2-prong+neutral`

While the `2-prong+neutral` category also contains a comparatively large admixture of τ-induced seeds with different decay mode origin, it is dominated by falsely classified seeds stemming from $\pi^\pm + n\pi^0$ decays ($\sim 67\%$), the remainder consisting of a roughly equal admixture of $3\pi^\pm$ and $3\pi^\pm + n\pi^0$. This asymmetry in the admixture makes it easier to identify defining features with separation power. The high fraction of $\pi^\pm + n\pi^0$ decays found in this category, motivates feature suites resembling those of `1-prong+neutral`. These are listed in Tables 2.4 and 2.5 and the corresponding feature distributions shown in Figures 2.33 and 2.34.

2.4.6   Likelihood discriminants and performance evaluation

As was already alluded to in Section 2.4.5, the discriminating power of the variables suites defined for each reconstruction category can typically be enhanced if the variables are combined into a single *multivariate* discriminant. While a wide range of methods of varying complexity (and transparency) are available, only a simple *projective likelihood* approach will be considered herein.

For a given reconstruction category, the projective likelihood is defined in terms of the *likelihood ratio*, which for *each* PanTau seed may be expressed as:

$$L_R = \frac{\mathcal{L}_\tau}{\mathcal{L}_\tau + \mathcal{L}_{\text{jet}}}. \tag{2.22}$$

The *likelihood functions* $\mathcal{L}_{\tau/\text{jet}}$ are products of the individual *probability density functions* $\mathcal{P}_{\tau/\text{jet}}$ of the input variables pertaining to the category under consideration:

$$\mathcal{L}_{\tau/\text{jet}} = \prod_{i=1}^{N_{\text{features}}} \mathcal{P}_{\tau/\text{jet}}^i(x_i) \tag{2.23}$$

The probability density functions $\mathcal{P}_{\tau/\text{jet}}$ are in turn derived from polynomial splines fitted to the input variable distributions listed in the previous section and normalized such that:

$$\int_{-\infty}^{+\infty} \mathcal{P}_{\tau/\text{jet}}(x_i)dx_i = 1 \tag{2.24}$$

As such, the likelihood ratio provides a comparatively simple way to combine the information in the various input variables into a single measure of the probability that a given PanTau seed might have originated from a true τ-decay ($L_R \to 1$) or from the hadronization of quarks and gluons ($L_R \to 0$).

While the projective likelihood as defined above will generally deliver optimal results with *uncorrelated* input variables, its performance is likely to degrade in the presence of correlations. The inclusion of strongly correlated feature variables has been avoided whenever possible in the feature selections presented in Section 2.4.5, however non-trivial and non-linear correlations do persist between input variables within in each category. In some cases, these correlations are observed to give rise to double peak structures (at $L_R \sim 0$ and $L_R \sim 1$) in the projective likelihoods for τ-induced and/or jet-induced seeds [72].

Correlations between input variables in a given reconstruction category can scarcely be avoided and some performance degradation is therefore expected to follow. However, more than optimizing the separation of τ-induced seeds from falsely classified jet-induced seeds, the purpose of the following study is to identify and highlight the merits and shortcomings of the PanTau approach to τ-reconstruction and identification compared to canonical approaches to τ-reconstruction in ATLAS. To this end, the projective likelihood presents itself as a simple and transparent method with respect to which more complicated and refined methods that are less sensitive to correlations may later be compared.

The likelihood distributions resulting from each of the variable suites presented in Section 2.4.5 are shown in Figures 2.16 and 2.17. Despite the strong resemblance between τ-induced and jet-induced seeds classified in the same category, a decent discrimination is achieved in most reconstructed categories, both at low and intermediate momenta. As expected, the separation power offered by the likelihood in the categories `1-prong` and `2-prong` is comparatively poor, a reflection of the difficulty of identifying sufficiently robust discriminating features in these categories.

In order to assess the utility of PanTau, it is helpful and instructive to compare its performance with standard τ-reconstruction tools in ATLAS. Such a comparison should ideally be insensitive to the details of any underlying technical differences between the algorithms or their reconstructed input. To this end, the performance comparison will herein be expressed in terms of the *signal identification efficiency* ϵ_S:

$$\epsilon_S = \frac{\text{Number of } \textit{tagged } \tau\text{-candidates} \wedge (\text{match to } \tau_{MC})}{\text{Number of } \tau_{MC}} \tag{2.25}$$

and the *fake rate*:

(a) `1-prong` (10-25 GeV)

(b) `1-prong` (25-50 GeV)

(c) `1-prong+neutral` (10-25 GeV)

(d) `1-prong+neutral` (25-50 GeV)

(e) `3-prong` (10-25 GeV)

(f) `3-prong` (25-50 GeV)

(g) `3-prong+neutral` (10-25 GeV)

(h) `3-prong+neutral` (25-50 GeV)
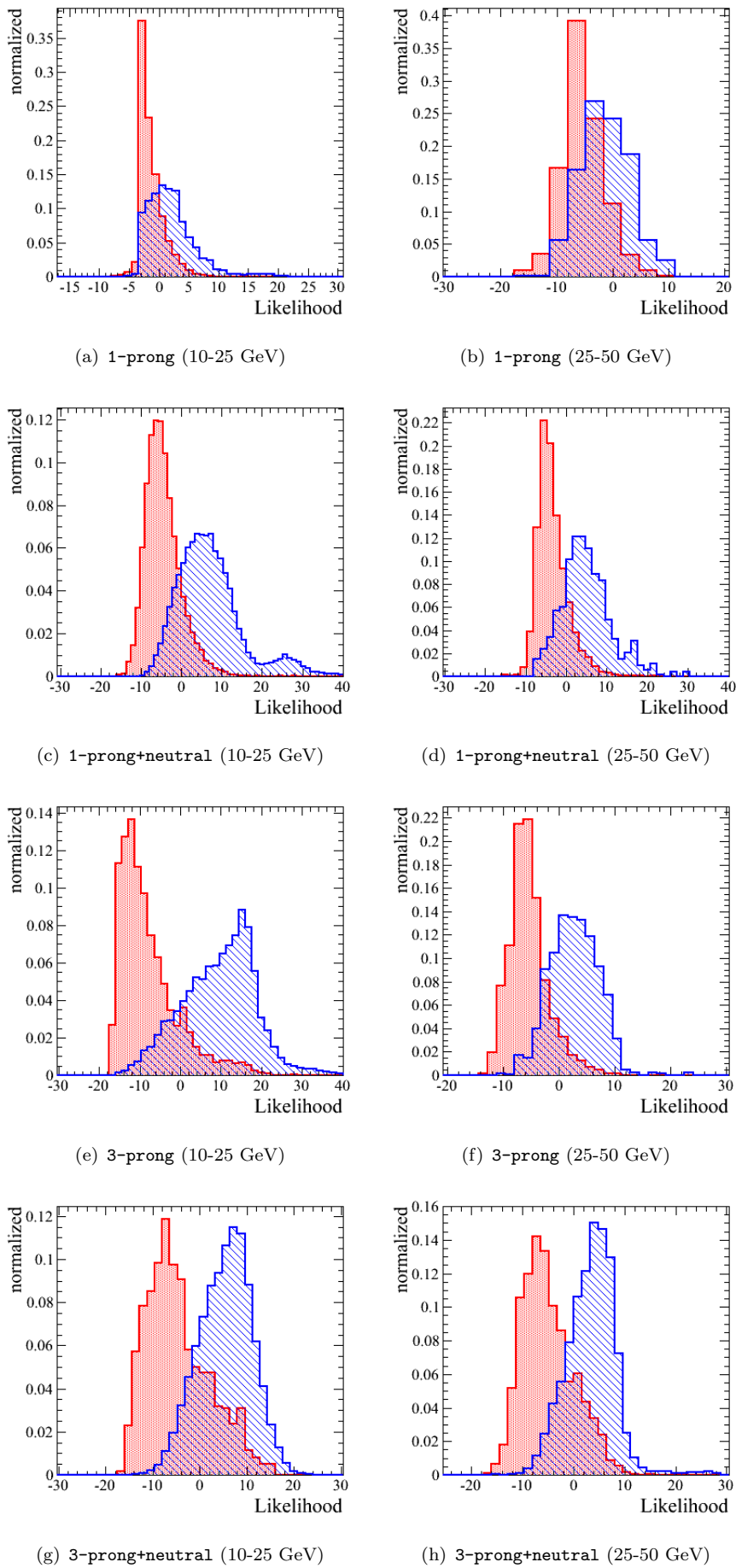
FIGURE 2.16: Likelihood distributions: 1-prong and 3-prong categories (all distributions are transformed by an inverse sigmoid).

(a) `2-prong` (10-25 GeV)

(b) `2-prong` (25-50 GeV)

(c) `2-prong+neutral` (10-25 GeV)

(d) `2-prong+neutral` (25-50 GeV)
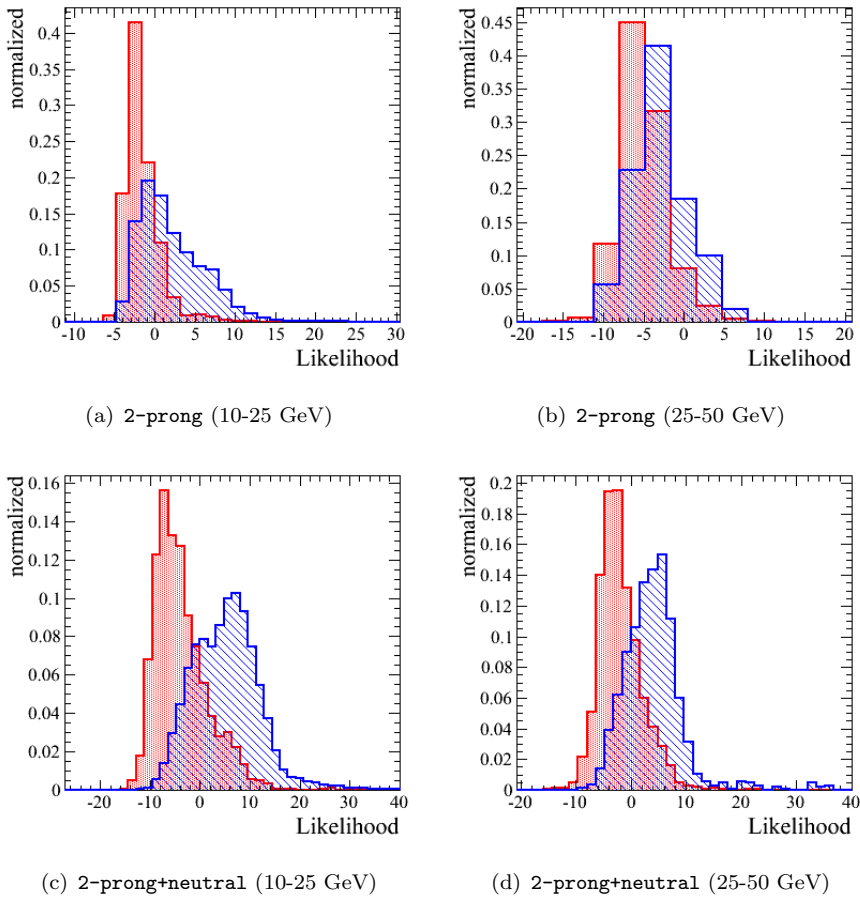
FIGURE 2.17: Likelihood distributions: 2-prong categories (all distributions are transformed by an inverse sigmoid).

$$\epsilon_{FR} = \frac{\text{Number of } tagged \ \tau\text{-candidates} \land \neg(\text{match to } \tau_{MC})}{\text{Number of events}} \tag{2.26}$$

The latter quantity may be more conveniently expressed in terms of the "rejection":

$$R = \frac{1 - \epsilon_{FR}}{\epsilon_{FR}} \tag{2.27}$$

In either case, a *tagged* τ-candidate is understood as a reconstructed and identified candidate produced by the algorithm under consideration. A track-based matching scheme has been employed to relate reconstructed τ-candidates with Monte Carlo τ (τ_{MC}) by way of an association between reconstructed and true tracks [73].

The reader is advised that the above definition of the rejection differs from the standard definitions of background rejection employed by the ATLAS Tau Working Group [55, 74]. The latter will typically define the rejection in terms of the background efficiency:

$$\epsilon_B = \frac{\text{Number of } tagged \ \tau\text{-candidates} \land \neg(\text{match to } \tau_{MC})}{\text{Number of MC jets}}$$

While this measure has the benefit of normalizing to a quantity that is independent of the details of the reconstruction, it fails to account for any effects or objects that may not find an appropriate Monte Carlo jet match, yet still generate a fake seed for the reconstruction algorithm. Alternatively, one may choose to replace the quantity in the denominator with the number of reconstructed τ-candidates. Such a measure would take due account of fake seeds without an appropriate Monte Carlo jet match, but equally be sensitive to differences in the way in which the algorithms define their τ-candidates (*i.e.* it is possible that a given seed for algorithm A would never qualify for algorithm B, and vice versa). In order to provide a measure of comparison where such subtle effects are minimized, the rejection is herein defined in terms of the fake rate as given by equation 2.26.

Performance comparisons in the $\epsilon_S - R$ plane for PanTau and the standard ATLAS τ-reconstruction package `tauRec` are provided below. It is notable that the comparison is performed against `tauRec` candidates that are either calorimeter seeded or both calorimeter *and* track seeded, *i.e.* two dedicated τ-reconstruction packages, rather than one. In all cases, $Z \to \tau\tau$ and $W \to \tau\nu_\tau$ has been used as sources of τ-induced seeds, whereas a cross-section weighted mixture of QCD dijets covering the hard scattering range 8-140 GeV has been used as a source of jet-induced seeds. Any jet-induced seeds from the Z and W samples have been omitted, as have any τ-induced seeds originating from non-isolated τ-leptons in QCD. All performance comparisons are performed within $|\eta_{\mathrm{seed}}| < 2.0$ to stay well within the sensitivity range of the inner detector.

Global performance

The overall performance of PanTau with respect to true 1-prong and 3-prong decays is compared to that of `tauRec` in Figures 2.18 and 2.19, respectively. The measure includes PanTau candidates from all reconstructed categories, save `Other`. For just comparison, `tauRec` candidates are required to have between 1 and 4 associated tracks.

PanTau is seen to underperform with respect to `tauRec`, whereby the relative differences in performance are more accentuated at low transverse momenta. At intermediate momenta, the performances are seen to converge at high efficiency ($\epsilon_S > 60\%$).

As was discussed above, the quality of the PanTau likelihood discriminants varies across the different reconstruction categories depending on the relative composition of τ-induced seeds in each category. Moreover, some categories are found to be significantly more sensitive to background contamination than others. Poor performance in one reconstruction category may therefore diminish the global performance considerably. It is therefore instructive to compare the reconstruction and identification performance of specific decay modes with due regard to the migration matrix shown in Figure 2.14.

1-prong performance

As indicated in Figure 2.14, the categories `1-prong+neutral` and `2-prong+neutral` both enjoy a high fraction of τ-induced seeds from $\tau_{vis} \to \pi^\pm + n\pi^0$ decays, with small or moderate admixtures of seeds from other decay modes. The high "purity" enjoyed
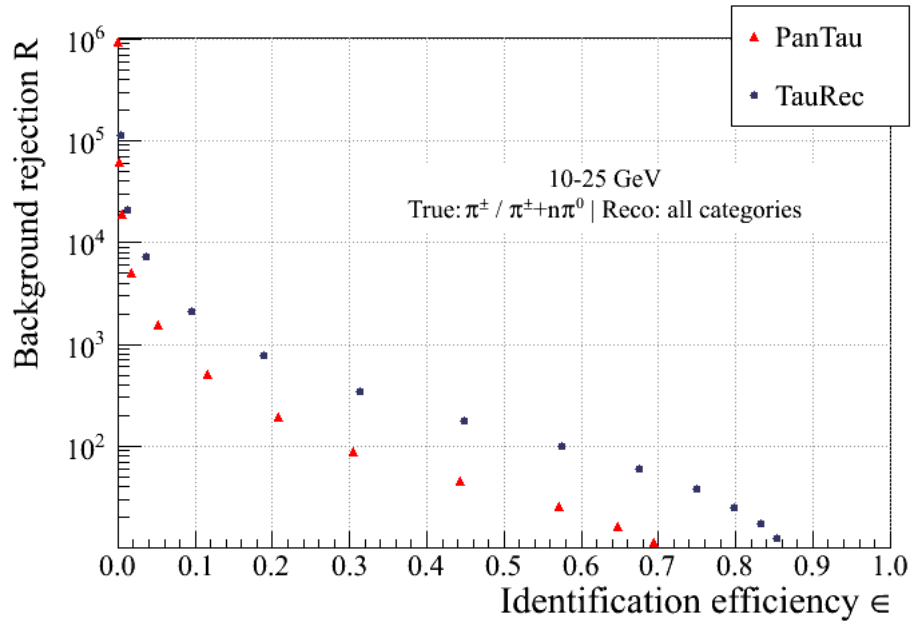
(a) 10-25 GeV
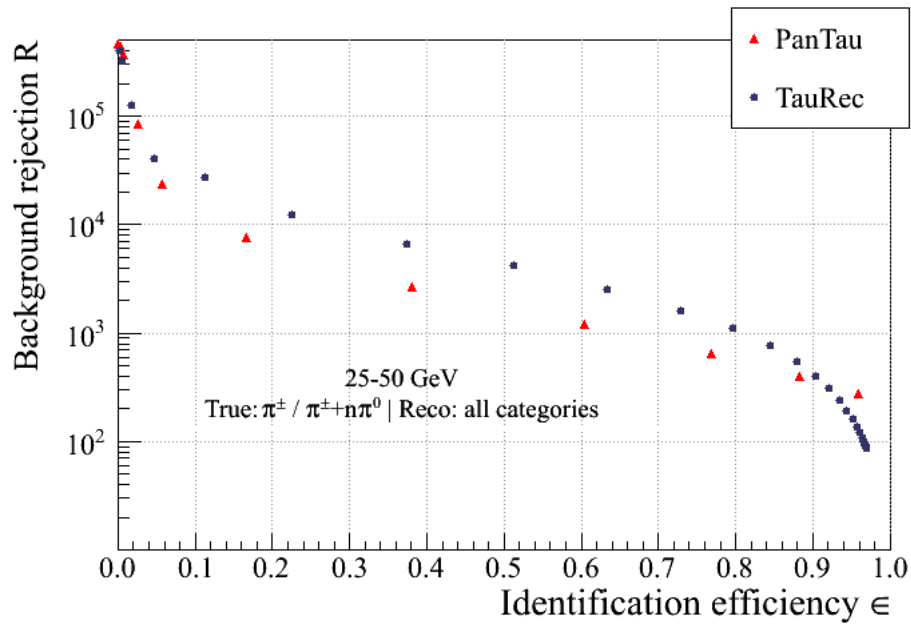
(b) 25-50 GeV

FIGURE 2.18: Global performance w.r.t. true 1-prong decays (excl. Kaons) for candidates with transverse momenta between (a) 10-25 GeV and (b) 25-50 GeV. PanTau candidates from all reconstructed categories except from `Other` are considered. `tauRec` candidates are accordingly required to have between 1 and 4 associated tracks.
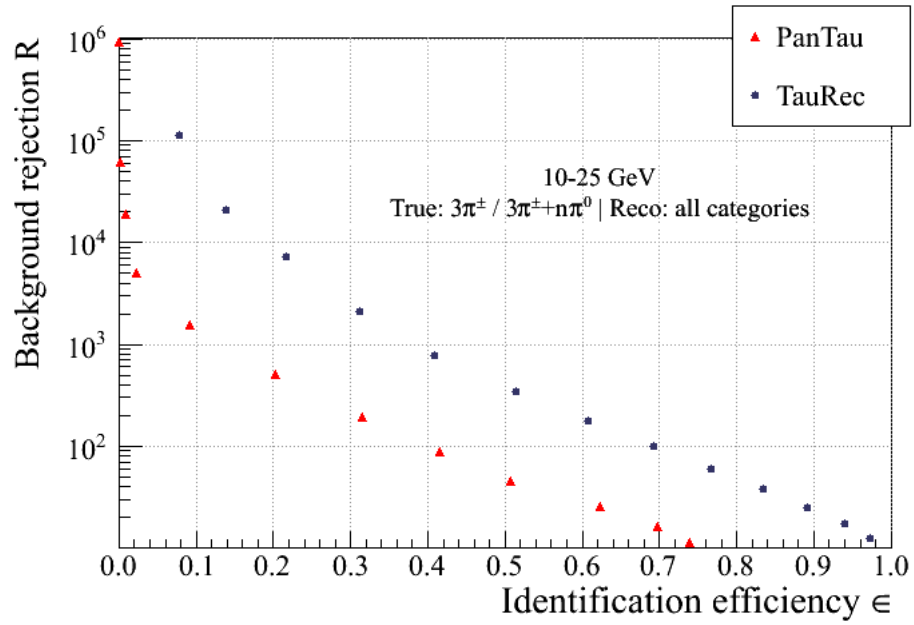
(a) 10-25 GeV
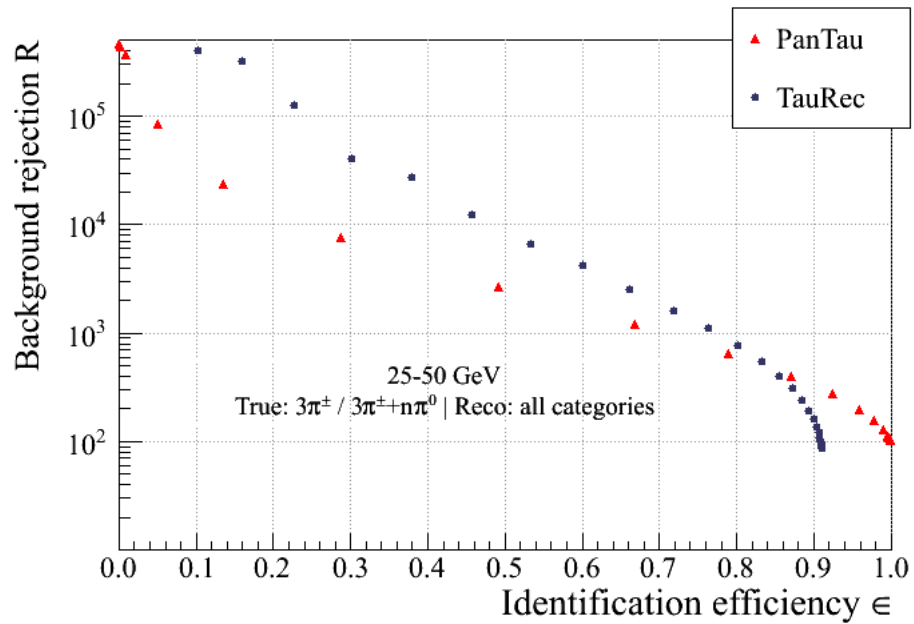
(b) 25-50 GeV

FIGURE 2.19: Global performance w.r.t. true 3-prong decays (excl. Kaons) for seeds with transverse momenta between (a) 10-25 GeV and (b) 25-50 GeV. PanTau candidates from all reconstructed categories except from `Other` are considered. `tauRec` candidates are accordingly required to have between 1 and 4 associated tracks.

in these categories better facilitates the construction of variables sensitive to the characteristic signatures of such decays, and consequently an improvement with respect to the global 1-prong performance might be expected in these channels.

Figure 2.20 compares the performance with respect to true $\tau_{vis} \rightarrow \pi^{\pm} + n\pi^0$ decays using only PanTau candidates from the categories `1-prong`, `1-prong+neutral` and `2-prong+neutral` and indicates that a more commensurate performance can be achieved when using 1-prong candidates from either of these categories. (The latter category is included in order to extend the efficiency beyond the $\sim 70\%$ of true $\tau_{vis} \rightarrow \pi^{\pm} + n\pi^0$ decays classified as `1-prong` or `1-prong+neutral`(see Figure 2.12)).

3-prong performance

A similar tendency is observed in the 3-prong sector, albeit only at intermediate transverse momenta. Here the `3-prong` category is the only category dominated by $\tau_{vis} \rightarrow \pi^{\pm}\pi^{\mp}\pi^{\pm}$ decays, although `2-prong` also contains a significant portion of $\tau_{vis} \rightarrow \pi^{\pm}\pi^{\mp}\pi^{\pm}$ induced seeds. The performance with respect to true $\tau_{vis} \rightarrow \pi^{\pm}\pi^{\mp}\pi^{\pm}$ decays in these categories is shown in Figure 2.21 which indicates a competitive performance at intermediate efficiencies ($\epsilon_S > 50\%$). At lower transverse momenta, the PanTau performance deteriorates as a result of the diminished likelihood separation in the `3-prong` category in this kinematic region.

While the above results indicate that further improvements are required before PanTau can be considered a mature and competitive τ-reconstruction tool, they also clearly vindicate the merits of the driving principles in PanTau. The performance convergence observed in the most performant and well-behaved reconstruction modi, successfully demonstrates that it is possible to apply the principles of particle flow to lepton reconstruction in ATLAS.

2.4.6.1 Transverse energy resolutions

It is instructive to compare the transverse energy resolutions of τ-candidates in PanTau and `tauRec`. The precise resolution of the final PanTau τ-objects made available for analysis are likely to depend on their precise definition[20]. At the time of writing these considerations are still ongoing, and the comparison herein will therefore include *all* constituent EFOs of a PanTau seed.

Figures 2.22 and 2.23 respectively compare the transverse energy resolutions of 1-prong induced candidates reconstructed as either `1-prong` or `1-prong+neutral` and that of 3-prong induced candidates reconstructed as either `3-prong` or `3-prong+neutral`. Distributions are shown before and after the application of a moderate identification selection corresponding to $\epsilon_S \sim 40\%$.

It is evident that PanTau tends to overestimate the E_T of both 1-prong and 3-prong induced candidates by roughly 6-8% at low transverse momenta and by 9-10% at more

---

[20]*i.e* should the final category `3-prong` candidate include *all* EFOs found in its corresponding seed, or just the three leading $EFO_q^{\pm}$?
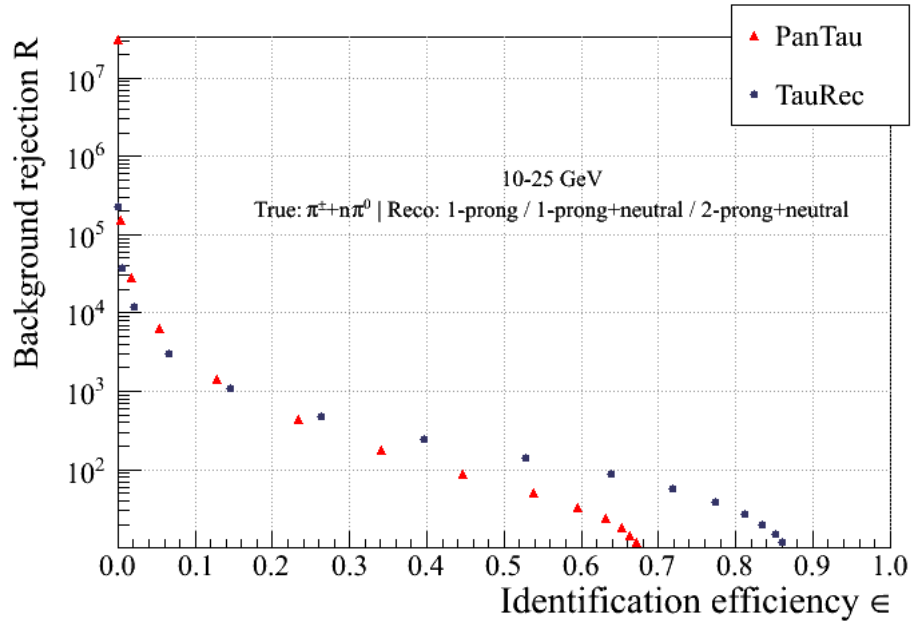
(a) 10-25 GeV
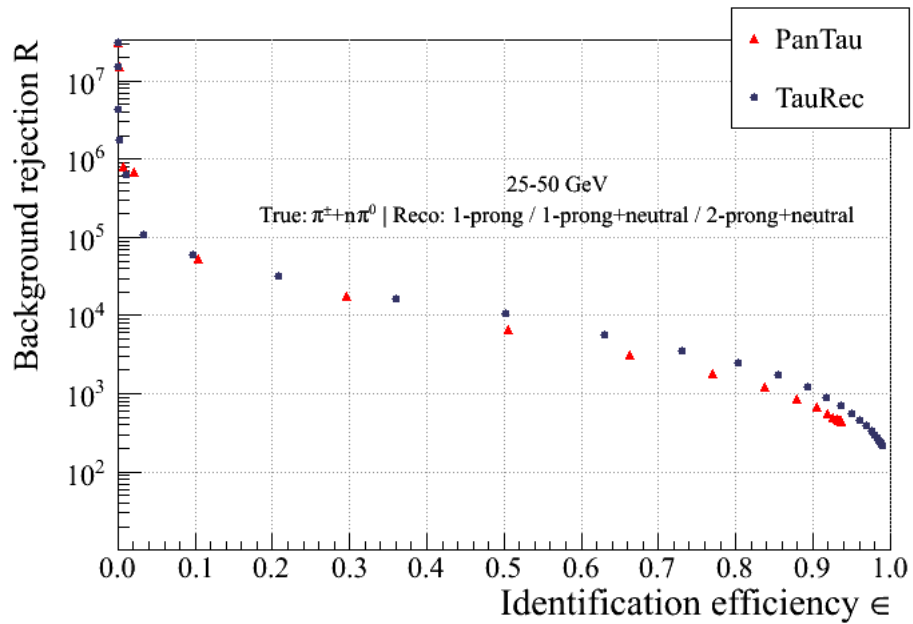
(b) 25-50 GeV

FIGURE 2.20: Performance comparison w.r.t. $\tau_{vis}^{\pm} \to \pi^{\pm} + n\pi^0$ decays for seeds with transverse momenta between (a) 10-25 GeV and (b) 25-50 GeV. Only candidates from the PanTau categories `1-prong`, `1-prong+neutral` and `2-prong+neutral` are considered. `tauRec` candidates are required to have between 1 and 2 tracks.
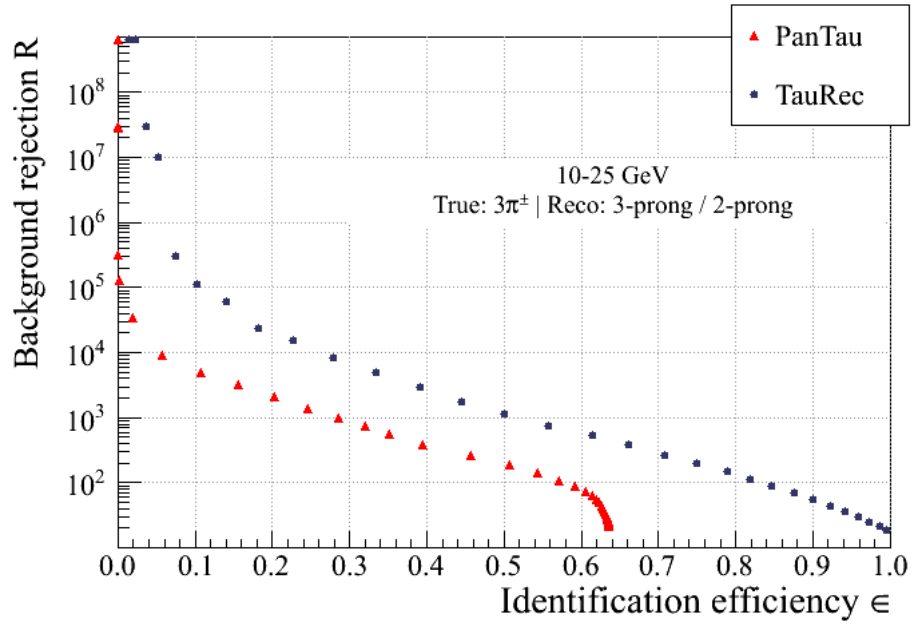
(a) 10-25 GeV
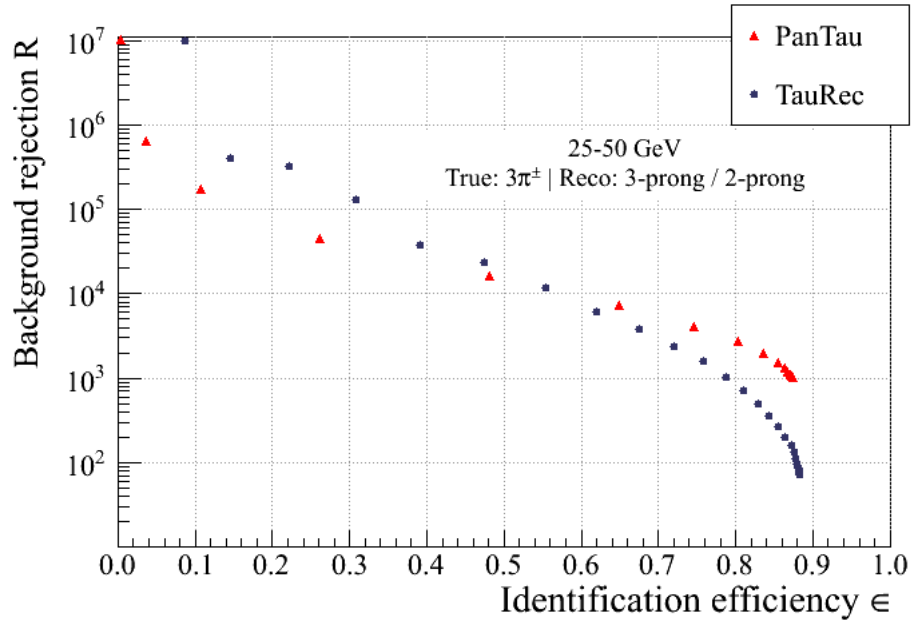
(b) 25-50 GeV

FIGURE 2.21: Performance comparison w.r.t. $\tau_{vis}^{\pm} \to 3\pi^{\pm}$ decays for seeds with transverse momenta between (a) 10-25 GeV and (b) 25-50 GeV. Only candidates from the PanTau categories `3-prong` and `2-prong` are considered. `tauRec` candidates are required to have between 2 and 4 tracks.

intermediate transverse momenta. By comparison, `tauRec` typically underestimates the E_T by circa 0.1-1% in the 1-prong sector and 2-5% in the 3-prong sector at all transverse momenta. The tendency for `eflowRec` to overestimate the energy scale of single 1-prong τ-leptons was briefly mentioned in Section 2.3.2.4 and is reported in [62], however it is notable that this effect appears to be more pronounced in PanTau, especially at intermediate transverse momenta[21]. In most cases, the identification is seen to be insensitive to the overestimation, save in the 3-prong sector at low transverse momenta where it is seen to favour candidates with an overesimated E_T.

The PanTau E_T-resolution distributions are moreover seen to be *positively skewed* (with broader right-sided tails). This (non-gaussian) asymmetry makes the determination of resolutions by way of gaussian fits challenging. Herein, the resolutions will therefore rather be compared in terms of *truncated standard deviations*. Table 2.6 compares the standard deviation of the resolution distributions for PanTau and `tauRec` truncated at 1.0σ and 1.5σ to either side of their respective means. The table also lists the associated *mean* ($\bar{x}$), *skewness*[22] (Γ) and *kurtosis*[23] (K). According to Table 2.6, PanTau typically achieves a better resolution at low transverse momenta, but deteriorates slightly with increasing τ-lepton energy. As expected, this effect is more pronounced in the 3-prong sector.

Even if the skews are reduced by $> 50\%$ after truncation, they remain large when compared to `tauRec`. The larger kurtoses observed in PanTau indicate that while the resolutions are more strongly peaked than in `tauRec` with the majority of candidates reconstructed with small deviations from the mean, broader and longer tails persist where deviations are considerable.

2.4.6.2 Resolving decay resonances

As was discussed early in this Chapter (Sections 2.1.2 and 2.1.3), analyses involving τ-leptons will sometimes want to extract polarization information from the reconstructed τ-object. The quality of any polarization sensitive measurement will typically depend on how well the τ-reconstruction tool is able to determine the original decay mode of the reconstructed τ-object [75]. Because the base unit of PanTau is a reconstructed "pion"-object, the algorithm is expected to retain a comparatively high degree of sensitivity to the details of the τ-decay. It is therefore instructive to consider how well the mass peaks corresponding to mesonic resonances by which the large majority of τ-leptons decay can be reconstructed.

---

[21]It should be noted that the simulated data samples used herein employ an older version of the eflowRec software than that used to produce the results reported in Section 2.3.2.4. Several bug-fixes in the underlying eflowRec software have since been introduced which may impact the results presented herein. At the time of writing, these new fixes have not been tested in the context of PanTau. Differences in the respective seed building procedures may also account for the higher overestimation observed in PanTau.

[22]The *skewness* provides a measure for the asymmetry of the distribution, where a *positive skew* ($\Gamma > 0$) corresponds to a left-skew and a *negative skew* ($\Gamma < 0$) corresponds to a right-skew.

[23]The *kurtosis* indicates how peaked the distribution is with respect to a gaussian distribution. A higher kurtosis implies that deviations from the mean are infrequent but large, rather than comparatively frequent, but small.

(a) 1-prong: 10-25 GeV, $|\eta| < 2.0$

(b) 1-prong: 25-50 GeV, $|\eta| < 2.0$
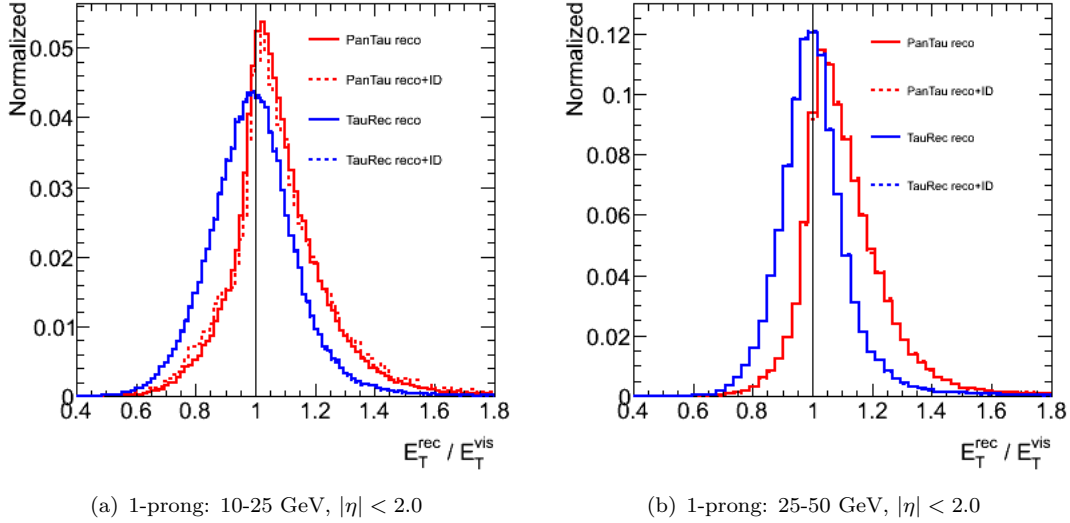
FIGURE 2.22: Transverse energy resolution of candidates matched to true 1-prong τ-leptons from $Z \to \tau\tau$. PanTau candidates are drawn from the `1-prong` and `1-prong+neutral` categories. `tauRec` candidates are required to have 1 associated track. The identification selection applied to PanTau candidates correspond to $\epsilon_S \sim$ 40%.

(a) 3-prong: 10-25 GeV, $|\eta| < 2.0$

(b) 3-prong: 25-50 GeV, $|\eta| < 2.0$
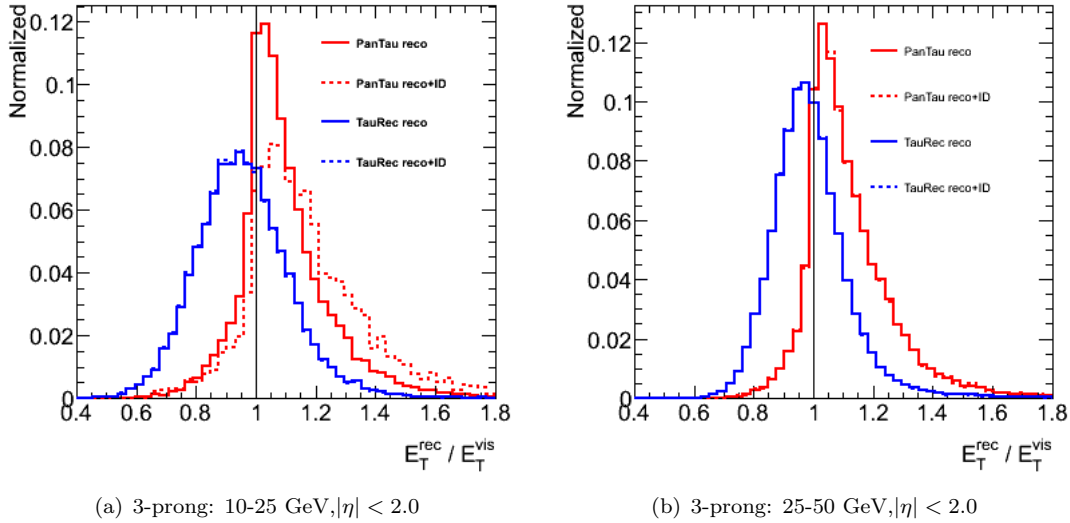
FIGURE 2.23: Transverse energy resolution of candidates matched to true 3-prong τ-leptons from $Z \to \tau\tau$. PanTau candidates are drawn from the `3-prong` and `3-prong+neutral` categories. `tauRec` candidates are required to have 3-4 associated tracks. The identification selection applied to PanTau candidates correspond to $\epsilon_S \sim 40\%$.

(a) 1-prong, 10-25 GeV

	Global (no truncation)		$\bar{x} \pm 1.0\sigma_x$		$\bar{x} \pm 1.5\sigma_x$	
	PanTau	TauRec	PanTau	TauRec	PanTau	TauRec
$\bar{x}$	1.0785±0.0006	0.9943±0.0005	1.0636±0.0003	0.9926±0.0003	1.0643±0.0004	0.9896±0.0004
σ	0.1596±0.0004	0.1504±0.0003	0.0780±0.0002	0.0779±0.0002	0.1036±0.0003	0.1046±0.0002
Γ	0.938±0.009	0.554±0.008	0.31±0.01	0.004±0.009	0.2718±0.009	0.003±0.008
K	2.90±0.02	2.32±0.02	-0.72±0.02	-0.93±0.02	-0.39±0.02	-0.69±0.02

(b) 1-prong, 25-50 GeV

	Global (no truncation)		$\bar{x} \pm 1.0\sigma_x$		$\bar{x} \pm 1.5\sigma_x$	
	PanTau	TauRec	PanTau	TauRec	PanTau	TauRec
$\bar{x}$	1.1095±0.0006	1.0100±0.0005	1.0890±0.0003	1.0027±0.0003	1.0908±0.0004	0.9989±0.0003
σ	0.1447±0.0004	0.1275±0.0004	0.0735±0.0002	0.0626±0.0002	0.0943±0.0003	0.0816±0.0002
Γ	1.49±0.01	1.67±0.01	0.38±0.01	0.11±0.01	0.38±0.01	0.10±0.01
K	4.94±0.02	8.18±0.02	-0.77±0.02	-0.80±0.02	-0.44±0.02	-0.45±0.02

(c) 3-prong, 10-25 GeV

	Global (no truncation)		$\bar{x} \pm 1.0\sigma_x$		$\bar{x} \pm 1.5\sigma_x$	
	PanTau	TauRec	PanTau	TauRec	PanTau	TauRec
$\bar{x}$	1.095±0.001	0.958±0.001	1.0730±0.0006	0.9535±0.0003	1.0766±0.0008	0.9505±0.0008
σ	0.1528±0.0008	0.1570±0.0007	0.0732±0.0004	0.0830±0.0004	0.0975±0.0005	0.1124±0.0005
Γ	1.14±0.02	0.59±0.02	0.48±0.02	0.07±0.02	0.44±0.02	0.07±0.02
K	3.19±0.04	1.77±0.03	-0.57±0.04	-0.99±0.04	-0.22±0.04	-0.78±0.03

(d) 3-prong, 25-50 GeV

	Global (no truncation)		$\bar{x} \pm 1.0\sigma_x$		$\bar{x} \pm 1.5\sigma_x$	
	PanTau	TauRec	PanTau	TauRec	PanTau	TauRec
$\bar{x}$	1.120±0.0008	0.9926±0.0009	1.092±0.0005	0.9825±0.0005	1.0960±0.0006	0.9787±0.0006
σ	1.149±0.0006	0.1359±0.0006	0.0755±0.0003	0.0689±0.0004	0.0960±0.0004	0.0907±0.0004
Γ	1.56±0.01	1.59±0.02	0.52±0.01	0.15±0.02	0.53±0.01	0.14±0.02
K	4.27±0.03	6.75±0.03	-0.64±0.03	-0.85±0.04	-0.33±0.03	-0.54±0.03

TABLE 2.6: Global and truncated *mean values* ($\bar{x}$), *standard deviations* (σ), *skewness* (Γ) and *kurtosis* (K) derived from E_T-resolution distributions for PanTau and `tauRec`. Truncations are performed at 1.0σ and 1.5σ to either side of the global mean.

Figure 2.24 shows an attempt to reconstruct the mass peaks corresponding to the two multi-pion 1-prong decays:

$$\tau_{vis}^{\pm} \to \rho^{\pm}(770 \text{ MeV}) \to \pi^{\pm}\pi^0$$

and

$$\tau_{vis}^{\pm} \to a_1^{\pm}(1230 \text{ MeV}) \to \pi^{\pm}\pi^0\pi^0$$

using τ-induced candidates from the `1-prong+neutral` category. Invariant mass distributions obtained using all EFOs in the seed-jet are contrasted with the corresponding distributions using only *significant* EFOs, where the latter quantity comprises all EFO$^{\pm}$ and all EFO$^0_{EM}$ in the seed.

The effect of additional non-*tau* related EFOs in the seed jet is to wash out the mass peaks. These mass peaks can be recovered if the appropriate particle objects are correctly identified, a task which becomes increasingly more difficult as the transverse

(a) PanTau: 10-25 GeV

(b) PanTau: 25-50 GeV

(c) TauRec
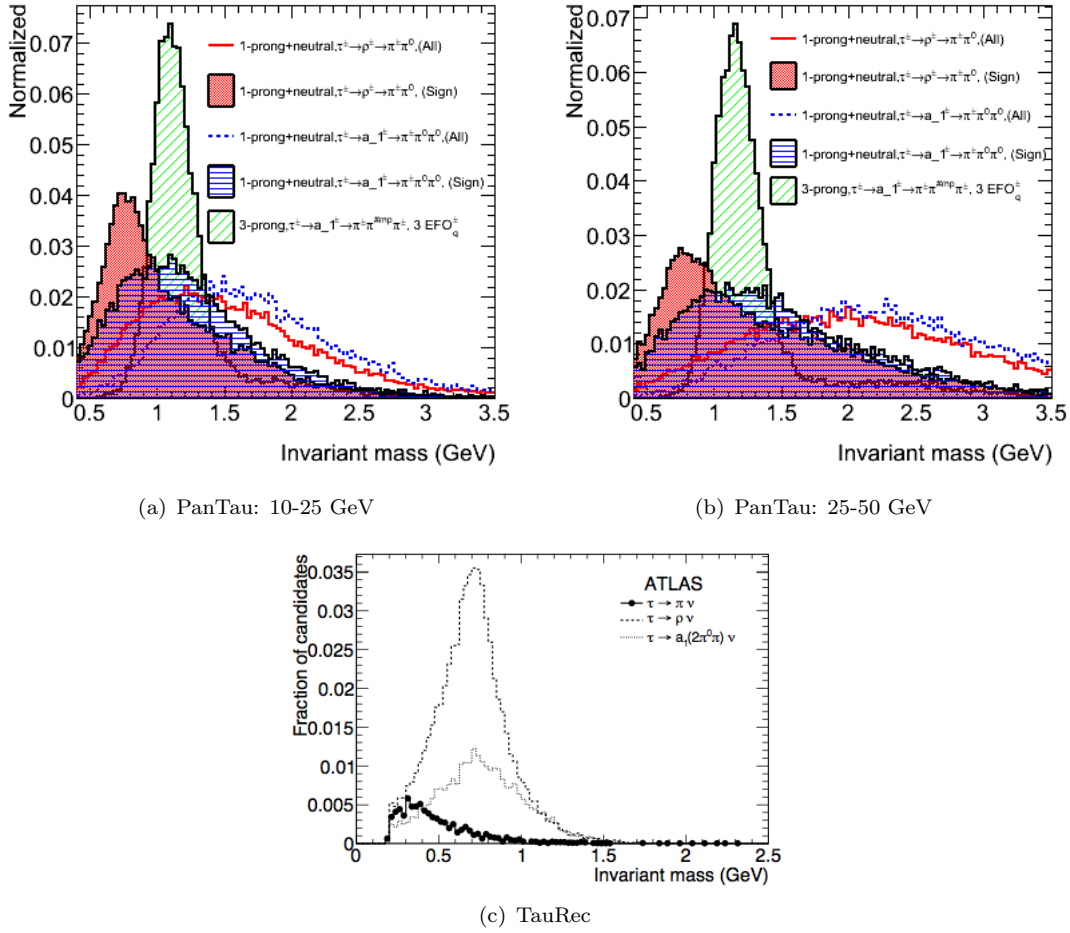
FIGURE 2.24: (a)-(b) Invariant mass distributions derived from τ-induced seeds classified in the category `1-prong+neutral`. The invariant mass of *all* constituents is contrasted with the invariant mass of $EFO^{\pm}$ and EFO^0_{EM}. Mass peaks are observable but are seen to wash out as the decay system becomes more collimated. The invariant mass distributions of the $EFO^{\pm}_q$-system in seeds from the category `3-prong` are shown for comparison. (c) Invariant mass using dedicated π^0-reconstruction in `tauRec` [55].

momenta increases and the boost renders the decay system more collimated. Despite the comparatively fat tails observed in the ρ-distributions in either regime (an effect which is believed to be related to the overestimation of energy in $\tau^{\pm}_{vis} \to \rho^{\pm} \to \pi^{\pm}\pi^0$ decays in `eflowRec`), the invariant mass distributions of PanTau are still seen to compare favourably to those obtained with dedicted π^0-subclustering routines in `tauRec`. The invariant mass of the $EFO^{\pm}_q$-sytem in `3-prong` reconstructed seeds originating from $\tau^{\pm}_{vis} \to a^{\pm}_1 \to \pi^{\pm}\pi^{\mp}\pi^{\pm}$ decays, is shown for comparison. It is evident that an accurate reconstruction and identification of π^0 inside the seed jet is an important prerequisite for a precise decay mode estimation.

2.5 Summary

In the hadronic environment of the LHC, accurate and efficient τ-reconstruction tools are imperative to enable a full exploitation of the physics potential of the LHC. The availability of several unique and distinct approaches to the reconstruction of τ-leptons is therefore an important asset to the experiment, which when used in combination may facilitate an improved interpretation of the recorded data.

With the development of ever more granular calorimeters capable of separating close lying showers, the concept of "particle flow" has emerged as a promising method of combining and condensing information from all subdetectors into an event description in which the unit objects may (ideally) be identified with the stable particles of the event. The prerequisites for successful particle flow calorimetry comprise both the *hardware* ability to resolve energy deposits from different particles and the *software* ability to reconstruct and identify deposits from individual particles. To ensure that both requirements are satisfied, both hardware and software for next generation collider experiments are typically developed in parallel, both driven by the concepts of particle flow [76]. As the ATLAS detector was conceived and constructed in a different manner, it is therefore not *a priori* clear to what extent a full-fledged particle level event description can be achieved.

The studies herein sought to explore the potential for applying the ideas of particle flow calorimetry in the context of τ-reconstruction and identification in ATLAS. To this end, a novel reconstruction algorithm named **PanTau** has been developed in a collaborative effort with S. Fleischmann.

It was shown that it is possible to disentangle the constituents of the τ-decay in the ATLAS calorimeters, and that improved energy resolutions can be obtained if the calorimetric energy deposits of charged particles is duly replaced by the corresponding momentum measurement from the tracker. In ATLAS, the latter operation is performed on all calorimeter clusters with an associated track using a generic energy flow technique known as `eflowRec`, the output of which forms the raw input to PanTau.

Rather than viewing the τ-lepton as a narrow jet, PanTau seeks to recognize decay topologies that are physically consistent with a hadronically decaying τ-lepton using information from the resolved objects in the decay wake. This approach allows for an early classification of τ-candidates according to their most probable decay mode and an equally early rejection of candidates found inconsistent with the decay of a τ-lepton. The classification scheme naturally invites usage of decay-mode specific discriminants against fake candidates from QCD, and it was demonstrated how discriminants with significant separation power can be built from the constituent objects alone, without directly drawing on information from the calorimeters or the tracker.

Though the overall identification performance was found lacking when compared to canonical τ-reconstruction tools in ATLAS, it was demonstrated that a comparable performance can be achieved in the most performant reconstruction modi of PanTau. While

further improvements are required before the algorithm is fully on par with existing τ-reconstruction tools in ATLAS, these results serve as a vindication of the feasibility of the method and the merits of the underlying ideas. It was also shown that Pan-Tau is sensitive to the decay modes of the τ-lepton and generally provides an improved transverse energy resolution. As all steps in the algorithm, including the building of discriminating features, rely squarely on the resolved objects of the decay, PanTau is distinguished insofar as it maintains a clear and natural separation between detector effects and the physics of the τ-lepton decay.

(a) $\sum Q$

(b) (*) $\overline{\Delta R}(\mathrm{EFO}^{\pm}, \mathrm{jet\ axis})$

(c) $\overline{\Delta R}(\mathrm{EFO}^{0}_{\mathrm{HAD}}, \mathrm{jet\ axis})$

(d) (*) $\mathcal{I}_{0.1/0.2} \times \sum E_{T}$

(e) (*) Sphericity $\mathcal{S}$

(f) (*) $\langle \Delta R \rangle (\mathrm{EFO}, \mathrm{jet\ axis})$
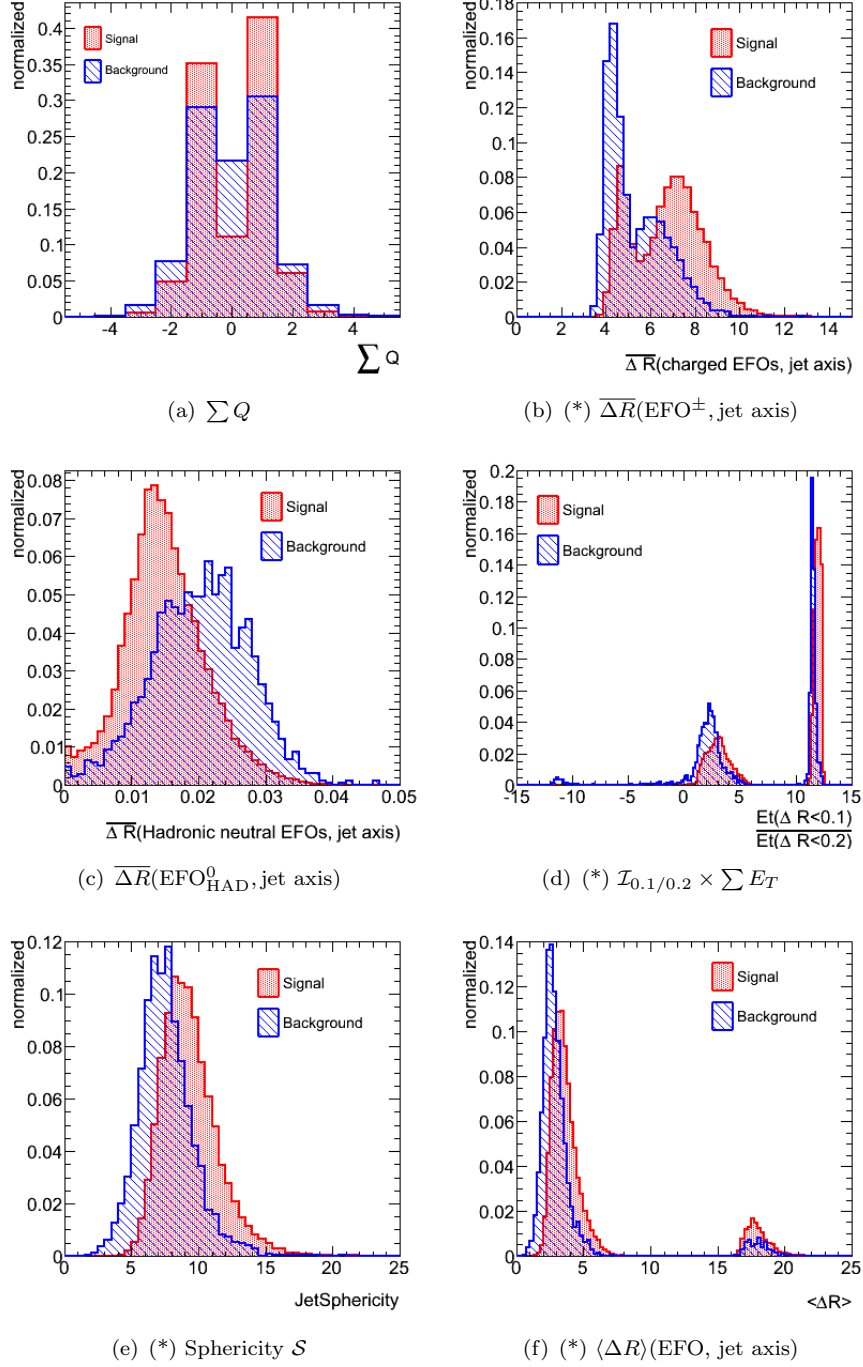
FIGURE 2.25: Feature distributions: `1-prong`, 10 GeV $< p_{T}^{\mathrm{seed}} <$ 25 GeV, $(|\eta^{\mathrm{seed}}| <$ 2.0). Distributions marked with an (*) are strongly peaked and have been transformed with an inverse sigmoid function.

(a) $\sum Q$

(b) $\overline{\Delta R}(\mathrm{EFO}_{\mathrm{EM}}^{0}, \mathrm{jet~axis})$

(c) $\langle \Delta R \rangle (\mathrm{EFO, jet~axis})$

(d) (*) $\mathcal{I}_{0.2/0.4}$

(e) $\angle(\mathrm{leading~EFO}_{q}^{\pm}, \mathrm{jet~axis})$

(f) $\angle(\mathcal{P}^{\pm}, \mathcal{P}^{0})$

(g) $d_{0}/\sigma_{d_{0}}$

FIGURE 2.26: Feature distributions: `1-prong+neutral`, $10~\mathrm{GeV} < p_{T}^{\mathrm{seed}} < 25~\mathrm{GeV}$, ($|\eta^{\mathrm{seed}}| < 2.0$). Distributions marked with an (*) have been transformed with an inverse sigmoid function.

(a) $\sum Q$

(b) $\overline{\Delta R}(\mathrm{EFO}^0_{\mathrm{EM}}, \mathrm{jet\ axis})$

(c) $\langle \Delta R \rangle (\mathrm{EFO}, \mathrm{jet\ axis})$

(d) (*) $\mathcal{I}_{0.2/0.4}$

(e) (*) Sphericity $\mathcal{S}$

(f) d_0/σ_{d_0}

FIGURE 2.27: Feature distributions: `1-prong` / `1-prong+neutral`, 25 GeV $< p_T^{\mathrm{seed}} <$ 50 GeV, ($|\eta^{\mathrm{seed}}| < 2.0$). Distributions marked with an (*) have been transformed with an inverse sigmoid function.

(a) $\sum Q$

(b) $\mathrm{Num}(\mathrm{EFO}_q^\pm)$

(c) $\overline{\Delta R}(\mathrm{EFO}_{\mathrm{HAD}}^0, \mathrm{jet\ axis})$

(d) $\langle \Delta R \rangle (\mathrm{EFO}^\pm, \mathrm{jet\ axis})$

(e) $\angle_{\mathrm{mean}}(3\ \mathrm{leading}\ \mathrm{EFO}_q^\pm)$

(f) $\overline{\Delta R}(\mathrm{leading}\ \mathrm{EFO}^\pm, \mathrm{EFO}^\pm)$

(g) (*) Sphericity $\mathcal{S}$

(h) (*) $\mathcal{I}_{0.1/0.4} \times \sum E_T$

100

FIGURE 2.28: Feature distributions: `3-prong`, 10 GeV $< p_T^{\mathrm{seed}} < 25$ GeV, ($|\eta^{\mathrm{seed}}| <$ 2.0). Distributions marked with an (*) have been transformed with an inverse sigmoid function.

(a) $\sum Q$

(b) $\mathrm{Num}(\mathrm{EFO}_q^{\pm})$

(c) $\langle \Delta R \rangle (\mathrm{EFO}^{\pm}, \text{jet axis})$

(d) $\angle_{\mathrm{mean}}(3 \text{ leading } \mathrm{EFO}_q^{\pm})$

(e) (*) Sphericity $\mathcal{S}$

(f) (*) $\mathcal{I}_{0.1/0.4} \times \sum E_T$

FIGURE 2.29: Feature distributions: `3-prong`, 25 GeV $< p_T^{\mathrm{seed}} < 50$ GeV, ($|\eta^{\mathrm{seed}}| <$ 2.0). Distributions marked with an (*) have been transformed with an inverse sigmoid function.

(a) $\sum Q$

(b) $\text{Num}(\text{EFO}_q^{\pm})$

(c) (*) $\mathcal{I}_{0.1/0.4} \times \sum E_T$

(d) $\langle \Delta R \rangle (\text{EFO}^{\pm}, \text{jet axis})$

(e) (*) Sphericity $\mathcal{S}$

(f) $\sigma_{E_T} / \sum E_T$

(g) $\left((\overline{\Delta R}(\text{EFO}_{\text{EM}}^0, \text{jet axis}))^2 + (\overline{\Delta R}(\text{EFO}_{\text{HAD}}^0, \text{jet axis}))^2 \right)^{\frac{1}{2}}$

FIGURE 2.30: Feature distributions: `3-prong+neutral`, $10 \text{ GeV} < p_T^{\text{seed}} < 25 \text{ GeV}$, $(|\eta^{\text{seed}}| < 2.0)$. Distributions marked with an (*) have been transformed with an inverse sigmoid function.

(a) $\sum Q$

(b) $\mathrm{Num}(\mathrm{EFO}_q^{\pm})$

(c) (*) $\mathcal{I}_{0.1/0.4} \times \sum E_T$

(d) $\langle \Delta R \rangle (\mathrm{EFO}^{\pm}, \text{jet axis})$

(e) (*) Sphericity $\mathcal{S}$

(f) $\sigma_{E_T} / \sum E_T$

(g) $\left((\overline{\Delta R}(\mathrm{EFO}_{\mathrm{EM}}^0, \text{jet axis}))^2 + (\overline{\Delta R}(\mathrm{EFO}_{\mathrm{HAD}}^0, \text{jet axis}))^2 \right)^{\frac{1}{2}}$

103

FIGURE 2.31: Feature distributions: `3-prong+neutral`, 25 GeV $< p_T^{\mathrm{seed}} <$ 50 GeV, ($|\eta^{\mathrm{seed}}| < 2.0$). Distributions marked with an (*) have been transformed with an inverse sigmoid function.

(a) $\langle \Delta R \rangle$(EFO, jet axis)

(b) (*) $\mathcal{I}_{0.1/0.4} \times \sum E_T$

(c) d_0/σ_{d_0}

(d) (*) Sphericity $\mathcal{S}$

FIGURE 2.32: Feature distributions: `2-prong`, 10 GeV $< p_T^{\mathrm{seed}} < 25$ GeV, ($|\eta^{\mathrm{seed}}| <$ 2.0). Distributions marked with an (*) have been transformed with an inverse sigmoid function.

(a) $\mathrm{Num}(\mathrm{EFO}^{\pm})$
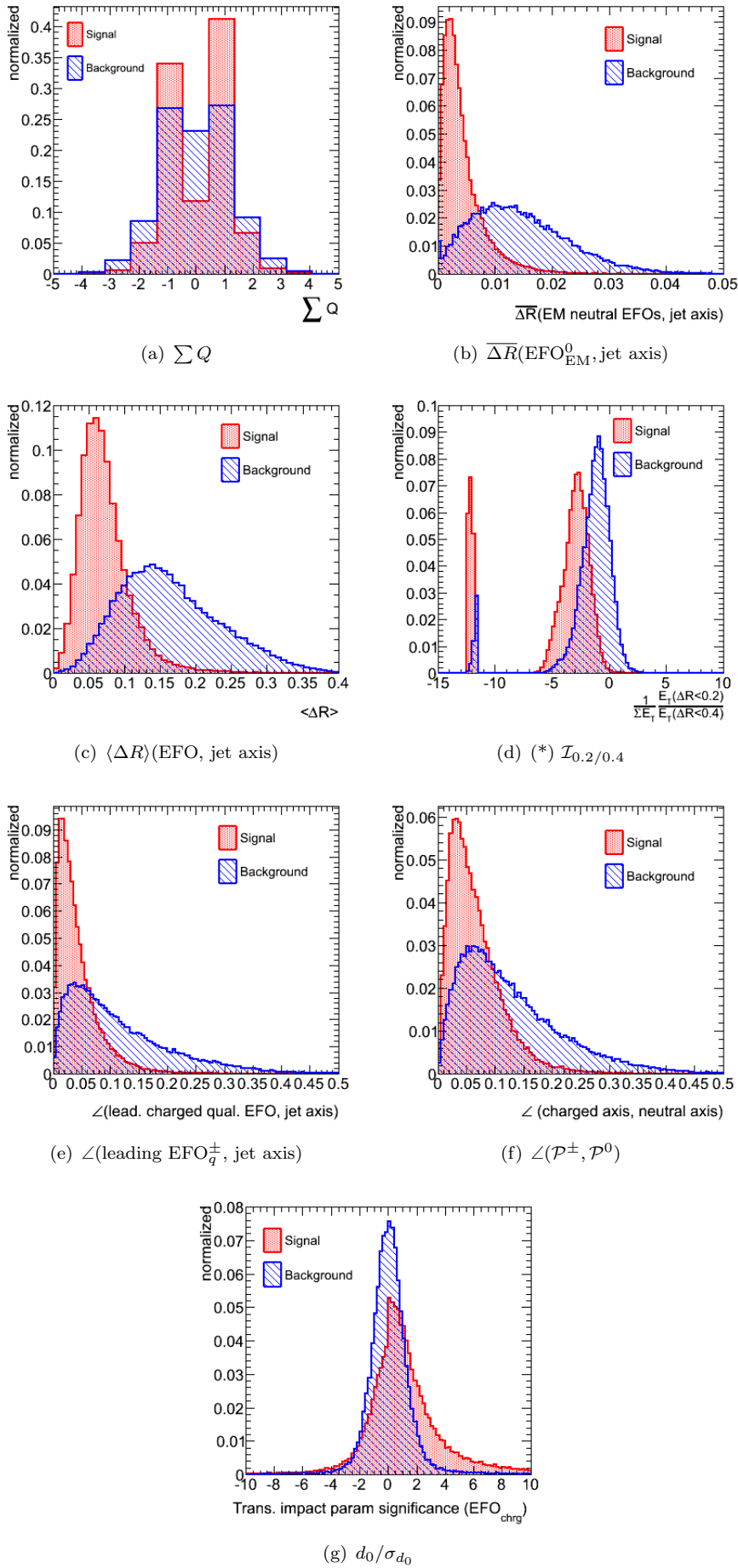
(b) $\langle \Delta R \rangle(\mathrm{EFO},\ \mathrm{jet\ axis})$

(c) (*) Sphericity $\mathcal{S}$

(d) $\sigma_{E_T}/\sum E_T$

(e) $\angle(\mathrm{leading\ EFO}_q^{\pm},\ \mathrm{jet\ axis})$

(f) $\angle(\mathcal{P}^{\pm},\mathcal{P}^{0})$

(g) $\overline{\Delta R}(\mathrm{EFO}_{\mathrm{EM}}^{0}, \mathrm{jet\ axis})$

(h) d_0/σ_{d_0}

105
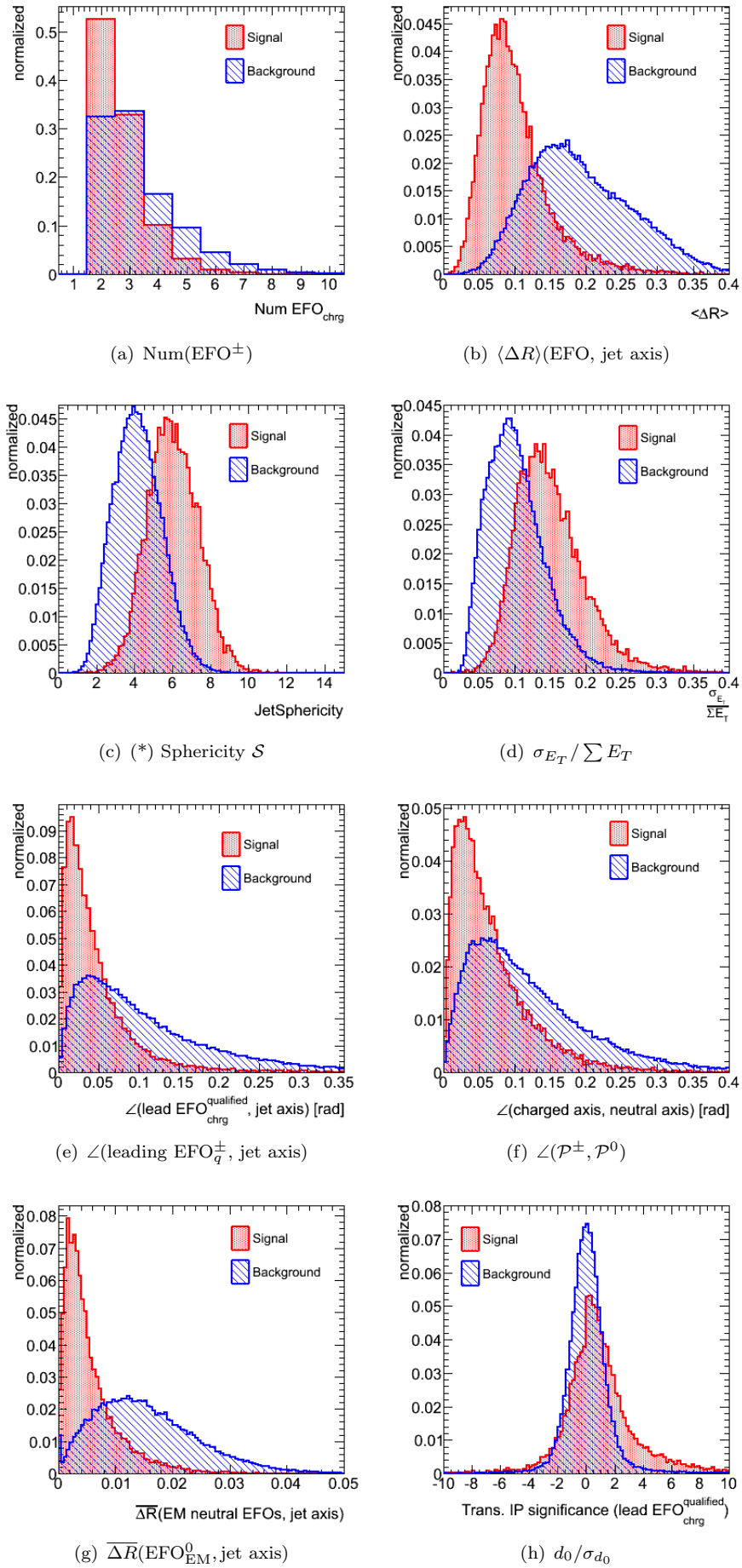
FIGURE 2.33: Feature distributions: `2-prong+neutral`, $10\ \mathrm{GeV} < p_T^{\mathrm{seed}} < 25\ \mathrm{GeV}$, $(|\eta^{\mathrm{seed}}| < 2.0)$. Distributions marked with an (*) have been transformed with an inverse sigmoid function.
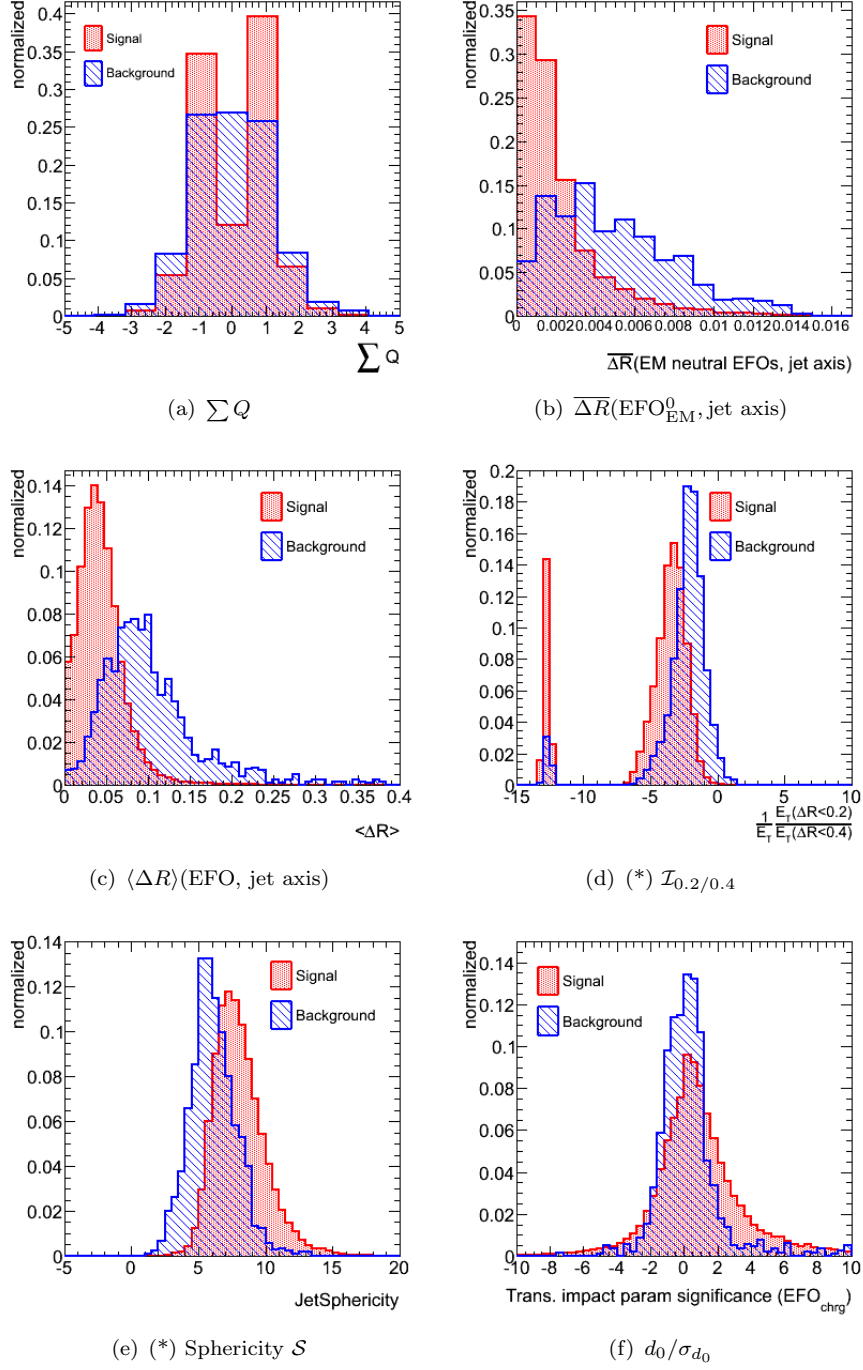
(a) Num(EFO$^\pm$)

(b) $\langle\Delta R\rangle$(EFO, jet axis)

(c) (*) Sphericity $\mathcal{S}$

(d) $\sigma_{E_T}/\sum E_T$

(e) $\overline{\Delta R}$(EFO$^0_{\mathrm{EM}}$, jet axis)

(f) d_0/σ_{d_0}
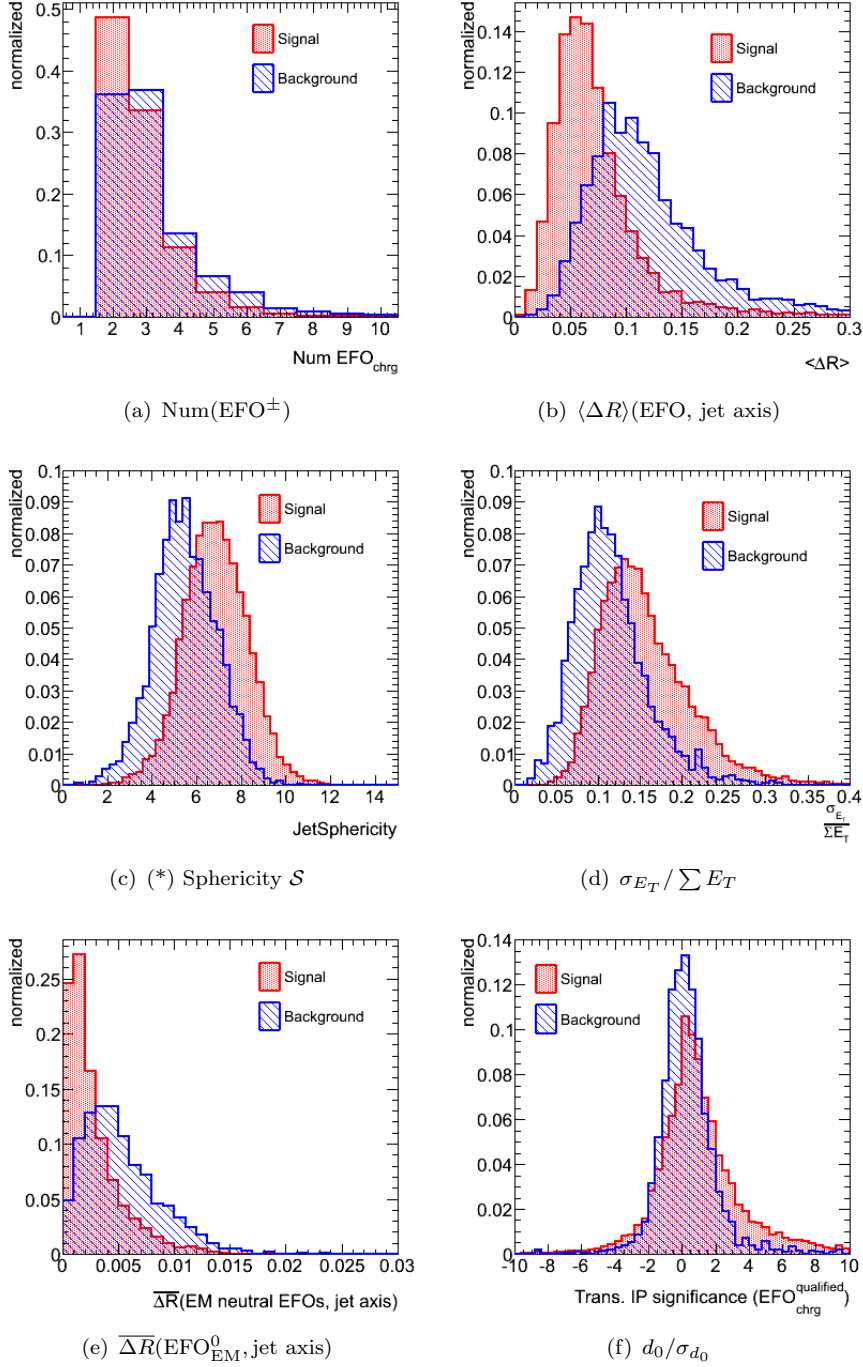
FIGURE 2.34: Feature distributions: `2-prong/2-prong+neutral`, 25 GeV $< p_T^{\mathrm{seed}} <$ 50 GeV, ($|\eta^{\mathrm{seed}}| < 2.0$). Distributions marked with an (*) have been transformed with an inverse sigmoid function.
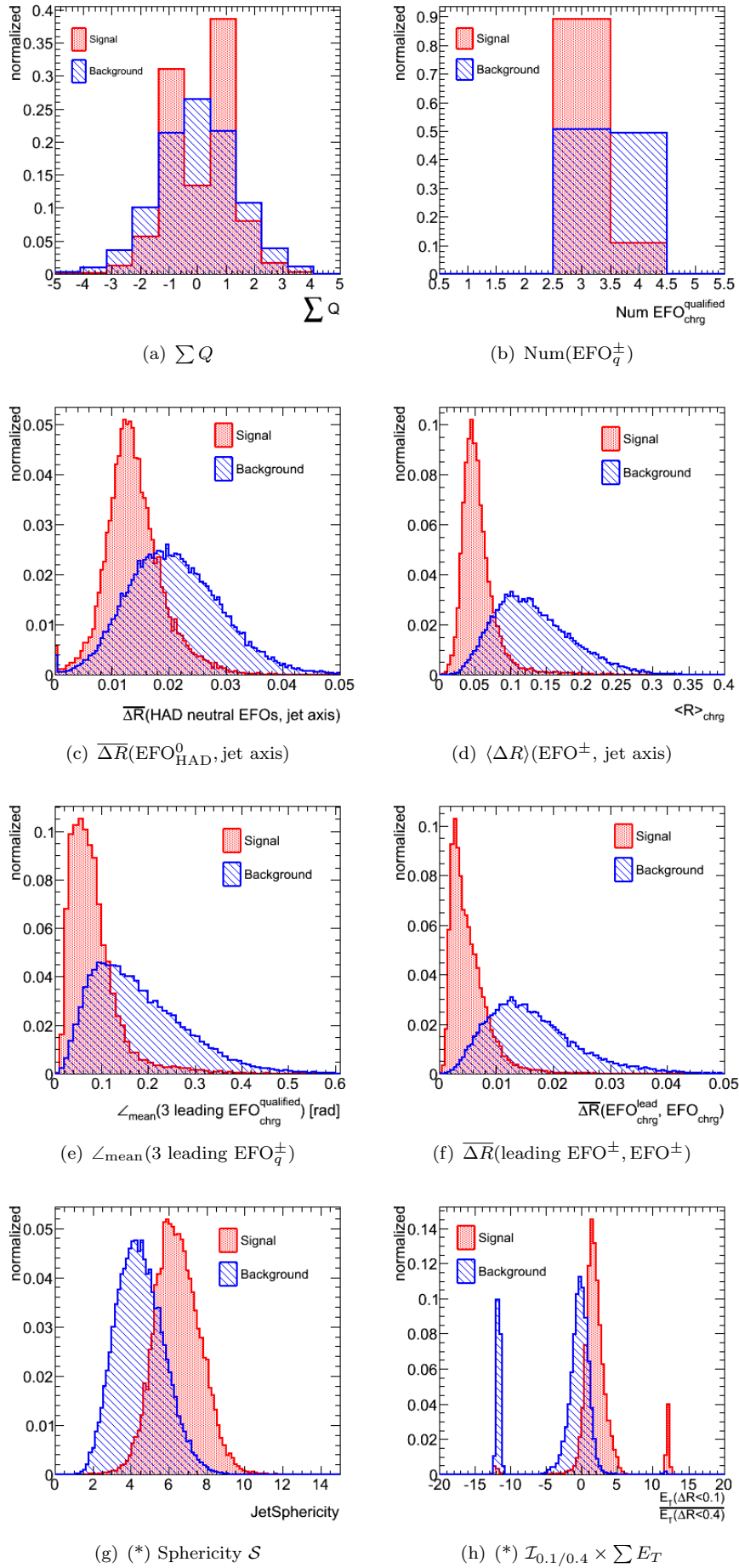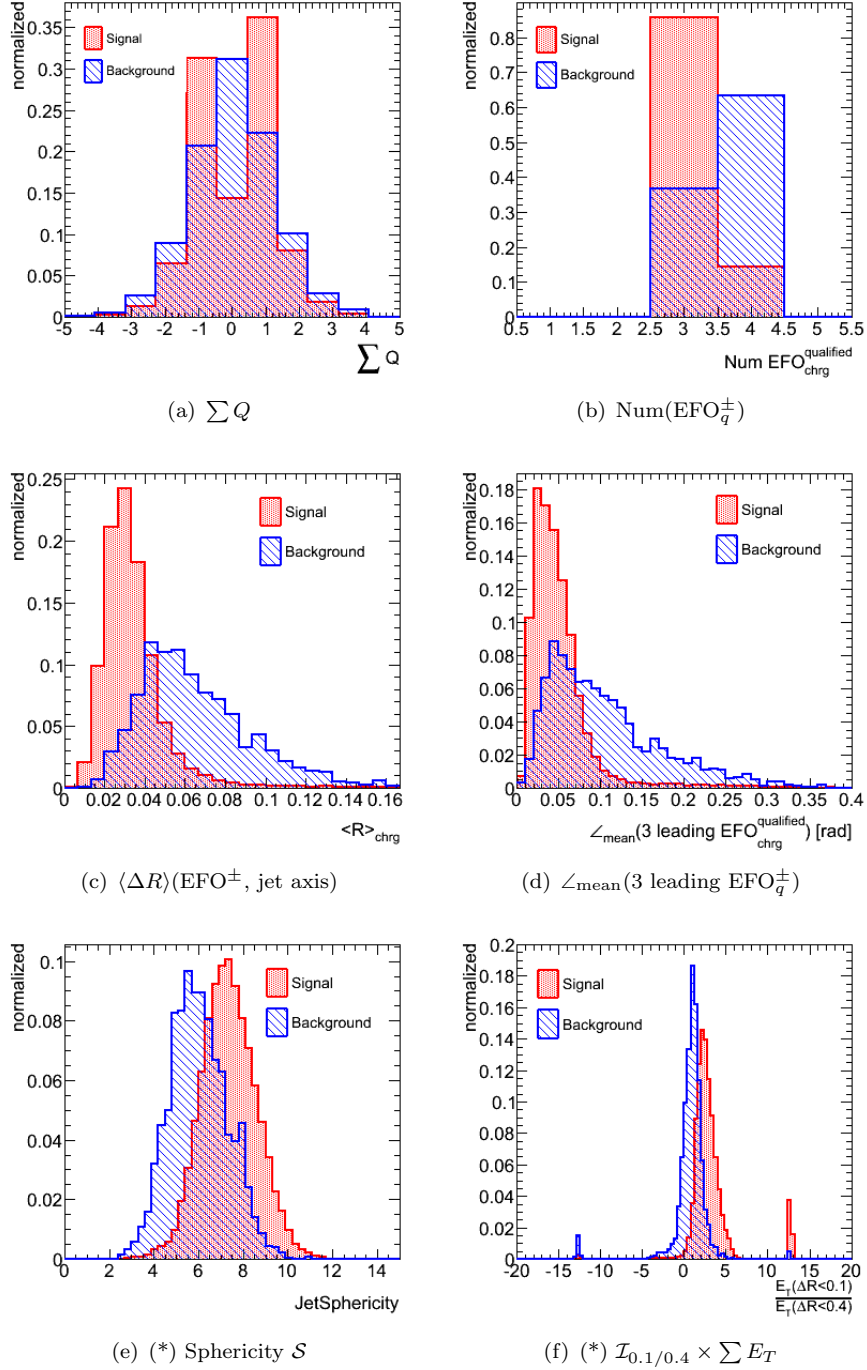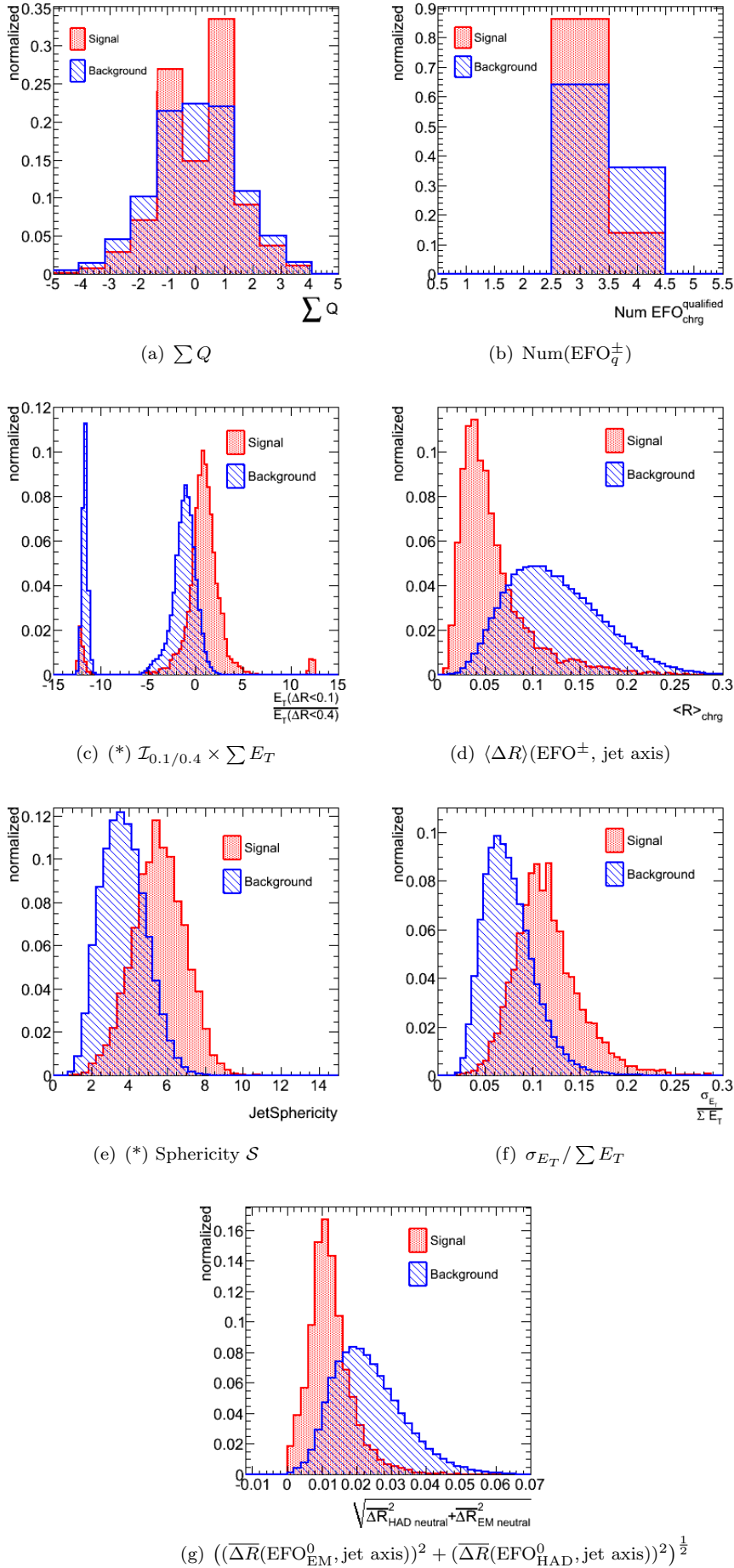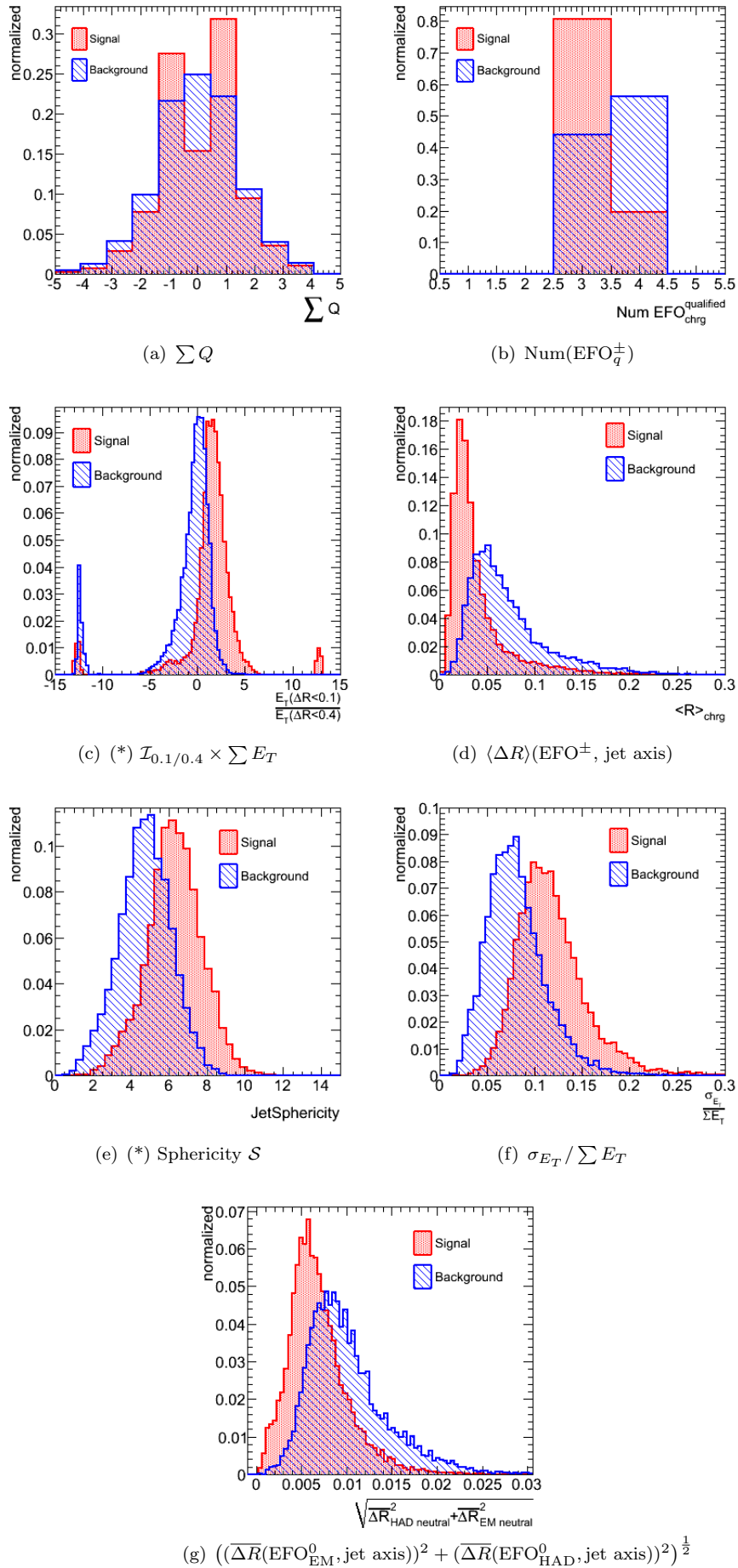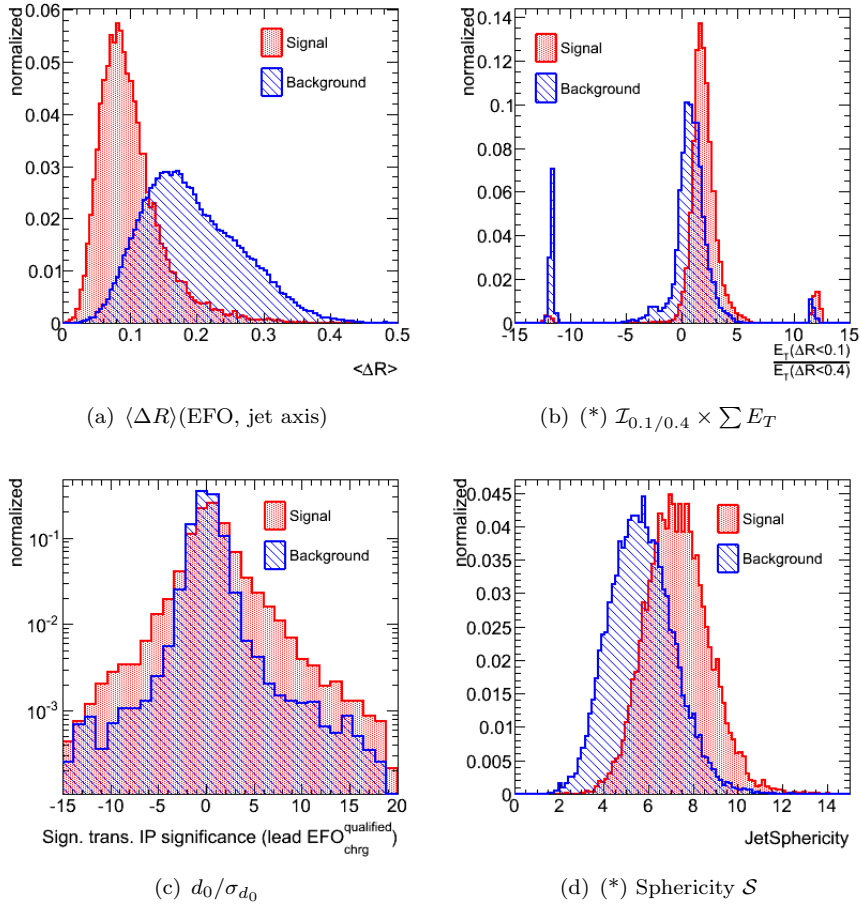
Chapter 3

A method to improve Monte Carlo statistics of QCD induced instrumental $\not{E}_T$

While most electromagnetically and hadronically interacting particles are absorbed in the calorimeters and the momenta of charged MIPs such as $\mu^{\pm}$ are measured in the muon spectrometer, *weakly interacting* (neutral) particles scarcely react with the detector material and consequently escape the experimental volume undetected.

The only method of identifying such particles is by way of inference: if all particles in the event were accounted for, the sum energy-momentum measured in the detector should ideally equal the $\sqrt{s}$ of the colliding beams. Any discrepancy, often termed $\not{E}$, may then be attributed to particles escaping undetected.

At hadron colliders such as the LHC however, this method cannot be straightforwardly applied to infer the presence of weakly interacting particles. As discussed in Section 1.3.1, the initial momentum fraction carried by the colliding parton constituents is *a priori* unknown and hadronic debris scattered at small angles down the beam pipe, render the longitudinal momentum component unmeasurable. However, insofar as the transverse momentum component of the incoming partons is negligible ($p_z \gg p_T$), a momentum balance may still be inferred in the transverse (x,y) plane:

$$\sum E_T + \not{E}_T = 0 \tag{3.1}$$

whereupon the *missing transverse energy* ($\not{E}_T$) can be defined as:

$$\not{E}_T = -\sqrt{\left(\sum_n E_x\right)^2 + \left(\sum_n E_y\right)^2}. \tag{3.2}$$

The sums in Equation 3.2 may run over calorimeter cells, energy flow objects, reconstructed particle object or combinations thereof.

The ν is the most frequent neutral weakly interacting particle to accompany both expected and anticipated processes at the LHC. Because ν emerge not only from τ-lepton decays as discussed in Chapter 2, but also from leptonic decays of W and Z bosons and from semi-leptonic decays heavy flavour quarks, they constitute a frequent source of $\not{E}_T$. The ability to accurately quantify the event $\not{E}_T$ induced from escaping ν is therefore of importance to both W and top mass measurements [32], as well as in the search and measurement of new physics processes such as $H \rightarrow W^{\pm}W^{\mp}$ or $H \rightarrow \tau^{\pm}\tau^{\mp}$. Moreover, underpinned by astrophysical data suggesting an abundance of *dark matter* in the Universe, several models of physics beyond the Standard Model predict heavy stable neutral weakly interacting particles. In particular, the collider phenomenology of all R-parity conserving SUSY models involves a stable and neutral lightest supersymmetric particle (LSP) which escapes direct experimental detection and typically renders the event separable from background by way of a large momentum imbalance. Signatures involving large $\not{E}_T$ beyond Standard Model predictions are thus strongly indicative of new physics and it is therefore critically important to correctly quantify the event $\not{E}_T$.

3.1 Calculating $\not{E}_T$ in ATLAS

ATLAS employs various methods to compute the event $\not{E}_T$, including the so-called *cell-based* method, the *object based* method and the *energy flow based* method [66]. As the standard method in ATLAS, the cell-based approach has been used in all studies presented herein. Therefore, the following provides a cursory description of the cell-based technique only.

The cell-based method computes the event $\not{E}_T$ as the vectorial sum of transverse energy deposited in the calorimeters and the momenta measured in the muon spectrometer, applying due corrections for potential energy losses in the cryostat surrounding the ECAL:

$$\not{E}_{x,y} = \not{E}_{x,y}^{\mathrm{calo}} + \not{E}_{x,y}^{\mathrm{cryo}} + \not{E}_{x,y}^{\mu}. \tag{3.3}$$

The first term $\not{E}_{x,y}^{\mathrm{calo}}$ is obtained by summing over all cells associated with topological clusters in the calorimeters (see Section 2.3.1):

$$\not{E}_{x,y}^{\mathrm{calo}} = -\sum_{\mathrm{clus}} \sum_{\mathrm{cell} \in \mathrm{clus}} E_{x,y}^{\mathrm{cell}} \tag{3.4}$$

whereby the topological cluster thresholds serve to suppress unwanted contributions from calorimeter noise. A global calibration of all cells ensues (following either the H1 prescription or the Local Calibration scheme) [32]. To improve on the comparatively crude global calibration, the calorimeter cells are associated with a reconstructed and

identified $e, \gamma, \mu, \tau_{had}$, b-jet or light-flavour jet and its calibration adjusted accordingly. Because such particle objects are generally calibrated to higher accuracy, the overall $\not{E}_T$ measurement thus profits from a more precise calibration. Any cells that cannot be associated to any reconstructed objects retain their initial global calibration.

In order to correct for undetected energy losses in the dead material of the cryostat between the ECAL and the HCAL, correlations between energy deposits in the sensitive layers to either side of the cryostat are exploited and folded into $\not{E}_{x,y}^{cryo}$ [56].

The last term accounts for any transverse momentum measured by the muon spectrometer

$$\not{E}_{x,y}^{\mu} = - \sum_{\text{rec } \mu} E_{x,y} \tag{3.5}$$

where the sum runs over all reconstructed muons. While a track match in the inner detector wherever possible is required to suppress falsely reconstructed muons, the momentum measurement is derived from the muon spectrometer alone to avoid double counting any energy losses in the calorimeters.

3.2 Fake contributions to $\not{E}_T$

A prerequisite for using the event $\not{E}_T$ to infer the presence of weakly interacting particles is the proper exclusion of all possible contributions to the measured $\not{E}_T$ that may arise from instrumental imperfections. The sum of all such contributions is often termed *fake* transverse missing energy ($\not{E}_T^{\text{fake}}$).

In order to enable an accurate measurement of the event $\not{E}_T$, a hermetically sealed detector is imperative, both in terms of its angular coverage and its ability to fully contain particles entering the detector volume. While the extended forward coverage of the ATLAS calorimetry discussed in Section 1.4.1.2 goes a long way towards providing hermetic sealing, a full 4π solid angle coverage cannot be achieved. Gaps in the coverage occur not only in the very forward regions where forward scattered debris escape unnoticed, but also in the form of narrow uninstrumented regions ("cracks") in the more central parts of the calorimeter volume which serve as necessary outlets for cabling and services. Particle showering in the vicinity of such cracks may lead to full or partial failure to register particle energies. The muon spectrometer by contrast provides a more limited forward coverage and like the calorimeter contains a crack to provide an access channel for services to the other detector systems ($|\eta| \sim 0$).

Very energetic jets may occasionally "punch through" the outer boundaries of the calorimeter volume leaking shower particles into the muon spectrometer which in turn may generate false muon candidates of arbitrary momenta. Very low energy charged particles by contrast, may evade the calorimeter altogether when sufficiently bent by the solenoid field of the inner detector.

Pathological instrumentation, in the form of noisy electronics or faulty ("dead") calorimeter cells may also contribute substantially to the event $\not{E}_T^{\text{fake}}$. Even nominally operating instrumentation may occasionally generate substantial $\not{E}_T^{\text{fake}}$. A frequent source of potential mismeasurements derives from the limited energy resolution and any potential non-linearities in the response of the hadronic calorimeters, a problem further aggravated by statistical fluctuations in the hadronic showering. As is further discussed in the sections below, jet fluctuations may generate significant contributions to the event $\not{E}_T^{\text{fake}}$ in the rich multi-jet environment of the LHC.

At nominal operation the aforementioned challenges are further compounded by overlapping contributions from pile-up, beam-halo muons[1] and cosmic ray bremstrahlung.

3.3 Accounting for QCD induced $\not{E}_T^{\text{fake}}$ from jet fluctuations

Because of its relevance as a key signature for new physics at the LHC, achieving a sound reconstruction of the event $\not{E}_T$ at an early stage of ATLAS operation is a matter of great importance. An early discovery in channels involving large $\not{E}_T$ is contingent on a comprehensive understanding of all contributions arising from not only undetected particles, but also any unwanted instrumental effects as discussed in Section 3.2. This is particularly important in the context of $\not{E}_T$-dependent SUSY searches, where a proper control of all backgrounds prone to generate large $\not{E}_T$ is mandatory [32].

While control samples from processes such as $Z \to ll$ may provide a handle on contributions from $Z \to \nu\bar{\nu}$, the effect of poorly reconstructed QCD multi-jet events inducing large $\not{E}_T$ is considerably harder to gauge. This problem is further exacerbated by the large QCD cross sections at the LHC. Even if QCD events faking large $\not{E}_T$ are comparatively rare, the enormous cross sections enjoyed by such processes generate non-negligible contributions to the high end of the measured $\not{E}_T$ spectrum. Large cross sections also prohibit the full simulation of a sufficiently large number of such rare events to obtain realistic estimates of QCD induced $\not{E}_T^{\text{fake}}$. This is particularly true of instrumental contributions arising from jet energy fluctuations. While contributions from faulty calorimeter cells or partial shower losses in crack regions can be gauged through the controlled introduction of faulty cells into the simulation or by restricting the simulation of jets to a problematic region of the detector, estimating the impact of jet energy fluctuations requires a large sample of fully simulated events across the full detector coverage with nominal simulation settings.

To partially counter the problem of simulating insufficient numbers of QCD events in face of large cross sections, the official ATLAS simulated dijet samples (`PYTHIA`) are generated in eight different bins of hard scattering p_T across the range 8 GeV $< p_T <$ 2280 GeV. While this strategy goes some way towards improving statistics across the full kinematic range, resulting reconstructed distributions are often still plagued by poorly populated

---

[1]Beam interactions with the beampipe may produce showers upstream of the detector. Muons buried in the shower debris may penetrate the protective shielding and interact inside the detector volume.
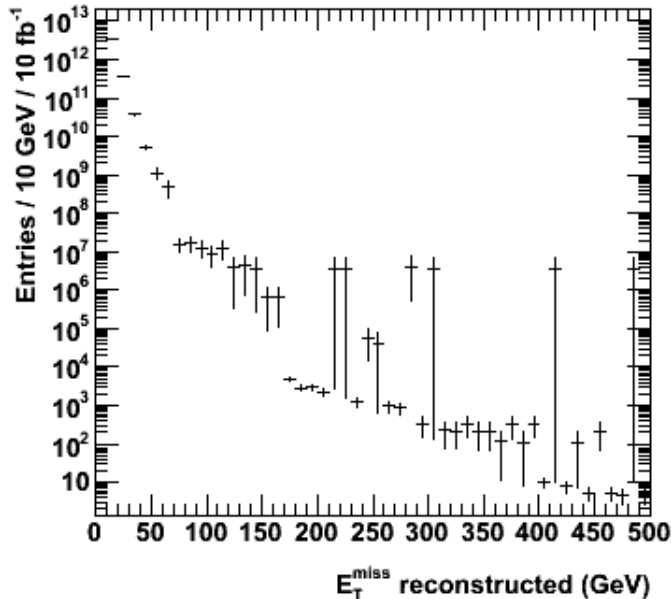
FIGURE 3.1: Combined reconstructed $\not{E}_T$ spectrum of simulated QCD dijets in all eight bins of hard scattering p_T. The high end of the kinematic range is plagued by large statistical uncertainties.

tails with large statistical uncertainties. Figure 3.1 shows the combined reconstructed $\not{E}_T$ spectrum of simulated QCD events in all eight bins of hard scattering p_T and clearly highlights the problem of large statistical uncertainties in the high end of the kinematic range.

Given the constraints on available CPU-time and storage, a proper estimation of $\not{E}_T^{\text{fake}}$ from jet fluctuations requires the aforementioned p_T-binning strategy to be supplemented by a generator filter which ensures that only events prone to produce large $\not{E}_T$ are passed on for full simulation and reconstruction, while all remaining events are discarded. While this is a trivial task for neutrino induced contributions, fake contributions to $\not{E}_T$ is an *a priori* instrumental effect which can only be properly determined after passing the event through the full simulation and reconstruction. Events prone to generate large $\not{E}_T^{\text{fake}}$ are therefore highly non-trivial to flag at the generator level.

In the following, a method is presented providing a probabilistic estimate for fluctuation-induced contributions to reconstructed $\not{E}_T$ for arbitrary jet configurations at the generator level.

3.4   The jet imbalance method

As a means of illustration it is instructive to consider a simple dijet event in which the two jets, $\mathcal{J}_1$ and $\mathcal{J}_2$, are azimuthally back-to-back. Such an event configuration is *a*

priori perfectly balanced in the transverse plane and in the absence of neutrinos buried in either jet, the event has zero $\not{E}_T$.

After the jet constituents have passed through the detector, the jet four-momenta are perturbed such that $\mathcal{P}_{\text{true}} \neq \mathcal{P}_{\text{meas}}$, where $\mathcal{P}_{\text{true}}$ and $\mathcal{P}_{\text{meas}}$ indicate the true and measured jet four vectors, respectively.

The difference,

$$\Delta\mathcal{P}^{\mathcal{J}_1+\mathcal{J}_2} = (\mathcal{P}_{\text{meas}}^{\mathcal{J}_1} + \mathcal{P}_{\text{meas}}^{\mathcal{J}_2}) - (\mathcal{P}_{\text{true}}^{\mathcal{J}_1} + \mathcal{P}_{\text{true}}^{\mathcal{J}_2}) \tag{3.6}$$

thus receives a non-zero transverse component $\Delta\mathcal{P}_T^{\mathcal{J}_1+\mathcal{J}_2}$ which can be identified with the event $\not{E}_T^{\text{fake}}$ resulting from instrumental "smearing".

To a good first approximation $\mathcal{P}_{\text{meas}}$ is spread in a gaussian manner about $\mathcal{P}_{\text{true}}$, so that each component of $\Delta\mathcal{P}_T^{\mathcal{J}_1+\mathcal{J}_2}$ may be expressed as a sum of two independent gaussians $\Delta\mathcal{P}_{\text{x,y}} = \Delta\mathcal{P}_{\text{x,y}}^{\mathcal{J}_1} + \Delta\mathcal{P}_{\text{x,y}}^{\mathcal{J}_2}$ with spreads $\sigma_{\mathcal{J}_{1(2)}}(E, \eta)$ about a mean of zero[2].

As is shown in Appendix C, the probability distribution of the resulting $\not{E}_T^{\text{fake}} = \Delta\mathcal{P}_T^{\mathcal{J}_1+\mathcal{J}_2}$ can be expressed analytically as:

$$\mathcal{F}(\Delta\mathcal{P}_T^{\mathcal{J}_1+\mathcal{J}_2}) = \frac{\Delta\mathcal{P}_T^{\mathcal{J}_1+\mathcal{J}_2}}{\sigma^2} \exp\left[\frac{-\left(\Delta\mathcal{P}_T^{\mathcal{J}_1+\mathcal{J}_2}\right)^2}{2\sigma^2}\right] \tag{3.7}$$

If the *mean value* of the above probability distribution $\mathcal{F}(\Delta\mathcal{P}_T)$ is now taken as an estimate for the magnitude of the $\not{E}_T^{\text{fake}}$ in the event, the *expected* $\not{E}_T^{\text{fake}}$ resulting from jet fluctuations can be expressed as:

$$\langle \not{E}_T^{\text{fake}} \rangle_{\mathcal{J}_1+\mathcal{J}_2} = \int \Delta\mathcal{P}_T^{\mathcal{J}_1+\mathcal{J}_2} \mathcal{F}(\Delta\mathcal{P}_T^{\mathcal{J}_1+\mathcal{J}_2}) d(\Delta\mathcal{P}_T^{\mathcal{J}_1+\mathcal{J}_2}) = \sqrt{\frac{\pi}{2}}\sigma \tag{3.8}$$

where $\sigma = \sqrt{\sigma_{\mathcal{J}_1}^2 + \sigma_{\mathcal{J}_2}^2}$. As detailed in Appendix C, this method of jet imbalance can easily be extended to arbitrary multi-jet configurations:

$$\langle \not{E}_T^{\text{fake}} \rangle_{N_{\text{jet}}} = \sigma_{N_{\text{jet}}} \sqrt{2} \frac{\Gamma\left(\frac{N_{\text{jet}}+1}{2}\right)}{\Gamma\left(\frac{N_{\text{jet}}}{2}\right)} \tag{3.9}$$

where N_{jet} is the number of jets in the event and $\sigma_{N_{\text{jet}}} = \sqrt{\sum_{j=1}^{N_{\text{jet}}} \sigma_{\text{j}}^2}$ is the root-square-sum of the assumed gaussian spreads associated with each individual jet.

---

[2]While the assumption of gaussian spreads is valid only to a first approximation, non-gaussian effects are less important in this particular context, as the objective is to construct a generator level quantity which correlates with the reconstructed event $\not{E}_T$

(a)

(b)
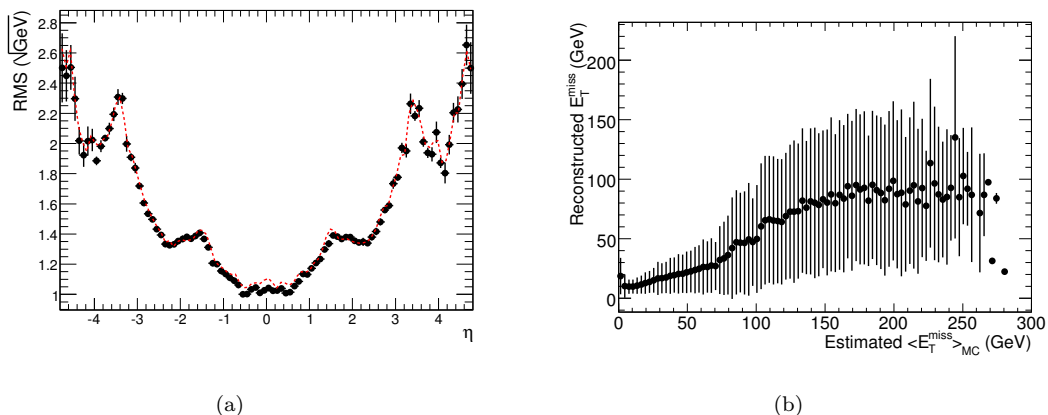
FIGURE 3.2: (a) $\lambda(E)_{RMS}$ versus η_j for fully simulated QCD jets in the kinematic range $35\text{GeV} < p_T < 1120\text{GeV}$. (b) Correlation between estimated $\langle \not{E}_T \rangle$ and reconstructed $\not{E}_T$.

3.4.1 Parametrizing the jet energy resolution

In order to compute the expected $\not{E}_T^{\text{fake}}$ as expressed by Equation 3.9, knowledge of the typical (transverse) energy resolutions σ_j associated with each jet in the event is required. As indicated in Section 1.4.1.2, the resolution $\sigma_j(E, \eta)$ will typically vary with the jet energy and the region of the calorimeters into which the jet constituents shower.

Using Equation 1.21, the jet energy resolution can be expressed in terms of stochastic fluctuations alone:

$$\frac{\sigma(E)}{E} \equiv \frac{a}{\sqrt{E}} \tag{3.10}$$

assuming contributions from other terms are negligible for the hard multi-jet event topologies most likely to generate large $\not{E}_T^{\text{fake}}$. Folding in the jet energy dependence, a significance measure $\lambda(\Delta E)$ for an energy fluctuation $\Delta E = E^{\text{meas}} - E^{\text{true}}$ can now be defined as:

$$\lambda(E) \equiv \frac{E_j^{\text{meas}} - E_j^{\text{true}}}{\sqrt{E_j^{\text{true}}}} \tag{3.11}$$

Figure 3.2(a) shows a profile of $\lambda(E)_{RMS}$ versus η_j derived from fully simulated QCD jets in the kinematic range $35 \text{ GeV} < p_T < 1120 \text{ GeV}$. Regions of the calorimeter with degraded jet energy resolution are clearly visible, *e.g.* the barrel-endcap boundary at $|\eta| \sim 1.4$ as well as the *crack* at $|\eta| \sim 3.2$. Jets directed into these regions are typically measured to lower accuracy and possess a higher probability to fluctuate.

A spline fit to the profile in Figure 3.2(a) allows for a simple parameterization of the jet transverse energy resolution as a function of η_j, which can now be expressed as:

113

$$\sigma_{\mathrm{j}}(E_{\mathrm{j}}, \eta_{\mathrm{j}}) = \lambda(E)_{RMS,\mathrm{j}} \times \sqrt{E_{\mathrm{j}}} \times \sin(\theta_{\mathrm{j}}) \tag{3.12}$$

where $\theta_{\mathrm{j}} = 2 \arctan\left(e^{-\eta_{\mathrm{j}}}\right)$ is the polar angle measured with respect to the beamline.

3.4.2 Expected $\not{E}_T$ versus reconstructed $\not{E}_T$

With an η-dependent parameterization from which the expected jet energy resolutions can be computed individually for each jet in the event, a generator level estimate for the magnitude of the $\not{E}_T$ can be expressed as a (scalar)[3] sum of all real and fake contributions:

$$\langle \not{E}_T \rangle = \sum \not{E}_T(\nu) + \langle \not{E}_T^{\mathrm{fake}} \rangle_{N_{\mathrm{jet}}} \tag{3.13}$$

where $\sum \not{E}_T(\nu)$ indicates a vectorial sum over all neutrino transverse momenta and $\langle \not{E}_T^{\mathrm{fake}} \rangle_{N_{\mathrm{jet}}}$ is given by Equation 3.9.

The resulting correlation between the generator level estimate $\langle \not{E}_T \rangle$ and the actual reconstructed $\not{E}_T$ as computed by the reconstruction algorithm described in Section 3.1, is shown in Figure 3.2(b). Because $\langle \not{E}_T \rangle$ is derived from the mean value of a probability distribution, the estimation method is inherently susceptible to statistical fluctuations. The reconstructed $\not{E}_T$ will therefore often fall low of $\langle \not{E}_T \rangle$. By the same token, events with small $\langle \not{E}_T \rangle$ will occasionally fluctuate to produce large reconstructed $\not{E}_T$. Even so, a correlation between $\langle \not{E}_T \rangle$ and reconstructed $\not{E}_T$ is observed, the predictive power of which enables a rough event categorization.

Figure 3.3 shows the reconstructed $\not{E}_T$ spectrum in simulated QCD dijet events, along with the subset of events flagged as belonging to either of the three categories: *low* ($\langle \not{E}_T \rangle < 50$ GeV), *intermediate* (50 GeV$< \langle \not{E}_T \rangle < 100$ GeV) and *large* ($\langle \not{E}_T \rangle > 100$ GeV).

While the method is susceptible to statistical fluctuations and the reconstructed $\not{E}_T$ will often be smaller than estimated at the generator level, the large majority of events with $\not{E}_T > 100$ GeV are nevertheless seen to be appropriately categorized as *large* by $\langle \not{E}_T \rangle$. Upward fluctuations will push a small fraction of events flagged as *intermediate* into the high tail of the reconstructed $\not{E}_T$ spectrum. Such fluctuations are inherent to the method and can scarcely be avoided. Finally, the tail is seen to contain a few events flagged with a low probability of producing large $\not{E}_T$. These are principally single events originating from low p_T scattering bins and consequently given large scaling weights. The large reconstructed $\not{E}_T$ in these events is likely to derive from other sources than jet fluctuations.

---

[3] A scalar summation, rather than a vectorial summation is employed because the expected fake contribution $\langle \not{E}_T^{\mathrm{fake}} \rangle$ is a scalar quantity determined by way of the mean value of a probability distribution. While a vectorial summation would be more correct, a scalar summation has the additional benefit that events containing hard neutrinos buried in jets are weighted without regard to $\langle \not{E}_T^{\mathrm{fake}} \rangle$, the latter of which may be subject to substantial fluctuations.
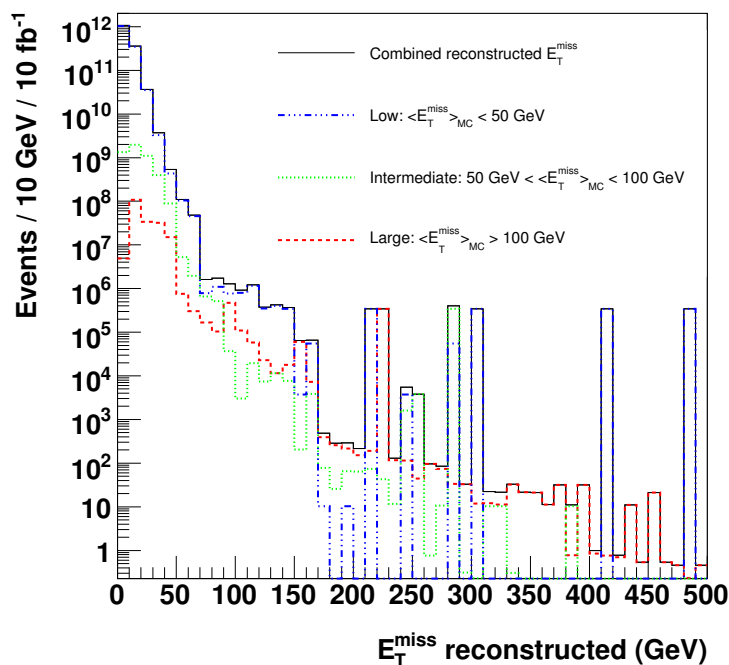
FIGURE 3.3: $\not{E}_T$ spectrum of simulated QCD dijets with subsets flagged with $\langle \not{E}_T \rangle$ *low, intermediate* and *high.*

3.5 The method applied as a generator filter

The ability of the method to correctly flag particle level event configurations prone to yield large reconstructed $\not{E}_T$, may be exploited in a *generator filter*. The application of such a filtering mechanism early in the simulation chain described in Section 1.6 allows for a targeted population of the tail region of the reconstructed $\not{E}_T$-spectrum by preferentially passing only those generated particle level event configurations prone to furnish large reconstructed $\not{E}_T$ through the full GEANT-based simulation. The resulting filtered samples with enhanced tail statistics may then be combined with unfiltered samples to significantly reduce statistical uncertainties across a broader kinematical regime, a feature which in turn facilitates the development of more accurate search strategies for new physics in channels involving large $\not{E}_T$.

3.5.1 Filter rejection and efficiency

The performance of the method when applied as a generator filter may be measured in terms of its ability to:

(A) reject all uninteresting events, thereby reducing the effective cross section as far as possible

(B) retain all events producing large reconstructed $\not{E}_T$

Jn	Total Rejection	Efficiency				
		>80 GeV	>100 GeV	>120 GeV	>150 GeV	>200 GeV
J3	$0.998 \pm < 10^{-4}$	0.3 ± 0.1	0.2 ± 0.1	0.2 ± 0.2	0.3 ± 0.2	0.0 ± 0.0
J4	$0.983 \pm < 10^{-3}$	0.67 ± 0.04	0.67 ± 0.06	0.4 ± 0.1	0.3 ± 0.1	0.1 ± 0.1
J5	0.876 ± 0.004	0.73 ± 0.05	0.81 ± 0.06	0.81 ± 0.07	0.6 ± 0.2	0.0 ± 0.0
J6	0.498 ± 0.003	0.68 ± 0.01	0.76 ± 0.01	0.82 ± 0.02	0.86 ± 0.02	0.89 ± 0.03
J7	0.140 ± 0.002	0.872 ± 0.003	0.875 ± 0.004	0.881 ± 0.005	0.900 ± 0.006	0.925 ± 0.008
J8	$0.004 \pm < 10^{-3}$	$0.996 \pm < 10^{-3}$	$0.996 \pm < 10^{-3}$	$0.996 \pm < 10^{-3}$	$0.996 \pm < 10^{-3}$	$0.996 \pm < 10^{-3}$

TABLE 3.1: Rejections and efficiencies w/ filter threshold at $\langle E_T^{miss} \rangle_{\mathrm{MC}} > 80$ GeV.

Jn	Total Rejection	Efficiency				
		>80 GeV	>100 GeV	>120 GeV	>150 GeV	>200 GeV
J3	$0.999 \pm < 10^{-4}$	0.2 ± 0.1	0.2 ± 0.1	0.2 ± 0.2	0.3 ± 0.2	0.0 ± 0.0
J4	$0.985 \pm < 10^{-3}$	0.58 ± 0.05	0.57 ± 0.07	0.3 ± 0.1	0.2 ± 0.1	0.0 ± 0.0
J5	0.959 ± 0.002	0.66 ± 0.05	0.79 ± 0.06	0.78 ± 0.08	0.6 ± 0.2	0.0 ± 0.0
J6	0.770 ± 0.002	0.49 ± 0.01	0.59 ± 0.02	0.70 ± 0.02	0.77 ± 0.02	0.79 ± 0.03
J7	0.344 ± 0.002	0.688 ± 0.004	0.702 ± 0.005	0.721 ± 0.006	0.758 ± 0.008	0.83 ± 0.01
J8	0.096 ± 0.001	0.906 ± 0.001	0.905 ± 0.002	0.905 ± 0.002	0.903 ± 0.002	0.906 ± 0.003

TABLE 3.2: Rejections and efficiencies w/ filter threshold at $\langle E_T^{miss} \rangle_{\mathrm{MC}} > 100$ GeV.

Jn	Total Rejection	Efficiency				
		>80 GeV	>100 GeV	>120 GeV	>150 GeV	>200 GeV
J3	$0.999 \pm < 10^{-4}$	0.0 ± 0.0	0.0 ± 0.0	0.0 ± 0.0	0.0 ± 0.0	0.0 ± 0.0
J4	$0.998 \pm < 10^{-3}$	0.45 ± 0.05	0.48 ± 0.07	0.25 ± 0.09	0.09 ± 0.09	0.0 ± 0.0
J5	0.985 ± 0.001	0.55 ± 0.05	0.70 ± 0.07	0.78 ± 0.08	0.6 ± 0.2	0.0 ± 0.0
J6	0.909 ± 0.002	0.36 ± 0.01	0.49 ± 0.02	0.61 ± 0.02	0.72 ± 0.02	0.77 ± 0.04
J7	0.594 ± 0.002	0.463 ± 0.005	0.482 ± 0.006	0.510 ± 0.007	0.58 ± 0.01	0.69 ± 0.01
J8	0.242 ± 0.002	0.760 ± 0.002	0.760 ± 0.002	0.761 ± 0.003	0.761 ± 0.003	0.765 ± 0.004

TABLE 3.3: Rejections and efficiencies w/ filter threshold at $\langle E_T^{miss} \rangle_{\mathrm{MC}} > 120$ GeV.
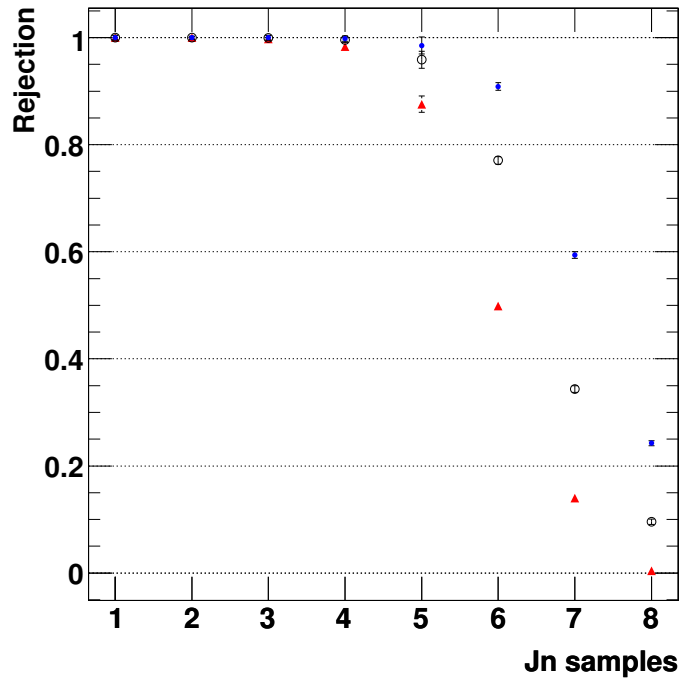
FIGURE 3.4: Filter rejections at three different filter thresholds: $\Lambda_{filter} > 80$ GeV (red, triangles), $\Lambda_{filter} > 100$ GeV (black, open circles) and $\Lambda_{filter} > 120$ GeV (blue, full circles).
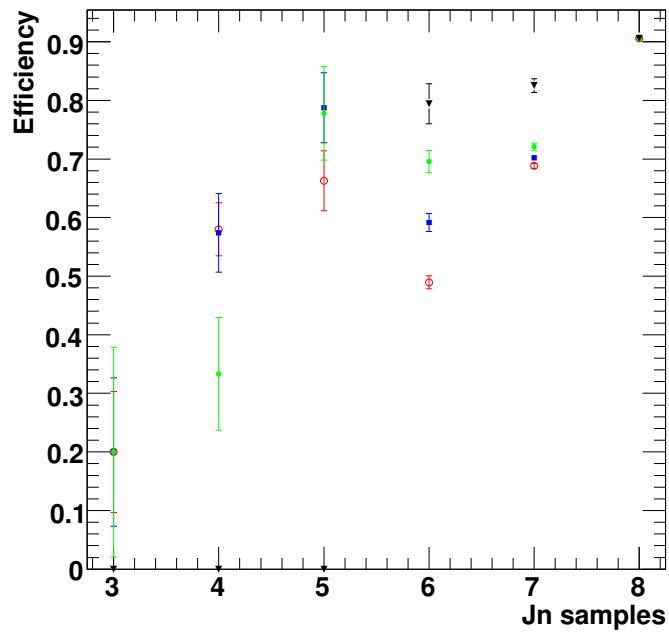

FIGURE 3.5: Filter efficiencies achieved with $\Lambda_{fiter} > 100$ GeV, evaluated at various thresholds of reconstructed $\not{E}_T$: 80 GeV (red, circle), 100 GeV (blue, square), 120 GeV (green, dot) and 200 GeV (black, triangle).

Figure 3.4 shows the total rejections and efficiencies obtained on simulated QCD dijets in various bins of hard scattering p_T, when the method is applied as a generator filter with $\langle {\not}E_T \rangle > \Lambda_{\text{filter}}$.

The *rejection* R_{filter} is herein defined as

$$R_{\text{filter}} = \frac{N_{\text{gen}} - N_{\text{gen}}^{\text{passed}}}{N_{\text{gen}}} \qquad (3.14)$$

where $N_{\text{gen}}^{\text{passed}}$ is the number of events passing the filter from a total of N_{gen} generated events. The accuracy of the filtering procedure is herein measured by the filter *efficiency*:

$$\epsilon_{\text{filter}} = \frac{N_{\text{gen}}^{\text{passed}}({\not}E_T > \Lambda_{\text{filter}})}{N_{\text{gen}}({\not}E_T > \Lambda_{\text{filter}})} \qquad (3.15)$$

where the numerator and denominator indicate the fraction of events with reconstructed ${\not}E_T$ above the filter threshold Λ_{filter}, in the filtered subset and the total sample, respectively.

With a filter threshold of $\Lambda_{\text{filter}} = 100$ GeV, Figure 3.4 indicates that rejections in excess of 90% are achieved in the intermediate bins of hard scattering p_T (140 GeV-560 GeV), consequently reducing the effective cross section by 1-2 orders of magnitude. In the bin beyond (560 GeV$< p_T <$1120 GeV), a rejection of $\sim 75\%$ is achieved, corresponding to a factor 4 reduction in the effective cross section.

The corresponding efficiencies are shown in Figure 3.5, from which efficiencies between 60% - 80% are observed across the central bins 140 GeV $< p_T <$ 1120 GeV. In the case of the upper bin (560 GeV $< p_T <$ 1120 GeV), in which a tail extends well beyond reconstructed ${\not}E_T > 100$ GeV, Table 3.2 indicates that efficiencies of roughly 70% and 80% are obtained above a reconstructed ${\not}E_T$ of 120 GeV and 200 GeV, respectively.

As indicated in Figure 3.3, events with reconstructed ${\not}E_T > 100$ GeV failing filter capture are typically flagged with $\langle {\not}E_T \rangle$ in the intermediate range. A lowering of Λ_{filter} will therefore improve filter efficiencies, albeit at the expense of lower filter rejections. Table 3.1 indicates that a lowering of the filter threshold will impact the efficiency-rejection trade-off in the various bins of hard scattering p_T differently. By way of example, a 15 % efficiency improvement against a marginal 0.2% fall in rejection is achieved in the lower central scattering bin (140 GeV-280 GeV) in the region of reconstructed ${\not}E_T > 100$ GeV by lowering the filter threshold Λ_{filter} from 100 GeV to 80 GeV. In the upper central bin (560 GeV-1120 GeV) by contrast, an efficiency improvement of roughly 30 % is achieved, but only at the cost of a non-negligible 35% reduction in the total rejection. In practical terms, the most appropriate filter threshold Λ_{filter} will therefore depend on the kinematic region of choice and the desired efficiency-rejection trade-off.

(a) 140 GeV $< p_T <$280 GeV

(b) 280 GeV$< p_T <$560 GeV

(c) 560 GeV $< p_T <$1120 GeV
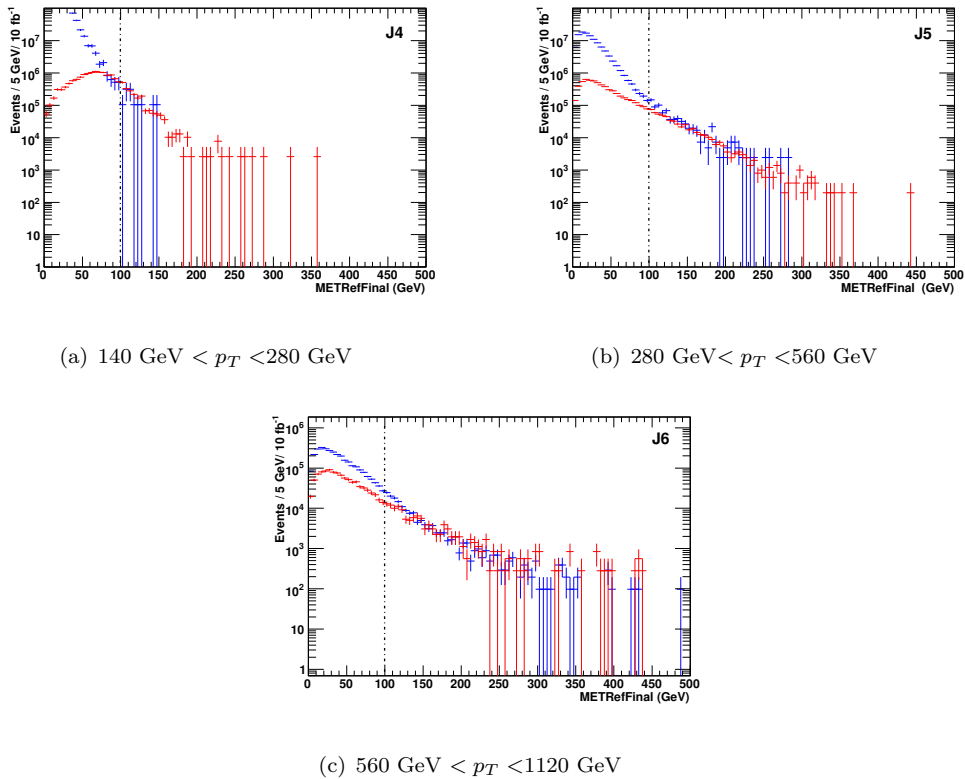
FIGURE 3.6: Reconstructed $\not{E}_T$-spectra in unfiltered (red) and filtered (blue) QCD dijet samples in three different bins of hard scattering p_T.

3.5.2 Filter performance

The technical implementation of the jet imbalance method in the ATLAS software framework ATHENA[77] is described in [78] and will not be detailed further herein. The following sections aim to validate the filter performance using the officially produced fully simulated QCD datasets listed in Appendix A. The filtered samples were produced with a combination of two independent generator filters to provide the composite filtering criteria:

$$N_{jet}(p_T > 40\text{GeV}, |\eta| < 5) \geq 2$$

$$N_{jet}(p_T > 80\text{GeV}, |\eta| < 5) \geq 1$$

$$\langle \not{E}_T \rangle > 100 \text{ GeV}$$

where the latter requirement is determined in accordance with Equation 3.13. Figure 3.6 compares the reconstructed $\not{E}_T$ spectra in both unfiltered and filtered samples in the three central bins of hard scattering p_T. The p_T requirements on the two leading jets were imposed on the unfiltered samples in order to single out the effects of the $\langle \not{E}_T \rangle$ selection. In each case, the filtered samples are seen to populate the tail of the spectra and significantly reduce statistical uncertainties the regions of large reconstructed $\not{E}_T$.

(a) No cuts

(b) SUSY cuts
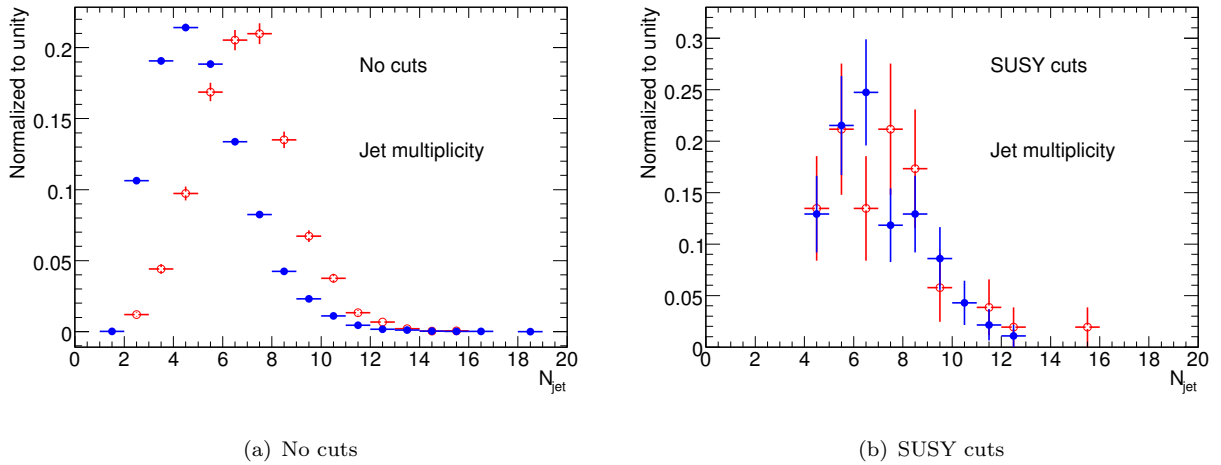
FIGURE 3.7: A comparison of the jet multiplicity in events from J5 (280 GeV$< p_T <$560 GeV) with reconstructed $\not{E}_T>$100 GeV, in unfiltered (blue, solid circle) and in filtered (red, empty circle) samples. In (a) no additional selection cuts are applied, in (b) typical SUSY selection cuts are applied.

3.5.3 Event kinematics in filtered events

The reconstructed event kinematics in filtered and unfiltered samples will naturally differ. With no further selection cuts applied, events from filtered samples with reconstructed $\not{E}_T > 100$ GeV will tend towards higher jet multiplicities and harder jet transverse momenta, as shown in Figure 3.7(a), as such event configurations are more likely to exhibit a greater degree of imbalance and hence produce larger $\not{E}_T^{\text{fake}}$ estimates.

Differences in event kinematics should however be duly considered within the context of the analysis in which the filtered samples are applied. Any differing behaviour in filtered events that are rejected by the basic selection criteria of the online trigger or offline selection is clearly of no consequence for the remaining analysis.

In order to compare unfiltered and filtered events within the context of a generic ATLAS inclusive supersymmetry search, the following selection was applied to both unfiltered and filtered samples [79]:

$\not{E}_T > 100$ GeV and $N_{jet} \geq 4$

$p_T^{\text{jet }1} > 100$ GeV and $p_T^{\text{jet }2,3,4} > 50$ GeV

transverse sphericity S_T[4] > 0.2

lepton veto

---

[4]The transverse sphericity $S_T \equiv \frac{2\lambda_2}{\lambda_1+\lambda_2}$ is defined in terms of the eigenvalues λ_1, λ_2 of the transverse sphericity tensor $S_{x,y} = \begin{pmatrix} p_x^{(i)} p_x^{(i)} & p_x^{(i)} p_y^{(i)} \\ p_x^{(i)} p_y^{(i)} & p_y^{(i)} p_y^{(i)} \end{pmatrix}$
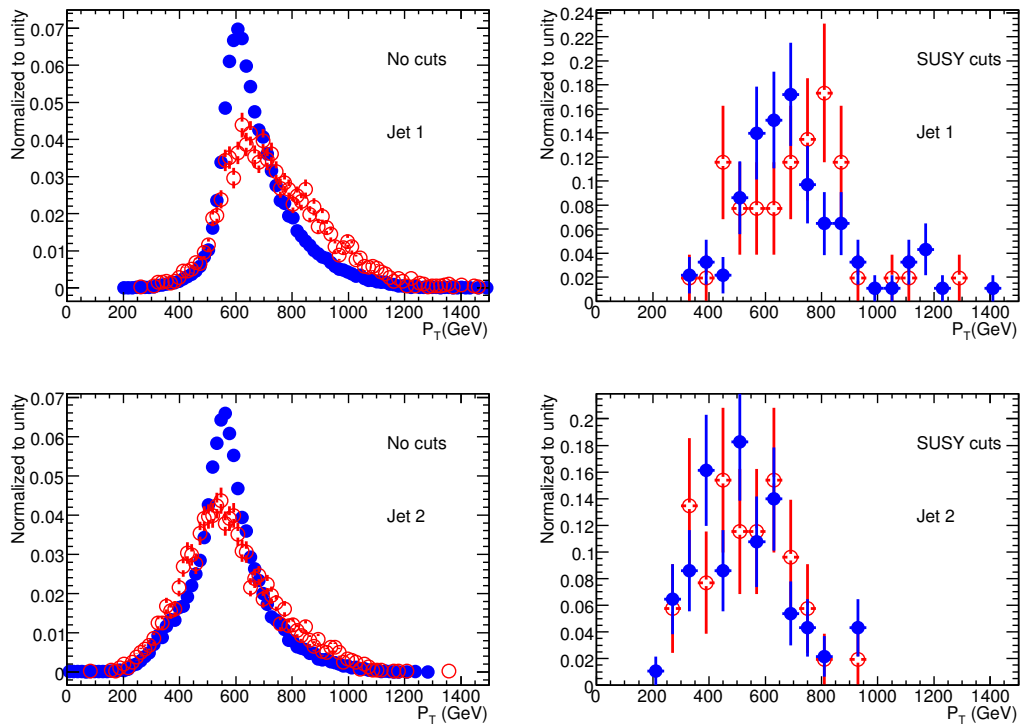
FIGURE 3.8: Transverse momentum spectra of the two leading jets in events from J5 (280 GeV$< p_T <$560 GeV) with reconstructed $\not{E}_T >$ 100 GeV, in unfiltered (blue, solid circle) and in filtered (red, empty circle) samples. Left: no additional cuts applied. Right: typical SUSY selection cuts applied.

Figures 3.7(b) and 3.8 indicate that the tendency towards higher jet multiplicities and larger transverse momenta is largely alleviated by the above selection. It was also found that events which were wrongfully rejected by the filtering method would also tend to fail the above selection cuts [78].

3.6 Summary

Proper understanding of event $\not{E}_T$ is crucial for the discovery of many new physics scenarios at the LHC. As a particular case in point, R-parity conserving supersymmetry scenarios are typically characterised by large $\not{E}_T$ signatures, making proper control of all backgrounds faking large $\not{E}_T$ an important prerequisite for discovery. In this context, fluctuating QCD jets pose a particular challenge, one further aggravated by very large cross sections.

This chapter introduced a probabilistic method to attain a *generator level* estimate of instrumental contributions to reconstructed $\not{E}_T$ originating from jet fluctuations in the calorimeters. The method accounts for detector resolution effects through a parametrization derived from fully simulated data. The estimated fake contributions are then combined with the true $\not{E}_T$ from non-interacting particles to yield an estimate for the total expected $\not{E}_T$ in the event.
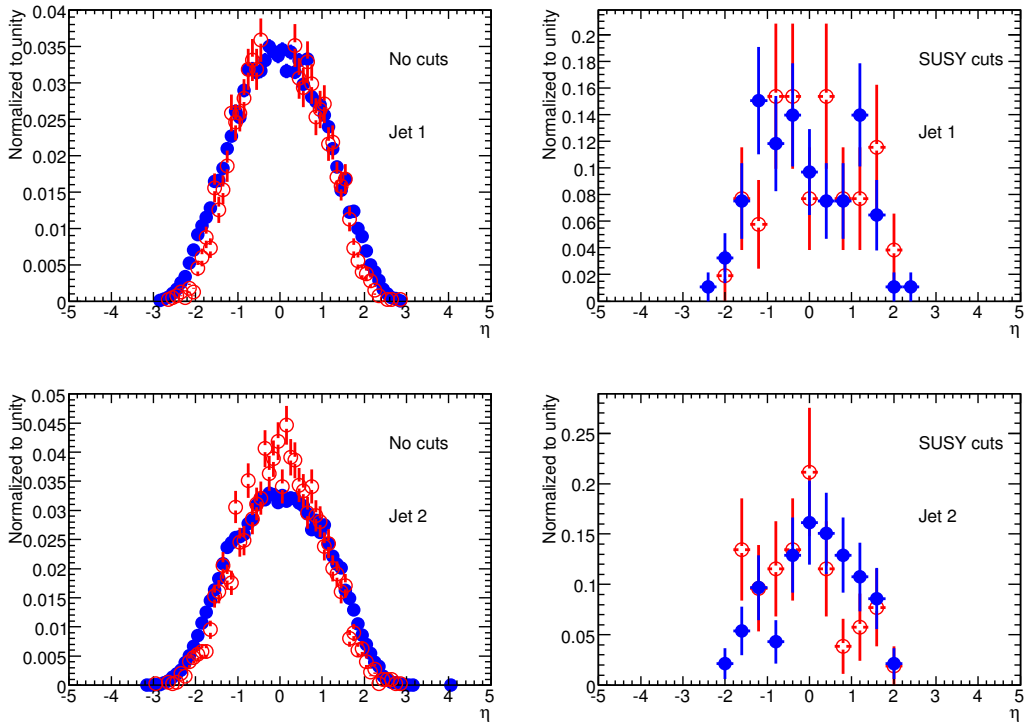
FIGURE 3.9: Pseudorapidity spectra of the two leading jets in events from J5 (280 GeV$< p_T <$560 GeV) with reconstructed $\not{E}_T >$100 GeV, in unfiltered (blue, solid circle) and in filtered (red, empty circle) samples. Left: no additional cuts applied. Right: typical SUSY selection cuts applied.

The method successfully flags the large majority of QCD events with large reconstructed $\not{E}_T$ at the generator level. When applied as a generator filter, significant rejections against small reconstructed $\not{E}_T$ events are achieved, whilst retaining the bulk of events with *large* reconstructed $\not{E}_T$. Filtered samples are found to populate the tail regions of the reconstructed $\not{E}_T$ spectrum and significantly reduce statistical uncertainties in the high end of the spectrum. Filter biases are in turn largely mitigated by generic supersymmetry selection criteria. The method thus presents a tenable strategy for boosting statistics of fully simulated QCD events with large fluctuation induced contributions to fake $\not{E}_T$.

Chapter 4

Photon-induced exclusive tau final states in early data

The mechanism by which colliding protons interact through the exchange of virtual photons arising from their electromagnetic fields, is discussed in Section 1.3.4.

An interesting subset of this class of events is the exchange exemplified in Figure 4.1, wherein the scattered protons emit virtual photons which in turn interact by way of a fermionic line of leptons. The emitted lepton pair may consist of either a pair of electrons, muons or tau leptons. Such exclusive production of like-flavour leptons is particularly attractive in the context of the LHC because of their remarkably *clean event topologies*, which set them aside from generic hadronic interactions. Insofar that the proton form factors are well understood, the elastic scatter depicted in Figure 4.1(a) may be regarded as an almost pure QED process with small associated theoretical uncertainties.

While theoretically similar, the experimental challenges associated with the detection of either lepton channel differ appreciably. Compared to exchanges involving light flavoured leptons, the short lived nature of τ-leptons makes the process $\gamma\gamma \to \tau\tau$ considerably more challenging to identify in the predominantly hadronic environment of the LHC.

(a) Elastic scatter   (b) Semi-elastic scatter

FIGURE 4.1: Exclusive di-lepton production via t-channel photon exchange. The scattered protons undergo a light forward d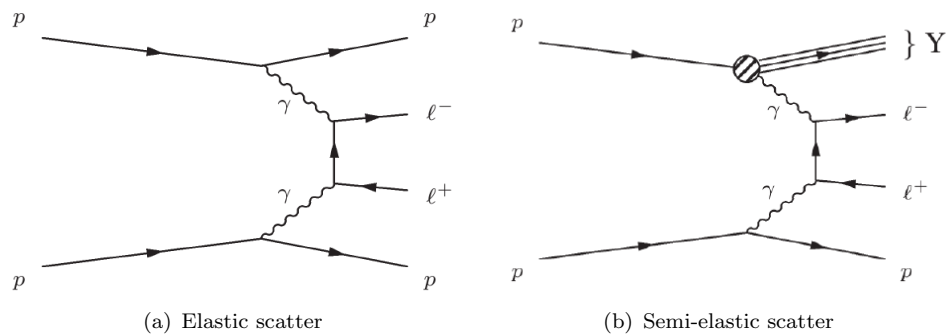eflection. Fully elastic scatters leave the protons intact. Inelastic scatters cause the protons to (excite and) dissociate.

In the following, a simulation study is presented which aims to evaluate the feasibility of detecting photon induced di-lepton final states during the early phase of ATLAS operation. After a brief introduction to two-photon physics at the LHC, an overview of expected cross sections and event kinematics as predicted by Monte Carlo simulation tools is provided. This is followed by a discussion of the experimental challenges which serve to complicate an offline selection alongside any assumptions made in the analysis. It is shown, that a common challenge in all three channels (e, μ, τ) is ineffective triggering. To this end a dedicated trigger strategy has been developed and implemented which offers early sensitivity to generic exclusive lepton final states. Drawing on these dedicated triggers, the offline selection potential in the experimentally most challenging process $\gamma\gamma \to \tau\tau$ is evaluated and results summarized for an integrated luminosity corresponding to 100 pb^{-1}.

4.0.1 Two-photon physics at other collider facilities

Exclusive di-lepton production as per mechanisms equivalent to those depicted in Figure 4.1, have been observed and studied by experiments at various other collider facilities in the past. These include the *electron-positron* collider LEP, the *electron-proton* collider HERA and more recently also the the *heavy ion* collider RHIC, as well as the *proton-antiproton* collider TEVATRON. Their continued study at a *proton-proton* collider such as the LHC is therefore warranted as a natural extension of a long existing programme.

The observation of photon induced lepton final states long remained elusive in hadron-hadron collisions. The production cross sections at early hadron colliders such as CERN's ISR (*proton-proton*) and S$p\bar{p}$S (*proton-antiproton*), were too minute for potential detection. A recent observation (2006) of exclusive di-leptons by the CDF(II) experiment at TEVATRON ($\sqrt{s} = 1.96$ TeV), therefore marked the first of its kind at a hadron collider facility. The experiment measured a cross section of $\sigma_{\text{excl ee}}^{E_T>5\text{GeV},|\eta|<2} = 1.6^{+0.5}_{-0.3}(\text{stat}) \pm 0.3(\text{sys})$ pb, corresponding to 16 exclusive e^+e^- candidates over a background expectation of 1.9 ± 0.3 events at an integrated luminosity of 532 pb^{-1}, where both cross section and kinematic distributions were found to agree well with theoretical predictions [80].

This measurement confirms the observability of two-photon interactions in hadron collider environments at TeV energies and partially warrants studies into applications at the LHC where production rates are expected to increase significantly.

While the process $\gamma\gamma \to \tau\tau$ has been observed and studied at LEP [81] and HERA [82], its observation remain elusive at hadron colliders at the time of writing. An observation of this process at the LHC would therefore potentially be the first of its kind at a hadron collider.

4.0.2 Early two-photon physics at the LHC

As a sizable fraction of pp collisions at the LHC will involve photon exchange interactions, the LHC may to some extent be considered both a $\gamma\gamma$ and a γp collider. As discussed

in Section 1.3.4, photon exchange interactions at the LHC are unique in that they may occur at energies in excess of the electroweak scale, thereby opening for searches and measurements of new physics coupling to photons [83]. While the effective luminosity of such collisions is relatively modest, the reward is better understood initial conditions and remarkably clean event topologies. This is especially true of elastic two-photon processes and consequently studies into their physics potential is currently receiving renewed attention.

All flavours of the process $\gamma\gamma \to ll$ will arguably form important control samples for searches for new physics by exclusive production mechanism. In addition, various proposals have been made for possible applications of photon induced dilepton processes at the LHC. These include:

- **Lepton reconstruction studies:** the absence of hadronic debris provides a unique setting in which to investigate the lepton reconstruction performance at low energies.

- **Absolute luminosity measurements:** the relatively large and well known cross section ($\mathcal{O}(1\%)$) of the process $\gamma\gamma \to \mu\mu$, makes it an intriguing candidate for absolute luminosity measurements at the LHC [26, 84–86]. This is particularly true in the early phase of operation when the machine luminosity is low and pile-up effects negligible. (In principle, the process $\gamma\gamma \to ee$ could be applied to the same ends, however the comparative ease with which soft muons can be identified renders the muon channel more favourable to this end).

- **Calibration of very forward detector systems:** from a measurement of the pseudorapidities and invariant mass of the dilepton system, the interacting photon energies can be estimated in the colinear approximation. Such a measurement is tantamount to an estimation of the proton energy loss $\frac{E_\gamma}{E_{\text{proton}}}$, which in turn can be used to calibrate and align very forward detector systems such as those described in Section 1.4.2.5 [87][26].

The range of applications available with exclusive di-tau processes naturally depends on the success with which such events can be selected at the LHC. While theoretically similar to the light flavour lepton channels, this process differs considerably in terms of its experimental detection and measurement. Tau leptons decay as detailed in Chapter 2, leaving neutrinos in their wake which alter the kinematic balance of the di-tau system. The escaping neutrinos also serve to reduce the effective cross section for τ-leptons in the detectable kinematic range, a challenge further compounded by the predominantly hadronic decay modi of the τ, making it harder to set apart in the hadronic environment of the LHC.

The detection of the process $\gamma\gamma \to \tau\tau$ is therefore in many ways a considerable experimental challenge in itself, and a confirmation of this process in early LHC data would not only be an important confirmation of Standard Model physics, but also serve as a vindication of the experimental capabilities of the ATLAS detector (potentially paving the way for more exotic searches in exclusive channels).

The striking simplicity of these events set them apart in an LHC context and may compensate for comparatively modest cross sections. For early τ-lepton reconstruction studies, this may prove to be an important supplement to more standard processes such as $Z(+\text{jets}) \to \tau\tau$ and $W(+\text{jets}) \to \tau\nu_\tau$. While such processes arguably enjoy higher production rates and well constrained kinematics, their event topologies are more involved and complex by comparison. Moreover, as discussed in Section 1.3 their production cross sections and kinematics are subject to uncertainties in both *non-perturbative* QCD effects and in the *parton distribution functions* of the colliding protons. The presence of additional jets (V+ jets), further necessitates a dependence on a proper understanding of the *jet energy scale* [32].

The almost pure QED nature of exclusive di-lepton processes make them relatively immune to the uncertainties of QCD induced physics. As such they may prove a useful complement to existing validation processes, such as gauge boson production. Because the cross section is strongly peaked at low values of lepton transverse momentum, the process $\gamma\gamma \to \tau\tau$ gives complementary access to a kinematic domain otherwise only available in the tails of the transverse momentum spectra of leptonic decays of heavy gauge bosons. Two-photon processes therefore offer an opportunity to collect a strikingly clean sample of τ-candidate around the sensitivity threshold of current τ-lepton reconstruction and identification tools in ATLAS. Such a sample may be used to shed light on the performance of the tau reconstruction in the extreme low-energy regime, an insight that may prove valuable in searches for new physics, such as *e.g.* certain SUSY searches where the presence of very low energetic τ-leptons is prolific and an efficient reconstruction and identification critical for the measurement of model parameters [52]

The cleanliness of exclusive events may potentially also make them attractive for studies into tau *substructure identification performance* in current reconstruction algorithms and provide a unique testbed for new and improved identification techniques. An overlay with a QCD rich sample may help uncover effects of the underlying event in a controlled manner.

4.1 Monte Carlo simulations and event characteristics

4.1.1 Monte Carlo simulations

All simulations of the exclusive two-photon process $\gamma\gamma \to ll$ employed in this study were performed with the event generator LPAIR [88, 89]. LPAIR performs a *leading order* Matrix Element calculation of the process $\gamma\gamma \to ll$. The production cross section is then computed as a convolution of the virtual photon fluxes and the cross section derived from the matrix element calculation. LPAIR will also correctly account for the changing kinematics of the di-lepton system expected in highly virtual photon exchanges. Elastic, semi-elastic and fully inelastic scatters simulated by LPAIR therefore yield different kinematic spectra. The hadronisation of the dissociated protons is not handled by LPAIR, and consequently not treated herein. The implications of this omission is further discussed in Section 4.2.2.

Further details pertaining to all simulated samples are given in Appendix B.3.

4.1.2 Expected cross sections

Process	σ_{tot} (pb)	
	$\sqrt{s} =$7 TeV	$\sqrt{s} =$14 TeV
$\gamma\gamma \to ee$ (pb)	5.48×10^9	7.05×10^9
$\gamma\gamma \to \mu\mu$ (pb)	114×10^3	147×10^3
$\gamma\gamma \to \tau\tau$ (pb)	154	220

TABLE 4.1: A comparison of total elastic scattering cross sections for the process $\gamma\gamma \to ll$ with $l = e, \mu, \tau$ at $\sqrt{s} = 7$ TeV and $\sqrt{s} =$14 TeV.

$p_T^{\tau_{1,2}}$ (GeV)	σ_{elastic} (pb)		$\sigma_{\text{semi-elastic}}$ (pb)		$\sigma_{\text{inelastic}}$ (pb)	
	7 TeV	14 TeV	7 TeV	14 TeV	7 TeV	14 TeV
≥ 0	53.3	68.0	37.7	48.1	28.7	36.5
≥ 5	4.28	5.87	3.75	5.10	3.97	5.41
≥ 10	0.811	1.16	0.849	1.23	1.03	1.50
≥ 15	0.284	0.426	0.331	0.502	0.435	0.662
≥ 20	0.132	0.213	0.166	0.260	0.228	0.360

TABLE 4.2: Elastic, semi-elastic and inelastic contributions to the total cross section for the process $\gamma\gamma \to \tau\tau$ for various cuts on the transverse momentum of the outgoing τ-leptons at $\sqrt{s} = 7$ TeV and $\sqrt{s} =$14 TeV. In all cases, both τ-leptons are required to be scattered within $|\eta| < 2.5$.

Table 4.1 compares expected total cross sections for the elastic scatter $\gamma\gamma \to ll$ at two prospective collision energies at the LHC. The table indicates that the total cross section for $\gamma\gamma \to \tau\tau$ is orders of magnitude smaller than the cross sections for light flavour leptons.

Elastic, semi-elastic and fully inelastic contributions to the cross section of the process $\gamma\gamma \to \tau\tau$ are separately tabulated in Table 4.2 for various cuts on the transverse momenta of the outgoing τ-pair. Both τ-leptons are required to be scattered within $|\eta| < 2.5$, reflecting the sensitivity reach of the inner detector tracker and consequently the reach of the offline tau reconstruction algorithms[1]. A sharp drop in the cross section with increasing lepton transverse momenta is observed. While this dependence is a generic feature of the photon induced processes, it is particularly injurious in the τ-channel where the partial decay into neutrinos will serve to reduce the visible cross section even further.

Figure 4.2(a) shows the normalized cross sections of the scatter $\gamma\gamma \to \tau^\pm\tau^\mp$ as a function of both the transverse momenta and the visible transverse momenta of the outgoing τ-leptons.

---

[1]Restricting the central lepton pair to $|\eta| < 2.5$ will significantly reduce the cross section at low transverse momenta, but will only have a marginal impact on the cross section at higher lepton transverse momenta to which the trigger and offline reconstruction is likely to be sensitive.

(a) $p_T(\tau)$ (GeV)

(b) $p_T^{vis}(\tau)$
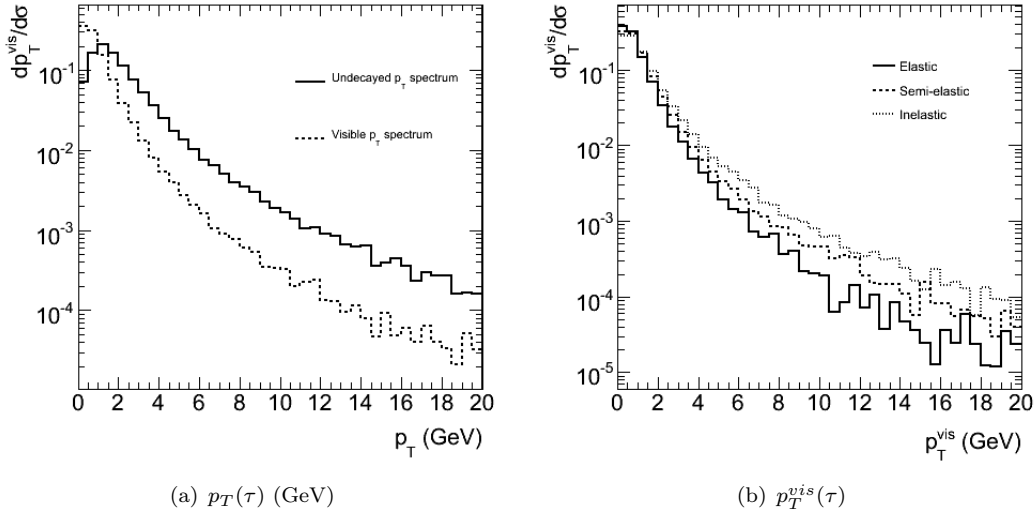
FIGURE 4.2: Transverse momentum spectra. (Two entries per event).

(a) $\Delta p_T(\tau\tau)$ (GeV)

(b) $\Delta\phi_{vis}(\tau\tau)$
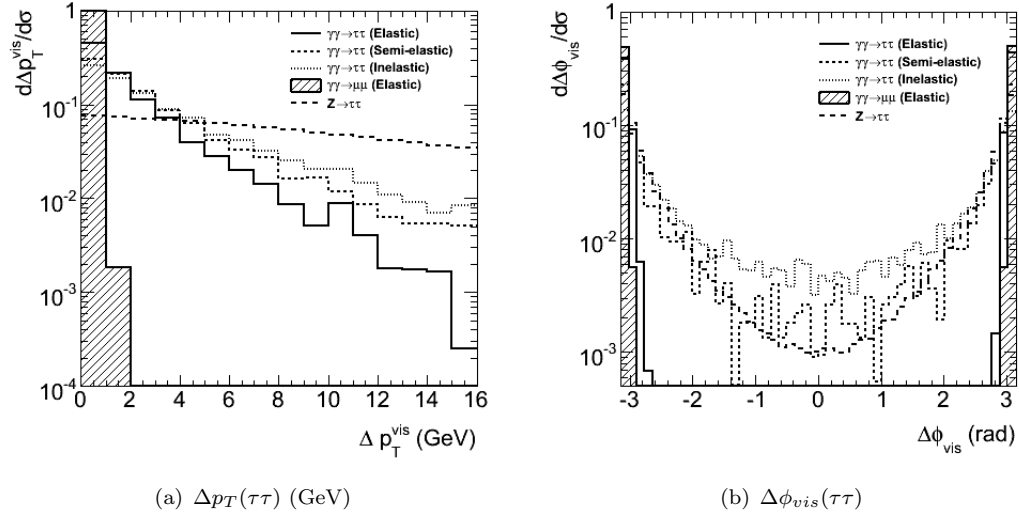
FIGURE 4.3: Kinematic balance of the central lepton system. (Two entries per event).

While the absolute *semi-elastic* and *inelastic* scattering contributions to the total cross section are somewhat smaller than the *elastic* contribution, they are expected to dominate at higher lepton transverse momenta, as seen in Figure 4.2(b).

At $\sqrt{s} = 7$ TeV, the combined cross section of all scattering contributions satisfying $p_T(\tau) > 10$ GeV and $|\eta(\tau)| < 2.5$ is seen to total ~ 2.7 pb. Neglecting the limited efficiencies of the online and offline selections, a maximum total ~ 270 events may be collected with 100 pb^{-1} of integrated luminosity. An observation of the process $\gamma\gamma \to \tau\tau$ in early data is therefore very challenging. By comparison, the processes $\gamma\gamma \to ee$ (p_T(e) >5 GeV) and $\gamma\gamma \to \mu\mu$ ($p_T(\mu)$ >4 GeV) enjoy total cross sections of ~ 13 pb and ~ 21 pb respectively, indicating that a few thousand events may be collected with 100 pb^{-1} of data.

4.1.3   Event kinematics

The kinematics of exclusive di-lepton events are characterized by a well balanced di-lepton system, both in transverse momentum ($\Delta p_T(l^\pm, l^\mp)$) and acoplanarity ($\Delta\phi(l^+, l^-)$). Figure 4.3 compares the balance of the *visible* di-tau system with that of an exclusive di-muon system in both of these quantities. The decay of either τ-lepton is seen to distort the *a priori* perfect balance in the di-tau system, as is reflected in the broadening of the Δp_T^{vis} and $\Delta\phi^{vis}$ spectra. Even so, the absence of additional gluon radiation is seen to furnish a comparatively well balanced visible di-tau system when contrasted with the balance in $Z \to \tau\tau$. Despite a relative deterioration when compared to the light flavour lepton channels, the balance of the visible di-tau system will therefore still prove to be a useful characteristic to exploit in the offline event selection.

4.2   A note on the experimental challenges and assumptions made

4.2.1   Event reconstruction and background suppression

At the very onset, the observation of the process $\gamma\gamma \to \tau\tau$ appears more challenging to detect than its light flavour counterparts. For one, the soft nature of the scattered leptons in photon induced processes is more damaging in the τ-channel, because the sensitivity reach of the reconstruction and identification of τ-leptons typically does not extend to such low values of transverse momentum as is the case for $e^\pm$ and $\mu^\pm$. The problem is further exacerbated by the decay into neutrinos which reduces the fraction of the total τ-momentum available for experimental detection and distorts the balance in the di-tau system. Because both online and offline τ-reconstruction tools are most sensitive to the higher end of the di-tau transverse momentum spectrum, any search will necessarily be susceptible to the theoretical uncertainties in the cross sections of *semi-elastic* and *inelastic* scatters.

The challenges of the τ-channel must also be viewed in light of the experimental climate of the LHC. Since the rate at which strong interactions occur far exceeds that of photon interactions, an accurate and efficient *identification mechanism* is essential to extract signal events from the overwhelming number of background events prone to mimic the signal signatures. Because both τ-leptons are very likely to decay hadronically, the signal will mostly appear strikingly similar to more prolific QCD-induced exclusive jet processes. Other potential backgrounds are discussed in Section 4.5.

4.2.2   Rapidity gaps and proton dissociation

A hallmark of exclusive two-photon events is the absence of activity to either side of the central system. Such an empty region of the detector will hence be referred to as a *large rapidity gap*. Exclusive elastic scatters should therefore always contain two large rapidity

(a)   (b)
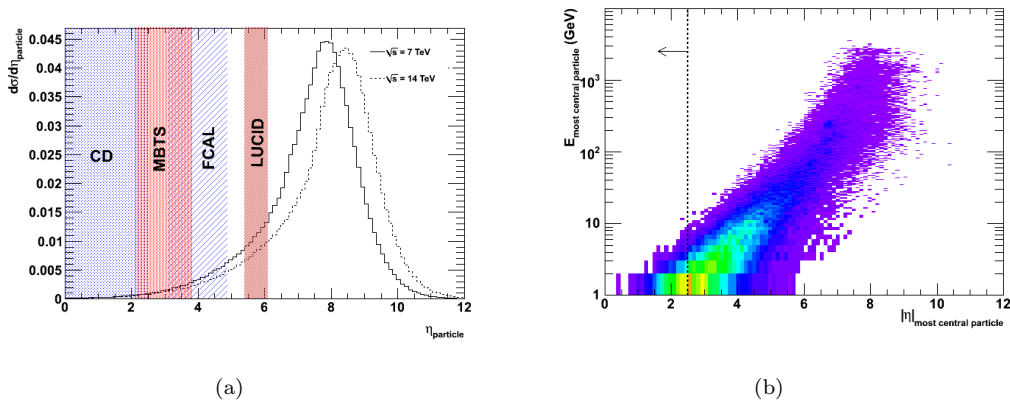
FIGURE 4.4: (a) The $|\eta|$-spectrum of forward scattered debris in semi-elastic $\gamma\gamma$ inter-actions. (b) The $|\eta|$ versus energy of the most central proton dissociation product in a $\sqrt{s} = 7$ TeV semi-elastic scatter.

gaps, a feature which stands in stark contrast to events where the hard scatter breaks the proton apart and sends the proton remnant into the forward region of the central detector. Properly identified rapidity gaps, are therefore powerful tools to suppress the bulk of hadronic interactions. A robust identification in turn rests on proper control of all physical and instrumental effects that may destroy the rapidity gaps.

Highly virtual photon emissions may excite the photon emitting proton and cause it to dissociate. Table 4.2 indicates that scatters involving τ-leptons with $p_T > 10$ GeV typically involve proton dissociation and consequently a non-zero probability that the rapidity gap is polluted by remnants of the dissociative system. However, because $\sqrt{s}_{\gamma\gamma} \ll \sqrt{s}_{pp}$ the dissociative system carries a large forward boost and will most likely escape undetected through the beam pipe. While proton debris might well appear in the very forward detector systems, the rapidity gaps in the central detector maintain a high probability of remaining intact. This is confirmed by the spectrum in Figure 4.4(a) in which the $|\eta|$-distribution of proton debris particles in semi-elastic $\gamma\gamma$-scatters is shown, as predicted by the MBR Monte Carlo [90][2]. The probability of rapidity gaps remain-ing intact in face of proton dissociation is seen to be very large. It is also noteworthy that debris particles scattered into the central detector region are very unlikely to have energies in excess of a few GeV, as indicated by Figure 4.4(b).

For this reason, this analysis assumes that the dissociative system in *semi-elastic* and *inelastic* scatters is *always* deflected at such small angles with respect to the beam pipe, that rapidity gaps are preserved and the events in the central detector appear indistinguishable from *elastic* scatters.

---

[2]The dissociation kinematics are provided by the `fragment_cluster` function of the *Minimum Bias Rockefeller* (MBR) Monte Carlo, in which the proton is fragmented into pions based on the kinematic input from LPAIR. The pions are then boosted back to the laboratory frame. I am indebted to A. Hamilton for providing the necessary code fragments.

4.2.3 Event pile-up

As discussed in Section 1.3.6, nominal luminosity running will see each hard scatter accompanied by several additional scatters taking place between other protons in the same bunch crossing. This effect is known as *event pile-up* and will typically result in several additional tracks and calorimeter hits in the central detector that bare no relation to the exclusive signal. Pile-up events are therefore potentially devastating to a search for exclusive photon induced processes, because the probability that rapidity gaps survive in the presence of pile-up is low. However, as discussed in Section 1.3.6, event pile-up in the early phases of LHC running is expected to be small. Consequently, pile-up effects will be neglected in this analysis. The challenge will therefore be to observe a signal and collect as large a sample as possible with low-luminosity data where pile-up effects are negligible.

4.2.4 Proton tagging with forward detectors

A commonly proposed method of dicerning exclusive photon interactions involves the use of *forward proton tagging*, where an attempt is made to identify the photon emitting protons in the very forward detector systems. Following the elastic emission of a photon, the unbroken proton is only lightly deflected and exits the central detector through the beam pipe along with the spectator protons of the beam. However, the slight loss in energy following the photon emission results in a larger deflection in the beam magnetic field and facilities a detection in near-beam detectors positioned at a large distance from the interaction point. While such techniques provide a potent means of tagging two-photon interaction processes even in the face of pile-up, the proton tagging devices discussed in Section 1.4.2.5 will not be available during early LHC operation. They will therefore not be considered in this study.

4.2.5 Trigger

Finally, an event is not available for offline selection if it does not pass the ATLAS L1 and HLT triggers. The enormous rates at which soft QCD interactions occur at the LHC severely restricts the extent to which ATLAS can afford to trigger on hadronic objects with low transverse momenta. Low energetic hadronically decaying τ-leptons can therefore only be triggered in conjunction with large prescales[3] which serve to keep trigger rates within required limits. Large prescales however, do not allow for efficient triggering on relatively *rare* processes such as $\gamma\gamma \to ll$. A central challenge for this analysis, and a prerequisite for an observation of the process $\gamma\gamma \to \tau\tau$ in early data, is therefore to find an efficient means of triggering on the signal at minimal cost to the overall trigger rate.

---

[3]Prescales are introduced as a means of reducing the number of events passing a given trigger chain. The *prescale factor* dictates the rate at which events satisfying the trigger criteria will be accepted. A prescale factor of 1000 signifies that only 1 in 1000 events satisfying the trigger criteria will be accepted. Prescales with different factors can be applied at all levels of the trigger chain.

4.3 The online selection of exclusive lepton final states

As explained in Section 1.5, any collision event is required to pass both the L1 trigger *and* the HLT triggers before the recorded data are made available for more detailed offline analysis. The soft nature of photon-induced di-lepton final states makes them particularly challenging processes to trigger on. As discussed in Chapter 2, this is especially true of the process $\gamma\gamma \to \tau_{\mathrm{had}}\tau_{\mathrm{had}}$, because hadronically decaying taus often leave more ambiguous and complicated signatures in the detector. The need to make a rapid decision on the basis of the comparatively crude information available will necessarily limit the ability of the L1 trigger to recognise tau signatures, a challenge further compounded by the necessity of keeping the enormous background rates within tolerable limits. At low transverse momenta, these challenges are typically met by either *raising the threshold* on the trigger objects or by applying suitable *prescale factors* to the trigger decision or indeed a combination of both. As is explained below, both strategies are detrimental to the efficiency of triggering on the signal, which is characterised by a comparatively modest cross-section falling quickly with the p_T of the outgoing lepton pair.

In the following, the shortcomings of default trigger chains in ATLAS with the respect to the process $\gamma\gamma \to ll$ are discussed, before a dedicated trigger strategy is developed which aims to target lepton final states from *all* exclusive sources.

4.3.1 Prospects with default triggers

While the ATLAS trigger chains are designed to retain sensitivity to a variety of different final states at a range of different energy scales, they typically target particle objects at higher transverse momenta than is characteristic of photon induced processes. The relatively high thresholds on the lowest energy leptons triggers is indicative of this fact.

Table 4.3 lists the lowest threshold lepton trigger chains available in the first draft trigger menu designed for deployment at $\mathcal{L} \sim 10^{31}\mathrm{cm}^{-2}\mathrm{s}^{-1}$ along with projected prescales. It also lists the efficiencies of these chains on various $\gamma\gamma \to ll$ processes with respect to the minimal offline selection criterion that leptons of the appropriate flavour as defined in Section 4.4 be reconstructed[4].

It should be noted that the ATLAS trigger menus are in flux and are continuously modified to best meet the needs of the collaboration in a given luminosity scenario provided by the LHC machine. In particular, early running at instantaneous luminosities $< 10^{31}\mathrm{cm}^{-2}\mathrm{s}^{-1}$ may well see ATLAS operate with lower prescales than reported herein. The configurations detailed in the following are all based on the draft menu for operation at $10^{31}\mathrm{cm}^{-2}\mathrm{s}^{-1}$ [32][91] which were valid at the time when the studies presented herein were conducted.

---

[4]In the tau channel, only one hadronic tau candidate is required. In the electron (muon) channel, two reconstructed electrons (muons) are required.

Lepton flavour	Signature	L1 item	Prescales (L1-L2-EF)	Efficiency
				$\epsilon\,(\gamma\gamma \to \tau_{\mathrm{had}}\tau_{\mathrm{had}})$
	tauNoCut	L1_TAU5	10000000-1-1	60%
Taus	tau12_loose	L1_TAU6	1-10-750	13%
	tau16_loose	L1_TAU9	1-600-1	9%
				$\epsilon\,(\gamma\gamma \to ee)$
	e5_medium	L1_EM3	60-1-1	82%
Electrons	e10_medium	L1_EM7	1-1-1	18%
	2e5_medium	L1_2EM3	1-1-1	43%
				$\epsilon\,(\gamma\gamma \to \mu\mu)$
	mu4	L1_MU4	1-5-300	84%
Muons	mu6	L1_MU6	1-1-30	38%
	2mu4	L1_2MU4	1-1-1	45%
	mu4_mu6	L1_2MU4_MU6	1-1-1	28%

TABLE 4.3: Lowest threshold lepton triggers for operation at $\mathcal{L} \sim 10^{31}\mathrm{cm}^{-2}\mathrm{s}^{-1}$ with their (unprescaled) efficiencies on $\gamma\gamma \to ll$. A minimal object selection as defined in Section 4.4 is applied to offline reconstructed leptons. The samples satisfy the generator selections: $p_T(\tau_{had})>10$ GeV, $p_T(e) > 5$ GeV and $p_T(\mu) > 4$ GeV.

Taus

As indicated by Table 4.3, the lowest threshold tau triggers are all assigned high prescales rendering them unsuitable for triggering on $\gamma\gamma \to \tau_{\mathrm{had}}\tau_{\mathrm{had}}$. Prescales aside, the thresholds are seen to be too high to secure an efficient signal event collection. The limited efficiency of even the fully inclusive chain `tauNoCut` is a reflection of the limited sensitivity reach of the ATLAS L1 tau triggers in the softest end of the tau p_T-spectrum.

Electrons

In contrast to hadronically decaying taus, electrons are by comparison easier to trigger on. This is reflected in the comparatively high efficiency of the lowest threshold trigger chain `e5_medium`. A low threshold, however, necessitates the application of a sizable prescale factor at L1. Prescales can be avoided in the di-electron trigger with the same threshold, but only at the cost of a $\sim 50\%$ reduction in efficiency with respect to $\gamma\gamma \to ee$. The second lowest single electron trigger is seen to operate with a threshold twice as high.

Muons

The high efficiency of the lowest threshold muon trigger is indicative of the comparative ease with which muons can be triggered even at very low transverse momenta. Both `mu4` and `mu6` are assigned prescales. Low threshold di-muon triggers may run unprescaled, albeit with lower efficiency.

In summary, the applicability of existing lepton triggers with respect to $\gamma\gamma \to ll$ is primarily restricted by:

- moderate trigger reconstruction and identification capabilities at low energies

- the need to apply large prescale factors on single lepton triggers in order to keep rates within limits

- the modest triggering efficiencies of unprescaled di-lepton triggers

It is notable that the lowest threshold single lepton trigger chains `tauNoCut`, `mu4` and `e5_medium` all have acceptable efficiencies in the absence of prescales. In the context of $\gamma\gamma \to \tau\tau$, *unprescaled* single lepton triggers are desirable because they would enable the unbiased collection of hadronically decaying taus by way of the processes $\gamma\gamma \to \tau_{\mathrm{had}}\tau_\mu$ and $\gamma\gamma \to \tau_{\mathrm{had}}\tau_{\mathrm{e}}$ with the highest possible efficiencies. The di-lepton triggers, while retaining some sensitivity to *e.g.* $\gamma\gamma \to \mu\mu$ and $\gamma\gamma \to ee$, could not be used towards this end.

4.3.2 Trigger strategy for exclusive leptonic final states

The poor efficiency with which photon-induced leptonic final states are selected by the default trigger chains, emphasize the need for a *dedicated* exclusive trigger strategy that specifically targets exclusive processes. In order to retain a sufficient fraction of the signal and make this available for offline analysis, such a trigger must necessarily be able to operate with low-p_T thresholds without relying on prescale factors to keep the integrated trigger rates within required limits.

One manifestation of this exclusivity, is the absence of detector activity in the forward regions of the detector. As discussed in Section 4.2, the elastic signal is not expected to leave any traces in the forward devices (save perhaps in the *very forward detectors* discussed in Section 1.4.2.5), while inelastic contributions to the signal may occasionally leave minor traces in the forward region. Rapidity gaps should therefore be visible to the trigger in the forward detector devices described in Section 1.4.2, such as the MBTS and LUCID. By the same token, the absence of forward rapidity gaps may be interpreted as a non-exclusive event. This feature can be exploited to suppress triggering of unwanted non-exclusive backgrounds, while letting existing low-threshold trigger items to run unprescaled. In the following, the prospect of using the MBTS to this end will be further explored[5].

4.3.2.1 Constructing MBTS veto triggers at L1

The MBTS technology and primary function is described in Section 1.4.2.1. As mentioned therein, its exposure to radiation limits the lifetime of the detector, whereby the scintillators are expected to deteriorate after 3-4 months of operation at $\mathcal{L}\sim 10^{31}\mathrm{cm}^{-2}\mathrm{s}^{-1}$ [35]. The use of the MBTS for rapidity gap identification is therefore restricted to the early phase of LHC operation.

The MBTS is characterised by two thresholds, `MBTS_A` and `MBTS_C`, referring to the multiplicities of hits on either side of the MBTS truncated to 3 bits [6]. These are used to define three L1 trigger items:

---

[5]I am indebted to A. Pilkington *et. al.* for suggesting this approach for triggering on two-photon processes with early data.

[6]"A" and "C" refer to the two ends of the ATLAS detector along the beampipe, where "A" points in the direction of the city of Geneva and "C" points to the Jura mountains.

- `MBTS_1`: ≥ 1 scintillator hit above threshold on at least one side of the MBTS (`MBTS_A(1)` OR `MBTS_C(1)`)

- `MBTS_2`: ≥ 2 scintillator hits above threshold on at least one side of the MBTS (`MBTS_A(2)` OR `MBTS_C(2)`)

- `MBTS_1_1`: ≥ 1 scintillator hit above threshold on either side of the MBTS (`MBTS_A(1)` AND `MBTS_C(1)`)

A veto on the latter item (`MBTS_1_1`) is therefore tantamount to requiring a rapidity gap within the coverage of the MBTS on *at least one side* of the ATLAS detector. Whereas a double sided rapidity gap is expected in two-photon processes, a single sided veto retains sensitivity to photoproduction processes and inelastic scatters where the proton dissociation products may occasionally be scattered into the central detector.

The coverage of the MBTS extends from $2.09 < |\eta| < 3.84$, and therefore partially protracts into the sensitivity reach of the inner detector and hence the forward reach of lepton reconstruction algorithms ($|\eta| < 2.5$). A small fraction of the signal will therefore potentially cause the MBTS to fire, while the large majority of interesting signal events are expected to leave no traces in the MBTS.

Henceforth, a veto on the L1 item `MBTS_1_1` will be labelled "MV". Such a veto may be combined with other available L1 items to form new dedicated L1 trigger items targeting exclusive final states.

The enormous rate at which soft QCD interactions occur, severely restricts the use of unprescaled low-p_T tau triggers at L1. Consequently, the lowest threshold L1 tau trigger items, `L1_TAU5` and `L1_TAU6`, carry prescales of $\mathcal{O}(10^7)$ and $\mathcal{O}(10^2)$, respectively. Single lepton triggers targeting soft electrons and muons can afford lower thresholds at a more moderate cost to the overall rate. By way of example, the the lowest threshold L1 muon trigger item (`L1_MU0`) runs unprescaled in both start-up and 10^{31} trigger menus[7]. The lowest unprescaled L1 trigger item targeting soft electrons has a sensitivity threshold of 7 GeV (`L1_EM7`). While these trigger items may run unprescaled at L1 in early phases of LHC operation, they may easily be awarded prescales if so required. Any combination with an MV should therefore ensure a rejection efficient enough to allow the full trigger chain to run unprescaled so as to retain the largest possible number of events for offline inspection.

Table 4.4 lists the overall efficiencies and estimated rates of the lowest threshold L1 single lepton and jet trigger items required in conjunction with an MV.

The efficiency estimates are measured with respect to the following three subsets of events in which the true decay of the di-tau system satisfies:

- Hadronic: $p_T^{1,2}(\tau_{had}) > 10$ GeV

- Semi-leptonic: $p_T(\mu) > 4$ GeV / $p_T(e) > 7$ GeV and $p_T(\tau_{had}) > 10$ GeV

Item	ϵ_{target} (%)	Rate (Hz)	Rate w/o MV (Hz)
L1_MU4_MV	75	1.7	1105 (prescale:1)
L1_EM3_MV	77	2.6	168 (prescale:60)
L1_TAU5_MV	78	4.4	4105 (prescale:1)
L1_J5_MV	94	19.2	13 (prescale:2000)
L1_J10_MV	74	2.1	1.8 (prescale:1000)

TABLE 4.4: Efficiency and rate estimates of LVL1 MBTS veto triggers. The rates correspond to $\mathcal{L}=10^{31} \text{cm}^2 \text{s}^{-1}$. The rates of the new MV trigger configurations were estimated with a combination of Minimum Bias and various low-p_T QCD samples. The rate estimates of the same items without MV applied were provided by the ATLAS trigger rate group [92].
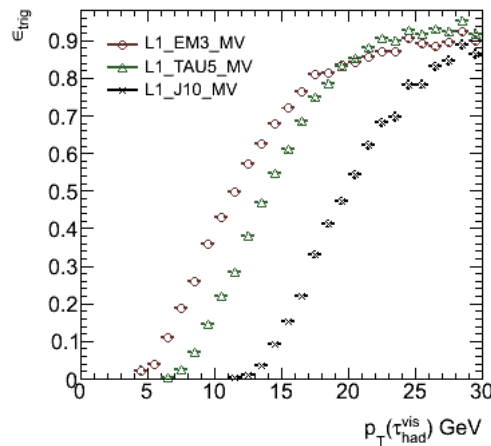
FIGURE 4.5: Trigger efficiency of various L1 MV items *w.r.t.* hadronic tau decays with true $p_T(\tau) > 10$ GeV.

Table 4.4 indicates a limited trigger efficiency with respect to the target true decays already at L1. This inefficiency is more a reflection of the limited trigger reconstruction efficiency at low transverse momenta than of shortcomings in the MV strategy. The MV trigger items are seen to reduce the integrated trigger rates considerably, in some cases allowing for unprescaled operation at L1.

In terms of integrated rates, the items L1_EM3_MV, L1_TAU5_MV and L1_J10_MV provide promising candidates for triggering on hadronic τ-decays. The efficiencies of each of these trigger items are shown in Figure 4.5, as a function of the true visible p_T. It is noteworthy that the item L1_EM3MV is not only seen to trigger efficiently in the electron channel, but also shows superior performance in the soft end of the p_T-spectrum in the hadronic channel. This is because soft hadronically decaying τ-leptons may deposit a sizeable fraction of their energy in the electromagnetic calorimeters[8], thereby causing L1_EM3 to fire.

---

[7]Single lepton chains seeded by L1MU0 are prescaled at HLT

[8]Such deposits will follow from $\pi^0 \to \gamma\gamma$ decays, but also in part from early $\pi^\pm$-showers initiated before the hadronic calorimeters.

4.3.2.2 Constructing new exclusive trigger chains

Despite its simplicity, the MV-strategy provides a potent means to significantly reduce the rate of L1 trigger items without notable loss in trigger efficiency with regard to exclusive photon induced final states.

The MV-items listed in Table 4.4 may therefore be employed to seed full trigger chains targeting generic exclusive final states with forward rapidity gaps. In light of the comparatively modest cross sections of most exclusive processes, the HLT suppression should ideally be efficient enough to allow the full chains to run *unprescaled* in all luminosity scenarios where the MBTS is expected to be operational.

To this end, *three* new single lepton trigger chains were developed with aim to retain sensitivity to all exclusive final states involving leptons in early data. In all three cases, the HLT configuration is congruent with their non-MV counterpart trigger chains, so as to facilitate easy comparison and accurate rate estimation from data. As a consequence, `L1_TAU5_MV` rather than `L1_EM3_MV` is used to seed the chain targeting hadronic τ-decays.

Signature	$\epsilon_{\mu\mu}$ (%)	ϵ_{ee} (%)	$\epsilon_{\tau\tau}$ (%)	Rate/10^{31}cm^{-2}s^{-1} (Hz)
EF_mu4_MV	82	-	-	0.1 ± 0.1
EF_e5medium_MV	-	77	-	0.03 ± 0.02
EF_tauNoCut_hasTrk_MV	-	-	31	0.62 ± 0.62

TABLE 4.5: Integrated efficiencies and rate estimates the single lepton MV-trigger chains. The rate estimates are provided by the ATLAS trigger rate group.

The integrated efficiencies and trigger rates of each trigger chain is listed in Table 4.5. The rates of all three trigger chains are seen to be very small to enable unprescaled operation. The efficiencies of the components of each trigger chain are shown as function of the transverse momentum and pseudorapidity of the true (visible) lepton in various $\gamma\gamma \to ll$ processes in 4.6.

While the MV-trigger chains discussed above were originally conceived with aim to trigger exclusive lepton final states from two-photon processes, their applicability (though not studied herein) principally extend beyond to include *all* exclusive final states with leptons. Exclusive production mechanisms to which the MV-triggers are expected to be sensitive are shown in Figure 4.7, and include among others the photon fusion process $\gamma\gamma \to W^{\pm}W^{\mp}$, the photoproduction process $\Upsilon \to l^{\pm}l^{\mp}$, as well as the central exclusive production of $\chi_b \to \gamma\Upsilon \to \gamma l^{\pm}l^{\mp}$. (In a similar manner, sensitivity is also retained to the exclusive production of new particles.) The use of *single* lepton triggers, rather than *double* lepton triggers, not only provides a higher triggering efficiencies in fully leptonic central systems, but also retains sensitivity to semi-leptonic $\gamma\gamma \to \tau\tau$ events. Requiring a *one-sided*, rather than a two-sided rapidity gap lessens the sensitivity to exclusive events where proton dissociation debris is scattered into the reach of the MBTS and retains sensitivity to exclusive photoproduction processes.
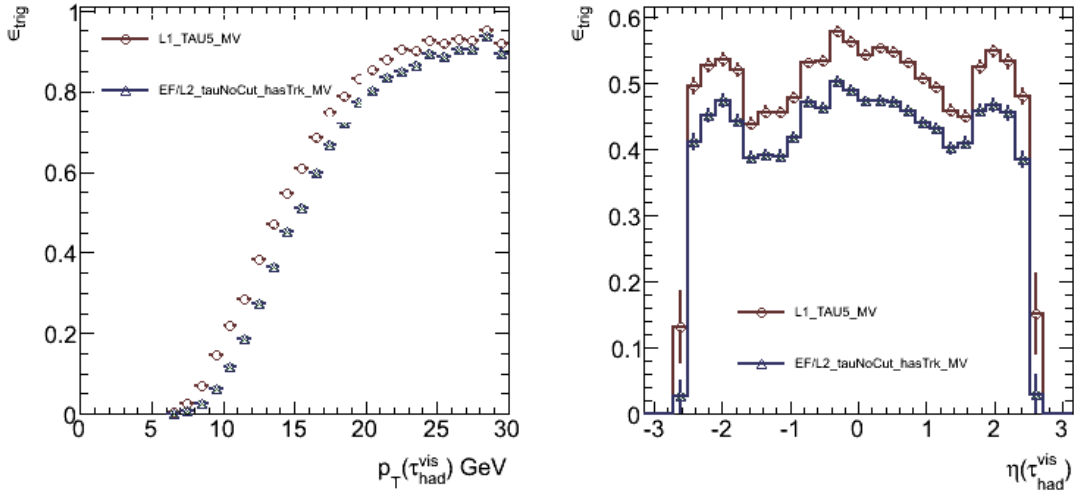
(a) $\gamma\gamma \to \tau_{\text{had}}\tau_{\text{had}}$ $(p_T^{vis}(\tau_{had})> 4$ GeV$)$
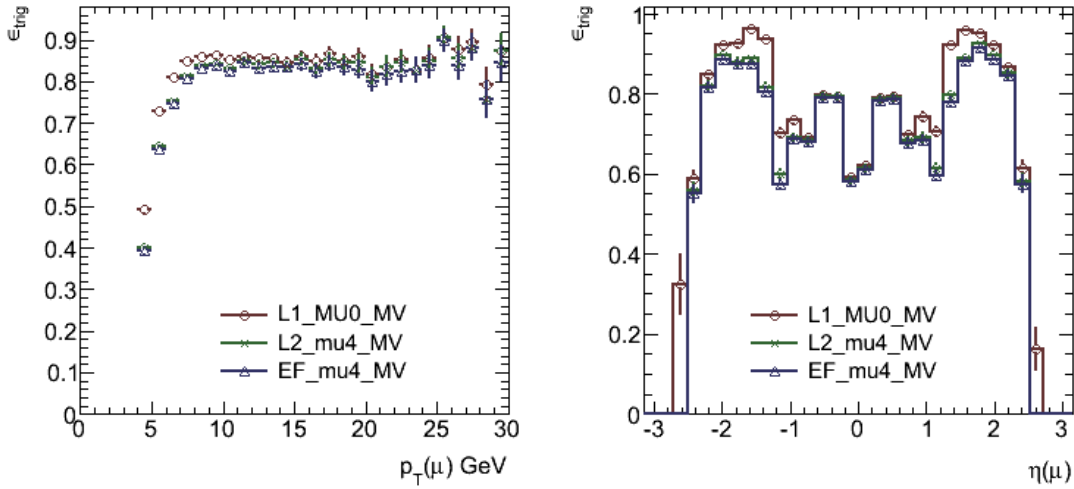
(b) $\gamma\gamma \to \mu\mu$ / $\gamma\gamma \to \tau_{\text{had}}\tau_\mu$ $(p_T(\mu) > 4$ GeV$)$
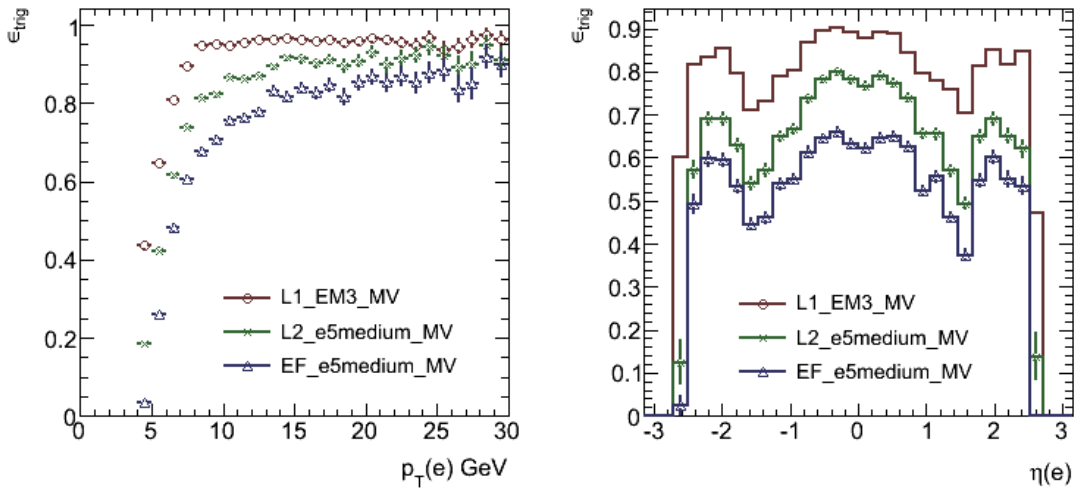
(c) $\gamma\gamma \to ee$ / $\gamma\gamma \to \tau_{\text{had}}\tau_{\text{e}}$ $(p_T(\text{e}) > 4$ GeV$)$

FIGURE 4.6: Trigger efficiencies of new MV-chains as a function of transverse momentum and pseudorapidity the true lepton in various two-photon processes.

(a) photon-fusion

(b) photo-production

(c) central exclusive production
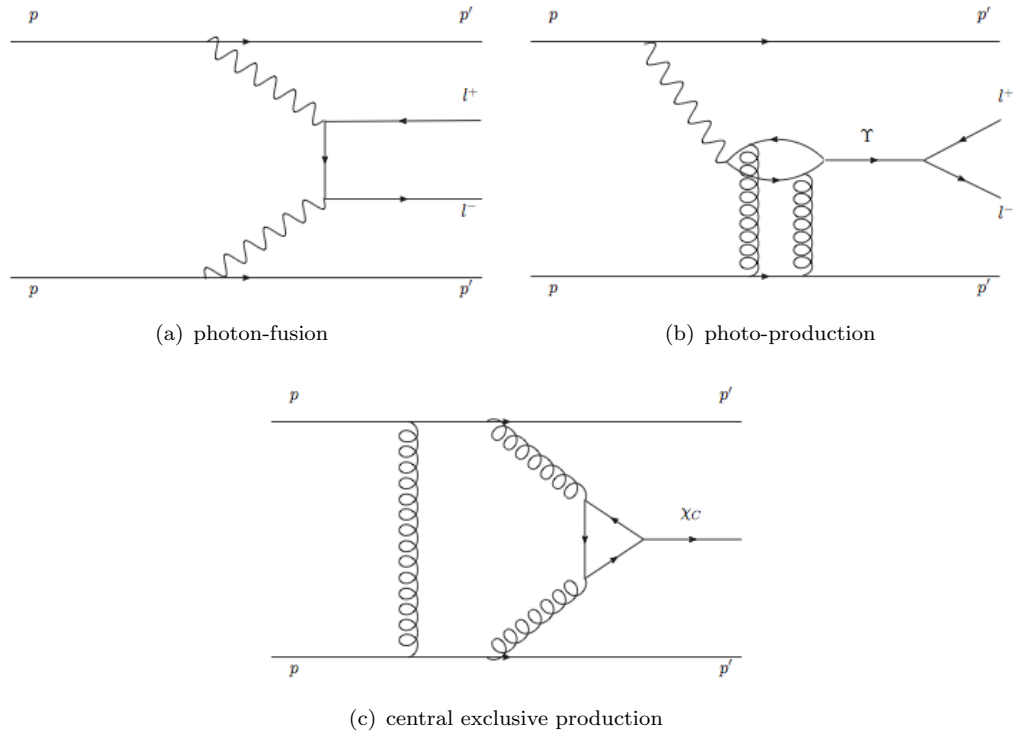
FIGURE 4.7: Diagrams of various exclusive processes with lepton final states (to which the MV-trigger items are expected to retain sensitivity).

4.3.2.3 Rate evolution with instantaneous luminosity

The importance of an unprescaled operation of the MV-triggers has been repeatedly stressed above. This condition is contingent on the trigger rates at each level of the ATLAS trigger chain remaining sufficiently low. The dominant rate suppression derives from the MV-veto implemented at L1. While the rates of most *inclusive* trigger chains are expected to increase with instantanous luminosity in the absence of prescales, the behaviour the MV-triggers is likely to depend on the structure of the collision at the interaction point. As discussed in Section 4.2, overlapping pile-up interactions are expected to spoil the experimental exclusivity, possibly causing the MV-condition to fail. To the extent that higher luminosity runs will be accompanied by additional pile-up interactions, the rates of all MV-trigger chains are therefore expected to fall with increasing instantaneous luminosity. It is hoped that this unique feature should enable the MV-triggers to run unprescaled for the duration of the lifetime of the MBTS. The rate estimates listed in Table 4.5 were derived in an idealized scenario assuming zero pile-up at $\mathcal{L} \sim 10^{31} \text{cm}^{-2} \text{s}^{-1}$. The true rates may therefore be slightly lower.

As already alluded to, the lifetime of the MBTS is restricted to the period of early operation. A more long term sustainable approach may be attainable by replacing the MBTS veto with a similar strategy involving LUCID. When pile-up effects become dominant, forward proton tagging discussed in Section 4.2 may be employed to identify exclusive processes. (Such approaches however, fall outside the scope of the studies presented herein).

4.4   Offline object definitions

Standard offline tools are employed for the reconstruction and identification of all final state objects. The following section briefly details the reconstruction algorithms, and if relevant, the identification and quality requirements imposed on the objects considered in the analysis.

4.4.1   Muons

As described in Section 1.4.1.3, ATLAS is equipped with a dedicated spectrometer whose primary function is to allow for efficient and precise muon reconstruction and identification for transverse momenta spanning from ∼3 GeV to ∼1 TeV. Since even the most energetic electrons, taus and jets are typically brought to a halt in the calorimeters, high QCD background rates do not impair the muon reconstruction performance to the same extent that they do *e.g.* the electron and tau reconstruction. While the muon spectrometers (MS) help a long way, peak performance is only achieved by appropriately combining information from the inner detector (ID) and the calorimeters. For this reason, the ATLAS muon reconstruction software adopts at least four different strategies for the reconstruction and identification of muons. These strategies are summarized in Table 4.6 and represent different ways of combining information from the various subdetectors.

Strategy	Description	STACO family	MuID family
(1) Standalone	Extrapolation of MS tracks to interaction point	**Muonboy**	**Moore**
(2) Combined	Match standalone muons to ID tracks and combine measurements	**STACO**	**MuID**
(3) Tagged	Extrapolate ID tracks with sufficient momentum to first MS station and match to nearby segments	**MuTag**	**MuGirl**

TABLE 4.6: ATLAS offline muon reconstruction strategies.

As indicated in Table 4.6, each of the strategies (1)-(3) have two different algorithmic implementations in the baseline reconstruction. These algorithms are in turn grouped into two distinct *families*, such that each family contains one algorithm for each strategy. The families are named after the *combined reconstruction* member in each family, `STACO` and `MuID`, whereby the former is regarded the default for physics analyses and hence also employed in this study. A cursory description of each strategy and their implementation in the `STACO` family follows:

Standalone reconstruction algorithms initially run pattern finding in each of the three stations of the MS described in Section 1.4.1.3 to construct *track segments* that are later linked to form *spectrometer tracks*. The spectrometer tracks are then inwardly extrapolated back to the interaction point, taking due account of multiple scattering

effects and potential energy loss in the calorimeters. The `Muonboy` algorithm of the `STACO` family estimates the expected energy loss as a function of the material traversed in the calorimeter. The standalone reconstruction relies only on information from the MS and can therefore provide extended coverage up to $|\eta| < 2.7$. This acceptance is limited at $\eta \sim 0$ where an outlet is provided for cables and cryogenic lines. The absence of the middle muon stations in the barrel/end-cap transition region in the early phases of ATLAS operation further degrades the acceptance in the region $1.1 < |\eta| < 1.3$. Additional drawbacks of the standalone approach include reconstruction inefficiencies of very soft muons failing to traverse all spectrometer stations and backgrounds from muons produced by pion punch-throughs or π/K decays in flight.

The **Combined** muon reconstruction can partially alleviate some of these problems by pairing up MS tracks with ID tracks at a small cost in the acceptance coverage ($|\eta| < 2.5$). The quality of the MS-ID track matching is given by the match χ^2 defined in terms of the difference between either track vector weighted by their combined *covariance matrix*:

$$\chi^2_{match} = (\mathbf{T}_{MS} - \mathbf{T}_{ID})^T (\mathbf{C}_{MS} + \mathbf{C}_{ID})^{-1} (\mathbf{T}_{MS} - \mathbf{T}_{ID}) \tag{4.1}$$

whereby $\mathbf{T}$ denotes a track vector and $\mathbf{C}$ its corresponding covariance matrix. To obtain the combined track-vector, the `STACO` algorithm employs a method by which the two algorithms are statistically combined:

$$\mathbf{T}_{comb} = (\mathbf{C}_{MS}^{-1} - \mathbf{C}_{ID}^{-1})^{-1} (\mathbf{C}_{MS}^{-1} \mathbf{T}_{MS} + \mathbf{C}_{ID}^{-1} \mathbf{T}_{ID}) \tag{4.2}$$

While the combined muon algorithms provide substantial improvements to the momentum resolution of muons with $p_T < 100$ GeV, their performance is partially limited by the efficacy of the standalone algorithms.

The **Tagged** muon algorithms do not initiate in the MS, but instead attempt to propagate all ID tracks with sufficient momentum to the first station of the MS and then associate the extrapolated ID tracks to nearby MS segments. To *tag* the ID track as corresponding to a muon, the `MuTag` algorithm of the `STACO` family defines a χ^2 from the difference of the position of nearby segments and the extrapolated ID track prediction. `MuTag` only makes use of ID tracks and MS segments not already used by the combined reconstruction algorithm `STACO`. As such, `MuTag` may be regarded a supplement to `STACO`, identifying muons missed by the combined reconstruction because no fully reconstructed MS tracks were produced.

The low transverse momentum of muons originating from the decay of a τ-lepton produced in a two-photon interaction, make them particularly challenging to reconstruct. The energy loss the muons undergo in the calorimeters ($\sim$3-5 GeV) becomes increasingly comparable to their momentum. Even if the muons penetrate into the MS, very soft muons do not always leave a proper signal in the outer MS stations. Such soft muons are additionally more sensitive to inhomogeneities in the magnetic field[9], which may

---

[9]The open air core toroids notably generate an inhomogeneous magnetic field that may lead to irregular particle trajectories at low transverse momenta.

(a) Muon reconstruction efficiency

(b) Electron reconstruction efficiency
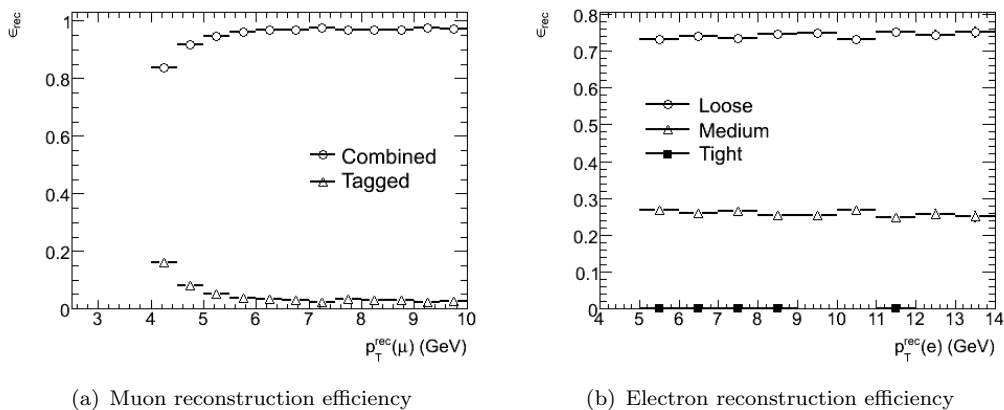
FIGURE 4.8: (a) Fractional reconstruction efficiency of muons reconstructed by `STACO` (Combined) and `MuTag` (Tagged) as a function of the selected reconstructed muon transverse momentum in $\gamma\gamma \to \mu\mu$ and $\gamma\gamma \to \tau_{\text{had}}\tau_\mu$. The reconstructed muons are required to satisfy the selection outlined in Table 4.7. (b) Reconstruction efficiency with various cut-based identification methods vs reconstructed electron transverse momentum in $\gamma\gamma \to ee$ ($p_T >5$ GeV)

result in complicated trajectories more difficult to reconstruct. Since `MuTag` does not rely on reconstructed MS tracks, it targets and improves the reconstruction efficiency in the very soft end of muon p_T spectrum. Moreover, it is less sensitive to regions of degraded performance in the MS.

Selection	Description
Combined or Tagged	Candidate is reconstructed by `STACO` or `MuTag`.
$\chi^2 < 100$	Match quality requirement on combined muon candidates
$p_T > 4$ GeV	Minimum transverse momentum requirement on muon candidate
`nucone40` < 5	Maximal number of tracks in an isolation cone of $\Delta R <0.4$

TABLE 4.7: Muon preselection requirements.

The muon selection employed in this analysis is summarized in Table 4.7. Figure 4.8(a) depicts the muon reconstruction efficiency of *combined* and *tagged* muons as a function of the reconstructed muon transverse momentum in $\gamma\gamma \to \mu\mu$ and $\gamma\gamma \to \tau_{\text{had}}\tau_\mu$.

4.4.2 Electrons

The high rate of QCD jet production at the LHC puts stringent requirements on the performance of electron identification tools in ATLAS. The ratio between the rates of isolated electrons to that of QCD jets ($20 < p_T^{\text{jet}} < 50$ GeV) is expected to be $\sim 10^{-5}$, a hundred times smaller than the corresponding ratio at the Tevatron [32]. In terms of electron transverse momentum, the reconstruction requirements demanded by the physics programme of ATLAS spans a broad kinematic range, from a few GeV to several TeV. The challenge of reconstructing soft electrons, such as those originating from two-photon processes, is exacerbated by the energy loss of electrons in the inner detector volume. To meet with these challenges, complementary electron reconstruction routines have been developed:

egamma is the standard *cluster based* electron reconstruction. The algorithm is seeded by $\simeq 3$ GeV *Sliding Window* clusters built in the electromagnetic calorimeters. Reconstructed ID tracks not belonging to a γ-conversion pair are extrapolated to the electromagnetic calorimeter and required to match the seed cluster within a $\Delta\eta \times \Delta\phi$ window of 0.05×0.10. If a match is found, the ratio of the cluster energy to the track momentum is required to satisfy $E_{\text{clus}}/p_{\text{track}} < 10$ before an electron candidate is built.

softe is a *track based* electron reconstruction algorithm targeting low-p_T electrons and electrons buried in jets. The algorithm is seeded by *standard* quality tracks from the inner detector with transverse momentum $p_T > 2$ GeV , whereby the track quality criteria follow a standard definition:

- ≥ 2 hits in the pixel detector, one of which is situated in the b-layer

- ≥ 7 precision hits in the pixel detector and the SCT

- Fraction of TRT hits ≥ 0.05 within $|\eta| < 2$

Selected seed tracks are extrapolated to the second sampling of the EM calorimeter, about which position a fixed size cluster of size

$$\Delta\eta \times \Delta\phi = \begin{cases} 0.075 \times 0.175 & \text{barrel} \\ 0.125 \times 0.125 & \text{end-cap} \end{cases}$$

is built. In order to locate a position with respect to which shower shapes can be computed, a search for the most energetic cell within a tight $\Delta\eta \times \Delta\phi$ window about the extrapolated track position is made. In a final measure to suppress fake candidates, the ratio of energy E in the EM cluster to the momentum p of the ID track is required to exceed 0.4.

The electron *identification* draws on information from calorimetric shower profiles, the quality of the track-cluster match and transition radiation information from the TRT. Various methods to combine and evaluate this information against an electron hypothesis are available, including various multivariate techniques. However, the recommendation for the early phase of ATLAS operation is the usage of a predefined cut-based identification method. The default cut-based identification includes the three levels of stringency outlined in Table 4.8. Figure 4.8(b) shows the reconstruction efficiency of identified electrons achieved in $\gamma\gamma \to ee$ events with the various cut-based selections. The `Loose` selection has been employed for electrons herein.

4.4.3 Taus

The baseline ATLAS τ-reconstruction and identification algorithms are described in Section 2.2 and will not be given further mention here.

Type	Description
Loose selection	
Acceptance coverage	$\lvert\eta\rvert <2.47$
Hadronic leakage	Ratio of E_T in 1st sampling of the HCAL to E_T of the EM cluster
2nd layer of ECAL	Ratio in η of ΣE_{cell} in 3×7 vs. 7×7
	Ratio in ϕ of ΣE_{cell} in 3×3 vs. 7×7
	Lateral width of the shower
Medium selection (includes loose selection)	
1st layer of ECAL	Difference between energy associated with the 2nd largest energy deposit and energy associated with the minimal value between the first and second maxima
	2nd largest energy deposit normalised to the cluster energy
	Total shower width
	Shower width for three strips around maximum strip
	Energy fraction outside core of three central strips but within seven strips
Track quality	Number of hits in pixel detector (≥ 1)
	Number of hits in the pixel and SCT detectors (≥ 9)
	Transverse impact parameter (<1 mm)
Tight selection (included medium selection)	
Isolation	Ratio of E_T in $\Delta R <0.2$ to total cluster E_T
Vertexing layer (b-layer)	Number of hits in vertexing layer (≥ 1)
Track matching	$\Delta\eta$(cluster, track) (<0.005)
	$\Delta\phi$(cluster, track) (<0.02)
	Ratio of cluster energy to track momentum
TRT	Total number of hits in the TRT
	Ratio of the number of high-threshold hits to the total number of hits in the TRT

TABLE 4.8: Description of variables employed in default cut-based electron identification.

The transverse momentum spectrum of reconstructed τ-candidates of either flavour (calorimeter/track seeded) in $\gamma\gamma \to \tau\tau$ events is depicted in Figure 4.9. The figure clearly indicates that a large portion of reconstructed τ-candidates are produced around the sensitivity threshold (6-10 GeV) of the offline τ-reconstruction algorithms in ATLAS. The unavailability of robust identification methods in this kinematic regime, makes the challenge of selecting τ-candidates from $\gamma\gamma \to \tau\tau$ offline particularly onerous.

As in the case of electrons discussed in Section 4.4.2, multivariate identification techniques are avoided during the initial data-taking period in favour of cut-based identification methods with three levels of stringency. These cut-based selections draw on
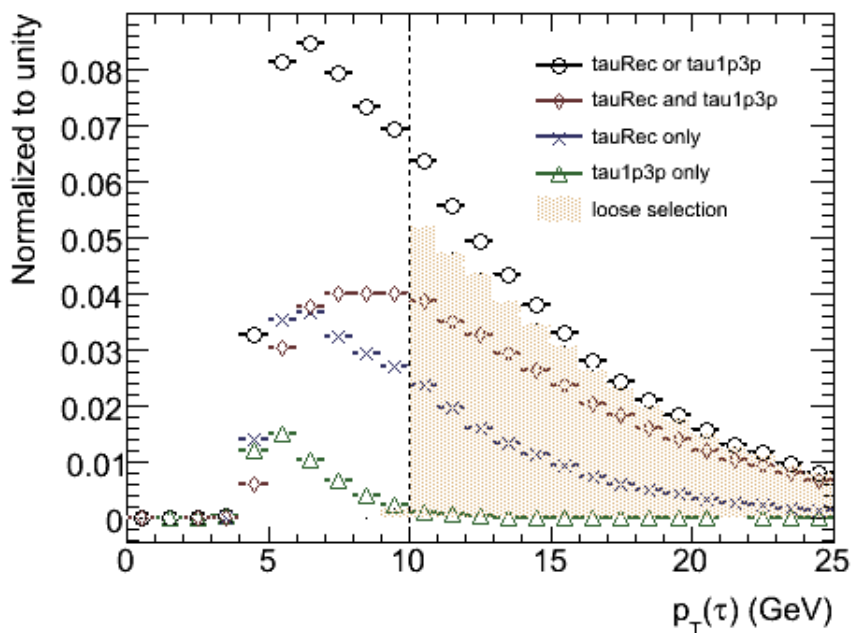
FIGURE 4.9: Transverse momentum spectrum of reconstructed tau candidates from $\gamma\gamma \to \tau\tau$, with $p_T^{\text{gen}}(\tau) > 10$ GeV.

discriminating quantities that have been deemed *robust* to the extent that they may be easily validated with a comparatively small amount of collected data [93]. While various cut-based selections have been developed in preparation for early data taking, they are all currently restricted to τ-candidates with transverse momenta beyond 10 GeV. The simplest selection considered herein (`TauCutSafeCalo`) utilizes a suite of four calorimetric variables: the *electromagnetic radius*, the E_T *spread in the η-strip layer*, the *fraction of E_T^{EM} in a narrow ring* $(0.1 < \Delta R < 0.2)$ about the τ-candidate and the *ratio of EM energy to total energy*. The cut based selection is separately optimized for 0/1 prong and multiprong candidates in bins of E_T^{vis}, the lowest of which ranges from 10-25 GeV.

Figure 4.9 also shows the fraction of the τ-candidate p_T-spectrum to which the loose `TauCutSafeCalo` selection is sensitive. While a good efficiency is achieved above 10 GeV, almost 50% of the τ-candidates produced in $\gamma\gamma \to \tau\tau$ $(p_T^{\text{gen}}(\tau) > 10$ GeV) events fall below the sensitivity reach of the cut-based selection. From these, the large majority of candidates are seen to be calorimeter seeded or both calorimeter and track seeded. A small fraction of candidates at very low transverse momenta are secured by the track-seeded algorithm alone.

Figure 4.10(a) compares the distribution of the *electromagnetic radius* in the calorimeter, defined as:

$$R_{\text{EM}} = \frac{\sum_{i=1}^{\Delta R < 0.4} E_{T,i}^{\text{EM}} \sqrt{(\eta_i^{\text{EM}} - \eta_{\text{seed}})^2 + (\phi_i^{\text{EM}} - \phi_{\text{seed}})^2}}{\sum_{i=1}^{\Delta R < 0.4} E_{T,i}^{\text{EM}}} \tag{4.3}$$

145

(a) EM radius

(b) Ratio of high to low TRT hits

(c) Hadronic energy fraction
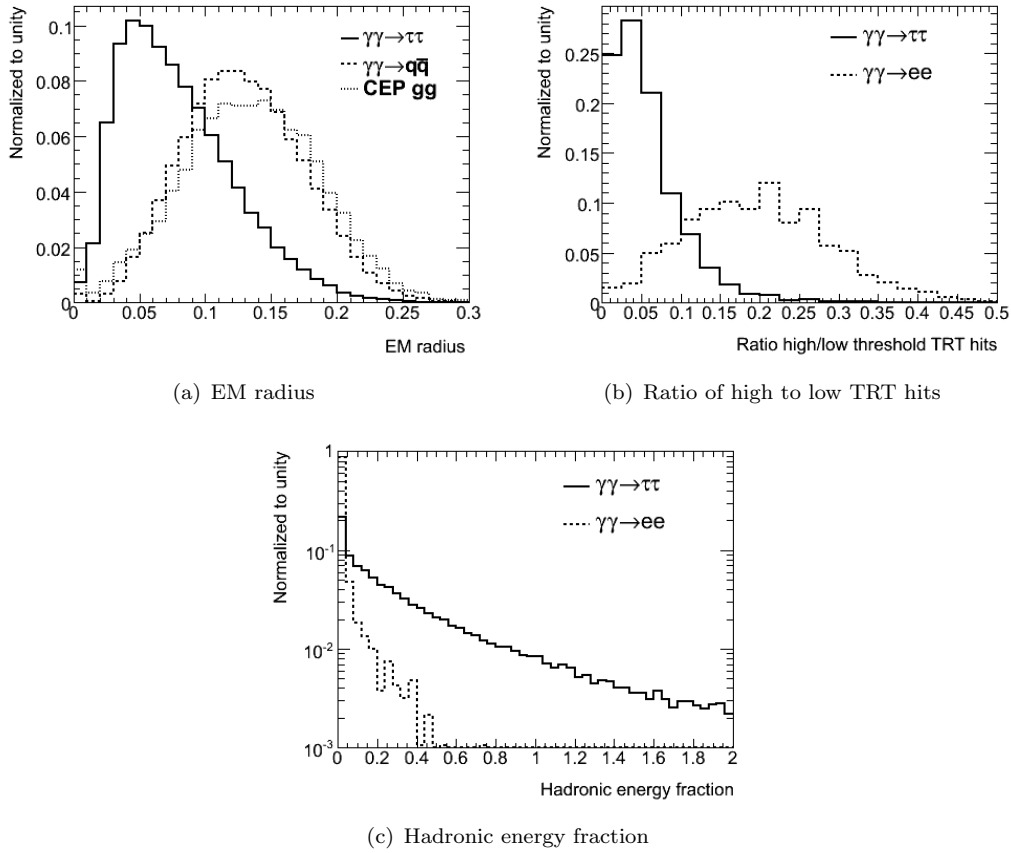
FIGURE 4.10: Variables used to facilitate tau/jet and tau/electron separation.

where the sum runs over all cells in topoclusters associated with the τ-candidate and η_i, ϕ_i and $E_{T,i}$ denote the cell positions and transverse energies, whereas η_{seed} and ϕ_{seed} denote the positions of the calorimeter seeded τ-candidate. The discriminating power retained in this quantity *electromagnetic radius* will later be exploited to suppress unwanted fake candidates originating from exclusive jet backgrounds.

Electrons failing the loose selection criteria outlined in Section 4.4.2, may readily be reconstructed and misidentified as (soft) τ-leptons, commanding a need for a suppression of false candidates originating from electrons. As is discussed in Section 1.4.1.1, electrons are prone to generate higher ratios of high to low threshold hits in the TRT (H_{TRT}). As seen in Figure 4.10(b), this feature may be exploited to separate false electron induced τ-candidates from true τ-candidates. Electron induced candidates will also typically have a very small hadronic energy fraction, as seen in Figure 4.10(c).

As discussed in Section 4.6, the required stringency of the τ-candidate selection will vary across the different search channels and depend on the background composition in each channel.

The initial basic selection therefore considers all τ-candidates generated by either `tauRec` or `tau1p3p` with no further cuts applied.

4.4.4 Jets

To the extent that the signal may be regarded a pure QED process free from additional hadronic activity such as *e.g.* small angle gluon radiation, additional jets beyond the two "τ-jets" are not expected to feature in the signal final states. However, soft hadronic τ-decays which fail to produce an accepted τ-candidate may well produce a jet in the central detector. As final state objects, jets should therefore not be fully disregarded in a search for the signal.

A multitude of different jet algorithms are available in ATLAS, each with their own merits and drawbacks. In the following analysis the ATLAS default *seeded fixed-cone jetfinder* is used, wherein a jet is defined as a collection of constituent particles inside a cone of fixed radius R_{cone} in the $\eta - \phi$ plane. While being theoretically disfavoured, the simplicity and robustness of the algorithm makes it an appropriate choice for early data.

The algorithm used herein, is seeded by calorimeter activity taking the form of *topological clusters* produced by the clustering algorithm described in Section 2.3.1. The input clusters are initially ordered by decreasing p_T, after which the leading object is selected. If the leading object p_T exceeds the *seed threshold* (>1 GeV), all surrounding objects within a radius $\Delta R = \sqrt{\Delta\eta^2 + \Delta\phi^2} < R_{cone}$ are collected and combined with the seed cluster. The combined four-momentum of this collection will provide a new jet axis about which a new cone is built. Objects within the new cone are (re-)collected to produce an updated jet axis about which a new cone is built. This process continues iteratively until a *stable jet* forms in which the jet axis no longer shifts after recombination. The process is repeated for all input seeds above threshold, to the effect that the final jet objects may partially overlap and share objects [10]. This renders the algorithm *infrared unsafe*, a problem which can be partially alleviated through the introduction of the split and merge step in which all jets sharing a substantial fraction of energy (50%) are merged or otherwise split.

4.4.5 Overlap removal

Because combined reconstruction algorithms often operate on the same tracks and calorimeter clusters, it is possible that the offline reconstruction will yield overlapping objects. Such overlaps may occur when *e.g.* a reconstructed electron-object and a reconstructed τ-object share the same track or cluster. To prevent the same track or cluster from forming part of several particle-objects in the offline analysis, an order of preference must be established. Such a preferential selection of objects is called an *overlap removal*.

Reconstructed objects with a spatial overlap of $\Delta R < 0.4$ are removed in the following order of preference: *Muons, Electrons, Taus* and *Jets*. A relatively broad overlap region can be afforded, because only two objects are expected in the final state.

---

[10]It is also possible that objects having contributed to an early iterative step during jet building "fall out" of the jet in a later step, should the jet axis move sufficiently far away from the object.

4.5   Backgrounds

An observation of the exclusive process $\gamma\gamma \rightarrow \tau\tau$ in early data relies on an efficient elimination of all *background* processes that may falsely mimic the event signatures of the signal process. The background processes may be classified as either *non-exclusive* or *exclusive*. Each of these two categories present distinct challenges to the offline selection. Each category also contains two classes of background processes, namely those containing two τ-leptons in the final state and those whose final states contain < 2 τ-leptons but other objects with a high likelihood of being falsely identified as τ-leptons.

4.5.1   Non-exclusive

Since the signal is characterised by a relatively balanced and central system accompanied by large rapidity gaps void of detector activity to either side of the di-lepton axis, a signal search criterium may be expressed as *exclusively two τ-leptons and nothing else*. Non-exclusive backgrounds comprise all processes that also produce final states with two central leptons, but always in company with *something else*. Most background processes stemming from hard pp interactions may readily be identified as non-exclusive. This is because the proton remnant in such scatters will typically leave signals in the forward region of the central detector. Their reducibility hinges on a proper identification of any additional activity between the leptons of the central system. While busier final states typically enable such an identification, events from non-exclusive sources may still *appear* exclusive if not all particles are properly accounted for, either because they are too soft or because they escape into insensitive regions of the detector. While the occurrence of such events is comparatively rare, the cross sections of most inclusive backgrounds are typicallly many orders of magnitude larger than that of the exclusive signal. Efficient suppression techniques are therefore called for.

A potential means of suppressing backgrounds from non-exclusive sources is by way of *calorimetric exclusivity*:

$$\Omega_{\mathrm{clus}} = \frac{\sum E_T^{\mathrm{clus}}(|\eta| < 2.5)}{\sum E_T^{\mathrm{clus}}} \tag{4.4}$$

where the sum in the numerator runs over all topological clusters within $|\eta| < 2.5$ and the sum in the denominator runs over all topological clusters in the event.

The distribution of Ω_{clus} for the exclusive signal and various non-exclusive backgrounds is shown in Figure 4.11(a). Calorimetric exclusivity as defined in Equation 4.4 is seen to provide a highly efficient means to separate exclusive events from non-exclusive events. This is particularly true for non-exclusive backgrounds where the energy scale of the central objects is comparable to that expected from the signal. As the energy deposits in the central calorimeters become large with respect to the forward deposits, the separation power of Ω_{clus} will naturally diminish. This effect is observed *e.g.* in the upper tail of the Drell-Yan (DY) spectrum shown Figure 4.11(a).
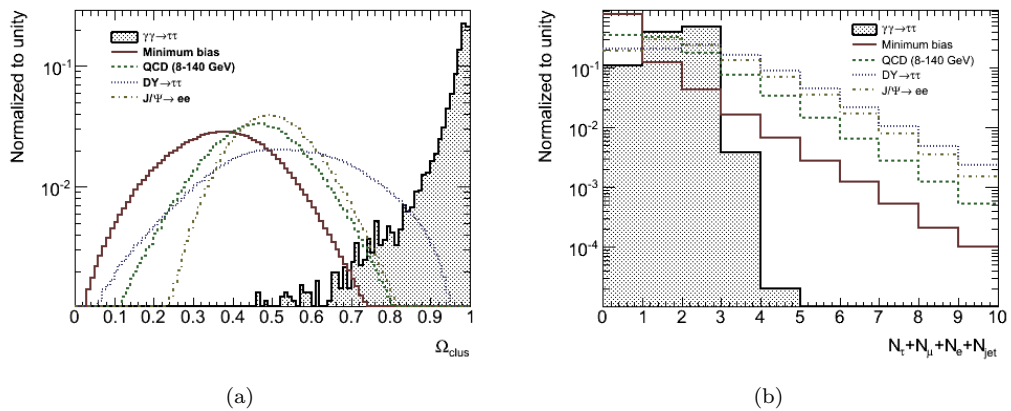
FIGURE 4.11: (a) Calorimetric exclusivity in exclusive and non-exclusive processes. (b) Multiplicity of reconstructed objects after overlap removal in exclusive and non-exclusive processes.

Event exclusivity may also be measured in terms of the multiplicity of reconstructed objects. Figure 4.11(b) shows the sum of reconstructed tau, muon, electron and jet objects after overlap removal. The number of reconstructed objects in the signal process will rarely exceed two. This sets two-photon processes apart from non-exclusive backgrounds, where additional activity beyond the hard scatter is likely to produce additional objects in the event. Some degree of suppression may therefore be achieved by removing events with an excess number of reconstructed objects. It is also noteworthy that the soft nature of the signal will often generate final states void of reconstructed objects, or final states with only one reconstructed object. An offline analysis requiring two reconstructed objects will therefore be insensitive to a large portion of the signal.

Non-exclusive backgrounds considered herein, include:

- Minimum bias (non-diffractive)

- QCD dijets ($8 < p_T < 140$ GeV)

- DY→ll (l=e,μ,τ)

- J/ψ →ll (l=e, μ)

- $\Upsilon \to \mu\mu$

Details pertaining to the Monte Carlo data samples are provided in Appendix B.3.

4.5.2 Exclusive backgrounds

Unlike non-exclusive backgrounds, *exclusive* backgrounds comprise all background processes in which the rapidity gaps remain intact. Any features for differentiating the exclusive signal from exclusive backgrounds must therefore be derived from the central system alone. Exclusive backgrounds typically have much smaller cross sections than do

(a) Central exclusive dijet production (b) Photon induced dijet production

FIGURE 4.12: Diagram for exclusive jet production at the LHC.

non-exclusive backgrounds, but similar event topologies make them considerably harder to suppress. Some are reducible, while others are *irreducible* and cannot be distinguished from the signal. By way of example, the reducibility of the tw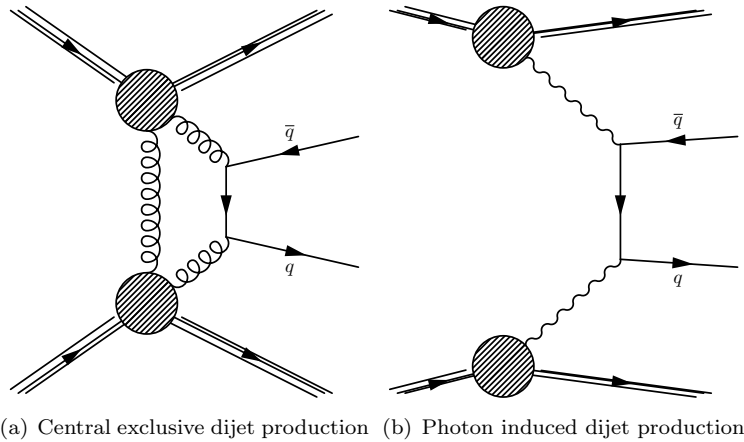o-photon process $\gamma\gamma \to ee$ rests on an efficient rejection of electrons falsely identified as hadronically (or leptonically) decaying τ-leptons[11]. The diffractive production of Υ mesons decaying into a tau pair, by contrast, represents an irreducible exclusive background to $\gamma\gamma \to \tau\tau$.

The unavailability of adequate simulation tools, restricts the spectrum of exclusive backgrounds considered in this analysis. Diffractive backgrounds are not considered[12]. The most dominant backgrounds however, are expected to arise from exclusive jet production, *e.g.* by way of either of the processes shown in Figure 4.12. Exclusive backgrounds considered herein are listed in Table 4.9 along with their respective cross-sections. Further details on these samples are provided in Appendix B.3. The suppression of exclusive backgrounds is further discussed in Section 4.6.3.

Process	Kinematic cuts	σ (pb)	Generator
$\gamma\gamma \to ee$	$p_T > 5$ GeV, $|\eta| < 2.5$	12.9	LPAIR
$\gamma\gamma \to \mu\mu$	$p_T > 4$ GeV, $|\eta| < 2.5$	21.1	LPAIR
$\gamma\gamma \to q\bar{q}$	$p_T > 10$ GeV, $|\eta| < 2.5$	6.6	SHERPA
CEP dijets	$E_T > 8$ GeV	262502	Exhume

TABLE 4.9: Exclusive backgrounds and their cross sections.
.

---

[11]In the context of $\gamma\gamma \to \tau\tau$, the sister processes $\gamma\gamma \to ee$ and $\gamma\gamma \to \mu\mu$ are regarded as backgrounds.

[12]Unavailability means that either no appropriate simulation tools were identified and attained by the author, that no appropriate tools exist within the ATLAS software or that no centrally produced samples were available. The analysis has tried to rely on simulated data samples produced centrally by the ATLAS collaboration whenever possible. Consistent single and double diffractive scattering samples were not available for the studies presented herein. Nor were samples involving the diffractive production of mesons.

4.5.3 Other background sources

In addition to inclusive and exclusive physics processes, various *coincidence backgrounds* may mimic the exclusive signal in the detector. Such backgrounds may fake an exclusive signature when several independent effects coincide.

Cosmic rays pass through ATLAS at random times. A cosmic event in the central detector coinciding with a beam crossing involving *e.g* two single diffractive events or one double diffractive event may well falsely appear as an exclusive signature.

By the same token, a cosmic event coinciding with an actual exclusive process may destroy the exclusivity of the recorded event. Similarly, beam halo particles traversing the long side of the detector may pollute the rapidity gaps of an exclusive event rendering it effectively non-exclusive[13].

Such effects are however expected to be small and will not be considered in the following.

4.6 Offline selection of the process $\gamma\gamma \to \tau\tau$

In the following, an offline selection strategy is developed with aim to determine the feasibility of extracting the process $\gamma\gamma \to \tau\tau$ from the first 100 pb^{-1} of $\sqrt{s} = 7$ TeV data recorded by ATLAS assuming stable operation at an instantaneous luminosity corresponding to $\mathcal{L} \sim 10^{31}$cm^{2}s^{-1} and a beam configuration were pile-up effects are negligible.

Differences in the experimental signatures associated with the signal and the various background processes discussed in Section 4.5 provide the basic tools for a search for the signal process in recorded data. The selection strategy attempts to target all possible exclusive final states concurring with the following subsets of the signal:

- Fully hadronic channel: $\gamma\gamma \to \tau_{\text{had}}\tau_{\text{had}}$

- Semi-leptonic channel: $\gamma\gamma \to \tau_{\text{had}}\tau_{\mu}$ and $\gamma\gamma \to \tau_{\text{had}}\tau_{\text{e}}$

- Fully leptonic channel: $\gamma\gamma \to \tau_{\mu}\tau_{\text{e}}$

The offline selection itself may be regarded as a three-step procedure involving an initial *trigger selection*, a secondary event *preselection*, followed by a more dedicated *final* search into each target final state. The details pertaining to each step in the selection procedure are given below.

---

[13]*Beam Halo* refers to secondary particles arising from elastic and inelastic beam proton scatters against residual gas inside the beam pipe.

4.6.1 Online trigger selection

As was discussed in Section 4.3.2.2, dedicated trigger chains were developed in order to retain online sensitivity to exclusive lepton final states during the period of early ATLAS operation. The optimal trigger selection will necessarily depend on the exact configuration of the trigger menu with which the recorded data is collected, and in particular on the availability of low threshold trigger chains. Herein, the offline inspection will restrict itself to events passing at least one of the following MV-trigger chains most of which were detailed in Section 4.3.2.2:

- `EF_tauNoCut_hasTrk_MV`

- `EF_j15_MV_MbSpTrk`[14]

- `EF_mu4_MV`

- `EF_e5medium_MV`

under the assumption that all other low-p_T trigger chains are rendered unsuitable by large prescales.

Table 4.10 summarizes the efficiencies after trigger selection with respect to the signal process and various exclusive and non-exclusive backgrounds.

While the trigger selection efficiency of the process $\gamma\gamma \to \tau\tau$ is limited, a large fraction of $\gamma\gamma \to ee$ and $\gamma\gamma \to \mu\mu$ events do pass the online trigger selection. While the explicit offline selection of these processes will not be considered in the following study, these processes are interesting in their own right. It is therefore notable that Table 4.10 indicates that sample sizes corresponding to approximately 1000 $\gamma\gamma \to ee$ ($p_T(e) > 5$ GeV) and 1800 $\gamma\gamma \to \mu\mu$ ($p_T(\mu) > 4$ GeV) are potentially made available for offline analysis with an integrated luminosity of 100 pb^{-1}.

The MBTS veto built into all the above trigger chains makes the trigger selection a formidable suppressor of non-exclusive backgrounds. As a case in point, the trigger selection efficiency of $J/\Psi \to ll$ is suppressed by $\mathcal{O}(10^3)$ with respect to $\gamma\gamma \to ll$. Because inclusive background processes invariably involve radiation and proton debris scattered into the pseudorapidity reach of the MBTS, they are highly unlikely to pass the online selection.

4.6.2 Offline preselection

The offline event preselection seeks to reject all events whose *global* features do not comply with the expected signatures of the signal. As discussed in Section 4.5, the signal is most strikingly characterized by a small number of reconstructed particle objects and minimal additional detector activity. *Particle multiplicity* and *event exclusivity* therefore form the corner stone of the preselection:

---

[14]This trigger requires a 15 GeV jet, an MBTS-veto and at least one space-point track at L2.

Process	Trigger		Multiplicity		Exclusivity A	
	$\epsilon_{\text{sel}}(\%)$	N$_{100}$	$\epsilon_{\text{sel}}(\%)$	N$_{100}$	$\epsilon_{\text{sel}}(\%)$	N$_{100}$
$\gamma\gamma \to \tau\tau$ (elastic)	38.16±0.22	30.9±0.2	37.00±0.22	30.0±0.2	36.32±0.22	29.4±0.2
$\gamma\gamma \to \tau\tau$ (semi-elastic)	44.51±0.28	37.7±0.2	43.19±0.28	36.6±0.2	39.59±0.28	33.6±0.2
$\gamma\gamma \to \tau\tau$ (inelastic)	50.20±0.24	51.9±0.2	48.70±0.23	50.4±0.3	41.02±0.23	42.4±0.2
$\gamma\gamma \to ee$ (elastic)	75.55±0.43	349.1±2.0	54.25±0.50	250.6±2.3	54.01±0.50	249.5±2.3
$\gamma\gamma \to ee$ (semi-elastic)	83.65±0.37	342.9±1.5	59.26±0.49	242.9±2.0	58.20±0.49	238.6±2.0
$\gamma\gamma \to ee$ (inelastic)	87.20±0.33	368.0±1.4	60.48±0.49	255.2±2.1	58.03±0.50	244.8±2.1
$\gamma\gamma \to \mu\mu$ (elastic)	81.61±0.39	655.3±3.1	3.66 ±0.19	29.3±1.5	3.55±0.19	28.5±1.5
$\gamma\gamma \to \mu\mu$ (semi-elastic)	87.86±0.32	572.8±2.1	4.37 ±0.21	28.4±1.4	4.19±0.20	27.3±1.3
$\gamma\gamma \to \mu\mu$ (inelastic)	90.30±0.29	586.9±2.0	4.32 ±0.21	28.0±1.3	4.00 ±0.20	26.0±1.3
Minimum bias (ND)	$(2.48 \pm 0.39) \cdot 10^{-4}$	$(12.0\pm1.86)\cdot10^{6}$	$(2.09 \pm 0.36) \cdot 10^{-4}$	$(10.0\pm1.7)\cdot10^{6}$	$(1.10^{+1.02}_{-0.62}) \cdot 10^{-5}$	$533966^{+495440}_{-303428}$
QCD dijets	0.014±0.002	$4.49\cdot10^{10} \pm 3.83 \cdot 10^{6}$	0.008±0.002	$1.40\cdot10^{10} \pm 3.82 \cdot 10^{6}$	0.002±0.0008	$1.03\cdot10^{9} \pm 1.05 \cdot 10^{6}$
DY(ee/$\mu\mu$/$\tau\tau$)	0.33±0.01	4355±55	0.20±0.01	2709±43	0.015±0.002	209.2±7.6
$J/\Psi\backslash\Upsilon$	0.04±0.02	$(103.11 \pm 3.52) \cdot 10^{6}$	0.005±0.006	$(15.4 \pm 1.32)\dot{1}0^{6}$	$(2.08 \pm 0.68) \cdot 10^{-6}$	534747 ± 170766

TABLE 4.10: Selection efficiencies (ϵ_{sel}) and projective event numbers at 100 pb^{-1} (N_{100}) of the trigger selection and event preselection.
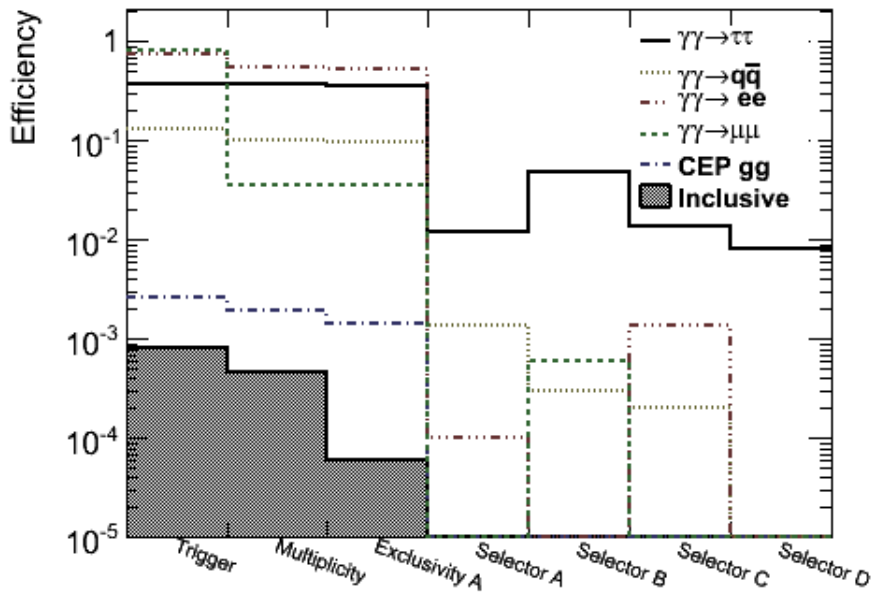
FIGURE 4.13: Fraction of events passing successive selection cuts for the signal and various background processes. The efficiencies are measured with respect to the total event sample in each process. Inclusive backgrounds are suppressed by $\mathcal{O}(\sim 10^5)$ through the online and offline preselection, while exclusive backgrounds are largely unaffected.

4.6.2.1 Multiplicity

Depending on just how the di-tau system decays, the reconstructed final state is expected to contain precisely two reconstructed τ-candidates or alternatively one τ-candidate accompanied by a reconstructed electron or muon. (To allow for the possibility that a hadronically decaying τ-lepton does not produce a τ-candidate, but is instead reconstructed as a jet, one single jet is permitted in the central detector ($|\eta| < 2.5$)). The *multiplicity preselection* may then be summarized as follows:

1. At least one, but no more than two reconstructed leptons:
   $0 < N_{\mathrm{leptons}} \leq 2$

2. No more than 1 light flavour lepton:
   $N_e \leq 1$ and $N_\mu \leq 1$

3. No additional jets:
   $N_{\mathrm{jets}}(|\eta| < 2.5) \leq 1$

where N_{leptons} signifies the sum of the number of selected electron object (N_e), muon objects (N_μ) and tau candidate objects (N_τ).

4.6.2.2 Exclusivity A

The maximal number of tracks in the event should not exceed the six expected from a fully hadronic double 3-prong decay. Moreover, significant energy deposits in the calorimeter are only expected in the central detector. The *exclusivity preselection* may therefore be summarized as:

1. Track multiplicity:
   $N_{\text{tracks}} \leq 6$

2. Calorimeter activity:
   $\Omega_{\text{clus}} > 0.9$

Figure 4.13 compares the cummulative selection efficiency of the trigger and preselection cuts in various processes.

In addition to reducing non-exclusive backgrounds with excess activity, the multiplicity preselection is seen to diminish contamination from $\gamma\gamma \to \mu\mu$. The exclusivity preselection is seen to significantly suppress inclusive backgrounds passing the online trigger selection.

4.6.3 Offline selectors

Events satisfying the event preselection are classified according to the particle content in the event and passed to a generic selector which checks the kinematic balance of the two-object system and checks for additional activity in between the pair of central objects. Four categories were implemented in reflection of the final states expected from the signal:

Selector A: targets the subprocess $\gamma\gamma \to \tau_{\text{had}}\tau_{\text{had}}$ and is seeded by events containing exclusively *two* τ-candidates.

Selector B: targets the subprocess $\gamma\gamma \to \tau_{\text{had}}\tau_\mu$ and is seeded by events containing exclusively *one* selected muon and *one* τ-candidate.

Selector C: targets the subprocess $\gamma\gamma \to \tau_{\text{had}}\tau_{\text{e}}$ and is seeded by events containing *one* selected electron and *one* τ-candidate.

Selector D: targets the subprocess $\gamma\gamma \to \tau_\mu\tau_{\text{e}}$ and is seeded by events containing *one* selected muon and *one* selected electron.

The object pair in each selector A-D are required to satisfy the following kinematic requirements:

$$|\Delta p_T| \leq 30 \text{ GeV} \text{ and } |\Delta\phi| > 2.5$$

155

Events satisfying the above kinematic constraints are further subjected to a second *exclusivity veto* ("Exclusivity B"), whereby events with any detector activity at a distance greater than $\Delta R > 0.8$ from both objects in a pair are rejected. Activity is defined in terms of calorimeter clusters with $E_{cluster} > 5$ GeV and tracks with $p_T^{\text{track}} > 1.5$ GeV.

The stringency on the τ-identification is tailored to the requirements imposed by the distribution of backgrounds across the various selectors. The τ-object selection applied in each selector are briefly summarized below.

Selector A

While the subprocess $\gamma\gamma \to \tau_{\text{had}}\tau_{\text{had}}$ accounts for the largest portion of the visible cross section for $\gamma\gamma \to \tau\tau$, its offline selection is considerably challenged by background from exclusive jet production. Moreover, soft electrons from $\gamma\gamma \to ee$ failing the electron selection may readily be misinterpreted as τ-candidates. Hence, comparatively vigorous methods for τ-identification and fake suppression are called for. Both selected τ-candidates are therefore required to satisfy the `TauCutSafeCaloLoose` selection and are further "fortified" with the following selection criteria:

- Low track multiplicity: $N_{\text{track}} = 0, 1$ or 3

- Small EM radius: $R_{\text{EM}} < 0.095$

- Significant hadronic component: $\frac{E_{\text{EM}}}{E_{\text{HAD}}} < 25$

- Small ratio of high to low threshold TRT hits: $H_{\text{TRT}} < 0.12$

A significant drop in the signal selection efficiency is expected to follow from the above object selection requirements, principally caused by the transverse momentum cut built into the `TauCutSafeCaloLoose` selection ($p_T > 10$ GeV). As indicated in Figure 4.9, most selected τ-candidates will have transverse momenta below this threshold.

Selector B

The presence of a muon significantly reduces backgrounds from exclusive jets and electrons, permitting a more relaxed τ-object selection. The selected τ-candidate is therefore only subjected to the following basic track requirement:

$$N_{\text{tracks}} = 1 \,\text{or}\, 3$$

To suppress fake candidates from $\gamma\gamma \to \mu\mu$, the selected τ-candidate is further required to pass the default muon veto in which track based τ-candidates with an energy compatible with a MIP muon are rejected.

Selector C

While the presence of an electron serves to suppress backgrounds from exclusive jets, this search channel is very susceptible to background from $\gamma\gamma \to ee$ where one electron failing the electron selection described in Section 4.4.2 is available to generate a fake τ-candidate.

Selector	N_S	N_B	Z_n (30%)	Z_n (50%)	Z_n(100%)
A	3.9 ± 0.1	$1.2^{+629.5}_{-0.2}$	2.3	2.1	1.6
B	12.6 ± 0.2	$1.2^{+629.5}_{-0.2}$	5.5	5.1	4.2
C	3.5 ± 0.1	$1.7^{+1.1}_{-0.3}$	1.7	1.6	1.1
D	2.0 ± 0.1	$0.04^{+0.1}_{-0.03}$	3.1	3.1	2.9

TABLE 4.11: Expected number of signal (N_S) and background (N_B) events in selectors A-D with $\int \mathcal{L}=$ 100pb^{-1} of data, along with associated significance Z_n achieved assuming 30%, 50% and 100% uncertainty on the background estimation.

To suppress backgrounds from $\gamma\gamma \rightarrow ee$, the selected τ-candidate is required to pass the following selection:

- $p_T > 6$ GeV and at least one associated track

- pass the *tight* electron veto if the candidate has an associated track seed

- significant hadronic energy fraction: $\frac{E_{\text{HAD}}}{E_{\text{EM}}+E_{\text{HAD}}} > 0.1$

- small ratio of high to low threshold TRT hits: $H_{\text{TRT}} < 0.12$

Selector D
While this channel is almost void of backgrounds from both exclusive and inclusive sources, it accounts for only $\sim 6\%$ of the total signal cross section, making it particularly challenging to select with modest integrated luminosities.

No further selection cuts of the muon and electron objects beyond those described in Sections 4.4.1 and 4.4.2 are applied.

4.6.4 Results

The selection efficiencies of each selector described in Section 4.6.3 are summarized in Tables 4.12-4.15. Backgrounds from which no selector seeds were generated have been omitted. The errors are purely statistical and correspond to a 68.3 % confidence level modelled on a binomial distribution [94]. The expected number of signal and background events after all selection cuts are listed in Table 4.11. The table also lists the signal significance Z_n [56, 95]:

$$Z_n = \sqrt{2}\text{Erf}^{-1}(1 - 2p) \tag{4.5}$$

where the p-value indicates the probability that the background fluctuates to $\geq n = N_S+N_B$. The p-value is here expressed in terms of a Poisson probability for a background fluctuation to the observed signal, convoluted with a Gaussian background probability density with mean value N_B and standard deviation σ_{N_B} encoding the uncertainty in the background estimation:

$$p = C \int_0^\infty db \; g(N_B, \sigma_{N_B}) \sum_{i=n}^\infty \frac{b^i}{i!} e^{-b} \tag{4.6}$$

The constant C in Equation 4.6 serves to normalize the p-value to unity. Table 4.11 lists the significance Z_n evaluated under the assumption of 30%, 50% and 100% total uncertainty on the background estimation[15] and singles out Selector B and D as the most promising for enabling an observation with early data.

The fraction of true decays satisfying $p_T^{vis}(\tau_{had}) > 10$ GeV and/or $p_T^{vis}(\tau_{lep}) > 4$ GeV, is shown in Figure 4.14(a) and highlights the limited absolute sensitivity to fully hadronic τ-final states. Figure 4.14(b) compares the transverse momentum spectra of τ-objects collected by either selector against the subset of the triggered sample with exactly two reconstructed objects in the final state. The subset of the triggered spectrum in which the true decay satisfies $p_T^{vis}(\tau_{had}) > 10$ GeV and $p_T^{vis}(\tau_{lep}) > 4$ GeV is also shown. It is evident that the current selection is limited by its restricted sensitivity to hadronically decaying τ-leptons, particularly in the region below 10 GeV, but also beyond. Selector B and C are both seen extend the sensitivity reach to transverse momenta below 10 GeV.

In all selectors the dominant background contributions arise from exclusive processes, with non-exclusive backgrounds heavily suppressed by the online and offline preselection. Not surprisingly, Drell-Yan events at comparatively high transverse momenta are seen to dominate the non-exclusive contributions passing the preselection. This tendency is expected to follow from the definition of Exclusivity A. These remaining non-exclusive contributions are mitigated by the activity veto enforced through the *Exclusivity B* requirement in each selector.

The object selection is seen to be particularly injurious in **Selector A**, where almost 90% of seeds are rejected. As was previously stated, a high seed rejection is expected because the majority of reconstructed τ-candidates will have transverse momenta below the 10 GeV threshold built into the `TauCutSafeLoose` selection. In order to retain a larger fraction of fully hadronic decays, the current identification methods must necessarily be extended below 10 GeV. Table 4.11 indicates that an observation by way of Selector A is arguably very challenging with early data.

Selector B by contrast, provides the most promising channel for an observation of the process $\gamma\gamma \to \tau\tau$ with early data. Here, backgrounds are small and easier to suppress with established reconstruction and identification tools. A relaxed τ-identification gives access to τ-candidates below $p_T \sim 10$ GeV and consequently returns a higher yield. As indicated in Figure 4.14(b), Selector B is the only channel in which good reconstruction efficiency is achieved across the full kinematic regime over which the reconstruction tools are sensitive.

Despite a comparatively high seed rejection ($\sim 60\%$), Table 4.11 indicates that **Selector C** may still offer some sensitivity to $\gamma\gamma \to \tau_{had}\tau_e$ events. The presence of an

---

[15]It is assumed that the uncertainty on the background estimation is dominated by systematic rather than statistical effects.
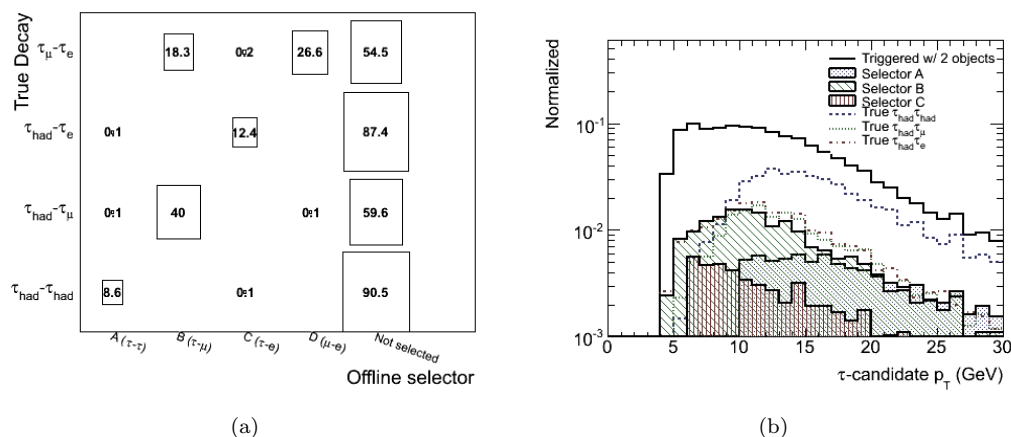
FIGURE 4.14: (a) The fraction of true decays satisfying $p_T^{vis}(\tau_{had}) > 10$ GeV and/or $p_T^{vis}(\tau_{lep}) > 4$ GeV, selected by each offline selector after online trigger selection. (b) Transverse momentum spectrum of τ-candidates in the subset of the triggered signal with exactly two reconstructed objects along with the subsets selected by Selectors A-C. The subsets corresponding to true $p_T(\tau_{had}) > 10$ GeV and $p_T(\tau_{lep}) > 4$ GeV are also shown for $\gamma\gamma \to \tau_{had}\tau_{had}$, $\gamma\gamma \to \tau_{had}\tau_\mu$ and $\gamma\gamma \to \tau_{had}\tau_e$ decays. Selector B is seen to be the only selector with a good efficiency with respect to the target process across the full spectrum.

electron effectively suppresses backgrounds from exclusive jet production. The remaining background therefore consists almost exclusively of poorly reconstructed events from $\gamma\gamma \to ee$. As such, any observation in this channel will hinge on a robust and well understood electron veto.

Virtually background free, **Selector D** provides another promising channel for the observation of the process $\gamma\gamma \to \tau\tau$ through the fully leptonic channel. Despite the comparatively small branching fraction of the process $\gamma\gamma \to \tau_\mu\tau_e$, Table 4.11 indicates that an observation may be possible in early data provided sufficient pile-up free data is at hand.

About 30% of triggered signal events have only one reconstructed object in the final state. Such events will automatically fail to qualify for any of the aforementioned selectors. While it may be possible to recover some of these events by loosening the requirements on the objects of the central system, (*e.g.* by seeding on a muon with back-to-back activity in the form of a track system or calorimeter clusters), initial studies have proven this a difficult task with only moderate gain.

The offline selection of fully leptonic same flavour decays, in which both τ-leptons decay into either a pair of muons or a pair of electrons has not been attempted herein. While such a selection is arguably very challenging in face of backgrounds from $\gamma\gamma \to \mu\mu$ and $\gamma\gamma \to ee$, the distorted kinematics of the central system and small $\not{E}_T$ caused by the decay neutrinos may possibly offer a handle on the offline selection.

Process	Seed		Object selection		Kinematics		Exclusivity B	
	$\epsilon_{\text{sel}}(\%)$	N_{100}	$\epsilon_{\text{sel}}(\%)$	N_{100}	$\epsilon_{\text{sel}}(\%)$	N_{100}	$\epsilon_{\text{sel}}(\%)$	N_{100}
$\gamma\gamma \to \tau\tau$	$(1.38 \pm 0.01) \cdot 10^{-1}$	37.3 ± 0.3	$(1.75 \pm 0.04) \cdot 10^{-2}$	4.7 ± 0.1	$(1.59 \pm 0.04) \cdot 10^{-2}$	4.2 ± 0.1	$(1.46^{+0.04}_{-0.03}) \cdot 10^{-2}$	3.9 ± 0.1
$\gamma\gamma \to ee$	$(1.41 \pm 0.02)10^{-1}$	183 ± 3	$(1.71^{+1.04}_{0.63}) \cdot 10^{-4}$	$0.22^{+0.14}_{-0.08}$	$(1.71^{+1.04}_{-0.63}) \cdot 10^{-4}$	$0.22^{+0.14}_{0.08}$	$(1.71^{+1.04}_{0.63}) \cdot 10^{-4}$	$0.22^{+0.14}_{0.08}$
$\gamma\gamma \to q\bar{q}$	$(9.0 \pm 0.3) \cdot 10^{-2}$	60 ± 2	$(1.80^{+0.46}_{-0.39}) \cdot 10^{-3}$	1.2 ± 0.3	$(1.80^{+0.46}_{-0.39}) \cdot 10^{-3}$	1.2 ± 0.3	$(1.50^{+0.42}_{-0.36}) \cdot 10^{-3}$	$0.9^{+0.3}_{-0.2}$
CEP gluons	$(1.1^{+0.2}_{-0.1}) \cdot 10^{-3}$	$(2.89^{+0.41}_{-0.37}) \cdot 10^{4}$	$< 2.30 \cdot 10^{-5}$	< 603	$< 2.30 \cdot 10^{-5}$	< 603	$< 2.30 \cdot 10^{-5}$	< 603
Z→ee/$\tau\tau$	$(5.71^{+0.4}_{0.3}) \cdot 10^{-5}$	9.7 ± 0.6	$(1.40 \pm 0.20) \cdot 10^{-5}$	2.4 ± 0.3	$(1.40 \pm 0.20) \cdot 10^{-5}$	2.4 ± 0.3	$< 3.18 \cdot 10^{-7}$	< 0.05
QCD dijets	$(2.93^{+0.48}_{-0.44})$	6437^{+1061}_{-956}	$(0.71^{+1.07}_{-0.52}) \cdot 10^{-6}$	156^{+236}_{-115}	$(0.71^{+1.07}_{-0.52}) \cdot 10^{-6}$	156^{+236}_{-115}	$< 8.22 \cdot 10^{-7}$	< 180

TABLE 4.12: Selector A: tau-tau

Process	Seed		Object selection		Kinematics		Exclusivity B	
	$\epsilon_{\text{sel}}(\%)$	N_{100}	$\epsilon_{\text{sel}}(\%)$	N_{100}	$\epsilon_{\text{sel}}(\%)$	N_{100}	$\epsilon_{\text{sel}}(\%)$	N_{100}
$\gamma\gamma \to \tau\tau$	$(5.51 \pm 0.07) \cdot 10^{-2}$	14.8 ± 0.2	$(5.51 \pm 0.07) \cdot 10^{-2}$	14.8 ± 0.2	$(4.94 \pm 0.06) \cdot 10^{-2}$	13.3 ± 0.2	$(4.70 \pm 0.06) \cdot 10^{-4}$	12.6 ± 0.2
$\gamma\gamma \to \mu\mu$	$(8.16^{+1.86}_{1.47}) \cdot 10^{-4}$	$1.7^{+0.4}_{-0.3}$	$(8.16^{+1.86}_{-1.47}) \cdot 10^{-4}$	$1.7^{+0.4}_{-0.3}$	$(5.69^{+1.61}_{-1.22}) \cdot 10^{-4}$	1.1 ± 0.3	$(5.69^{+1.61}_{1.22}) \cdot 10^{-4}$	1.1 ± 0.3
$\gamma\gamma \to q\bar{q}$	$(1.47^{+0.43}_{-0.36}) \cdot 10^{-3}$	$0.9^{+0.3}_{-0.2}$	$(3.16^{+2.26}_{-1.52}) \cdot 10^{-4}$	$0.2^{+0.2}_{-0.1}$	$(3.16^{+2.26}_{-1.52}) \cdot 10^{-4}$	$0.2^{+0.2}_{-0.1}$	$(3.16^{+2.26}_{-1.52}) \cdot 10^{-4}$	$0.2^{+0.2}_{-0.1}$
CEP gluons	$(4.17^{+3.87}_{-2.37}) \cdot 10^{-4}$	1093^{+1015}_{-621}	$< 2.39 \cdot 10^{-5}$	< 628	$< 2.39 \cdot 10^{-5}$	< 628	$< 2.39 \cdot 10^{-5}$	< 628
$Z \to \tau\tau$	$(2.13^{+0.43}_{-0.38}) \cdot 10^{-5}$	$1.82^{+0.37}_{-0.32}$	$(1.45^{+0.36}_{-0.31}) \cdot 10^{-5}$	$1.23^{+0.31}_{0.26}$	$1.22^{+0.34}_{-0.28}$	$1.04^{+0.28}_{-0.24}$	$< 8.77 \cdot 10^{-7}$	0.07

TABLE 4.13: Selector B: tau-muon

Process	Seed		Object selection		Kinematics		Exclusivity B	
	$\epsilon_{\text{sel}}(\%)$	N_{100}	$\epsilon_{\text{sel}}(\%)$	N_{100}	$\epsilon_{\text{sel}}(\%)$	N_{100}	$\epsilon_{\text{sel}}(\%)$	N_{100}
$\gamma\gamma \to \tau\tau$	$(4.37 \pm 0.06)10^{-2}$	11.7 ± 0.2	$(1.57 \pm 0.04) \cdot 10^{-2}$	4.2 ± 0.1	$(1.41 \pm 0.03) \cdot 10^{-2}$	3.7 ± 0.1	$(1.32 \pm 0.03) \cdot 10^{-2}$	3.5 ± 0.1
$\gamma\gamma \to ee$	$(3.99 \pm 0.03) \cdot 10^{-1}$	518 ± 4	$(1.4 \pm 0.2) \cdot 10^{-3}$	1.8 ± 0.3	$(1.3 \pm 0.2) \cdot 10^{-3}$	1.7 ± 0.3	$(1.2 \pm 0.2) \cdot 10^{-3}$	1.6 ± 0.3
$\gamma\gamma \to q\bar{q}$	$(1.1 \pm 0.4) \cdot 10^{-3}$	0.7 ± 0.2	$(2^{+2}_{-1}) \cdot 10^{-4}$	$0.13^{+0.12}_{-0.08}$	$(2^{+2}_{-1}) \cdot 10^{-4}$	$0.13^{+0.12}_{-0.08}$	$(2^{+2}_{-1}) \cdot 10^{-4}$	$0.13^{+0.12}_{-0.08}$
DY	$(5.3^{+0.7}_{-0.6}) \cdot 10^{-5}$	32 ± 4	$(5.0^{+2.7}_{-1.7}) \cdot 10^{-6}$	$3.0^{+1.6}_{1.0}$	$(4.6^{+2.7}_{-1.7})$	$2.8^{+1.7}_{-1.0}$	$< 1.66 \cdot 10^{-6}$	< 1.0

TABLE 4.14: Selector C: tau-electron

Process	Seed		Object selection		Kinematics		Exclusivity B	
	$\epsilon_{\text{sel}}(\%)$	N_{100}	$\epsilon_{\text{sel}}(\%)$	N_{100}	$\epsilon_{\text{sel}}(\%)$	N_{100}	$\epsilon_{\text{sel}}(\%)$	N_{100}
$\gamma\gamma \to \tau\tau$	$(8.59^{+0.27}_{-0.26}) \cdot 10^{-3}$	2.3 ± 0.1	$(8.53^{+0.27}_{-0.26}) \cdot 10^{-3}$	2.2 ± 0.1	$(7.78^{+0.26}_{-0.25}) \cdot 10^{-3}$	2.0 ± 0.1	$(7.54^{+0.25}_{-0.24}) \cdot 10^{-3}$	2.0 ± 0.1
$\gamma\gamma \to ee$	$(3.33^{+7.40}_{2.44}) \cdot 10^{-5}$	$0.04^{+0.10}_{-0.03}$	$(3.33^{+7.40}_{-2.44}) \cdot 10^{-5}$	$0.04^{+0.10}_{-0.03}$	$(3.33^{+7.40}_{-2.44}) \cdot 10^{-5}$	$0.04^{+0.10}_{-0.03}$	$(3.33^{+7.40}_{-2.44}) \cdot 10^{-5}$	$0.04^{+0.10}_{-0.03}$
$Z \to \tau\tau$	$(2.03^{+1.22}_{-0.87}) \cdot 10^{-6}$	0.17 ± 0.01	$(2.03^{+1.22}_{-0.87}) \cdot 10^{-6}$	0.17 ± 0.01	$(2.03^{+1.22}_{-0.87}) \cdot 10^{-6}$	0.17 ± 0.01	$< 5.84 10^{-7}$	< 0.05

TABLE 4.15: Selector D: muon-electron

4.6.5 A note on systematic uncertainties

While the results summarized in Section 4.6.4 suggest that an observation of the process $\gamma\gamma \to \tau\tau$ in early data collected by ATLAS may be possible, such an observation hinges on a proper understanding and control of all possible effects that may introduce systematic errors into the analysis. While a full consideration of systematic effects is outside the scope of this analysis, a few potential sources of systematic uncertainties are listed below.

The analysis is particularly vulnerable to any effects that might distort the *exclusive appearance* of the signal. Even in the absence of additional pile-up interactions, such distortions may arise from various machine backgrounds, as discussed in Section 4.5.3.

Moreover, the *calorimetric exclusivity* as enforced through the Exclusivity A and B selections in the offline analysis, is likely to be sensitive to the noise level in the calorimeters. If noise fluctuations are large, an exclusive event may be mistakenly rejected as an inclusive events. Dead cells, while less likely to affect the signal selection efficiency, may weaken the rejection of non-exclusive events [16]. In a similar fashion, the online selection will necessarily be sensitive to variations in the noise level and response pattern of the MBTS.

The strong dependence of the cross section on the transverse momentum of the outgoing central lepton pair, arguably makes the analysis sensitive to variations in both online and offline object reconstruction efficiencies. Because the analysis presented herein utilizes reconstruction tools close to their respective sensitivity thresholds, any degradation in the reconstruction performance at low transverse momenta may severely impede a successful observation.

4.7 Extending the reach with heavy ions

As was mentioned in Section 1.3.4, the LHC programme will include regular shorter periods ($\sim$1 month) of collision runs with heavy ions, during which the coherent action of all the protons in a nucleus will serve to significantly enhance the production cross section for two-photon processes. In recognition of this potential, studies have been undertaken to explore the prospects offered by ultra-peripheral heavy ion collisions [96][97]. While a study into the feasibility of utilizing such runs for the collection of $\gamma\gamma \to \tau\tau$ events is outside the scope of this analysis, it is amusing to consider the prospects offered by early heavy ion runs.

Table 4.16 lists cross sections as predicted by TPHIC MC [98][17] for the process $\gamma\gamma \to ll$ in Pb-Pb (Z=82) collisions at $\sqrt{s_{NN}} = 4/5.5$ TeV/n.

The production cross sections are seen to increase significantly. Assuming early operation with Pb-Pb collision at $\sqrt{s_{NN}} =$4 TeV, Table 4.16 indicates that a few hundred $\gamma\gamma \to$

---

[16]Noisy cells may be identified and appropriately masked using data from collisions with empty events. Dead cells in the forward calorimeters should be identifiable with non-exclusive events.

[17]I am grateful to V. Pozdnyakov for providing the code.

Process	σ (pb)		
	$\sqrt{s_{pp}} = 7$ TeV	$\sqrt{s_{NN}} = 4$ TeV	$\sqrt{s_{NN}} = 5.5$ TeV
$\gamma\gamma \to ee$ ($p_T > 5$ GeV, $|\eta| < 2.5$)	4.6	3.2×10^8	5.3×10^8
$\gamma\gamma \to \mu\mu$ ($p_T > 4$ GeV, $|\eta| < 2.5$)	8.0	3.1×10^8	4.8×10^8
$\gamma\gamma \to \tau\tau$ ($p_T > 10$ GeV, $|\eta| < 2.5$)	0.8	5.6×10^6	10.6×10^6

TABLE 4.16: Production cross sections for two-photon processes in pp collisions at $\sqrt{s_{pp}} = 7$ TeV and in Pb-Pb collisions at $\sqrt{s_{NN}} = 5.5$ TeV.

$\tau\tau$ events may be produced within one month of operation at $\mathcal{L} \sim 10^{25} \text{cm}^{-2}\text{s}^{-1}$. At nominal collision energy ($\sqrt{s_{NN}} = 5.5$ TeV), an integrated luminosity of 0.5 nb (roughly corresponding to the data collected during the yearly LHC operative period in heavy ion mode), should yield approximately 5000 $\gamma\gamma \to \tau\tau$ events.

4.8 Summary

Two-photon exchange processes at the LHC have received renewed attention in recent years. The studies presented herein aimed to explore the feasibility of observing the process $\gamma\gamma \to ll$ in early ATLAS data, with particular emphasis on the $\gamma\gamma \to \tau\tau$ channel. Remarkably clean event final states void of hadronic debris, set such processes apart from the large majority of interactions at the LHC. In the absence of forward proton tagging devices, the offline selection of such events is largely constrained to the early phase of data taking when pile-up effects prone to destroy the exclusive appearance of such events are negligible.

While the total cross sections are large, the production rates reduce rapidly with the energy of the outgoing lepton pair. Despite the tendency to produce final states below the sensitivity reach of the ATLAS detector, the visible cross sections for the processes $\gamma\gamma \to ee$ and $\gamma\gamma \to \mu\mu$ are found to remain sufficiently large (> 10 pb) in $\sqrt{s} = 7$ TeV proton-proton collisions to enable a sizeable offline selection with early data. The decay of the τ-lepton renders the visible cross section for the process $\gamma\gamma \to \tau\tau$ significantly smaller, making an offline selection with early data more challenging. Futhermore, the majority of τ-leptons from two-photon exchanges are produced in a unique soft kinematic regime, for which current online and offline reconstruction tools are not properly optimized. Adding to the requirement of a low pile-up environment, these features pose unique challenges to both online and offline selections.

The online selection of exclusive lepton final states was found to be challenged primarily by the application of large prescales on all low threshold single lepton triggers. To circumvent this problem, three new trigger chains were developed with which unprescaled running of low threshold triggers is enabled through a veto on the MBTS at minimal cost to the integrated rate. The new trigger chains were shown to enable an efficient collection of $\gamma\gamma \to ee$ and $\gamma\gamma \to \mu\mu$ events, counting $\mathcal{O}(1000)$ events with 100 pb^{-1} of pile-up free data, when all scattering contributions are combined. Similar trigger efficiencies are achieved on semi-leptonic $\gamma\gamma \to \tau\tau$ events, whereas a more moderate efficiency is achieved with respect to fully hadronic events. The trigger chains are not

restricted to $\gamma\gamma \to ll$, but should be sensitive to generic exclusive final states involving leptons.

Finally, an offline selection strategy for the process $\gamma\gamma \to \tau\tau$ was presented targeting fully hadronic, semi-leptonic and fully-leptonic final states. The offline selection is challenged by large, but reducible non-exclusive backgrounds, various exclusive backgrounds and inefficiencies of the reconstruction algorithms at low transverse momenta. An efficient suppression of all large non-exclusive backgrounds is achieved. Suppression of remaining exclusive backgrounds is best achieved in search channels targeting $\gamma\gamma \to \tau_{\mathrm{had}}\tau_\mu$ and $\gamma\gamma \to \tau_\mu\tau_{\mathrm{e}}$ events, both in which an observation of the process $\gamma\gamma \to \tau\tau$ may be possible with 100 pb^{-1} of pile-up free data. Such an observation would be the first observation of the process $\gamma\gamma \to \tau\tau$ at a hadron collider facility.

Appendix A

The ATLAS coordinate system and associated nomenclature

ATLAS employs a right-handed Cartesian coordinate system, whose origin is located at the center of the detector and in which

> the z-axis (horizontal) is directed along the beamline,
>
> the x-axis (horizontal) points to the center of the LHC ring,
>
> and the y-axis (vertical) points vertically upwards.

The associated polar coordinate system more commonly used herein is defined in terms of:

> The *azimuthal* angle $\phi \equiv \arctan \frac{p_y}{p_x}$, $\phi \in [-\pi, +\pi]$, where $\phi = 0$ corresponds to +x and $\phi = \frac{\pi}{2}$ corresponds to +y.
>
> The *polar* angle $\theta \equiv \arctan \frac{p_T}{p_z}$, $\theta \in [0, 2\pi]$, where $\theta = 0$ corresponds to +z and $\theta = \pi$ corresponds to -z

The polar angle is commonly parametrized in terms of the *pseudorapidity* η:

$$\eta = -\ln\left[\tan\left(\frac{\theta}{2}\right)\right] = \frac{1}{2}\ln\left(\frac{|\mathbf{p}| + p_z}{|\mathbf{p}| - p_z}\right) \tag{A.1}$$

which approaches the true rapdidity $y = \frac{1}{2}\ln\left(\frac{E+p_z}{E-p_z}\right)$ in the massless limit $|\mathbf{p}| \sim E$.

It is often convenient to parametrize the detector volume in terms of η and ϕ. The direction of a particle can be expressed as a point in (η, ϕ)-space and the distance between two locations (η_1, ϕ_1) and (η_2, ϕ_2) as $\Delta R \equiv \sqrt{(\eta_2 - \eta_1)^2 - (\phi_2 - \phi_1)^2}$.

Appendix B

Monte Carlo Event Samples

Details pertaining to simulated data used in the various studies presented herein.

B.1 Chapter 2: PanTau

AODs where privately reconstructed from the centrally produced RDO datasets listed in Table B.1. The following tags of the `eflowRec` package were used for reconstruction in ATHENA `15.4.0`:

  `eflowRec-00-02-30`

  `eflowEvent-00-01-49`

  `eflowEventTPCnv-00-00-13`

  `eflowAthenaPool-00-00-05`

Process	Data sample	Kinematic cuts
$Z \to \tau\tau$	misal1_mc12.005179.ZtautauNoEF.digit.RDO.v12000605	-
$W \to \tau\nu_\tau$	misal1_csc11.005107.pythia_Wtauhad.digit.RDO.v12003103	$p_T(\tau_{vis}) > 12$ GeV
QCD dijets (J0)	misal1_csc11.005009.J0_pythia_jetjet.digit.RDO.v12003103	8-17 GeV
QCD dijets (J1)	misal1_csc11.005009.J0_pythia_jetjet.digit.RDO.v12003103	17-35 GeV
QCD dijets (J2)	misal1_csc11.005009.J0_pythia_jetjet.digit.RDO.v12003103	35-70 GeV
QCD dijets (J3)	misal1_csc11.005009.J0_pythia_jetjet.digit.RDO.v12003103	70-140 GeV

TABLE B.1: Monte Carlo RDO datasets employed in the development of PanTau.

B.2 Chapter 3: $\langle \not{E}_T \rangle$

Various samples were used, all centrally produced. These include CSC11 QCD dijet samples J1-J8, where simulation, digitization and reconstruction were performed with AtlasProduction caches 11.0.41 and 11.0.42.

Data set	Data sample	p_T-bin (GeV)	Cross-section (mb)	No. of events
trig1_misal1_csc11.005013.J4_pythia_jetjet.recon.v12000605	005013 (J4)	140-280	3.077×10^{-4}	26.6k
trig1_misal1_csc11.005014.J5_pythia_jetjet.recon.v12000605	005014 (J5)	280-560	1.258×10^{-5}	46.7k
trig1_misal1_csc11.005015.J6_pythia_jetjet.recon.v12000605	005015 (J6)	560-1120	3.584×10^{-7}	33.0k
trig1_misal1_csc11.005016.J7_pythia_jetjet.recon.v12000605	005016 (J7)	1120-2280	5.757×10^{-9}	0k
trig1_misal1_csc11.005017.J8_pythia_jetjet.recon.v12000605	005017 (J8)	> 2280	2.042×10^{-11}	0k
trig1_misal1_mc12.008090.pythia_J4_Nj2_FMET100.recon.v12000605	008090 (J4)	140-280	3.077×10^{-4}	5k/10k
trig1_misal1_mc12.008091.pythia_J5_Nj2_FMET100.recon.v12000605	008091 (J5)	280-560	1.258×10^{-5}	33.3k/60k
trig1_misal1_mc12.008092.pythia_J6_Nj2_FMET100.recon.v12000605	008092 (J6)	560-1120	3.584×10^{-7}	4k/20k
trig1_misal1_mc12.008093.pythia_J7_Nj2_FMET100.merge.v12000605	008093 (J7)	1120-2280	5.757×10^{-9}	0k/5k
trig1_misal1_mc12.008094.pythia_J8_Nj2_FMET100.merge.v12000605	008094 (J8)	> 2280	2.042×10^{-11}	0k/5k

TABLE B.2: Monte Carlo sample statistics.

Validation studies of the generator filter mechanism with centrally produced unfiltered and filtered samples were performed with the datasets listed in Table B.2. These samples were passed through `HighPtView-00-00-40` in ATHENA 12.0.6.

B.3 Chapter 4: $\gamma\gamma \to \tau\tau$

B.3.1 Exclusive signal and exclusive backgrounds

All $\gamma\gamma \to ll$ samples were privately generated with **LPAIR** [88, 89]. All $\gamma\gamma \to q\bar{q}$ samples (q=u,d,s,c,b) were privately generated with **SHERPA** 1.2.1 [99] using the proton photon PDFs:

```
(isr){
  PDF_LIBRARY=MRST04QEDSherpa
  PDF_SET=MRST04QED
  PDF_GRID_PATH=MRST04Grid
}(isr)
```

The output of either Monte Carlo generator was interfaced to ATHENA for full simulation, digitization and reconstruction. `AtlasProduction` cache 15.6.6.5 was used throughout with:

- DB release: `9.6.1`

- Conditions tag: `OFLCOND-DR-BS7T-ANom-11`

- Trigger configuration: `MCRECO:DB:TRIGGERDBMC:107,61,92`, corresponding to the `MC_lumi1E31_simpleL1Calib_physics_prescale` trigger menu.

All other settings were concordant with the following production tags: `s765` and `r1250`.

CEP gluon-gluon samples were centrally generated with **Exhume** [100] and privately reprocessed with the aforementioned simulation and reconstruction settings. All exclusive samples used are listed in Table B.3.

B.3.2 Non-exclusive background processes

All non-exclusive background samples used were centrally produced and are listed in Table B.4.

Process	Kinematics	σ (pb)	Events
$\gamma\gamma \to \tau\tau$	p_T >10 GeV, $|\eta| < 2.5$; elastic	0.81	50000
$\gamma\gamma \to \tau\tau$	p_T >10 GeV, $|\eta| < 2.5$; semi-elastic	0.85	31000
$\gamma\gamma \to \tau\tau$	p_T >10 GeV, $|\eta| < 2.5$; inelastic	1.04	44499
$\gamma\gamma \to \tau\tau$	p_T >15 GeV, $|\eta| < 2.5$; elastic	0.28	30000
$\gamma\gamma \to \tau\tau$	p_T >15 GeV, $|\eta| < 2.5$; semi-elastic	0.33	30000
$\gamma\gamma \to \tau\tau$	p_T >15 GeV, $|\eta| < 2.5$; inelastic	0.44	9999
$\gamma\gamma \to \tau\tau$	p_T >20 GeV, $|\eta| < 2.5$; elastic	0.13	10000
$\gamma\gamma \to \mu\mu$	p_T >4 GeV, $|\eta| < 2.5$; elastic	8.03	10000
$\gamma\gamma \to \mu\mu$	p_T >4 GeV, $|\eta| < 2.5$; semi-elastic	6.52	10000
$\gamma\gamma \to \mu\mu$	p_T >4 GeV, $|\eta| < 2.5$; inelastic	6.50	10000
$\gamma\gamma \to ee$	p_T >5 GeV, $|\eta| < 2.5$; elastic	4.62	10000
$\gamma\gamma \to ee$	p_T >5 GeV, $|\eta| < 2.5$; semi-elastic	4.10	10000
$\gamma\gamma \to ee$	p_T >5 GeV, $|\eta| < 2.5$; inelastic	4.22	9881
$\gamma\gamma \to q\bar{q}$	p_T >5 GeV, $|\eta| < 2.5$; (inelastic)	26.1	10000
$\gamma\gamma \to q\bar{q}$	p_T >10 GeV, $|\eta| < 2.5$; (inelastic)	6.66	10000
$\gamma\gamma \to q\bar{q}$	p_T >15 GeV, $|\eta| < 2.5$; (inelastic)	2.77	10000
$\gamma\gamma \to q\bar{q}$	p_T >20 GeV, $|\eta| < 2.5$; (inelastic)	1.43	9500
$pp \oplus gg \oplus pp$	$E_T > 8$GeV, CEP	2.63×10^5	30000
$pp \oplus gg \oplus pp$	$E_T > 17$GeV, CEP	7.46×10^3	30000
$pp \oplus gg \oplus pp$	$E_T > 35$GeV, CEP	202	30000

TABLE B.3: Privately produced samples for various exclusive processes employed in $\gamma\gamma \to \tau\tau$ analysis.

Process	σ (pb)	Events	ATLAS dataset (Prefix: mc09_7TeV., Suffix: _r1260)
Minimum bias (ND)	$484.45{\times}10^8$	$1.81{\times}10^7$	105001.pythia_minbias.merge.AOD.e517_s787_s767_r1250
QCD (8-17 GeV)	$985.34{\times}10^7$	$1.10{\times}10^6$	105009.J0_pythia_jetjet.merge.AOD.e468_s766_s767_r1251
QCD (17-35 GeV)	$678.03{\times}10^6$	$1.08{\times}10^6$	105010.J1_pythia_jetjet.merge.AOD.e468_s766_s767_r1251
QCD (35-70 GeV)	$409.79{\times}10^5$	$1.40{\times}10^6$	105011.J2_pythia_jetjet.merge.AOD.e468_s766_s767_r1251
QCD (70-40 GeV)	$219.60{\times}10^4$	$1.40{\times}10^6$	105012.J3_pythia_jetjet.merge.AOD.e468_s766_s767_r1251
$Z^0/\gamma \to e^{\pm}e^{\mp}$	855.75	$4.54{\times}10^6$	106046.PythiaZee_no_filter.merge.AOD.e468_s765_s767_r1250
$Z^0/\gamma \to \mu^{\pm}\mu^{\mp}$	855.64	$4.43{\times}10^6$	106047.PythiaZmumu_no_filter.merge.AOD.e468_s765_s767_r1250
$Z^0/\gamma \to \tau^{\pm}\tau^{\mp}$	854.02	$1.97{\times}10^6$	106052.PythiaZtautau.merge.AOD.e468_s765_s767_r1250
DY low M $\mu^{\pm}$ (3 GeV)	4407	$4.99{\times}10^5$	108321.PythiaDrellYanLowM_mu3.merge.AOD.e518_s765_s767_r1250
DY low M $e^{\pm}$ (3 GeV)	4406.1	$4.99{\times}10^5$	108322.PythiaDrellYanLowM_ee3.merge.AOD.e518_s765_s767_r1250
DY low M $\tau^{\pm}$ ($M_{\tau\tau}$ >10 GeV)	3443.4	$1.95{\times}10^5$	107055.PythiaDrellYanLowMtautau_M10.merge.AOD.e526_s765_s767_r1250
$J/\psi \to \mu^{\pm}\mu^{\mp}$	$2.31{\times}10^9$	$4.97{\times}10^6$	108496.Pythia_directJpsimu0mu0.merge.AOD.e540_s765_s767_r1250
$J/\psi \to \mu^{\pm}\mu^{\mp}$ (4 GeV)	$2.308{\times}10^9$	$1.82{\times}10^6$	108407.Pythia_directJpsimu4mu4.merge.AOD.e477_s765_s767_r1250
$J/\psi \to e^{\pm}e^{\mp}$ (3 GeV)	$246.58{\times}10^6$	$8.99{\times}10^5$	105734.Pythia_direct_Jpsie3e3.merge.AOD.e511_s765_s767_r1250
$\Upsilon \to \mu^{\pm}\mu^{\mp}$ (4 GeV)	$19.728{\times}10^6$	$9.50{\times}10^4$	108484.Pythia_directUpsilonmu4mu4.merge.AOD.e477_s765_s767_r1250

TABLE B.4: Data samples for various inclusive processes employed in $\gamma\gamma \to \tau\tau$ analysis.

Appendix C

$\displaystyle{\not{E}_T^{\textbf{fake}}}$ probability distribution function

Derivation of the probability density distribution of N independent gaussian random variables as a function of radial distance in the space defined by those variables.

Consider N independent gaussian random variables $g(x_i)$ of the general form:

$$g(x_i) = \frac{1}{\sigma\sqrt{2\pi}} \exp\left(\frac{x_i^2}{2\sigma^2}\right)$$

where $i \leq N$.

The probability $\mathcal{P}(R)$ of being in a small shell of volume dV at radius R is:

$$
\begin{aligned}
\mathcal{P}(R) &= g(x_1, ..., x_i, ..., x_N)dV \\
&= \prod_{i=1}^{N} g(x_i)dV \\
&= \frac{1}{\sigma^N (2\pi)^{\frac{N}{2}}} \exp\left(\frac{-r^2}{2\sigma^2}\right)dV \\
&= \mathcal{F}_N(r)dr
\end{aligned}
$$

where $\mathcal{F}_N(r)$ is the probability density of the this probability sphere as a function of $r = \sqrt{\sum_{i=1}^{N} x_i^2}$.

With the volume element dV is given as:

$$dV = \frac{\pi^{\frac{N}{2}}}{\Gamma\left(\frac{N}{2} + 1\right)} N r^{N-1} dr$$

the probability density $\mathcal{F}_N(r)$ can now be explicitly computed:

$$\mathcal{F}_N(r) = \left[(\sqrt{2})^{N-2} \sigma^N \Gamma\left(\frac{N}{2} \right) \right]^{-1} r^{N-1} \exp\left(\frac{-r^2}{2\sigma^2} \right)$$

Finally, the mean value $\langle r \rangle$ of the probability density function $\mathcal{F}_N(r)$ is given as:

$$\begin{aligned}
\langle r \rangle &= \int r \mathcal{F}_N(r) dr \\
&= \left[(\sqrt{2})^{N-2} \sigma^N \Gamma\left(\frac{N}{2} \right) \right]^{-1} \int_0^\infty r^N \exp\left(\frac{-r^2}{2\sigma^2} \right) dr \\
&= \sqrt{2} \sigma \frac{\Gamma\left(\frac{N+1}{2} \right)}{\Gamma\left(\frac{N}{2} \right)}.
\end{aligned}$$

Bibliography

[1] Lyndon Evans. *The Large Hadron Collider: a marvel of technology*. Fundamental Sciences. EPFL Press, Lausanne, 2009.

[2] John Ellis and Keith A Olive. Supersymmetric Dark Matter Candidates. (CERN-PH-TH-2010-004), Jan 2010. URL http://cdsweb.cern.ch/record/1234835?ln=en.

[3] Christiane Lefevre. The CERN accelerator complex. Complexe des accélérateurs du CERN. Jun 2006.

[4] Stefano Catani. Aspects of QCD, from the Tevatron to the LHC, 2000. URL http://www.citebase.org/abstract?id=oai:arXiv.org:hep-ph/0005233.

[5] Brüning, Oliver Sim. LHC challenges and upgrade options. *J. Phys.: Conf. Ser.*, 110:112002, 2008.

[6] Rüdiger Schmidt. The LHC accelerator: technology and first commissioning. 430. WE-Heraeus-Seminar: Accelerators and Detectors at the Technology Frontier, 2009. URL http://rudi.home.cern.ch/rudi/docs/Hereaus-Bad-Honnef-2009.ppt.

[7] Brüning, Oliver Sim and Collier, Paul and Lebrun, P and Myers, Stephen and Ostojic, Ranko and Poole, John and Proudlock, Paul. *LHC Design Report*. CERN, Geneva, 2004. URL http://cdsweb.cern.ch/record/782076.

[8] Tevatron Run II Handbook, 2001. URL http://www-bd.fnal.gov/runII/.

[9] CERN Press Office. LHC to restart in 2009, 2008. URL http://press.web.cern.ch/press/PressReleases/Releases2008/PR17.08E.html.

[10] CERN Press Office. LHC to run at 3.5 TeV for early part of 2009-2010 run rising later, 2009. URL http://press.web.cern.ch/press/PressReleases/Releases2009/PR13.09E.html.

[11] M. Giovannozzi W. Herr J. Jowett M. Lamont E. Shaposhnikova R. Assmann, M. Ferro-Luzzi. Beam parameters and machine performance to be reached in 2010. 2010. URL http://lhc-commissioning.web.cern.ch/lhc-commissioning/luminosity/MG_2010_parameters.pdf.

[12] Michelangelo L Mangano and T J Stelzer. Tools for the simulation of hard hadronic collisions. *Annu. Rev. Nucl. Part. Sci.*

[13] F Petriello. Perturbative QCD for LHC Physics, 2009. URL http://www-conf.slac.stanford.edu/ssi/2009/images/petriello080709.pdf.

[14] Michael E Peskin and Daniel V Schroeder. *An Introduction to Quantum Field Theory; 1995 ed.* Westview, Boulder, CO, 1995.

[15] T. Ohl. Feynmanndiagramme fur Anfänger, 40. Herbstschule Maria Laach, 2.-12.09.08, 2008. URL http://maria-laach.physik.uni-siegen.de/Folien/2008/Ohl/Laach2008.pdf.

[16] V. N. Gribov and L. N. Lipatov. Deep inelastic e p scattering in perturbation theory. *Sov. J. Nucl. Phys.*, 15:438–450, 1972.

[17] Guido Altarelli and G. Parisi. Asymptotic Freedom in Parton Language. *Nucl. Phys.*, B126:298, 1977.

[18] Yuri L. Dokshitzer. Calculation of the Structure Functions for Deep Inelastic Scattering and e+ e- Annihilation by Perturbation Theory in Quantum Chromodynamics. *Sov. Phys. JETP*, 46:641–653, 1977.

[19] John C. Collins, Davison E. Soper, and George Sterman. Factorization of Hard Processes in QCD. *Adv. Ser. Direct. High Energy Phys.*, 5:1–91, 1988. URL http://aps.arxiv.org/abs/hep-ph/0409313v1.

[20] M. A. Dobbs et al. Les Houches guidebook to Monte Carlo generators for hadron collider physics. 2004. URL http://arxiv.org/abs/hep-ph/0403045.

[21] B. R. Webber. Soft QCD and Monte Carlo, 2000. URL http://moriond.in2p3.fr/QCD00/transparencies/4_wednesday/am/webber/proceedings.ps.gz.

[22] Bo Andersson, G. Gustafson, G. Ingelman, and T. Sjostrand. Parton Fragmentation and String Dynamics. *Phys. Rept.*, 97:31–145, 1983.

[23] B. R. Webber. A QCD Model for Jet Fragmentation Including Soft Gluon Interference. *Nucl. Phys.*, B238:492, 1984.

[24] The two-photon particle production mechanism. physical problems. applications. equivalent photon approximation. *Physics Reports*, 15(4):181 – 282, 1975. ISSN 0370-1573.

[25] J. de Favereau de Jeneret et al. High energy photon interactions at the LHC. 2009. URL http://arxiv.org/abs/0908.2020.

[26] Xavier Rouby. Measurements of photon induced processes in CMS and forward proton detection at the LHC.

[27] K. Hencken et al. The Physics of Ultraperipheral Collisions at the LHC. *Phys. Rept.*, 458:1–171, 2008. URL http://arxiv.org/abs/hep-ex/0201034v1.

[28] G. Baur et al. Hot topics in ultra-peripheral ion collisions. 2002. URL http://arxiv.org/abs/hep-ex/0201034v1.

176

[29] M. G. Albrow et al. The FP420 R&D Project: Higgs and New Physics with forward protons at the LHC. *JINST*, 4:T10001, 2009. URL http://arxiv.org/pdf/0806.0302v2.

[30] F. Abe et al. (CDF Collaboration). Double parton scattering in $p\bar{p}$ collisions at $\sqrt{s} = 1.8 TeV$. *Phys. Rev. D*, 56(7):3811–3832, Oct 1997.

[31] Mario Deile. Pileup Probabilities and Events per Bunch-Crossing. May 2007. URL http://cdsweb.cern.ch/record/1109356/.

[32] G Aad. *Expected performance of the ATLAS experiment: detector, trigger and physics.* CERN, Geneva, 2009. URL http://cdsweb.cern.ch/record/1125884.

[33] Predicted cross sections in mb from Phojet 1.12 and Pythia 6.420. URL http://project-atlas-lucid.web.cern.ch/project-atlas-lucid/taskforce/predicted_xs.pdf.

[34] David G. d'Enterria. Forward Physics at the LHC. 2007. URL http://arxiv.org/abs/0708.0551.

[35] R. Kwee. Studies for the Development of a Minimum Bias Trigger at Low Luminosities in the ATLAS-Experiment at the Large Hadron Collider, 2007. URL http://www-atlas.desy.de/theses/Kwee_dipl.pdf.

[36] *ATLAS: technical proposal for a general-purpose pp experiment at the Large Hadron Collider at CERN.* LHC Tech. Proposal. CERN, Geneva, 1994. URL http://cdsweb.cern.ch/record/290968?ln=it.

[37] G. Aad et al. The ATLAS Experiment at the CERN Large Hadron Collider. *JINST*, 3:S08003, 2008.

[38] Claude Amsler et al. Review of particle physics. *Phys. Lett.*, B667:1, 2008.

[39] W. R. Leo. *Techniques for Nuclear and Particle Physics Experiments.* Springer, 1987.

[40] W H Bell, D Berge, J A Gray, R Kwee, B T Martin, A Messina, E L Nurse, A J Richards, and P A Steinberg. MBTS trigger efficiency for the minimum bias analysis using Inner Detector tracks from pp interactions at sqrt(s) = 900 GeV. Technical Report ATL-COM-DAQ-2010-003, CERN, Geneva, Jan 2010. URL http://cdsweb.cern.ch/record/1235379/.

[41] Joleen Pater. The FP420 Project: The challenge of measuring forward protons at the LHC. *J. Phys. Conf. Ser.*, 110:092022, 2008. URL http://iopscience.iop.org/1742-6596/110/9/092022/.

[42] S. Agostinelli *et al.* G4–a simulation toolkit. *Nuclear Instruments and Methods in Physics Research Section A: Accelerators, Spectrometers, Detectors and Associated Equipment*, 506(3):250 – 303, 2003. URL http://www.sciencedirect.com/science/article/B6TJM-48TJFY8-5/2/23ea98096ce11c1be446850c04cfa498.

[43] K Edmonds, S Fleischmann, T Lenz, C Magass, J Mechnich, and A Salzburger. The Fast ATLAS Track Simulation (FATRAS). Technical Report ATL-SOFT-PUB-2008-001. ATL-COM-SOFT-2008-002, CERN, Geneva, Mar 2008. URL http://cdsweb.cern.ch/record/1091969.

[44] Michael Duehrssen and Karl Jakobs. *Study of Higgs bosons in the WW final state and development of a fast calorimeter simulation for the ATLAS experiment.* PhD thesis, Freiburg, University Freiburg, Freiburg, 2009. URL http://cdsweb.cern.ch/record/1261372?ln=en.

[45] M. L. Perl, G. S. Abrams, A. M. Boyarski, M. Breidenbach, D. D. Briggs, F. Bulos, W. Chinowsky, J. T. Dakin, G. J. Feldman, C. E. Friedberg, D. Fryberger, G. Goldhaber, G. Hanson, F. B. Heile, B. Jean-Marie, J. A. Kadyk, R. R. Larsen, A. M. Litke, D. Lüke, B. A. Lulu, V. Lüth, D. Lyon, C. C. Morehouse, J. M. Paterson, F. M. Pierre, T. P. Pun, and P. A. Rapidis. Evidence for anomalous lepton production in $e + -e-$ annihilation. *Phys. Rev. Lett.*, 35(22):1489–1492, Dec 1975. URL http://prl.aps.org/abstract/PRL/v35/i22/p1489_1.

[46] A. Pich. Tau physics. *Adv. Ser. Direct. High Energy Phys.*, 15:453–492, 1998. URL http://arxiv.org/abs/hep-ph/9704453.

[47] Bechtle *et al.* Identification of hadronic tau decays with ATLAS detector. Technical Report ATL-PHYS-INT-2008-003. ATL-COM-PHYS-2007-066, CERN, Geneva, Sep 2007. URL http://cdsweb.cern.ch/record/1059599?ln=en.

[48] C Limbach. Leptonische Tau-Zerfälle in supersymmetrischen Prozessen im ATLAS-Detektor, 2009. URL http://lhc-ilc.physik.uni-bonn.de/thesis/Diplomarbeit_climbach.pdf.

[49] Abdelhak Djouadi. The Anatomy of electro-weak symmetry breaking. II. The Higgs bosons in the minimal supersymmetric model. *Phys. Rept.*, 459:1–241, 2008. URL http://arxiv.org/abs/hep-ph/0503172v2.

[50] Kaoru Hagiwara, (Ed.), J. Kanzaki, (Ed.), and N. Okada, (Ed.). Supersymmetry and unification of fundamental interactions. Proceedings, 12th International Conference, SUSY 2004, Tsukuba, Japan, June 17-23, 2004. Prepared for 12th International Conference on Supersymmetry and Unification of Fundamental Interactions (SUSY 04), Tsukuba, Japan, 17-23 Jun 2004.

[51] Ian Hinchliffe. Use of Taus in ATLAS. (hep-ph/0210340):6 p, Oct 2002. URL http://cdsweb.cern.ch/record/588795/.

[52] C. Zendler. Studie zu supersymmetrischen Prozessen mit Taus im Endzustand im ATLAS-Experiment am LHC, 2007. URL http://lhc-ilc.physik.uni-bonn.de/thesis/Zendler.pdf.

[53] Till Nattermann, Klaus Desch, Peter Wienemann, and Carolin Zendler. Measuring τ-polarisation in $\tilde{\chi}_2^0$ decays at the LHC. *Journal of High Energy Physics*, 2009(04): 057, 2009. URL http://stacks.iop.org/1126-6708/2009/i=04/a=057.

[54] Ketevi A Assamagan and Y Coadou. Determination of the charged Higgs mass and of tan(beta) with ATLAS. Technical Report ATL-PHYS-2001-017, CERN, Geneva, Nov 2001. URL http://cdsweb.cern.ch/record/685304?ln=en.

[55] A Christov, Y Coadou, Z Czyczula, M Janus, L Janyst, A Kaczmarska, A Kalinowski, J Komaragiri, S Lai, W Mader, N Meyer, E Richter-Was, Ch Ruwiedel, and M Wolter. Performance of the tau reconstruction and identification algorithm with release 14.2.20 and mc08 data. Technical Report ATL-COM-PHYS-2009-229, CERN, Geneva, Apr 2009. URL http://cdsweb.cern.ch/record/1174957?ln=en.

[56] G. Aad et al. Expected Performance of the ATLAS Experiment - Detector, Trigger and Physics. 2009.

[57] Matteo Cacciari, Gavin P. Salam, and Gregory Soyez. The Anti-k(t) jet clustering algorithm. *JHEP*, 0804:063, 2008. URL http://arxiv.org/abs/0802.1189.

[58] C. Schwanenberger. The Jet Calibration in the H1 Liquid Argon Calorimeter. *ArXiv Physics e-prints*, September 2002. URL http://arxiv.org/abs/physics/0209026.

[59] Buskulic *et. al.* Performance of the ALEPH detector at LEP. *Nucl. Instrum. Methods Phys. Res., A*, 360(CERN-PPE-94-170. FSU-SCRI-95-70):481–506. 44 p, Nov 1994. URL http://cdsweb.cern.ch/record/272484/?ln=it.

[60] M A Thomson. Particle Flow Calorimetry and the PandoraPFA Algorithm. Technical Report arXiv:0907.3577. CU-HEP-09-11, Jul 2009. URL http://cdsweb.cern.ch/record/1192027/?ln=de.

[61] A. Bocci, S. Kuhlmann, S. Lami, G. Latino, and A. Bocci. Study of Jet Energy Resolution at CDF. *International Journal of Modern Physics A*, 16:255–258, 2001. URL http://adsabs.harvard.edu/abs/2001IJMPA..16S.255B.

[62] M C Hodgkinson, D R Tovey, and R Duxfield. Energy Flow Reconstruction with the eflowRec Combined Reconstruction Software in Athena 15.6.9.8. Technical report, CERN, Geneva. Note in preparation.

[63] Joanna Weng. A Global Event Description using Particle Flow with the CMS Detector. Technical Report arXiv:0810.3686, Oct 2008. URL http://cdsweb.cern.ch/record/1135775. Comments: Poster at ICHEP08, Philadelphia, USA, July 2008. 3 pages.

[64] W Lampl, S Laplace, D Lelas, P Loch, H Ma, S Menke, S Rajagopalan, D Rousseau, S Snyder, and G Unal. Calorimeter Clustering Algorithms: Description and Performance. Technical Report ATL-LARG-PUB-2008-002. ATL-COM-LARG-2008-003, CERN, Geneva, Apr 2008. URL http://cdsweb.cern.ch/record/1099735/.

[65] J.-W. Tsung. Identification of 1-prong τ-decays into nπ^0 Final States Using Topological Clusters with ATLAS, 2008. URL http://lhc-ilc.physik.uni-bonn.de/thesis/Diplomarbeit_climbach.pdf.

[66] M C Hodgkinson, D R Tovey, and R Duxfield. Energy Flow Reconstruction with eflowRec Combined Reconstruction Software in Athena 12.0.6. Technical Report ATL-COM-PHYS-2007-082, CERN, Geneva, Oct 2007. URL https://cdsweb.cern.ch/record-restricted/1064042/.

[67] T Barillari, E Bergeaas Kuutmann, T Carli, J Erdmann, P Giovannini, K J Grahn, C Issever, A Jantsch, A Kiryunin, K Lohwasser, A Maslennikov, S Menke, H Oberlack, G Pospelov, E Rauter, P Schacht, F Span, P Speckmayer, P Stavina, and P Strzenec. Local Hadronic Calibration. Technical Report ATL-LARG-PUB-2009-001. ATL-COM-LARG-2008-006, CERN, Geneva, Jun 2008. URL http://cdsweb.cern.ch/record/1112035?ln=pl.

[68] Private communication with M. Hodgkinson.

[69] S Fleischmann, C Limbach, R Prabhu, and P Wienemann. PanTau: An energy-flow based approach to τ-reconstruction in ATLAS. ATLAS note in preparation.

[70] Torbjorn Sjostrand, Stephen Mrenna, and Peter Z. Skands. PYTHIA 6.4 Physics and Manual. *JHEP*, 05:026, 2006. URL http://arxiv.org/abs/hep-ph/0603175v2.

[71] J Dingfelder, M Janus, and V Scharf. π^0 Reconstruction in Tau Decays. Talk given at the *2009 ATLAS Workshop on tau lepton physics (Copenhagen, Denmark)*.

[72] A Hcker, J Stelzer, F Tegenfeldt, H Voss, K Voss, A Christov, S Henrot-Versill, M Jachowski, A Krasznahorkay, Y Mahalalel, X Prudent, and P Speckmayer. TMVA - Toolkit for Multivariate Data Analysis with ROOT: Users guide. Technical Report CERN-OPEN-2007-007, CERN, Geneva, Mar 2007. URL http://tmva.sourceforge.net/docu/TMVAUsersGuide.pdf.

[73] S Fleischmann. Truth matching for reconstructed taus: Track-based matching and ΔR matching. Talk given in ATLAS Tau Working Group Meeting, Jun 2009. URL http://indico.cern.ch/contributionDisplay.py?contribId=5&confId=54879.

[74] Standard Definitions of Efficiency and Rejection for the Tau Working Group. URL https://twiki.cern.ch/twiki/bin/view/AtlasProtected/TauIdentification. ATLAS Tau Working Group internal TWIKI page.

[75] T Nattermann. Studie zu Effekten der Tau-Polarisation in den $\tilde{\chi}_2^0$-Zerfällen mit dem ATLAS-Experiment, 2008. URL http://lhc-ilc.physik.uni-bonn.de/thesis/DiplomarbeitNattermann.pdf.

[76] M Thomson. Particle Flow Calorimetry and ILC Detector Design. Seminar talk given at Bonn University, Jan 2008. URL http://pi.physik.uni-bonn.de/events.php?id=406.

[77] *ATLAS computing: Technical Design Report*. Technical Design Report ATLAS. CERN, Geneva, 2005. URL http://cdsweb.cern.ch/record/837738. revised version submitted on 2005-06-20 16:33:46.

[78] R Prabhu, K Desch, and P Wienemann. Estimating Missing Transverse Energy at the Generator Level. Technical Report ATL-COM-PHYS-2007-019, CERN, Geneva, Mar 2007. URL http://cdsweb.cern.ch/record/1024673/.

[79] *ATLAS detector and physics performance: Technical Design Report, 2.* Technical Design Report ATLAS. CERN, Geneva, 1999. URL http://cdsweb.cern.ch/record/391177.

[80] A. Abulencia et al. Observation of exclusive electron positron production in hadron hadron collisions. *Phys. Rev. Lett.*, 98:112001, 2007. doi: 10.1103/PhysRevLett.98.112001. URL http://arxiv.org/abs/hep-ex/0611040v2.

[81] P. Achard et al. Muon pair and tau pair production in two-photon collisions at LEP. *Phys. Lett.*, B585:53–62, 2004. doi: 10.1016/j.physletb.2004.02.012.

[82] A. Aktas et al. Tau lepton production in e p collisions at HERA. *Eur. Phys. J.*, C48:699–714, 2006. doi: 10.1140/epjc/s10052-006-0028-2.

[83] J. de Favereau de Jeneret et al. High energy photon interactions at the LHC. 2009.

[84] Valery A. Khoze, Alan D. Martin, R. Orava, and M. G. Ryskin. Luminosity monitors at the LHC. *Eur. Phys. J.*, C19:313–322, 2001. doi: 10.1007/s100520100616.

[85] Bryan Lawrence Caron. Luminosity measurement at the Large Hadron Collider. UMI-NR-13944.

[86] V. I. Telnov A.G. Shamov. Precision luminosity measurement at LHC using two-photon production of $\mu^+\mu^-$ pairs. *Nucl. Inst. & Meth.*, A 494:51–56, 2002.

[87] M Albrow and *et al.* Technical report.

[88] J. A. M. Vermaseren. Two Photon Processes at Very High-Energies. *Nucl. Phys.*, B229:347, 1983. doi: 10.1016/0550-3213(83)90336-X.

[89] S. P. Baranov, O. Duenger, H. Shooshtari, and J. A. M. Vermaseren. LPAIR: A generator for lepton pair production. In *Hamburg 1991, Proceedings, Physics at HERA, vol. 3*1478-1482. (see HIGH ENERGY PHYSICS INDEX 30 (1992) No.12988).

[90] F. *et al* Abe. Measurement of $p\bar{p}$ single diffraction dissociation at $\sqrt{s}$ =546 and 1800 GeV. *Phys. Rev. D*, 50(9):5535–5549, Nov 1994. URL http://prd.aps.org/abstract/PRD/v50/i9/p5535_1.

[91] 10^{31} Trigger Menu justification document for the old L1 calibration. ATLAS internal Twiki. URL https://twiki.cern.ch/twiki/bin/view/Atlas/L31TriggerMenuOldL1Calib#Primary_egamma_triggers.

[92] Atlas Trigger Rates. URL https://twiki.cern.ch/twiki/bin/view/Atlas/AtlasTriggerRates.

[93] Cut based identification of hadronic tau decays. Technical Report ATL-PHYS-PUB-2010-001. ATL-COM-PHYS-2009-583, CERN, Geneva, Jan 2010. URL http://cdsweb.cern.ch/record/1233743?ln=en.

[94] Marc Paterno. Calculating efficiencies and their uncertainties. 2003. URL `http://home.fnal.gov/~paterno/images/effic.pdf`. FERMILAB-TM-2286-CD.

[95] G Cowan. Discovery significance with statistical uncertainty in the background estimate. URL `http://www.pp.rhul.ac.uk/~cowan/stat/notes/SigCalcNote.pdf`.

[96] Ultraperipheral collisions with the ATLAS detector. *Nuclear Physics B - Proceedings Supplements*, 184:180 – 181, 2008. ISSN 0920-5632. Proceedings of the International Conference on the Structure and Interactions of the Photon, Including the 17th International Workshop on Photon-Photon Collisions and the International Workshop on High Energy Photon Linear Colliders - PHOTON 2007.

[97] A Angerami, A Ajitanand, G Atoian, M D Baker, S Bathe, W K Brooks, P Chung, B Cole, R Debbe, D Derendarz, J Dolejsi, N Grau, J Hill, W Holzmann, V Issakov, J Jia, R Lacey, A Lebedev, M Leite, S Milov, P Nevski, A Olszewski, A Poblaguev, V Pozdynakov, M Rosati, L Rosselet, M Rybar, H Santos, M Spousta, P Steinberg, H Takai, S Timoshenko, A Trzupek, I Tserruya, F Videbaek, S White, B Wosiek, K Wozniak, and M Zeller. Heavy Ion Physics with the ATLAS Detector at the LHC. Technical Report ATL-COM-PHYS-2009-439, CERN, Geneva, Aug 2009. URL `http://cdsweb.cern.ch/record/1200454?ln=en`.

[98] K. Hencken, Yu. V. Kharlov, G. V. Khaustov, S. A. Sadovsky, and V. D. Samoylenko. TPHIC, event generator of two photon interactions in heavy ion collisions. URL `http://web.ihep.su/library/pubs/prep1996/96-38-e.htm`. IFVE-96-38.

[99] T. Gleisberg, S. Hche, F. Krauss, M. Schnherr, S. Schumann, F. Siegert, and J. Winter. Event generation with SHERPA 1.1. *Journal of High Energy Physics*, 2009(02):007, 2009. URL `http://stacks.iop.org/1126-6708/2009/i=02/a=007`.

[100] J. Monk and A. Pilkington. ExHuME: A Monte Carlo event generator for exclusive diffraction. *Comput. Phys. Commun.*, 175:232–239, 2006. URL `http://arxiv.org/abs/hep-ph/0502077`.